A Functional Renormalization Group Perspective

on

Quantum Spin Liquids

in

Three-Dimensional Frustrated Magnets

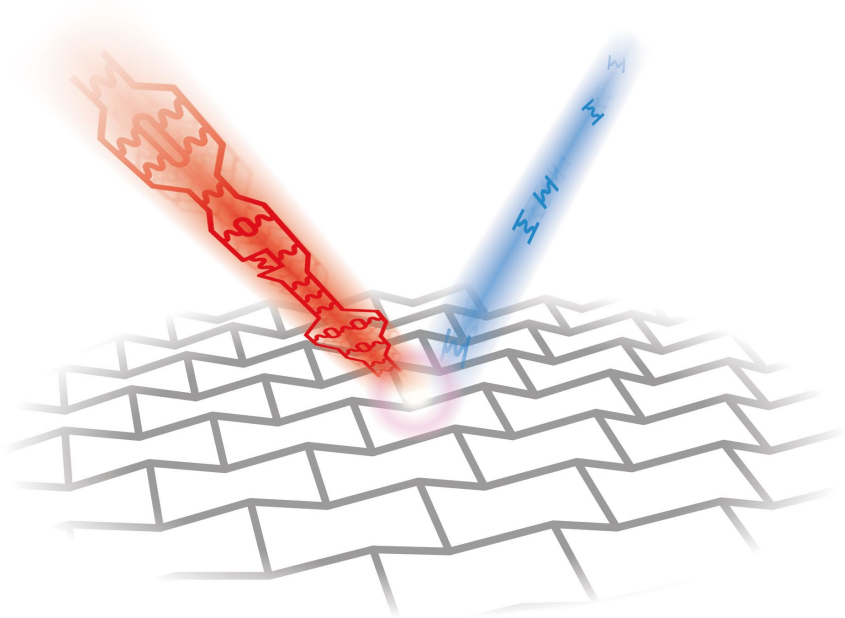

Finn Lasse Buessen

Dissertation

A Functional Renormalization Group Perspective on Quantum Spin Liquids in Three-Dimensional Frustrated Magnets

Inaugural-Dissertation

zur

Erlangung des Doktorgrades

der Mathematisch-Naturwissenschaftlichen Fakultät

der Universität zu Köln

vorgelegt von

Finn Lasse Büßen

aus Flensburg

Köln 2019

Berichterstatter:	Prof. Dr. Simon Trebst
	Priv.-Doz. Dr. Michael Scherer
	Prof. Dr. Ronny Thomale
Tag der mündlichen Prüfung:	23.08.2019

Abstract

When sizable quantum fluctuations and strong frustration mechanisms act in concert to repel the formation of conventional long-range order in quantum magnets, they can make way for massively entangled spin liquid phases which may imbue the material with extraordinary properties. The search for such curious phases of matter has proceeded for several decades, gaining extra momentum some fifteen years ago when Kitaev proposed an analytically solvable model for a quantum spin liquid with anyonic excitations on the basis of realistic microscopic spin exchange terms [Kitaev, Annals of Physics 321, 2 (2006)]. Attempts to identify different models or materials which harbor quantum spin liquid ground states have kept researchers – experimentalists and theorists alike – in suspense ever since. However, the simulation of quantum many-body systems poses a serious challenge even to modern numerical techniques, particularly in the case of frustrated quantum magnetism in three spatial dimensions. Such models evade tractability by many established approaches, leaving a methodological void.

In this thesis, we report on recent progress in cutting-edge implementations of the pseudo-fermion functional renormalization group (pf-FRG), which has originally been proposed by Reuther and Wölfle in the context of two-dimensional frustrated quantum magnetism with highly symmetric spin interactions [Reuther and Wölfle, Phys. Rev. B 81, 144410 (2010)]. Reflecting the growing interest in models with SU(2) symmetry-breaking spin exchange terms that has followed the unearthing of Kitaev's honeycomb model, we present a generalized implementation of the pf-FRG which is suited to numerically simulate arbitrary microscopic models with diagonal or off-diagonal two-spin interactions, even in three-dimensional frustrated quantum magnets. We provide insight into the inner workings of the method which has emerged over the course of the last couple of years, arguing that the pf-FRG formalism simultaneously combines aspects of a large-S expansion as well as a large-N expansion on equal footing, thus being able to resolve the subtle interplay between magnetic ordering tendencies and disruptive quantum fluctuations.

Moreover, on a case by case basis we explore the stability of quantum spin liquids in paradigmatic models of frustrated quantum magnetism and elucidate the joint action of geometric frustration, exchange frustration, and quantum fluctuations to inhibit the formation of magnetic long-range order. Examples include: (i) a Heisenberg spin model on the three-dimensional diamond lattice where geometric frustration arises from antiferromagnetic next-nearest neighbor interactions. The additional competition with nearest neighbor interactions leads to an unusually large ground state degeneracy already on classical level. The quantum-to-classical transition is studied by systematically varying the spin length and the different roles of quantum fluctuations and thermal fluctuations are discussed. The theory is applied to interpret experiments on the spin-liquid candidate $NiRh_2O_4$; (ii) a Heisenberg antiferromagnet on the face centered cubic

lattice which is augmented by competing bond-directional interactions, evolving around the concurrent manifestation of geometric frustration and exchange frustration. A situation is identified where both mechanisms collude to give rise to an unusually large degree of frustration over a wide parameter regime. We discuss related experimental findings on the highly frustrated iridate compound Ba_2CeIrO_6; (iii) a Heisenberg antiferromagnet on the kagome lattice with additional Dzyaloshinskii-Moriya interactions. The robustness of the unperturbed kagome antiferromagnet's spin liquid ground state against low-symmetry Dzyaloshinskii-Moriya interactions is investigated. Implications for the spin-liquid candidate herbertsmithite are discussed.

Kurzzusammenfassung

Wenn starke Quantenfluktuationen und Frustrationsmechanismen mit geeinten Kräften die Bildung von konventioneller langreichweitiger Ordnung verhindern, können stattdessen massiv verschränkte Spinflüssigkeitszustände entstehen, die dem Material außerordentliche Eigenschaften verleihen. Die Suche nach solch merkwürdigen Zuständen in Materie läuft seit einigen Jahrzenten; Besonderen Nachdruck verliehen hat ihr vor etwa 15 Jahren die Entdeckung eines analytisch exakt lösbaren Modells einer Quantenspinflüssigkeit mit anyonischen Anregungszuständen und realistischen mikroskopischen Kopplungen durch Kitaev [Kitaev, Annals of Physics 321, 2 (2006)]. Die Bemühungen, verschiedene Modelle und Materialien zu identifizieren, die Spinflüssigkeits-Grundzustände beherbergen, hat Forscher – Theoretiker und Experimentalphysiker gleichermaßen – seitdem in Atem gehalten. Allerdings stellt die Simulation von Quantenvielteilchensystemen sogar für moderne numerische Techniken eine große Herausforderung dar, insbesondere im Falle von frustriertem Quantenmagnetismus in drei räumlichen Dimensionen. Derartige Modelle entziehen sich einer Beschreibung durch viele konventionelle Ansätze und sind daher methodisch schwer zugänglich.

In dieser Arbeit berichten wir über aktuelle Fortschritte in modernen Implementierungen der pseudo-fermionischen funktionellen Renormierungsgruppe (pf-FRG), welche ursprünglich von Reuther und Wölfle im Kontext von zweidimensionalem Quantenmagnetismus mit hochsymmetrischen Wechselwirkungen eingeführt wurde [Reuther und Wölfle, Phys. Rev. B 81, 144410 (2010)]. Wir präsentieren, das wachsende Interesse an SU(2)-symmetriebrechenden Spinwechselwirkungen widerspiegelnd welches auf die Entdeckung von Kitaevs Honigwabenmodell zurückgeht, eine verallgemeinerte Formulierung der pf-FRG, die imstande ist, beliebige mikroskopische Modelle mit diagonalen oder nicht-diagonalen paarweisen Spinwechselwirkungen numerisch abzubilden – sogar Modelle von dreidimensionalem frustrierten Magnetismus. Wir setzen uns mit Erkenntnissen zur Funktionsweise der Methode auseinander, die im Laufe der vergangenen Jahre gewonnen werden konnten, und argumentieren dass der pf-FRG-Formalismus auf gleichberechtigte Art verschiedene Aspekte von systematischen Reihenentwicklungen in der Spinlänge und der Spinsymmetrie verbindet, was dessen Fähigkeit begründet, das subtile Zusammenspiel von magnetischen Ordnungstendenzen und Unordnung schaffenden Quantenfluktuationen aufzulösen.

Außerdem untersuchen wir anhand von aussagekräftigen Fallbeispielen die Stabilität von Quantenspinflüssigkeiten und erörtern das Zusammenwirken von geometrischer Frustration, Austauschfrustration und Quantenfluktuationen im Hinblick auf die Unterdrückung von langreichweitiger magnetischer Ordnung. Die Fallbeispiele umfassen: (i) Ein Heisenberg-Modell auf dem dreidimensionalen Diamantgitter, welches mit geometrischer Frustration versehen ist, die auf antiferromagnetische Übernächste-Nachbar-

Wechselwirkungen zurückgeht. Der zusätzliche Wettstreit mit Nächsten-Nachbar-Wechselwirkungen führt schon im klassischen Modell zu einer außergewöhnlich hohen Grundzustandsentartung. Der Übergang vom klassischen Fall zum Quantenfall wird untersucht indem systematisch die Spinlänge variiert wird, und es werden die unterschiedlichen Auswirkungen von Quantenfluktuationen und thermischen Fluktuationen diskutiert. Das Modell wird herangezogen, um Experimente an dem Spinflüssigkeitskandidaten $NiRh_2O_4$ zu interpretieren; (ii) Einen Heisenberg-Antiferromagneten auf dem kubisch flächenzentrierten Gitter, welcher mit zusätzlichen richtungsabhängigen Wechselwirkungen versehen ist und somit gleichzeitig geometrische Frustration und Austauschfrustration aufweist. Es wird eine Bedingung identifiziert, unter der sich beide Mechanismen gegenseitig verstärken und zu ungewöhnlich starker Frustration über einen großen Parameterbereich führen. Der Bezug zu Experimenten an dem hochfrustrierten Iridat Ba_2CeIrO_6 wird hergestellt; (iii) Einen Heisenberg-Antiferromagneten auf dem Kagome-Gitter mit zusätzlichen Dzyaloshinskii-Moriya-Wechselwirkungen. Die Stabilität der ursprünglichen Kagome-Spinflüssigkeit gegenüber den niedrigsymmetrischen Dzyaloshinskii-Moriya-Wechselwirkungen wird untersucht. Die Implikationen für den Spinflüssigkeitskandidaten Herbertsmithit werden thematisiert.

Contents

1. Introduction

Quantum spin liquids are curious phases of matter in which the proliferation of magnetic order is impeded by the presence of strong quantum fluctuations even at lowest temperatures down to absolute zero. The term *quantum spin liquid* is a tribute to the early observation that magnetic moments in such a phase of matter, despite exhibiting strong short-range correlations, seem to remain disordered across longer distances – just like particles in a conventional liquid. Yet, while the absence of magnetic long-range order is a pivotal aspect of quantum spin liquids, it constitutes only a negative definition, characterizing what a spin liquid is *not* – and, more importantly, it conceals the significant progress that has been achieved in carving out the extraordinary properties of quantum spin liquids that by no means can be associated with conventional liquids. Converging towards a universal, positive definition of quantum spin liquids remains difficult, but some aspects have received a great deal of attention in the past: (i) quantum spin liquids are understood to be highly entangled states of matter, (ii) they have the ability to host non-local excitations which are associated with the fractionalization of the original spin degrees of freedom and emergent gauge fields, and (iii) they can have topological properties [1, 2].

All three aspects are intimately linked to each other by the implication of non-locality. The property of massive entanglement can be understood to guarantee that any finite part of the system cannot be smoothly connected to a simple product state, which is essential in order to enable the system to host non-local excitations, quasiparticles, whose appearance can be explained in a framework of fractionalization of the original degrees of freedom into a new type of particle, partons, that live in the background of an emergent gauge field. The partons may carry fractional quantum numbers and have decisively different physical properties than any of the constituents in the original physical system. In particular, their physical properties can be of a form which cannot be generated from any finite number of local operators in the original model – if the latter was the case, the parton state could be labeled by a combination of all quantum numbers involved in the sequence of local operations, and the composite operator would consequently describe a well-defined object that has a finite spatial extent. This would be at odds with the emergent partons' ability to have non-trivial exchange statistics, requiring them to 'sense' each others presence at arbitrary distance [1]. Similar reasoning holds for the relation between entanglement and the formation of topological properties – which are, by definition, non-local [3].

Being at the foundation of many fascinating, yet intricate, many-body phenomena, the inherently quantum mechanical nature of highly entangled states of matter also implies great challenges in their analysis in terms of analytic approaches as well as numerical simulations. Despite these deep-rooted difficulties, unparalleled insight into

the phenomenology of quantum spin liquids has been drawn from the revelation of the much celebrated Kitaev honeycomb model [4]. Being amenable to an exact solution, direct investigation of the fractionalization process of the original spin degrees of freedom into emergent Majorana fermions and an accompanying static $\mathbb{Z}_2$ gauge field is possible. It was quickly appreciated that non-diagonal spin interactions of Kitaev type can be realized in actual materials, which has sparked formidable activity in the search for geniune Kitaev materials [5].

Yet the search for quantum spin liquids is neither constrained to the Kitaev honeycomb model nor to two-dimensional models. Various spin liquid candidates have also been identified in three-dimensional materials, where frustrated interactions and quantum fluctuations may remain sufficiently strong to defy magnetic order, despite the generally larger coordination numbers in higher dimensional lattice graphs. The theoretical analysis of three-dimensional frustrated quantum magnets, however, poses a serious challenge to modern quantum many-body simulation techniques.

In this thesis, we attack the elusive field of three-dimensional frustrated quantum magnetism by adopting a functional renormalization group (pf-FRG) formalism which brings together aspects of modern quantum field theory and state of the art numerical techniques. The technique was first employed by Reuther and Wölfle in 2010 [6] and has since been refined significantly. Many important results in this thesis go back to significant progress in method development around the pf-FRG approach. Consequently, the thorough review of the current state of the pf-FRG formalism as a tool for the simulation of frustrated quantum magnets is a central goal of this thesis.

However, equally important, this thesis is devoted to the exploration of frustrated quantum magnets and microscopic models thereof as potential platforms to stabilize spin liquid ground states, with a focus on three-dimensional models. Mediating at the interface between aesthetically pleasing minimal models which strive for maximum elegance and simplicity on the one hand, and intricate models which reflect the experimental reality of imperfect materials and the involvement of unfavorable spin exchange terms on the other hand, we are interested in the stability of quantum spin liquid phases under perturbations of the underlying models. Any knowledge about the stability of spin liquid regimes and the relevance of perturbations provides valuable guidance for material design and contributes to our chances to unveil new materials which can cultivate spin liquid ground states.

We specifically address three different incarnations of frustrated quantum magnets, where in each case we formulate a microscopic model, make predictions based on pf-FRG simulations, and relate the predictions to experiment: (i) We address a model of Heisenberg spins on the diamond lattice, where geometric frustration arises from antiferromagnetic next-nearest neighbors. We illustrate the formation of a quantum spiral spin liquid ground state that benefits from an unconventionally large classical ground-state degeneracy whose details depend on the precise ratio of involved nearest neighbor and next-nearest neighbor spin interactions. We resolve the connection between the quantum model and the classical limit in greater detail by systematically manipulating the spin length, in order to trace the subtle competition between disordering quantum

fluctuations and thermal order-by-disorder effects. We relate our findings to recent measurements on the spin-1 spinel material $NiRh_2O_4$ where no indications of magnetic order have been reported. (ii) We address a model of antiferromagnetic Heisenberg interactions on the face centered cubic lattice which are augmented by additional bond-directional Kitaev-like exchange couplings. We focus on the concurrent manifestation of geometric frustration and exchange frustration, and we identify a parameter regime where both mechanism collude to give rise to an unusually large degree of frustration. We invoke this theory on the spin-orbit entangled $j = 1/2$ iridate compound Ba_2CeIrO_6 to interpret recent experimental findings. (iii) Finally, we consider the kagome Heisenberg antiferromagnet in the presence of additional Dzyaloshinskii-Moriya interactions as an example of a model where off-diagonal spin interactions become relevant. The theory is applied to the kagome material herbertsmithite.

The remainder of this introductory chapter covers two complementary themes: what physical mechanisms may give rise to quantum spin liquids, and which techniques can be used to simulate microscopic models of frustrated quantum magnetism. The first question is addressed in Section 1.1, where we review a number of motifs which frequently appear in models and materials that ultimately harbor spin liquid phases. The aim of this section is to convey a feeling of what knobs and handles can be turned in an attempt to engineer spin liquid phases, or to push proximate spin liquid materials closer to a true quantum spin liquid ground state. We eventually follow up on these motifs in Chapter 3 where they make recurrent appearances in our studies of the various models of frustrated quantum magnetism mentioned above, and we shall indeed see how they give rise to quantum spin liquid ground states in realistic settings. The second question is addressed in Section 1.2, where we briefly review some of the most important methods and numerical approaches which researchers have been using in the past to study frustrated quantum magnets. The section is intended to provide context on the method development and to prepare for the review of the pseudo-fermion functional renormalization group, which is the main subject in Chapter 2 of the thesis.

1.1. Recurring motifs in spin liquids

While no sure formula exists to engineer quantum spin liquid phases, there are some guiding themes which have proven helpful in the search for this elusive phase of matter. In this first section, we review several aspects that frequently seem to play a central role in finding ways to repel magnetic order. These facets include the role of classically degenerate ground states and thermal fluctuations, quantum fluctuations, resonating valence bonds, and frustration.

1.1.1 Classical spins. Classical spins are intuitive objects. A classical spin is conventionally associated with a vector in three-dimensional space, meaning that its configuration is uniquely determined by a length and a sense of orientation. By means of this identification one can adopt the formalism of vector calculus to model the interaction of two (or more) spins. A quantitative description of the interaction of spins is naturally given by their exchange energy – a number which determines whether a given local configuration is favorable (the configuration has a low exchange energy) or unfavorable (it has a high exchange energy). In many materials the exchange energy of two spins is modeled sufficiently well by assuming isotropic interactions, where the exchange energy is computed as the scalar product of two interacting spins. This model is referred to as the classical Heisenberg model and its Hamiltonian reads

$$H = \sum_{i,j} J_{ij} \vec{\mathbf{s}}_i \vec{\mathbf{s}}_j \quad , \tag{1.1}$$

where $\vec{\mathbf{s}}_i$ and $\vec{\mathbf{s}}_j$ are vectors on the unit sphere representing (normalized) spins at lattice sites i and j, respectively. The interaction parameter J_{ij} quantifies the interaction strength between pairs of spins. The sign of the coupling constant determines whether the exchange energy is minimized by a ferromagnetic state ($J_{ij} < 0$) or an antiferromagnetic configuration ($J_{ij} > 0$). The interaction constant can in principle be assigned an arbitrary value for any two pairs of spins, but for meaningful physical models it is constrained by symmetries of the underlying lattice. Furthermore, realistic interactions are often short-ranged since the magnitude of the effective interaction results from the overlap of localized electronic orbitals [7]. Yet, the exchange constants can also become long-ranged, e.g. in the presence of dipolar interactions [8], or in more exotic superstructure materials [9]. In general, there is no upper limit for potential complications to add to the model. One can study anisotropies in the spin interaction, where the coupling constant is different for every component of the spins. One can study lattice anisotropies which strengthen or weaken interactions along certain lattice directions. One can study three-spin interactions, or even higher orders. One can add a magnetic field. There is a long list of more intricate models which have become popular enough to coin their own names. Any of these models can – and often do – give rise to a rich field of physics that is worth studying on its own. Some of the models aim at establishing unconventional forms of magnetic order [10], while other models aim at suppressing magnetic order altogether, giving way to potential spin liquid phases.

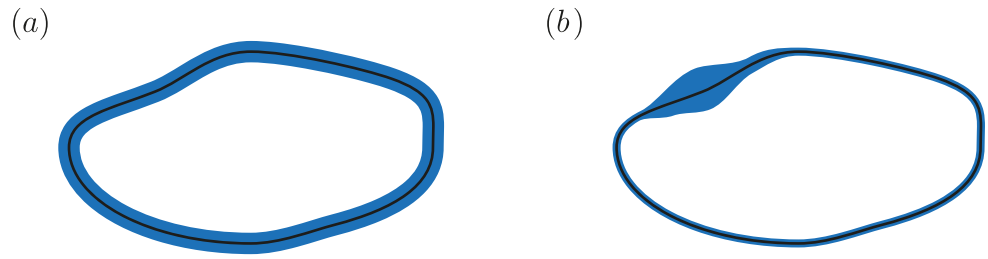

Figure 1.1. **Order by disorder.** (a) A degenerate manifold of states (black line) with thermally accessible excitations (blue region). Every configuration in the manifold is associated with the same number of thermally accessible excitations. (b) A subset of states in the degenerate manifold has access to significantly more excited states (top left region of the manifold). The larger entropy generated from the enhanced number of thermally accessible configurations reduces the free energy for certain configurations within the degenerate manifold, and those configurations are likely to be selected as the ground state of the system.

1.1.2 Order by disorder. Aiming for the cultivation of a spin liquid is challenging. A classical spin liquid, which does not exhibit magnetic long-range order, arises from the presence of an extensively degenerate ground state which is often the result of fine tuning of parameters – as such it is fundamentally different from a quantum spin liquid, which can be captured by a single quantum mechanical wave function (we discuss this in the next sections). Sustaining an ensemble of degenerate states at non-zero temperatures is even more challenging, since this does not just require the states to have the same energy, but it also requires the states to have similar excitations. If a subset of the degenerate states has lower excitations than the remaining configurations, those configurations will have a lower free energy since thermal fluctuations may occupy a more expansive number of excited states which results in a larger entropy (see Fig. 1.1). The subset of configurations which minimizes the free energy is likely to be selected as the ground state of the system. Therefore, thermal fluctuations can potentially stabilize a particular configuration of magnetic order out of an ensemble of otherwise degenerate states. Consequently, the mechanism was coined 'order by disorder' [11].

In Sec. 3.1, we discuss an exemplary model where order by disorder plays a decisive role. We make the connection between a classical version of the spin model, which hosts a (sub-)extensive number of degenerate ground state configurations, to the quantum version of the model, where thermal fluctuations are accompanied by quantum fluctuations. We shall see that both, thermal fluctuations and quantum fluctuations lift the ground state degeneracy by means of order by disorder and quantum order by disorder, respectively. Yet, we shall further see that classical spins eventually undergo a thermal phase transition into magnetic long-range order while quantum order by disorder may not be strong enough to induce magnetic order, such that quantum spins remain fluctuating even at lowest temperatures.

1.1.3 Quantum spins. Within this thesis, we are interested in the study of spin liquids, more specifically quantum spin liquids. Promoting classical spins to quantum spins introduces quantum fluctuations which can help to suppress magnetic order, given that the ordering tendency is not too strong. In analogy to the classical Heisenberg model (1.1), the quantum version of the Heisenberg model is given by the Hamiltonian

$$H = \sum_{i,j} J_{ij} \mathbf{S}_i \mathbf{S}_j \quad . \tag{1.2}$$

The quantum mechanical spin-1/2 moments are now represented by the operator-valued vectors $\mathbf{S}_i$ with three components S_i^α, where $\alpha \in \{x, y, z\}$. Unlike in the classical model, the individual spin components no longer commute. Instead, they obey the commutation relations of the SU(2) algebra,

$$\left[S_i^\alpha, S_j^\beta\right] = \delta_{ij} \epsilon_{\alpha\beta\gamma} S_i^\gamma \quad , \tag{1.3}$$

and can thus be represented in the basis of Pauli matrices

$$S_i^\alpha = \frac{1}{2} \sigma^\alpha \quad , \tag{1.4}$$

where the three Pauli matrices σ^α are given by

$$\sigma^x = \begin{pmatrix} 0 & 1 \\ 1 & 0 \end{pmatrix} \qquad \sigma^y = \begin{pmatrix} 0 & -i \\ i & 0 \end{pmatrix} \qquad \sigma^z = \begin{pmatrix} 1 & 0 \\ 0 & -1 \end{pmatrix} \quad . \tag{1.5}$$

This specific choice of representation in terms of hermitian 2×2 matrices implies that the spin operators act on the two-dimensional spinor space of spin-1/2 moments. The two dimensions of the spinor are identified with the two eigenstates of the S^z operator, which have eigenvalues $+1/2$ (spin up) and $-1/2$ (spin down). We denote these basis states as $|\uparrow\rangle$ and $|\downarrow\rangle$, respectively, and refer to them as the S^z-basis. We shall remind ourselves at this point that the spin length is encoded in the dimensionality of the representation of the SU(2) group (which in this case is two), not in the choice of the symmetry group itself (which in this case is SU(2)). It is therefore possible to change the spin length and the spin symmetry independently; later on in this thesis, we explicitly construct SU(N) generalized spin models, see Sec. 2.5.4.

1.1.4 Quantum fluctuations. Two of the three components of a spin operator can equivalently be rewritten in terms of spin raising and lowering operators

$$S_i^+ = S_i^x + i S_i^y \quad S_i^- = S_i^x - i S_i^y \quad , \tag{1.6}$$

which are obtained as linear combinations of the original operators. They act on the basis states according to

$$S^+ |\uparrow\rangle = 0 \qquad S^+ |\downarrow\rangle = |\uparrow\rangle \qquad S^- |\uparrow\rangle = |\downarrow\rangle \qquad S^- |\downarrow\rangle = 0 \quad . \tag{1.7}$$

As suggested by the naming, the spin raising operator can raise the z-component of a spin from $-1/2$ to $+1/2$, but it annihilates a $+1/2$ state. Conversely, the spin lowering operator changes a spin state $+1/2$ into $-1/2$. We may specify arbitrary spin configurations in the S^z-basis, such that they are eigenstates of the S^z operator by construction. Yet, if the Hamiltonian of the microscopic spin model contains not only S^z operators it evidently generates transitions between different spin configurations via spin raising or lowering operations, and it is even likely to return superpositions of different configurations. These quantum fluctuations between different spin configurations can drive the system away from magnetic order and remain present down to zero temperature, where thermal fluctuations fade out.

The strength of quantum fluctuations depends on the spin length S, which we previously assumed to be 1/2. In the limit of large spins $S \to \infty$ the quantum fluctuations become irrelevant and one approaches the classical limit. We have pointed out in Sec. 1.1.3 that the spin length is represented by the dimensionality of the SU(2) representation; generally, the dimensionality of the representation for arbitrary spin length S is $2S + 1$, i.e. there are $2S + 1$ different eigenstates of the S^z operator with eigenvalues ranging from $-S$ to $+S$. Intuitively, considering the large-S limit where the number of different S^z-components becomes infinite, the quantization constraint becomes negligible and one should expect to approach the classical (non-quantized) limit. More formally, the large-S limit is convenient to study by employing the Holstein-Primakoff transformation [12], which is used to represent the spin operators

$$S^+ = \left(\sqrt{2S - b^\dagger b}\right) b \qquad S^- = b^\dagger \sqrt{2S - b^\dagger b} \qquad S^z = S - b^\dagger b \tag{1.8}$$

in terms of bosonic creation and annihilation operators $b^\dagger$ and b, respectively. The square roots in the expressions for the spin raising and lowering operators can be expanded, with higher order correction terms becoming irrelevant for large spin values S.

In practice, spin liquids often persist only for small quantum spins $S = 1/2$ or $S = 1$ while at larger spin lengths the quantum effects are no longer strong enough to destabilize magnetic order. We investigate such a transition in Sec. 3.1. The question of the stability of spin liquids against variation of the spin length is by no means purely academic: in the synthesis of spin liquid materials, one can not freely vary the ingredients to match any desired spin length, but one is restricted to those choices of constituents that result in stable compounds.

The strength of quantum fluctuations also depends on the spin symmetry group, which we have assumed to be SU(2) so far. In general, the symmetry group can be extended to SU(N), where N is arbitrary. The enhancement of quantum fluctuations at larger values of N is traced back to the observation that the number of generators which are required to form the SU(N) group grows with N; the conventional SU(2) group is spanned by three

generators (which are identified as the x-, y-, and z-components of the spin operator), while the general SU(N) group requires N^2-1 generators. Meanwhile, the commutation relations of the generators remain non-trivial and there can only be a single well-defined quantization axis. The remaining N^2-2 dimensions generate quantum fluctuations within the configuration space and can potentially defy the onset of magnetic ordering.

Similar to the intuition which we have developed for the large-S limit, it seems likely that in an excessively enlarged symmetry group SU(N) the discrete character of a finite number of generators may become negligible. Indeed, spin models in the large-N limit often give rise to particularly simple forms of quantum order [13], thereby offering a good entry point for a deeper analysis that could allow to make predictions even for smaller values of N [14] – we discuss this more extensively in Sec. 2.5.4. The emergence of quantum order can be related to the formation of singlet states (valence bonds) which are an inherently quantum superposition of two states; we elaborate on this in the subsequent section. Conventional SU(2)-symmetric quantum spins can form one such valence bond per two spins, while generalized SU(N) spins can form up to N/2 valence bonds per two spins [15].

The generalization of magnetic moments to SU(N) symmetry is worthwhile also because systematical variation of the symmetry group SU(N) offers a way to tune the strength of quantum fluctuations while keeping the spin length fixed, hence we can obtain additional information about the stability of magnetic order and spin liquid phases without explicitly turning quantum spins more classical. Last but not least, generalized SU(N) models away from $N = 2$ can be realized experimentally. Examples of such models have been known in optical lattices [16], while recently SU(4) models have also received attention as possible effective descriptions for bilayer heterostructures [17, 18] in condensed matter systems.

1.1.5 Resonating valence bonds. Based on the reasoning in the previous sections, we can assume that the spin-1/2 quantum Heisenberg model is a sensible starting point in our pursuit of quantum spin liquid states since it naturally entails strong quantum fluctuations. However, quantum fluctuations alone are not necessarily strong enough to destabilize magnetic order. For example, it has been established that the nearest neighbor Heisenberg antiferromagnet on the square lattice has a magnetically ordered ground state despite the Néel ordered ground state not being an eigenstate of the Hamiltonian [19]. In this subsection, we discuss the implications of this finding.

The Hamiltonians for the nearest neighbor Heisenberg ferromagnet (HFM) and the nearest-neighbor Heisenberg antiferromagnet (HAFM) on the square lattice are defined as

$$H = J \sum_{\langle i,j \rangle} \mathbf{S}_i \mathbf{S}_j \quad , \tag{1.9}$$

where $J = -1$ corresponds to the HFM and $J = +1$ is the HAFM and the notation $\sum_{\langle i,j \rangle} \cdot$ indicates a summation over all pairs of nearest neighbor lattice sites on the square lattice. Both models are constrained versions of the general Heisenberg model in Eq. (1.2) in the sense that the spin exchange terms are limited to nearest neighbors and

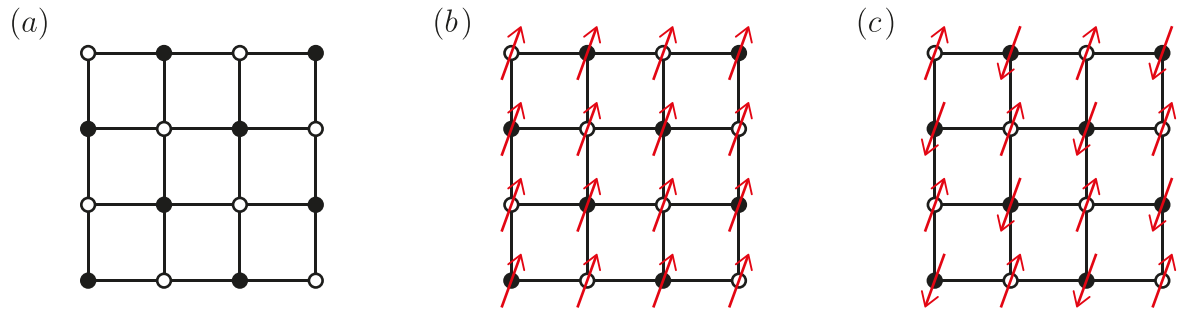

Figure 1.2. **Heisenberg model on the square lattice.** (a) Bipartite character of the square lattice. The lattice can be divided into two subsets A and B, where each site only has neighbors of the opposite subset. The two different sublattices are indicated by black and white colored lattice sites. (b) Ferromagnetic configuration on the square lattice. At each site, the S^z-component of the spin has the same value. (c) Néel configuration on the square lattice. Up and down pointing spins occupy the two sub-lattices A and B, respectively.

they all have equal strength.

The classical analogue of this model turns out to be fairly simple regardless of the sign of the coupling constant. This is due to the fact that the square lattice is bipartite, which means that the lattice can be sub-divided into two sublattices A and B such that each site in in sublattice A only has neighbors in sublattice B, and vice versa (see Fig. 1.2a). Ferromagnetic couplings are easily satisfied by a configuration where all spins point in the same direction (Fig. 1.2b). On any bipartite lattice it is also straightforward to satisfy antiferromagnetic couplings by constructing a configuration where the spins on the two sublattices point in opposite directions. Such a configuration is referred to as a Néel state, see Fig. 1.2c. Both configurations are equivalent (up to the staggered minus sign in the spin orientation) and minimize the energy of their respective Hamiltonian to contribute an exchange energy of $-J/4$ on every lattice bond. Magnetically ordered phases are therefore particularly favorable on lattices with a large coordination number, i.e. a large number of lattice bonds per spin.

In the quantum model, the ferromagnetic and antiferromagnetic configurations are no longer equivalent. For illustration, let us consider a single pair of quantum spins. The Heisenberg exchange between the two spins, in terms of spin raising and lowering operators (1.6), is given by

$$H = \frac{J}{2}\left(S_i^+ S_j^- + S_i^- S_j^+\right) + J S_i^z S_j^z \quad . \tag{1.10}$$

This Hamiltonian has four eigenstates: three triplet states and one singlet state (Fig. 1.3). The ferromagnetic state in Fig. 1.3a, which we know is also the ground state of the classical model (up to the two-fold degeneracy of all spins pointing up or down, respectively), is an eigenstate of the Hamiltonian (1.10) and minimizes its energy. We note that although the Hamiltonian does not induce transitions between the two degenerate states, thermal fluctuations may still drive a transition. In real systems, however, those transitions are

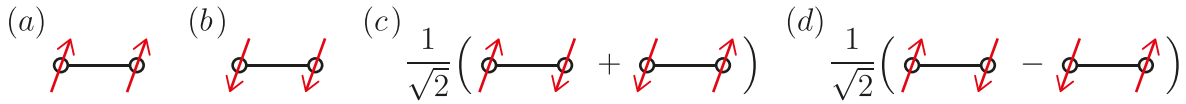

Figure 1.3. **A pair of quantum spins**. The Hilbert space of a single spin is two-dimensional. A system of two such spins is therefore expected to have dimension 4. By convention, the four basis states are grouped into three triplet states, (a) – (c), and one singlet state, (d). The grouping goes back to the fusion rules of angular momenta – two spin-1/2 operators together form either a spin-1 operator (the triplet states with S^z-components -1, 0, and +1) or a spin-0 operator (the singlet state with vanishing S^z-component).

suppressed exponentially in the system size (for two or three-dimensional systems) since the nucleation of a puddle of opposite polarization creates a phase boundary whose defect energy scales with the boundary length, such that in the thermodynamic limit only a single configuration is observed.

In contrast, the Néel configuration is not an eigenstate of the Hamiltonian, which automatically implies additional quantum fluctuations. Furthermore, the energy of a classical antiferromagnetic bond is $-J/4$ while the energy of an inherently quantum mechanical singlet pair (Fig. 1.3d) is $-3J/4$, which gives further preference towards quantum fluctuations. Extending the concept of singlet bonds from a single pair of spins to an entire lattice in the thermodynamic limit, one of two things can happen. Either the outcome is a long-range ordered Néel configuration, which comes with an energy gain on every bond, but which does not gain energy from singlet fluctuations. Alternatively, the outcome could be an extension of the singlet state which is constructed by arranging singlet bonds within the lattice such that every spin is part of a singlet pair. The latter minimizes the energy on singlet bonds at the cost of losing potential energy gain on other bonds. It is not easy to make a prediction on which mechanism dominates in the thermodynamic limit. It seems that on bipartite lattice geometries (e.g. the square lattice [19]) the Néel configuration is the preferred ground state of the Heisenberg antiferromagnet. On non-bipartite lattices the situation can be more complicated, as we shall see in Sec. 1.1.6.

Nevertheless, constructions based on singlet pairs have been discussed extensively in the field of quantum spin liquids. The most straightforward way to construct a macroscopic spin configuration from singlet pairs would be to arrange them in a regular pattern (Fig. 1.4a). Such a state is called a valence bond crystal (VBC). It breaks lattice symmetries and, more importantly, due to its periodic arrangement of singlet bonds it can be broken down into individual, finite clusters. As such, the VBC configuration does not satisfy our expectation for a quantum spin liquid to have massive long-range entanglement. A symmetry preserving construction which cannot be reduced to finite clusters has been proposed by Anderson [20] and is known as the resonating valence bond (RVB) state. It is based on superposing different arrangements of singlet pairs (Fig. 1.4b), leading to highly entangled states of matter which do not break any lattice symmetries. Short-range RVB states have a finite energy gap which corresponds to breaking a single valence bond. However, the construction is not constrained to short-

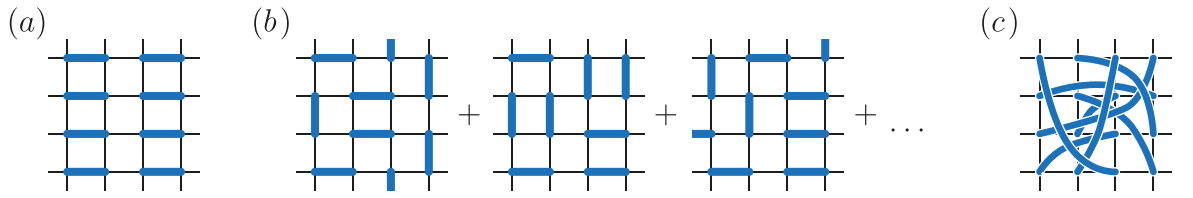

Figure 1.4. **Spin singlet configurations.** (a) Valence bond crystal with periodic arrangement of singlet pairs. (b) Resonating valence bond state constructed from the superposition of different arrangements of singlet bonds. (c) Long-range valence bond configuration.

range valence bonds. One can also envision a long-range RVB state where valence bonds go beyond nearest neighbors (see Fig. 1.4c). Such configurations also support gapless low-energy excitations [21].

VBS and RVB states frequently appear in the discussion of frustrated magnetism and spin liquid candidates. Besides emerging as ground state candidates for various conventional spin models, there exist models which are explicitly constructed in a way that favors valence bond configurations. Such quantum dimer models are often described by Hamiltonians that operate on the manifold of all dimer configurations and contain terms which induce transitions between different dimer states [1, 14].

1.1.6 Frustration. We have argued in the previous subsection that singlet configurations offer a way to minimize the energy on selected lattice bonds at the cost of losing correlation with spins along other bonds. However, this is often unfavorable on bipartite lattices which are naturally compatible with a Néel configuration. In order to further suppress magnetic long range order one needs to introduce frustration – a mechanism which, on Hamiltonian level, introduces a set of constraints or exchange couplings which cannot be satisfied simultaneously. Usually, two different kinds of frustration mechanisms are distinguished: geometric frustration and exchange frustration.

Geometric frustration refers to a situation where a single type of exchange interactions cannot be simultaneously satisfied on all lattice bonds as a consequence of the lattice geometry, even on a classical level. This occurs naturally in non-bipartite lattices with antiferromagnetic interactions, the simplest example being the Heisenberg antiferromagnet on the triangular lattice. On each triangular plaquette the interaction energy can only be minimized on two bonds at a time, while the third bond necessarily violates the antiferromagnetic coupling (at least in the picture of classical spins, see Fig. 1.5a). The triangular HAFM has been discussed extensively in the past and it seems that the ground state exhibits magnetic long range order despite the presence of quantum fluctuations and geometric frustration [22]. Quantum fluctuations are even stronger in a closely related model, the HAFM on the kagome lattice. The kagome lattice is composed of corner sharing triangles, and can be derived from the triangular lattice by depletion of one quarter of the sites (Figs. 1.5b–c). The lower coordination number (four, as opposed to six in the triangular lattice) and a large classical ground-state degeneracy tilt the scales further away from a magnetically ordered ground state. Indeed, the kagome

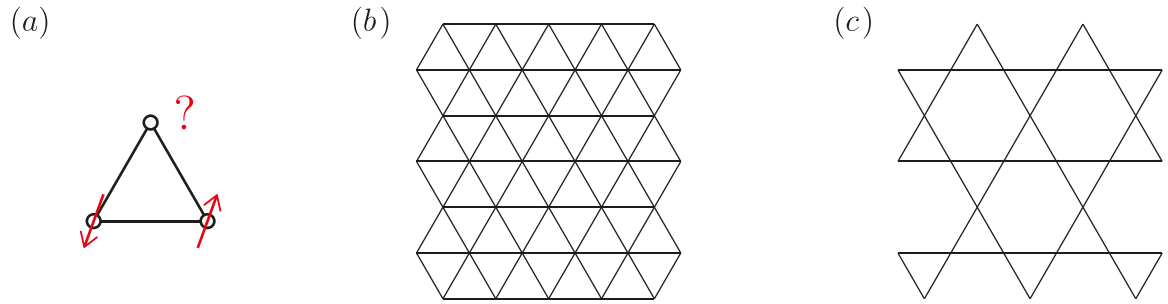

Figure 1.5. **Geometric frustration.** (a) Cartoon picture of geometric frustration. In a triangular plaquette, two spins can be arranged antiferromagnetically. The third spin can only couple antiferromagnetically to one of them, resulting in an energetic penalty on the remaining bond. (b) Triangular lattice. (c) Kagome lattice obtained from the triangular lattice by 1/4 site depletion.

HAFM is widely believed to host a quantum spin liquid ground state [23].

Exchange frustration describes a scenario where multiple competing exchange terms cannot be satisfied simultaneously. Such a situation can be constructed by extending the nearest neighbor Heisenberg model to include interactions between sites that are further apart. A prominent example is the J_1J_2-Heisenberg model on the square lattice (Fig. 1.6a), which is governed by the Hamiltonian

$$H = J_1 \sum_{\langle i,j \rangle} \mathbf{S}_i \mathbf{S}_j + J_2 \sum_{\langle\langle i,j \rangle\rangle} \mathbf{S}_i \mathbf{S}_j \quad , \tag{1.11}$$

where $\langle i,j \rangle$ indicates a sum over nearest neighbors, $\langle\langle i,j \rangle\rangle$ denotes a sum over next-nearest neighbors, and both coupling constants are chosen to be antiferromagnetic. When J_1 is much larger than J_2, the ground state is Néel ordered, i.e. nearest neighbor spins align antiferromagnetically. On the other hand, when J_2 is much larger than J_1, the system exhibits collinear order where next-nearest neighbors align antiferromagnetically. As a result of the competing interactions there exists a regime without magnetic long range order between $J_2/J_1 \approx 0.4$ and $J_2/J_1 \approx 0.6$, whose true nature is still under debate [1].

An alternative way to generate exchange frustration which has grown very popular since the conception of the Kitaev honeycomb model [4] is to define bond-dependent exchange terms where different spin components are coupled along different bond types. For illustration, consider the Kitaev honeycomb Hamiltonian

$$H = K \sum_{\langle i,j \rangle_\gamma} S_i^\gamma S_j^\gamma \quad , \tag{1.12}$$

where $\langle i,j \rangle_\gamma$ runs over nearest neighbors on the tricoordinate honeycomb lattice and γ labels the three types of bonds emanating from each lattice site by x, y, and z as depicted in Fig. 1.6b. Already on a classical level frustration arises from the length constraint

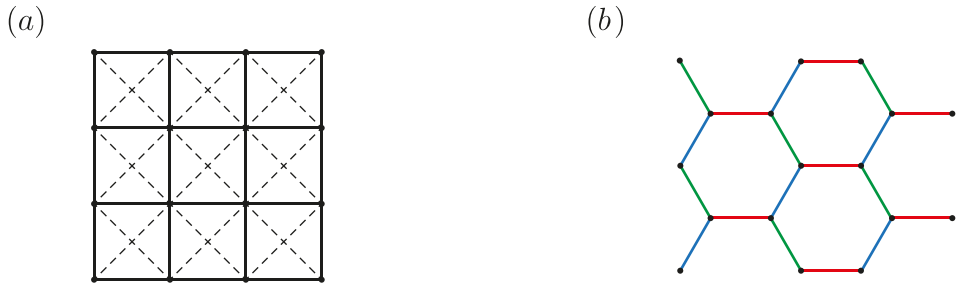

Figure 1.6. **Exchange frustration.** (a) Exchange frustration in the J_1J_2-Heisenberg model on the square lattice. Solid lines denote interactions of strength J_1, dashed lines represent J_2. Antiferromagnetic coupling cannot be simultaneously satisfied for both types of interactions. (b) Exchange frustration in the Kitaev honeycomb model. The x-component of spin operators is coupled along red lattice bonds, the y and z components along green and blue bonds, respectively.

of a spin since it cannot maximize all three components simultaneously; quantum spins naturally introduce further quantum fluctuations. The Kitaev honeycomb model is one of the few models with a quantum spin liquid ground state, where the existence of a quantum spin liquid ground state can be proven analytically [4].

1.2. Simulation techniques for spin liquids

There is only a limit set of techniques available which are suited for the analysis of frustrated quantum magnetism and which remain largely unbiased towards either magnetic ordering tendencies or spin liquid behavior. Three prominent examples among them are (i) exact diagonalization, (ii) different flavors of quantum Monte Carlo techniques, and (iii) the density matrix renormalization group. These methods significantly contribute to the foundation on which modern (numerical) studies of strongly correlated systems are built. In this section we briefly review main aspects of the different techniques, their strengths and their shortcomings. The goal of this section is to provide some context in the landscape of methods in condensed matter theory – and to convey a feeling of when it is appropriate to utilize these established methods, and when the situation might call for a different approach.

1.2.1 Exact diagonalization. Exact diagonalization (ED) can be considered the most direct way to approach a quantum many-body system. It is the brute force way of exactly computing all eigenstates and eigenenergies of an arbitrary Hamiltonian by the numerical diagonalization of the Hamilton matrix acting on a finite dimensional Hilbert space. This has two implications: firstly, the Hilbert space has to be finite. For lattice spin models one needs to operate on lattice graphs with a finite number of sites, which necessarily introduces a boundary to the system. Yet, one may vary the nature of the boundary conditions (make them open boundary conditions or periodic boundary

conditions) and perform a systematic finite-size analysis to obtain an estimate of the impact of boundaries on the bulk system.

The second implication is that one needs to express the model in an explicit basis of the Hilbert space. A straightforward way of doing this is to rewrite spin operators in terms of spin raising and lowering operators, thus formulating everything in the S^z basis (see Sec. 1.1.4). Every spin on the lattice has a local basis of two dimensions, and the total Hilbert space for a lattice of N spins grows exponentially as 2^N. Consequently, the associated Hamilton matrix acting on the Hilbert space has dimension $2^N \times 2^N$. The diagonalization of the Hamilton matrix amounts to the solution of the Schrödinger equation $H|\psi\rangle = E_\psi|\psi\rangle$ in the Hilbert space of enumerated spin configurations $|\psi\rangle = \left|\sigma_1^z \dots \sigma_{2^N}^z\right\rangle$. With the knowledge of all eigenstates it is possible to compute any physical properties of the system, at least in principle. However, due to the exponentially large size of the Hamilton matrix one is restricted to very small system sizes and even after a careful finite-size extrapolation the results may still be severely affected by boundary effects.

Although the overall system sizes which are amenable to treatment by ED remain relatively small, some improvements over the brute force approach are possible. Making use of symmetries and the associated conserved quantities of the Hamiltonian allows a significant reduction of the computational costs of the solution. In the ED formulation, symmetries have a direct impact on the structure of the Hamiltonian matrix; it assumes a block-diagonal form where each block is associated with a fixed set of conserved quantities and any transitions between different configurations can only occur within that block. Such a block-diagonal structure can be diagonalized more efficiently. Furthermore, one often is only interested in low-lying eigenstates of the system, i.e. states with the lowest associated eigenvalues. In order to obtain them it is not necessary to diagonalize the Hamiltonian matrix exactly, but one can make use of algorithms that approximately compute only the low-energy states, e.g. the Lanczos algorithm [24]. Yet, if one is interested in thermodynamic behavior or excited states in general, precise knowledge of all eigenstates is inevitable.

In summary, the advantage of ED is its applicability to arbitrary systems with the only limitation being severe restrictions on the system size. ED studies are often sufficient to obtain insight into two-dimensional quantum magnets, but complex three-dimensional lattice models where already a single unit cell of the lattice can become quite large remain out of reach.

1.2.2 Quantum Monte Carlo. The simulation of quantum magnetism by means of Monte Carlo (MC) techniques is very desirable. MC techniques are stochastic approaches and as such they generate statistical errors. Yet, the error is well controlled and converges towards zero in the limit of long run-times of the simulation; hence, the notion of run-time (or simulation time) is a central measure in MC calculations. The main idea of MC is to generate a finite set of configurations whose statistical distribution adheres to the Boltzmann distribution of the system in thermal equilibrium. The amount of simulation time which has been invested in the calculation directly enters in the number

of configurations which can be generated. In general, the total configuration space is exponentially large, and computing the Boltzmann distribution of all configurations thus is exponentially difficult (c.f. the discussion of exact diagonalization) – within Monte Carlo, however, meaningful results can be achieved in much shorter time by efficiently sampling only a subset of the configuration space, weighted by the Boltzmann distribution. Configurations which are more likely to appear in a real system and therefore have a relatively large impact on observable quantities are also likely to appear in the finite sample of configurations generated in a MC simulation.

Classical magnetism can often be efficiently simulated via Monte Carlo. The trick which allows MC to sample arbitrary probability distributions efficiently is to generate a chain of configurations by iteratively applying local changes until the configurations effectively become independent of each other. The procedure of iteratively applying local changes becomes difficult near phase transitions – in proximity to a phase transition the intrinsic length scale of the system (the correlation length) may diverge and cause fluctuations on all length scales to become equally relevant. Further problems may arise for example in spin glass phases where an extensive number of local energy minima slows down the simulation dramatically and causes it to remain in local energy minima for a significant amount of simulation time. Just like exact diagonalization, MC explicitly operates on the phase space of spin configurations, and thus only finite lattice graphs can be simulated. The system size which can be simulated in MC is much larger than in ED, but in certain models boundary conditions may still become relevant. In chapter 3.1 we discuss such an example where the ground state is characterized by the formation of incommensurate spiral patterns, i.e. spin configurations which are neither compatible with open boundary conditions nor with periodic boundary conditions.

For quantum systems, the set of models that withstand an efficient solution via Monte Carlo techniques is much larger. The non-trivial commutation relations in fermionic quantum many-body systems can lead to negative statistical weights, but the MC algorithm can only work efficiently for positive definite weights – otherwise terms with opposite weight cancel, resulting in a fatal slowdown of statistical error convergence. This is referred to as the 'sign problem' in quantum Monte Carlo. It is often the highly frustrated quantum spin models of interest, which are plagued by the sign problem. Yet, specialized quantum Monte Carlo algorithms have been demonstrated to overcome the sign problem in certain cases, e.g. for the Hubbard model on bipartite lattices [25], or for the Kitaev honeycomb model [26].

Not relying on any severe approximations, quantum Monte Carlo often is the tool of choice for models which are sign-problem free.

1.2.3 Density matrix renormalization group. A third, popular technique in the description of quantum many-body systems is the density matrix renormalization group (DMRG) [27, 28], which is conceptionally very different from the previous two methods. DMRG outlines an algorithm to iteratively adjust and trim the number of internal degrees of freedom in a quantum many-body system as a way to retain only the most relevant bits of information, hence the reference to 'renormalization group' in the naming.

In its modern interpretation, different flavors of DMRG exist that may either aim to describe infinite systems (infinite-system DMRG) or operate on finite systems (finite-system DMRG). The latter can be understood also as an optimization problem with the goal to describe a physical spin configuration in terms of a (position dependent) matrix product state.

An arbitrary quantum mechanical wave function which describes a cluster of N quantum mechanical spins, where each spin at position i has its local configuration space $\{\sigma_i\} = \{\uparrow, \downarrow\}$, is approximated by the matrix product state

$$|\psi\rangle = \sum_{\sigma_1 \ldots \sigma_N} \mathrm{Tr}\left(\prod_{i=1}^{N} A_i[\sigma_i]\right) |\sigma_1 \ldots \sigma_N\rangle \quad , \tag{1.13}$$

where DMRG provides a way to determine the entries of the $M \times M$ matrices $A_i[\sigma_i]$. The quality of the approximation depends on the dimension M of these matrices (which also determines the computational complexity of the algorithm) as well as on the speed at which the eigenvalues of the matrix decay. The eigenvalue scaling can be one of the four qualitatively different scenarios [28]: (i) In the best case scenario the true eigenstate of the system is represented by a matrix product state. In this case there is only a finite number of non-zero eigenvalues and DMRG is able to represent the exact solution. (ii) Similarly well behaved is the scenario of exponentially fast decaying eigenvalues, which is the case for one-dimensional gapped quantum systems. Under these circumstances DMRG is still able to efficiently capture the relevant physics and to predict observables with an accuracy close to machine precision. (iii) It gets more difficult when the decay of eigenvalues slows down with increasing system size, which is the case for critical one-dimensional quantum systems. The slow decay of eigenvalues for larger systems implies that DMRG is unable to faithfully capture the thermodynamic limit in these systems. (iv) In two dimensions and higher, the number of relevant eigenvalues grows with increasing system size. These systems are most difficult to treat in DMRG. In practice, one may estimate the truncation error which results from finite matrix dimensions M by comparing calculations at different values for the dimensionality M of the matrix product states at any given system size. Being able to estimate numerical errors it is still possible to make predictions about two-dimensional systems, despite the scaling behavior of relevant eigenvalues being unfavorable. One is, however, restricted to relatively small systems – this is also the reason that DMRG studies of two-dimensional systems are usually only performed on stripe (or cylinder) geometries, keeping the total system size small and at the same time making the system quasi one-dimensional.

In summary, DMRG is very powerful for most one-dimensional systems, yielding results of remarkable precision. For systems of this kind, DMRG is the method of choice. Unlike Monte Carlo, DMRG does not know a sign problem and hence may also be applied to frustrated quantum magnets. Despite its reduced performance in two dimensions, DMRG is an immensely valuable tool also in the field of two-dimensional frustrated quantum magnetism, in particular for models which are not amenable to a treatment by Monte Carlo. In recent years, the use of DMRG has helped to reach im-

portant milestones in the research of quantum spin liquids. For example, with the help of DMRG, unambiguous evidence for the existence of a chiral spin liquid on the kagome lattice with Heisenberg interactions up to third neighbors has been provided [29, 30]. Furthermore, the use of DMRG has made valuable contributions to the discussion of the kagome Heisenberg antiferromagnet, with current simulations making a strong point that the ground state is a gapless U(1)-Dirac spin liquid [23]; these contributions, however, also spotlight the subtleties of DMRG in two dimensions. Discriminating the two competing proposals of a gapless U(1) and a gapped $\mathbb{Z}_2$ spin liquid might sound simple, but it has proven to be a great challenge in finite cylinder geometries, and a lot of thought has to be put into understanding the impact of boundary conditions. Finally, employing DMRG may also give direct access to subtle properties like the entanglement structure in two-dimensional quantum many-body systems. Three dimensional systems, however, are much less well behaved and are currently out of reach for DMRG.

1.2.4 Functional renormalization group. Throughout the remainder of this thesis, the method of choice is going to be the pseudo-fermion functional renormalization group (pf-FRG), which is a relatively new addition to the toolset of numerical approaches in frustrated quantum magnetism. We have seen in the previous discussions that the main workhorses in the numerical study of frustrated quantum magnetism are often not suited to faithfully describe three-dimensional frustrated quantum magnets, leaving a methodological void in the field. In the next part of the thesis, Chapter 2, we introduce the pseudo-fermion functional renormalization group formalism, which we shall see can also be applied to simulate frustrated quantum magnetism in three spatial dimensions; the chapter is dedicated to a pedagogical introduction to the method itself, the theory behind it, and its practical implementation. Thereafter, in Chapter 3, we provide several examples from the field of frustrated quantum magnetism where we study model Hamiltonians that support the emergence of quantum spin liquid phases – guided by applications to real materials.

2. The pseudo-fermion functional renormalization group

In the previous chapter we have discussed some of the most pervasive techniques in the field of frustrated quantum magnetism: exact diagonalization, quantum Monte Carlo, and the density matrix renormalization group. All of these methods are quite powerful in the study of two-dimensional frustrated magnetism. Yet, exact diagonalization and density matrix renormalization group are not suitable for applications in three dimensions, and quantum Monte Carlo is often impaired by the infamous sign problem when applied to models of frustrated magnetism.

A complementary numerical approach has been pursued by Reuther and Wölfle (2010) [6]: the pseudo-fermion functional renormalization group (pf-FRG). In its early days the method has been successfully applied to various paradigmatic models of frustrated quantum magnetism in two dimensions, ranging from the triangular antiferromagnet [31] via the kagome antiferromagnet [32] to the Kitaev honeycomb model [33], and more [34, 35]. In the continuous development of the approach it was quickly realized that the method is straightforwardly applicable also to three-dimensional frustrated quantum magnetism [36], allowing access to prototypical models of frustration on the hyperkagome lattice [P1] and on the pyrochlore lattice [37]. The great success in the study of a long list of archetypal examples of frustrated magnetism has demonstrated that the pf-FRG offers a promising perspective and can help to diminish the methodological void around the field of frustrated quantum magnetism in three dimensions.

While in the early days of pf-FRG the use of the method has been justified mostly by its successful applications, in more recent days additional insight has been gained into the validity of the approximation schemes which the approach is built on. For example, it has been shown that the pf-FRG becomes exact in the classical limit of large spins [38] as well as in the large-N limit of enhanced SU(N) spin symmetry [P2, P3]. Moreover, the pf-FRG has been further refined to be applicable to models with less symmetric off-diagonal spin interactions including, but not limited to, Dzyaloshinskii-Moriya interactions [39, P6, P7]. Unrelated to the original formulation of pf-FRG, efforts are being made in the development of a functional renormalization group scheme which operates directly on the internal spin degrees of freedom instead of re-casting them in terms of pseudo-fermions [40]. The latter approach is a very recent development and it remains to be seen how feasible it is in practical calculations.

The aim of this chapter is to review the theory behind the pseudo-fermion functional renormalization group (pf-FRG), putting strong emphasis on its practical application. Understanding pf-FRG is a three step process which can be broken down into (i) the

derivation of the general functional renormalization group (FRG) flow equations, (ii) the construction and symmetry analysis of the pseudo-fermion Hamiltonian which acts as a fermionic representation of the spin Hamiltonian, and (iii) refining the general functional renormalization group scheme by implementing specific symmetries and approximation schemes for the pseudo-fermionic model. We address the first step only briefly. There already exists an extensive body of literature on the general formulation of the functional renormalization group with applications of FRG covering not just condensed matter systems but also being influential in high-energy physics and quantum gravity [41]; a pedagogical review of the general formalism would fill a book on its own. For more details on the general concept of the functional renormalization group we instead refer the reader to text books [42], review articles [43–45], or influential papers [46] on the subject. A lot of work has been done on FRG implementations for fermionic models in condensed matter theory and there is a long record of discussions of different approximation schemes and their validity. However, making the transition from conventional fermionic systems to pseudo-fermionic models, which we shall see have very different symmetry implications compared to regular fermions, requires us to re-evaluate the applicability of approximation schemes. Therefore our focus is put on the discussion of original aspects about the pf-FRG which go beyond the implementation of conventional fermionic FRG schemes.

After a brief general introduction to the functional renormalization group in Sec. 2.1 we discuss the characteristic properties of the pseudo-fermion Hamiltonian in Sec. 2.2. In Sec. 2.3 we derive the pf-FRG flow equations, followed by a discussion of their numerical solution (Sec. 2.4) and selected aspects about the interpretation of pf-FRG calculations (Sec. 2.5).

2.1. Functional renormalization group

Conceptually, the functional renormalization group (FRG) can be thought of as the rewriting of a functional integral, which serves as a central object in many-body quantum field theories from which physical observables may be computed,

$$Z = \int \mathcal{D}(\bar{\psi}, \psi) e^{-S_0 - S_{\text{int}}} \quad , \tag{2.1}$$

into an infinite hierarchy of integro-differential equations

$$\frac{\mathrm{d}}{\mathrm{d}\Lambda} \gamma_m(k_{1'}, \ldots, k_{m'}; k_1, \ldots, k_m) = \mathcal{F}_m^{\Lambda}\left(\gamma_0, \gamma_2, \gamma_4, \ldots, \gamma_{m+2}\right) \quad , \tag{2.2}$$

where the expressions $\mathcal{F}_m$ on the right hand side of the equation can be complicated non-linear integral expressions (their precise form and notation is introduced later in this chapter). We shall see below that the rewriting is exact and that both formulations – the functional integral expression and the differential equation – thus contain the same information. Both formulations are intrinsically difficult to solve for strongly interacting many-body systems: the functional integral contains a sizable quartic contribution S_{int} which spoils the solubility of the Gaussian integral, while the differential equations cannot be solved because their structure is an infinite hierarchy of coupled expressions. In non-interacting systems, on the other hand, both formulations are inherently simple. The functional integral becomes Gaussian, while the initial conditions of the differential equations are such that only a single component can become non-zero, while all other orders in the infinite hierarchy vanish.

Operating in a regime which lies in between non-interacting systems and strongly interacting systems one needs to lean on approximation schemes which are often well behaved in the weak coupling limit and become less controlled as the interaction strength is increased. In this regime the liberty to switch between the integral formalism and the differential formalism becomes immensely valuable because both approaches are amenable to different approximation schemes. While the functional integral formulation is often used in combination with traditional renormalization group (RG) schemes in order to determine a small set of renormalized interaction constants, the FRG approach provides an overarching concept for the renormalization of much larger sets of interaction parameters (c.f. Fig. 2.1) which defines a natural language to compute diagrammatic resummations of interaction vertices.

In the remainder of this section we derive the general form of fermionic FRG flow equations. For the derivation we closely follow the steps as outlined in Ref. [43]. The same conceptional steps are also described in textbook style with more elaborate commentary in Ref. [42] – however, their notation is overly complicated for our purpose since they operate in a superspace of combined fermionic and bosonic theories where the particle number is no longer preserved.

As a starting point for our derivation we consider a general fermionic model with quartic interactions whose Hamiltonian $H = H_0 + H_{\text{int}}$ can be split into two contributions

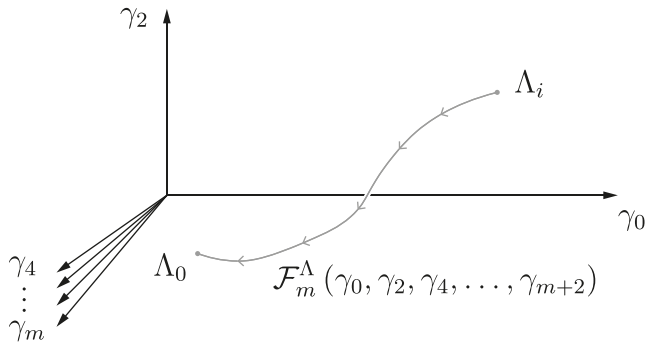

Figure 2.1. **Functional renormalization group** as a concept for the concurrent renormalization of an extensive number of coupling constants. The interaction vertices $\gamma_m(k_{1'}, \ldots, k_{m'}; k_1, \ldots, k_m)$ span a high-dimensional parameter space in which a cutoff scale Λ is introduced in order to successively thin out the system's internal degrees of freedom, thereby generating the RG flow $\mathcal{F}_m^\Lambda(\gamma_0, \gamma_2, \gamma_4, \ldots, \gamma_{m+2})$. The RG flow connects an initial point at Λ_i, which is chosen to be particularly simple and analytically tractable, to an end-point at Λ_0 which marks the effective set of parameters of the fully interacting model.

which represent the kinetic term

$$H_0 = \sum_{k'k} h_{k',k}\ f^\dagger_{k'} f_k \tag{2.3}$$

and the interaction term

$$H_{\text{int}} = \frac{1}{4} \sum_{k_{1'},k_{2'},k_1,k_2} v_{k_{1'},k_{2'},k_1,k_2}\ f^\dagger_{k_{1'}} f^\dagger_{k_{2'}} f_{k_1} f_{k_2} \quad , \tag{2.4}$$

where we assume the indices k_i to represent all relevant quantum numbers, e.g. a combination of momentum, spin, and Matsubara frequency. Aiming for a description in the language of quantum field theory we may equivalently represent the system by its action S, which appears naturally in the construction of the functional integral. In analogy to the Hamiltonian formulation the action decomposes into a non-interacting part S_0 and an interacting part S_{int}. The non-interacting part is given by

$$S_0 = -\left(\bar{\psi}, G_0^{-1}\psi\right) = -\sum_{k'k} \bar{\psi}_{k'} [G_0^{-1}]_{k',k} \psi_k \quad , \tag{2.5}$$

where $\bar{\psi}$ and ψ denote Grassmann numbers and we have introduced the free propagator $[G_0^{-1}]_{k',k} = -i\omega\delta_{k',k} + h_{k',k}$ of the model as well as a shorthand notation $(\cdot,\cdot)$ for the summation over internal indices. By convention we assume that the summations include all appropriate normalization factors, in particular a factor $1/\beta$ for sums over Matsubara frequencies, where β denotes the inverse temperature. The interacting part of the action

is defined as

$$S_{\rm int} = S_{\rm int}(\{\bar{\psi},\psi\}) = \frac{1}{4}\sum_{k_{1'},k_{2'},k_1,k_2} v_{k_{1'},k_{2'},k_1,k_2}\ \bar{\psi}_{k_{1'}}\bar{\psi}_{k_{2'}}\psi_{k_1}\psi_{k_2} \quad . \tag{2.6}$$

The partition function of the system in the functional integral formalism follows the usual construction [47, 48] and assumes the form

$$Z = \int \mathcal{D}(\bar{\psi},\psi)\exp\left\{\left(\bar{\psi},G_0^{-1}\psi\right) - S_{\rm int}(\{\bar{\psi},\psi\})\right\} \quad . \tag{2.7}$$

The functional renormalization group approach aims for a description of the system in terms of its correlation functions of fermionic field operators. The unique characterization of the system requires knowledge of all correlation functions up to infinite order – which can only be feasible if we put forth an efficient notation. We shall thus introduce the notion of generating functionals before we dive into the derivation of the flow equations. By adding external source fields $\bar{\eta}$ and η to the functional integral construction we obtain the generating functional of the (disconnected) Green's function

$$W(\{\bar{\eta},\eta\}) = \frac{1}{Z_0}\int \mathcal{D}(\bar{\psi},\psi)\exp\left\{\left(\bar{\psi},G_0^{-1}\psi\right) - S_{\rm int}(\{\bar{\psi},\psi\}) - \left(\bar{\psi},\eta\right) - \left(\bar{\eta},\psi\right)\right\} \quad , \tag{2.8}$$

which is constructed such that arbitrary m-particle Green's functions can be generated by applying functional derivatives,

$$G_m(k_{1'},\ldots,k_{m'};k_1,\ldots,k_m) = \frac{\delta^m}{\delta\bar{\eta}_{k_{1'}}\ldots\delta\bar{\eta}_{k_{m'}}}\frac{\delta^m}{\delta\eta_{k_m}\ldots\delta\eta_{k_1}}W(\{\bar{\eta},\eta\})\bigg|_{\bar{\eta}=\eta=0} \quad . \tag{2.9}$$

Furthermore we will make use of the generating functional for connected m-particle Green's functions,

$$W^c(\{\bar{\eta},\eta\}) = \ln W(\{\bar{\eta},\eta\}) \quad , \tag{2.10}$$

from which the connected m-particle Green's functions are obtained as

$$G^c_m(k_{1'},\ldots,k_{m'};k_1,\ldots,k_m) = \frac{\delta^m}{\delta\bar{\eta}_{k_{1'}}\ldots\delta\bar{\eta}_{k_{m'}}}\frac{\delta^m}{\delta\eta_{k_m}\ldots\delta\eta_{k_1}}W^c(\{\bar{\eta},\eta\})\bigg|_{\bar{\eta}=\eta=0} \quad . \tag{2.11}$$

Finally, we also introduce the generating functional for one-particle irreducible Green's functions which is obtained from W^c via a Legendre transformation (for later convenience we add an extra term that contains the bare propagator),

$$\Gamma(\{\bar{\varphi},\varphi\}) = -W^c(\{\bar{\eta},\eta\}) - (\bar{\varphi},\eta) - (\bar{\eta},\varphi) + \left(\bar{\varphi},G_0^{-1}\varphi\right) \quad , \tag{2.12}$$

and which depends on the conjugate source fields

$$\bar{\varphi} = \frac{\delta W^c}{\delta\eta} \quad \text{and} \quad \varphi = -\frac{\delta W^c}{\delta\bar{\eta}} \quad . \tag{2.13}$$

Differentiation with respect to the conjugate source fields gives rise to the one-particle irreducible vertex functions

$$\gamma_m(k_{1'},\ldots,k_{m'};k_1,\ldots,k_m) = \frac{\delta^m}{\delta\bar{\varphi}_{k_{1'}}\ldots\delta\bar{\varphi}_{k_{m'}}}\frac{\delta^m}{\delta\varphi_{k_m}\ldots\delta\varphi_{k_1}}\Gamma(\{\bar{\varphi},\varphi\})\bigg|_{\bar{\varphi}=\varphi=0} \quad . \tag{2.14}$$

The generating functional $\Gamma(\{\bar{\varphi},\varphi\})$ is referred to as the effective action. The circumstance that the vertex functions γ_m are in fact the one-line irreducible diagrams can be seen by explicitly relating them to the connected diagrams (by making use of the relation between their generating functionals), which yields e.g. the Dyson equation for the single-particle vertex γ_1 [48]. More importantly, the relation also shows that all connected Green's functions can be constructed from one-line irreducible diagrams by means of a tree expansion, i.e. a diagrammatic construction which does not introduce loop structures. Any complicated internal structure – in particular divergences which are driven by loop integrals – is thus encapsulated in the vertex functions γ_m, making them a convenient, low-overhead starting point for our renormalization group analysis.

The renormalization group flow is generated by replacing the bare propagator G_0 with the modified propagator function G_0^Λ which depends on a cutoff parameter Λ. The functional dependence on the cutoff parameter can be arbitrary but we require the modified propagator to match the original bare propagator when the cutoff is set to zero,

$$G_0^{\Lambda=0} = G_0 \quad , \tag{2.15}$$

and we require it to vanish when the cutoff approaches infinity,

$$G_0^{\Lambda\to\infty} = 0 \quad . \tag{2.16}$$

By virtue of this construction all quantities which depend on the bare propagator necessarily inherit the cutoff dependence; this especially holds for the generating functionals and the vertex functions.

The goal is now to derive a differential equation which captures the evolution of the effective action under variation of the cutoff parameter. To this end we evaluate the cutoff derivative of the generating functional for connected Green's functions

$$\frac{\mathrm{d}}{\mathrm{d}\Lambda}W^{c,\Lambda}(\{\bar{\eta},\eta\}) = -\operatorname{Tr}\left(Q^\Lambda G_0^\Lambda\right) + \operatorname{Tr}\left(Q^\Lambda\frac{\delta^2 W^{c,\Lambda}}{\delta\bar{\eta}\delta\eta}\right) - \left(\frac{\delta W^{c,\Lambda}}{\delta\eta}, Q^\Lambda\frac{\delta W^{c,\Lambda}}{\delta\bar{\eta}}\right) \quad , \tag{2.17}$$

where we have used

$$Q^\Lambda = \frac{\mathrm{d}}{\mathrm{d}\Lambda}\left[G_0^\Lambda\right]^{-1} \quad . \tag{2.18}$$

The derivative of the effective action computes as

$$\frac{\mathrm{d}}{\mathrm{d}\Lambda}\Gamma^\Lambda(\{\bar{\varphi},\varphi\}) = -\frac{\mathrm{d}}{\mathrm{d}\Lambda}W^{c,\Lambda}(\{\bar{\eta}^\Lambda,\eta^\Lambda\}) - \left(\bar{\varphi},\frac{\mathrm{d}}{\mathrm{d}\Lambda}\eta^\Lambda\right) - \left(\frac{\mathrm{d}}{\mathrm{d}\Lambda}\bar{\eta}^\Lambda,\varphi\right) + \left(\bar{\varphi},Q^\Lambda\varphi\right) \quad . \tag{2.19}$$

Combining Eqs. (2.17) and (2.19) and considering that the change of fundamental variables in the Legendre transformation introduces a cutoff dependence in the source fields $\bar{\eta}$ and η, we obtain the expression

$$\frac{\mathrm{d}}{\mathrm{d}\Lambda}\Gamma^{\Lambda}(\{\bar{\varphi},\varphi\}) = \mathrm{Tr}\left(Q^{\Lambda}G_0^{\Lambda}\right) - \mathrm{Tr}\left(Q^{\Lambda}\frac{\delta^2 W^{c,\Lambda}}{\delta\bar{\eta}^{\Lambda}\delta\eta^{\Lambda}}\right) \quad . \tag{2.20}$$

Since the effective action and the generating functional for connected Green's functions are connected by a Legendre transformation (up to an extra term) their second derivatives are the inverse of each other (up to an extra term) [48], and we may rewrite the differential equation for the effective action to obtain

$$\frac{\mathrm{d}}{\mathrm{d}\Lambda}\Gamma^{\Lambda}(\{\bar{\varphi},\varphi\}) = \mathrm{Tr}\left(Q^{\Lambda}G_0^{\Lambda}\right) - \mathrm{Tr}\left(Q^{\Lambda}V_{1,1}\right) \quad , \tag{2.21}$$

where $V_{1,1}$ is the top left entry of the matrix

$$V = \begin{pmatrix} \frac{\delta^2\Gamma^{\Lambda}}{\delta\bar{\varphi}\delta\varphi} + [G_0^{\Lambda}]^{-1} & \frac{\delta^2\Gamma^{\Lambda}}{\delta\bar{\varphi}\delta\bar{\varphi}} \\ \frac{\delta^2\Gamma^{\Lambda}}{\delta\varphi\delta\varphi} & \frac{\delta^2\Gamma^{\Lambda}}{\delta\varphi\delta\bar{\varphi}} - [[G_0^{\Lambda}]^{-1}]^T \end{pmatrix}^{-1} \quad . \tag{2.22}$$

The flow equation for the generating functional can be broken down into a set of differential equations for the individual vertex functions. To this end we expand the generating functional in its external source fields on both sides of the equation and collect terms of different orders in the source fields. We have already established that the vertex functions are obtained via differentiation of the generating functionals, hence they must naturally appear as coefficients in the series expansion of the effective action

$$\Gamma^{\Lambda}(\{\bar{\varphi},\varphi\}) = \sum_m \frac{(-1)^m}{(m!)^2} \sum_{k_{1'},\ldots,k_{m'}} \sum_{k_1,\ldots,k_m} \gamma_m^{\Lambda}(k_{1'},\ldots,k_{m'};k_1,\ldots,k_m)\bar{\varphi}_{k_{1'}},\ldots,\bar{\varphi}_{k_{m'}}\varphi_{k_m},\ldots,\varphi_{k_1} \quad . \tag{2.23}$$

Furthermore, it is helpful to define the matrix

$$\tilde{V} = \left[1 - \begin{pmatrix} -G^{\Lambda} & 0 \\ 0 & [G^{\Lambda}]^T \end{pmatrix} \begin{pmatrix} U & \frac{\delta^2\Gamma^{\Lambda}}{\delta\bar{\varphi}\delta\bar{\varphi}} \\ \frac{\delta^2\Gamma^{\Lambda}}{\delta\varphi\delta\varphi} & -U^T \end{pmatrix}\right]^{-1} \quad , \tag{2.24}$$

where we have used

$$U = \frac{\delta^2\Gamma^{\Lambda}}{\delta\bar{\varphi}\delta\varphi} - \gamma_1^{\Lambda} \quad , \tag{2.25}$$

as well as

$$G^{\Lambda} = [[G_0^{\Lambda}]^{-1} + \gamma_1^{\Lambda}]^{-1} \quad . \tag{2.26}$$

The latter identity resembles the Dyson equation and implies that the one-line irreducible

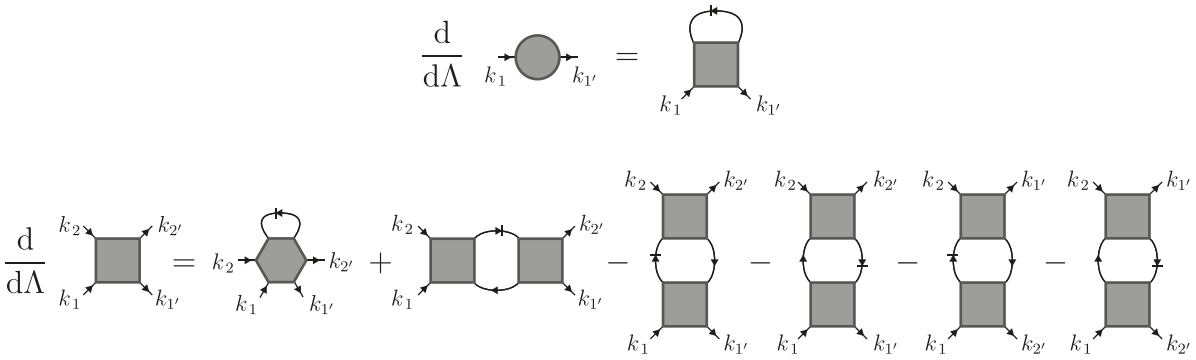

Figure 2.2. **Fermionic flow equations** for the one-line irreducible vertex functions. The solid propagator lines represent the cutoff dependent propagator G^Λ and slashed propagator lines indicate the single-scale propagator S^Λ. (a) Flow equations for the single-particle vertex. (b) Flow equation for the two-particle vertex.

vertex γ_1 equals the self energy up to a minus sign [43]. With these substitutions the flow equation assumes the form

$$\frac{\mathrm{d}}{\mathrm{d}\Lambda}\Gamma^\Lambda(\{\bar{\varphi},\varphi\}) = \mathrm{Tr}\left(Q^\Lambda G_0^\Lambda\right) - \mathrm{Tr}\left(G^\Lambda Q^\Lambda \tilde{V}_{1,1}\right) \quad . \tag{2.27}$$

It is now straightforward to expand the effective action on the left hand side of the equation according to Eq. (2.23), and on the right hand side of the equation to expand the geometric series (2.24). Collecting the terms of first and second order in the source fields obtains the flow equations for the single-particle vertex

$$\frac{\mathrm{d}}{\mathrm{d}\Lambda}\gamma_1^\Lambda(k_{1'};k_1) = \sum_{k_{2'},k_2} \gamma_2^\Lambda(k_{1'},k_{2'};k_1,k_2) S^\Lambda(k_2;k_{2'}) \tag{2.28}$$

and the flow equations for the two-particle vertex

$$\begin{aligned}\frac{\mathrm{d}}{\mathrm{d}\Lambda}\gamma_2^\Lambda(k_{1'},k_{2'};k_1,k_2) = &\sum_{k_{3'},k_3} \gamma_3^\Lambda(k_{1'},k_{2'},k_{3'};k_1,k_2,k_3) S^\Lambda(k_3;k_{3'}) \\ &+ \sum_{k_{3'},k_3,k_{4'},k_4} \big[\gamma_2^\Lambda(k_{1'},k_{2'};k_3,k_4)\gamma_2^\Lambda(k_{3'},k_{4'};k_1,k_2) \\ &- \gamma_2^\Lambda(k_{1'},k_{4'};k_1,k_3)\gamma_2^\Lambda(k_{3'},k_{2'};k_4,k_2) - (k_{3'} \leftrightarrow k_{4'}, k_3 \leftrightarrow k_4) \\ &+ \gamma_2^\Lambda(k_{2'},k_{4'};k_1,k_3)\gamma_2^\Lambda(k_{3'},k_{1'};k_4,k_2) + (k_{3'} \leftrightarrow k_{4'}, k_3 \leftrightarrow k_4)\big] \\ &\times G^\Lambda(k_3;k_{3'}) S^\Lambda(k_4;k_{4'}) \quad ,\end{aligned} \tag{2.29}$$

where we have introduced the so-called single-scale propagator

$$S^\Lambda = G^\Lambda Q^\Lambda G^\Lambda \quad . \tag{2.30}$$

The flow equations are pictorially shown in Fig. 2.2. The appearance of a second derivative with respect to the external source fields in the geometric series on the right hand side of the flow equation (2.27) gives rise to an infinite hierarchy of differential equations where the flow of the m-particle vertex γ_m^Λ depends on all vertex functions up to order $m+1$. Up to this point we have not employed any approximations and the flow equation for the effective action is an exact rewriting of the functional integral into a differential expression. In any practical calculation, however, one needs to truncate the hierarchy of differential equations in order to obtain a closed set of equations for the vertex functions. We shall see that the inclusion of the three-particle vertex or higher orders is not feasible in pf-FRG calculations, which is why we only explicitly stated the flow equations for the single-particle vertex and the two-particle vertex.

The initial conditions for the flow equations can be computed in a lengthy but straightforward manner from the expression for the effective action at infinite cutoff $\Lambda \to \infty$ [49], but they can also be understood intuitively: in the limit of infinite cutoff the bare propagator vanishes and the only diagrams which can be non-zero are the ones which are already present in the bare action. Hence, the initial conditions are given by the interaction constants defined in the original Hamiltonian [43]:

$$\gamma_1^{\Lambda\to\infty}(k_{1'};k_1) = 0 \quad \text{and} \quad \gamma_2^{\Lambda\to\infty}(k_{1'},k_{2'};k_1,k_2) = v_{k_{1'},k_{2'},k_1,k_2} \quad . \tag{2.31}$$

2.2. The pseudo-fermion Hamiltonian

In the previous section we have outlined the general formulation of the fermionic FRG flow equations. Our next step in the derivation of the pseudo-fermion functional renormalization group is to derive the pseudo-fermion Hamiltonian itself and to understand its symmetries, which, in turn, allows us to refine the general FRG flow equations by incorporating the symmetries of pseudo-fermions. The discussion of the pseudo-fermion symmetries is based on our results as presented in Ref. [P6].

We begin our analysis by considering a general Hamiltonian of two-spin interactions,

$$H = \sum_{i,j} J_{ij}^{\mu\nu} S_i^\mu S_j^\nu \quad , \tag{2.32}$$

where the sum runs over lattice sites i and j, and the operator S_i^μ represents the μ-th component of an SU(2)-symmetric spin-1/2 moment where μ is either x, y, or z. Furthermore we assume all coupling constants $J_{ij}^{\mu\nu}$ to be real numbers. This general form of the spin Hamiltonian is suitable to represent a plethora of different models including, but not limited to, models of Heisenberg and Kitaev type – the general form of the Hamiltonian also covers less symmetric spin interactions, e.g. Dzyaloshinskii-Moriya interactions or Γ-interactions which frequently appear in the discussion of spin liquid candidate materials [50, 51]. We note that the general Hamiltonian (2.32) fulfills two important symmetry properties: it preserves time-reversal symmetry and it is hermitian, which we shall see later is important to reduce the complexity of the flow equations to a manageable level.

In the first step we introduce Abrikosov fermions (pseudo-fermions) [52] via the substitution rule

$$S_i^\mu = \frac{1}{2} f_{i\alpha}^\dagger \sigma_{\alpha\beta}^\mu f_{i\beta} \tag{2.33}$$

as a fermionic representation of the spin operators. The pseudo-fermionic Hilbert space is larger than the original spin Hilbert space and the parton construction is only a faithful representation of the spin algebra when the additional local half-filling constraint

$$\sum_\alpha f_{i\alpha}^\dagger f_{i\alpha} = 1 \tag{2.34}$$

is fulfilled. Since the system is particle-hole symmetric the constraint can be fulfilled on average by setting the chemical potential to zero. It has been seen in previous pf-FRG calculations that this is a good approximation [6], although the constraint can in principle also be fulfilled exactly by introducing an artificial complex chemical potential following a construction put forward by Popov and Fedotov [53, 54] – yet this would spoil the hermitian symmetry of the Hamiltonian. The fact that it is sufficient to fulfill the half-filling constraint on average may be attributed to the structure of the pseudo-fermion Hamiltonian; the Hamiltonian only generates transitions within the physical subspace of the Hilbert space which corresponds to half-filling, such that its dynamics

is not affected by the unphysical sector of the Hilbert space. The full partition sum, in contrast, contains also unphysical contributions. Those contributions, however, can be expected to be small because the unphysical (doubly occupied or vacant) fermionic states correspond to energetically unfavorable defects in the spin lattice and their thermal weight becomes negligible at low temperatures.

The form of the Hamiltonian after applying the substitution of the spin operators according to Eq. (2.33) is given by

$$H = \sum_{ij} \frac{J_{ij}^{\mu\nu}}{4} \sigma_{\alpha\beta}^{\mu} \sigma_{\gamma\delta}^{\nu} \; f_{i\alpha}^{\dagger} f_{j\gamma}^{\dagger} f_{j\delta} f_{i\beta} \quad , \tag{2.35}$$

i.e. the Hamiltonian assumes a quartic form in the pseudo-fermion operators. Most importantly, the Hamiltonian does not have any quadratic contribution and as such the model is not amenable to a perturbative treatment around a Gaussian theory – which is why we are going to employ a functional renormalization group approach instead. We have seen in Sec. 2.1 that the FRG approach is a comprehensive framework to treat a large number of effective coupling constants simultaneously; as such it can be leveraged to approximate relevant interactions in the pseudo-fermion model by a massively large (yet not infinitely large) space of coupling parameters which, as we shall see later, can be made large enough to capture the phenomenology of the pseudo-fermion model despite the absence of quadratic terms (which nominally corresponds to infinitely strong coupling). Applying the FRG formalism in this way formally is an uncontrolled approximation but we will discuss in the next sections that the approach is nevertheless sensible and even becomes exact (on a mean-field level) in the classical limit of large spins as well as for SU(N) generalized quantum spins in their large-N limit.

We shall now proceed with the symmetry analysis of the pseudo-fermion Hamiltonian (2.35). Per construction the Hamiltonian has an inherent local SU(2) gauge redundancy in the fermionic Hilbert space, which is introduced in the fermionization procedure. A subgroup thereof, a local U(1) gauge redundancy, is immediately visible in the substitution rule (2.33), being implemented via a multiplication of the fermionic operators with a complex phase. The full SU(2) gauge redundancy can be made more explicit by rewriting the substitution rule from a vector-matrix-vector product into the trace over a matrix-matrix-matrix product [55],

$$S_i^{\mu} = \frac{1}{4} F_{i,\alpha\beta}^{\dagger} \sigma_{\beta\gamma}^{\mu} F_{i,\gamma\alpha} \quad , \tag{2.36}$$

where the 2×2 matrix F_i of pseudo-fermionic operators is defined as

$$F_i = \begin{pmatrix} f_{i\uparrow} & f_{i\downarrow}^{\dagger} \\ f_{i\downarrow} & -f_{i\uparrow}^{\dagger} \end{pmatrix} \quad . \tag{2.37}$$

The equivalence between the two notations can be verified by a straightforward calculation. The gauge redundancy is now implemented via the usual representation of

the SU(2) group by complex 2×2 matrices, i.e. its representation g_{local} follows the defining property $g^\dagger_{\text{local}} g_{\text{local}} = 1$. The local SU(2) transformation acts on the space of pseudo-fermions by right-multiplication of the fermionic operators with g_{local},

$$\tilde{F}_i = F_i \; g_{\text{local}} \quad . \tag{2.38}$$

In this notation the invariance of the spin operator representation (2.36) is a direct consequence of the invariance of the trace under cyclic permutations. Furthermore, in this notation the (unphysical) SU(2) gauge redundancy can easily be told apart from the (physical) global SU(2) spin rotation. Unlike the local transformation which is defined as right-multiplication, the global transformation g_{global} is implemented as left-multiplication,

$$\tilde{F}_i = g_{\text{global}} \; F_i \quad , \tag{2.39}$$

implying that the transformations to dot cancel out and, as expected, act on the spin space by a rotation of the basis

$$\tilde{\sigma}^\mu = g^\dagger_{\text{global}} \sigma^\mu g_{\text{global}} \quad . \tag{2.40}$$

In the remainder of this section we individually address the list of different projective symmetries on the pseudo-fermion space. For every symmetry we suggest a specific implementation in second quantized language acting on the fermionic Hilbert space and discuss its implication on the structure of correlation functions. For the purpose of this discussion we split the SU(2) gauge redundancy into its U(1) subgroup and a local particle-hole symmetry since these two transformations have very different implications on the functional form of correlation functions. Thereafter, we conclude the section by summarizing the role of symmetry constraints in the parametrization of the one-line irreducible vertex functions.

2.2.1 U(1) gauge redundancy. We begin the symmetry analysis by discussing a local U(1) transformation which is a subgroup of the local SU(2) gauge redundancy in the construction of pseudo-fermionic spin representations. As such, the symmetry is present in every pseudo-fermion Hamiltonian. The action of a local U(1) rotation by an angle of φ_i is defined as

$$g_{\varphi_i} \begin{pmatrix} f^\dagger_{i\alpha} \\ f_{i\alpha} \end{pmatrix} g^{-1}_{\varphi_i} = \begin{pmatrix} e^{i\varphi_i} f^\dagger_{i\alpha} \\ e^{-i\varphi_i} f_{i\alpha} \end{pmatrix} \quad , \tag{2.41}$$

i.e. the transformation amounts to a multiplication of the pseudo-fermion operators with a phase of φ_i. In the notation which we are using throughout this section the index i usually refers to a lattice site (which is not to be confused with the imaginary unit, the difference should be clear from the context) and the index $\alpha = \pm 1$ denotes spin. This transformation leaves every individual spin operator invariant and thus is a symmetry of the spin Hamiltonian – which is to be expected because it is a subgroup of the larger SU(2) group of gauge redundancies.

We are interested in the implications of symmetry transformations on the functional

form of two-point and four-point correlations in the pseudo-fermions. Our objects of study are the single-particle (two-point) correlation function

$$G(1';1) = \left\langle f^\dagger_{1'} f_1 \right\rangle \tag{2.42}$$

and the two-particle (four-point) correlation function

$$G(1',2';1,2) = \left\langle f^\dagger_{1'} f^\dagger_{2'} f_1 f_2 \right\rangle \quad , \tag{2.43}$$

where we have introduced composite indices $n = (i_n, \omega_n, \alpha_n)$ that represent the tuple of lattice site index i_n, Matsubara frequency ω_n, and spin index α_n, respectively. We shall use this composite notation whenever suitable, but we may also fall back to explicitly stating all three indices separately when necessary. Since our general Hamiltonian of interest (2.35) also has a global U(1) symmetry, which implies the conservation of particle numbers, we constrain our analysis to correlation functions with an equal number of fermionic creation and annihilation operators. We dress the fermionic operators with an additional imaginary-time dependence, which in the Heisenberg picture of operators reads

$$\begin{pmatrix} f^\dagger_{i\tau\alpha} \\ f_{i\tau\alpha} \end{pmatrix} = \begin{pmatrix} e^{\tau H} f^\dagger_{i\alpha} e^{-\tau H} \\ e^{\tau H} f_{i\alpha} e^{-\tau H} \end{pmatrix} \quad . \tag{2.44}$$

For convenience we subsequently apply a Fourier transformation to re-express the imaginary time dependence in terms of Matsubara frequencies ω (where the discreteness of Matsubara frequencies is implicit).

Application of the U(1) transformation (2.41) to the two-point correlator yields

$$\left\langle g_{\varphi_{i'}} g_{\varphi_i} f^\dagger_{i'\omega'\alpha'} f_{i\omega\alpha} g^{-1}_{\varphi_i} g^{-1}_{\varphi_{i'}} \right\rangle = e^{i(\varphi_{i'} - \varphi_i)} \left\langle f^\dagger_{i'\omega'\alpha'} f_{i\omega\alpha} \right\rangle \quad . \tag{2.45}$$

Since the transformation is a symmetry of the Hamiltonian the correlation function must necessarily also be invariant under the transformation. Furthermore, since the transformation is local and thus allows for different rotation angles at every lattice site, the correlation function must vanish for $i' \neq i$. A similar implication holds for the four-point correlator, which transforms as

$$\begin{aligned} &\left\langle g_{\varphi_{i_{1'}}} g_{\varphi_{i_{2'}}} g_{\varphi_{i_1}} g_{\varphi_{i_2}} f^\dagger_{1'} f^\dagger_{2'} f_1 f_2 g^{-1}_{\varphi_{i_2}} g^{-1}_{\varphi_{i_1}} g^{-1}_{\varphi_{i_{2'}}} g^{-1}_{\varphi_{i_{1'}}} \right\rangle \\ &\quad = e^{i(\varphi_{i_{1'}} + \varphi_{i_{2'}} - \varphi_{i_1} - \varphi_{i_2})} \left\langle f^\dagger_{1'} f^\dagger_{2'} f_1 f_2 \right\rangle \quad . \end{aligned} \tag{2.46}$$

In order for the four-point correlator to vanish it has be to bi-local, meaning that the two incoming lattice sites (by incoming indices we mean those associated with annihilation operators) have to match the two outgoing lattice sites (by outgoing indices we refer to indices of creation operators). The two possible choices to pair up the indices correspond to the presence or absence of particle exchange throughout the course of an interaction process, which relates them by a minus sign.

We make use of the local U(1) gauge redundancy by explicitly imposing locality on the single-particle correlator

$$G(1';1) = G(1';1)\delta_{i'i} \tag{2.47}$$

and by imposing bi-locality on the two-particle correlator

$$G(1',2';1,2) = G(1',2';1,2)\delta_{i_{1'}i_1}\delta_{i_{2'}i_2} - G(2',1';1,2)\delta_{i_{2'}i_1}\delta_{i_{1'}i_2} \quad . \tag{2.48}$$

The parametrization of the latter is chosen such that it fulfills the anti-symmetry of the correlator upon particle exchange. The (bi-)locality constraint is one of the most important implications of the pseudo-fermion Hamiltonian; regular fermionic models do not share this property. Mobile fermions are often more convenient to treat in a momentum-space picture while for local pseudo-fermions it is preferential within FRG to work in a real-space picture. We discuss this in more detail once we derive the pf-FRG flow equations in Sec. 2.3.

2.2.2 Particle-hole gauge redundancy. We proceed with the study of a local particle-hole transformation which is another subgroup of the full SU(2) gauge redundancy of the pseudo-fermion Hamiltonian. As such, the symmetry is present in all pseudo-fermion models. Its action on the space of pseudo-fermions is defined by

$$g \begin{pmatrix} f^\dagger_{i\alpha} \\ f_{i\alpha} \end{pmatrix} g^{-1} = \begin{pmatrix} \alpha f_{i\bar{\alpha}} \\ \alpha f^\dagger_{i\bar{\alpha}} \end{pmatrix} \quad , \tag{2.49}$$

where the spin index α assumes the value $+1$ or -1, representing the spin-up and spin-down configuration, respectively. The notation $\bar{\alpha} = -\alpha$ indicates that the spin has been inverted. Note that unlike a physical particle-hole transformation this transformation is not anti-unitary. The labeling of 'particle-hole' only refers to the exchange of creation and annihilation operators.

The transformation acts on local two-point correlators (we have learned in Sec. 2.2.1 that all non-vanishing two-point correlators must be local) according to

$$\left\langle g_i f^\dagger_{i\omega'\alpha'} f_{i\omega\alpha} g_i^{-1} \right\rangle = -\alpha'\alpha \left\langle f^\dagger_{i-\omega\bar{\alpha}} f_{i-\omega'\bar{\alpha}'} \right\rangle \quad . \tag{2.50}$$

On a bi-local four-point correlator (we have learned in Sec. 2.2.1 that all non-vanishing four-point correlators must be bi-local) the local particle-hole transformation at lattice site i_1 acts as

$$\begin{aligned} &\left\langle g_{i_1} f^\dagger_{i_1\omega_{1'}\alpha_{1'}} f^\dagger_{i_2\omega_{2'}\alpha_{2'}} f_{i_1\omega_1\alpha_1} f_{i_2\omega_2\alpha_2} g_{i_1}^{-1} \right\rangle \\ &\quad = -\alpha_{1'}\alpha_1 \left\langle f^\dagger_{i_1-\omega_1\bar{\alpha}_1} f^\dagger_{i_2\omega_{2'}\alpha_{2'}} f_{i_1-\omega_{1'}\bar{\alpha}_{1'}} f_{i_2\omega_2\alpha_2} \right\rangle \quad . \end{aligned} \tag{2.51}$$

An analogous expression can be derived by applying the transformation on the other lattice site i_2 (not stated explicitly here). In summary, this allows us to make use of the

symmetry relation

$$G(1';1)\delta_{i_{1'}i_1} = -\alpha_{1'}\alpha_1 G(i_1 - \omega_1\bar{\alpha}_1; i_1 - \omega_{1'}\bar{\alpha}_{1'})\delta_{i_{1'}i_1} \tag{2.52}$$

for the single-particle correlation function and of the two independent relations

$$\begin{aligned} &G(1',2';1,2)\delta_{i_{1'}i_1}\delta_{i_{2'}i_2} \\ &\quad = -\alpha_{1'}\alpha_1 G(i_1 - \omega_1\bar{\alpha}_1, i_2\omega_{2'}\alpha_{2'}; i_1 - \omega_{1'}\bar{\alpha}_{1'}, i_2\omega_2\alpha_2)\delta_{i_{1'}i_1}\delta_{i_{2'}i_2} \\ &\quad = -\alpha_{2'}\alpha_2 G(i_1\omega_{1'}\alpha_{1'}, i_2 - \omega_2\bar{\alpha}_2; i_1\omega_1\alpha_1, i_2 - \omega_{2'}\bar{\alpha}_{2'})\delta_{i_{1'}i_1}\delta_{i_{2'}i_2} \end{aligned} \tag{2.53}$$

for the two-particle correlator. We point out that the last two symmetries also hold independently for purely local correlators where $i_1 = i_2$: formally, the particle-hole transformation is not just local but it is inherently tied to the pseudo-fermion construction and it acts on pairs of fermions which represent same spin operator. Since these fermion pairs necessarily live on the same lattice site it is convenient to refer to the particle-hole transformation as local. Yet in expressions which involve multiple spin operators on the same lattice site (like the purely local two-particle correlator) it is therefore still possible to transform both spin operators (i.e. both pairs of fermions) independently. In a more rigorous treatment one would need to introduce an additional label to the fermions in order to indicates the spin operator with which each fermion is associated. The particle-hole transformation would then act locally in the extra label. However, in an attempt to keep the notation tidy we suppress this extra label and simply impose that the symmetry relations (2.53) also hold for purely local correlators.

2.2.3 Lattice symmetries. Next, we focus on lattice symmetries. Just like the local U(1) transformation they can be exploited to constrain the spatial structure of the correlation functions. Lattice symmetries naturally exist in every pseudo-fermion Hamiltonian, since the underlying microscopic spin model is per construction defined on a lattice graph. The specific choice of a lattice determines the size and the generators of the symmetry group, yet there is no conceptual difference between different choices of lattices. In particular, on a technical level there is no qualitative difference between two-dimensional lattices and three-dimensional lattices. Any lattice consists of an underlying Bravais lattice which is decorated either with a single-atomic or multi-atomic unit cell. In conventional lattice calculations it is often helpful to constrain the lattice symmetry group to translational symmetries of the Bravais lattice only and to represent the remaining symmetries via the introduction of an extra band index which distinguishes different basis sites within the unit cell. In pf-FRG calculations, however, it is more convenient to consider the full set of lattice automorphisms T which map the lattice onto itself. In this picture every lattice site is assumed to be identical and it is possible to map any lattice site to any other site via a symmetry transformation. On the space of pseudo-fermions a lattice transformation T acts on the lattice site index

$$g_T \begin{pmatrix} f^\dagger_{i\alpha} \\ f_{i\alpha} \end{pmatrix} g_T^{-1} = \begin{pmatrix} f^\dagger_{T(i)\alpha} \\ f_{T(i)\alpha} \end{pmatrix} \quad , \tag{2.54}$$

leaving all remaining indices invariant. This definition is sufficient for spin models which have identical spin interactions on all lattice bonds, which is often the case for Heisenberg models. For models which incorporate bond-dependent couplings, as for example the Kitaev model, one can refine the definition operate on the combined space of lattice and spin indices, thereby restoring lattice symmetries which have originally been broken by bond-dependent interactions. We provide a concrete example of such combined symmetries in Sec. 2.5.3 when we discuss specialized pf-FRG implementations for the Kitaev model.

Applying the lattice transformation to a local two-point correlator obtains

$$\left\langle g_T f^\dagger_{i\omega'\alpha'} f_{i\omega\alpha} g_T^{-1} \right\rangle = \left\langle f^\dagger_{T(i)\omega'\alpha'} f_{T(i)\omega\alpha} \right\rangle \quad . \tag{2.55}$$

Similarly, the bi-local four-point correlator transforms as

$$\begin{aligned} &\left\langle g_T f^\dagger_{i_1\omega_{1'}\alpha_{1'}} f^\dagger_{i_2\omega_{2'}\alpha_{2'}} f_{i_1\omega_1\alpha_1} f_{i_2\omega_2\alpha_2} g_T^{-1} \right\rangle \\ &\quad = \left\langle f^\dagger_{T(i_1)\omega_{1'}\alpha_{1'}} f^\dagger_{T(i_2)\omega_{2'}\alpha_{2'}} f_{T(i_1)\omega_1\alpha_1} f_{T(i_2)\omega_2\alpha_2} \right\rangle \quad . \end{aligned} \tag{2.56}$$

In combination with the local U(1) symmetry the lattice symmetries can be used to dramatically reduce the complexity of the correlation functions; for the local single-particle correlation function

$$G(1';1)\delta_{i_{1'}i_1} = G(T(i_1)\omega_{1'}\alpha_{1'}; T(i_1)\omega_1\alpha_1)\delta_{i_{1'}i_1} \tag{2.57}$$

the lattice transformation T can be chosen such that it always maps the lattice site i_1 to an arbitrary reference site, making the correlator effectively lattice site independent. The bi-local two-particle correlator

$$\begin{aligned} &G(1',2';1,2)\delta_{i_{1'}i_1}\delta_{i_{2'}i_2} \\ &\quad = G(T(i_1)\omega_{1'}\alpha_{1'}, T(i_2)\omega_{2'}\alpha_{2'}; T(i_1)\omega_1\alpha_1, T(i_2)\omega_2\alpha_2)\delta_{i_{1'}i_1}\delta_{i_{2'}i_2} \end{aligned} \tag{2.58}$$

can similarly be simplified to depend only on a single lattice site.

2.2.4 Time-reversal symmetry. We now incorporate a genuinely physical symmetry: time-reversal invariance. The invocation of time-reversal on a magnetic moment maps the spin operator S^μ to its negative, $-S^\mu$. Consequently, only Hamiltonians which comprise interaction terms with an even number of spin operators can be invariant under time-reversal symmetry (assuming that all coupling constants are real numbers). The general Hamiltonian (2.32) which we consider here has been chosen to fulfill this property. We shall take note that the requirement to fulfill time-reversal symmetry forbids the analysis of quantum magnets in the presence magnetic fields since the coupling between spin operators and the magnetic field $\sim S^\mu B^\mu$ explicitly breaks time-reversal invariance. Naturally, time-reversal symmetry also excludes spin models that comprise three-spin interactions, which have been explored in the past as a mechanism to engineer chiral

quantum spin liquids [56, 57]. Acting on the space of pseudo-fermions, time-reversal symmetry can be implemented via

$$g \begin{pmatrix} f^\dagger_{i\alpha} \\ f_{i\alpha} \end{pmatrix} g^{-1} = \begin{pmatrix} e^{i\pi\alpha/2} f^\dagger_{i\bar{\alpha}} \\ e^{-i\pi\alpha/2} f_{i\bar{\alpha}} \end{pmatrix} \quad , \tag{2.59}$$

where g is anti-unitary. The necessity of the anti-unitary property may be intuitively understood by envisioning the effect of time-reversal on a quantum mechanical many-body system: time reversal should leave the positions of all particles invariant and reverse their momentum but at the same time it must not break the commutation relation of position and momentum operators as an underlying fundamental principle of quantum mechanics – hence the additional complex conjugation is necessary. Note, however, that the projective definition of time-reversal symmetry on the fermionic Hilbert space is not unique since it can always be composed with any transformation from the local SU(2) gauge redundancy group.

Under time-reversal symmetry the local two-point correlator transforms as

$$\left\langle g f^\dagger_{i\omega'\alpha'} f_{i\omega\alpha} g^{-1} \right\rangle^* = \alpha'\alpha \left\langle f^\dagger_{i-\omega'\bar{\alpha}'} f_{i-\omega\bar{\alpha}} \right\rangle^* \quad , \tag{2.60}$$

where the star denotes complex conjugation and we have simplified the resulting phase factor $e^{i\pi(\alpha-\alpha')/2} = \alpha'\alpha$ into a simple product of spin indices. Furthermore we have used that the thermal expectation value of an operator A transforms as $\langle A \rangle \to \langle gAg^{-1} \rangle^*$ under an anti-unitary transformation, which can be verified by explicitly writing out the expectation value as a trace over all possible configurations of the system, weighted by the density matrix, and making use of the defining relation $\langle g\psi | g\psi \rangle = \langle \psi | \psi \rangle^*$. In the same way we may evaluate the transformation behavior of the bi-local four-point correlator

$$\begin{aligned} &\left\langle g f^\dagger_{i_1\omega_{1'}\alpha_{1'}} f^\dagger_{i_2\omega_{2'}\alpha_{2'}} f_{i_1\omega_1\alpha_1} f_{i_2\omega_2\alpha_2} g^{-1} \right\rangle^* \\ &\quad = \alpha_{1'}\alpha_{2'}\alpha_1\alpha_2 \left\langle f^\dagger_{i_1-\omega_{1'}\bar{\alpha}_{1'}} f^\dagger_{i_2-\omega_{2'}\bar{\alpha}_{2'}} f_{i_1-\omega_1\bar{\alpha}_1} f_{i_2-\omega_2\bar{\alpha}_2} \right\rangle^* \quad . \end{aligned} \tag{2.61}$$

These identities, which derive from time-reversal invariance of the system, are particularly helpful because they relate the real part and the imaginary part of the correlators, thus opening up the possibility to parametrize the correlation functions by a single real number instead of a complex number (or a pair of real numbers). Comparison with the non-transformed correlators allows us to make use of the identities

$$G(1';1)\delta_{i_{1'}i_1} = \alpha_{1'}\alpha_1 G(i_1 - \omega_{1'}\bar{\alpha}_{1'}; i_1 - \omega_1\bar{\alpha}_1)^* \delta_{i_{1'}i_1} \tag{2.62}$$

for the single-particle correlation function, and

$$\begin{aligned} &G(1',2';1,2)\delta_{i_{1'}i_1}\delta_{i_{2'}i_2} \\ &\quad = \alpha_{1'}\alpha_{2'}\alpha_1\alpha_2 G(i_1 - \omega_{1'}\bar{\alpha}_{1'}, i_2 - \omega_{2'}\bar{\alpha}_{2'}; i_1 - \omega_1\bar{\alpha}_1, i_2 - \omega_2\bar{\alpha}_2)^* \delta_{i_{1'}i_1}\delta_{i_{2'}i_2} \end{aligned} \tag{2.63}$$

for the two-particle correlation function.

2.2.5 Hermitian symmetry. At last, we consider a hermitian symmetry of the Hamiltonian. Since every spin operator itself is already hermitian, the overall Hamiltonian is hermitian if all interaction constants are real numbers. We have already included this constraint in the formulation of our general Hamiltonian of study. Given the hermitian property we may explicitly evaluate the complex conjugation of a correlation function by promoting it to a conjugate transpose ('dagger'). The conjugate transpose reverses the order of operators, but being a symmetry of the Hamiltonian it leaves the thermal weights in the expectation value invariant such that we obtain for the local two-point correlator

$$\left\langle f^\dagger_{i\omega'\alpha'} f_{i\omega\alpha} \right\rangle^* = \left\langle f^\dagger_{i-\omega\alpha} f_{i-\omega'\alpha'} \right\rangle \tag{2.64}$$

and for the bi-local four-point correlator

$$\begin{aligned} &\left\langle f^\dagger_{i_1\omega_{1'}\alpha_{1'}} f^\dagger_{i_2\omega_{2'}\alpha_{2'}} f_{i_1\omega_1\alpha_1} f_{i_2\omega_2\alpha_2} \right\rangle^* \\ &\quad = \left\langle f^\dagger_{i_1-\omega_1\alpha_1} f^\dagger_{i_2-\omega_2\alpha_2} f_{i_1-\omega_{1'}\alpha_{1'}} f_{i_2-\omega_{2'}\alpha_{2'}} \right\rangle \quad . \end{aligned} \tag{2.65}$$

In combination with time-reversal invariance these relations become particularly powerful since both symmetries, time-reversal invariance and the hermitian property, imply relations between the real part and the imaginary part of the correlators; the composition of both symmetries thus defines constraints purely within the real part or the imaginary part of the correlators. The hermitian symmetry of the Hamiltonian implies the relation

$$G(1';1)\delta_{i_{1'}i_1} = G(i_1-\omega_1\alpha_1; i_1-\omega_{1'}\alpha_{1'})^* \delta_{i_{1'}i_1} \tag{2.66}$$

for the single-particle correlation function, and for the two-particle correlation function we have

$$\begin{aligned} &G(1',2';1,2)\delta_{i_{1'}i_1}\delta_{i_{2'}i_2} \\ &\quad = G(i_1-\omega_1\alpha_1, i_2-\omega_2\alpha_2; i_1-\omega_{1'}\alpha_{1'}, i_2-\omega_{2'}\alpha_{2'})^* \delta_{i_{1'}i_1}\delta_{i_{2'}i_2} \quad . \end{aligned} \tag{2.67}$$

2.2.6 Implications on vertex functions. In the beginning of this section we have constrained ourselves to spin models with general diagonal or off-diagonal two-spin interactions which are well described by the Hamiltonian given in Eq. (2.32),

$$H = \sum_{i,j} J^{\mu\nu}_{ij} S^\mu_i S^\nu_j \quad . \tag{2.68}$$

We assumed all interaction constants to be real, such that the Hamiltonian is time-reversal invariant and hermitian. Those two physical symmetries are augmented by an artificial local SU(2) gauge redundancy which is introduced by the fermionization procedure (2.33). Under these assumptions, in Sections 2.2.1 – 2.2.5, we have derived a list of symmetry constraints on the disconnected correlation functions for pseudo-

$$
\begin{aligned}
G(1';1) &= G(i_1\omega_{1'}\alpha_{1'};i_1\omega_1\alpha_1)\delta_{i'i} && \text{(Local U(1))}\\
G(1';1)\delta_{i_{1'}i_1} &= -\alpha_{1'}\alpha_1 G(i_1-\omega_1\bar{\alpha}_1;i_1-\omega_{1'}\bar{\alpha}_{1'})\delta_{i'i} && \text{(Local PH)}\\
G(1';1)\delta_{i_{1'}i_1} &= G(T(i_1)\omega_{1'}\alpha_{1'};T(i_1)\omega_1\alpha_1)\delta_{i'i} && \text{(Lattice)}\\
G(1';1)\delta_{i_{1'}i_1} &= \alpha_{1'}\alpha_1 G(i_1-\omega_{1'}\bar{\alpha}_{1'};i_1-\omega_1\bar{\alpha}_1)^*\delta_{i'i} && \text{(Time reversal)}\\
G(1';1)\delta_{i_{1'}i_1} &= G(i_1-\omega_1\alpha_1;i_1-\omega_{1'}\alpha_{1'})^*\delta_{i'i} && \text{(Hermiticity)}\\
G(1';1)\delta_{i_{1'}i_1} &= G(i_1\omega_1\alpha_{1'};i_1\omega_1\alpha_1)\delta_{i_{1'}i_1}\delta_{\omega_{1'}\omega_1} && \text{(Energy conservation)}
\end{aligned}
$$

Table 2.1. **Symmetries of the single-particle correlation function** for time-reversal invariant models. The composite index $n=\{i_n,\omega_n,\alpha_n\}$ represents tuples of lattice site index i_n, Matsubara frequency ω_n, and spin index α_n. The labels refer to the underlying physical symmetries which have been used to derive the relations.

$$
\begin{aligned}
&G(1',2';1,2)\\
&\quad = G(1',2';1,2)\delta_{i_{1'}i_1}\delta_{i_{2'}i_2} - G(2',1';1,2)\delta_{i_{2'}i_1}\delta_{i_{1'}i_2} && \text{(Local U(1))}\\
&G(1',2';1,2)\delta_{i_{1'}i_1}\delta_{i_{2'}i_2}\\
&\quad = -\alpha_{1'}\alpha_1 G(i_1-\omega_1\bar{\alpha}_1,i_2\omega_{2'}\alpha_{2'};i_1-\omega_{1'}\bar{\alpha}_{1'},i_2\omega_2\alpha_2)\delta_{i_{1'}i_1}\delta_{i_{2'}i_2} && \text{(Local PH 1)}\\
&G(1',2';1,2)\delta_{i_{1'}i_1}\delta_{i_{2'}i_2}\\
&\quad = -\alpha_{2'}\alpha_2 G(i_1\omega_{1'}\alpha_{1'},i_2-\omega_2\bar{\alpha}_2;i_1\omega_1\alpha_1,i_2-\omega_{2'}\bar{\alpha}_{2'})\delta_{i_{1'}i_1}\delta_{i_{2'}i_2} && \text{(Local PH 2)}\\
&G(1',2';1,2)\delta_{i_{1'}i_1}\delta_{i_{2'}i_2}\\
&\quad = G(T(i_1)\omega_{1'}\alpha_{1'},T(i_2)\omega_{2'}\alpha_{2'};T(i_1)\omega_1\alpha_1,T(i_2)\omega_2\alpha_2)\delta_{i_{1'}i_1}\delta_{i_{2'}i_2} && \text{(Lattice)}\\
&G(1',2';1,2)\delta_{i_{1'}i_1}\delta_{i_{2'}i_2} = \alpha_{1'}\alpha_{2'}\alpha_1\alpha_2\delta_{i_{1'}i_1}\delta_{i_{2'}i_2}\\
&\qquad \times G(i_1-\omega_{1'}\bar{\alpha}_{1'},i_2-\omega_{2'}\bar{\alpha}_{2'};i_1-\omega_1\bar{\alpha}_1,i_2-\omega_2\bar{\alpha}_2)^* && \text{(Time reversal)}\\
&G(1',2';1,2)\delta_{i_{1'}i_1}\delta_{i_{2'}i_2}\\
&\quad = G(i_1-\omega_1\alpha_1,i_2-\omega_2\alpha_2;i_1-\omega_{1'}\alpha_{1'},i_2-\omega_{2'}\alpha_{2'})^*\delta_{i_{1'}i_1}\delta_{i_{2'}i_2} && \text{(Hermiticity)}\\
&G(1',2';1,2)\delta_{i_{1'}i_1}\delta_{i_{2'}i_2}\\
&\quad = G(1',2';1,2)\delta_{i_{1'}i_1}\delta_{i_{2'}i_2}\delta_{w_{1'}+w_{2'}-w_1-w_2} && \text{(Energy conservation)}\\
&G(1',2';1,2)\delta_{i_{1'}i_1}\delta_{i_{2'}i_2}\\
&\quad = G(2',1';2,1)\delta_{i_{1'}i_1}\delta_{i_{2'}i_2} && \text{(Particle exchange)}
\end{aligned}
$$

Table 2.2. **Symmetries of the two-particle correlation function** for time-reversal invariant models. The composite index $n=\{i_n,\omega_n,\alpha_n\}$ represents tuples of lattice site index i_n, Matsubara frequency ω_n, and spin index α_n. The labels refer to the underlying physical symmetries which have been used to derive the relations.

fermions. For the sake of clarity we provide a summary of the list of symmetry constraints on the single-particle correlation function in Table 2.1 and extend it by adding Matsubara frequency conservation which stems from translational symmetry in imaginary time (not explicitly shown here). To the list of symmetries of the two-particle correlation function (Table 2.2) we add frequency conservation as well as the simultaneous exchange of both incoming and outgoing fermionic operators, which is a trivial symmetry that is implied by the anti-commutation relation of fermions. The aim of this subsection is to combine the individual symmetries in order to bring them in a form which is more convenient for practical FRG calculations, and to argue that the symmetry constraints which we have derived for the the disconnected correlation functions carry over to the one-line irreducible vertex functions, whose notion we have introduced in Sec. 2.1.

We first consider the single-particle correlation function $G(1';1)$. We have used the invariance under a local U(1) transformation to argue that the correlator must be purely local. We have further argued that as a consequence of lattice symmetries the correlation function is identical at every lattice site, allowing us to suppress the lattice site dependence altogether in our notation – this is true for most spin lattice models although some more exotic models may define bond-directional interactions which break this property, e.g. the Yao-Kivelson model on the decorated honeycomb lattice where the equality of lattice sites is spoiled by different spin interactions within and between triangular plaquettes [58]. Nevertheless, in such a case the symmetry can still be restored by defining composite symmetry transformations in spin space and lattice space, see Sec. 2.5.3. Next, we impose frequency conservation and expand the remaining dependence of the correlation function on the spin indices in the basis of Pauli matrices such that the expression for the correlation function assumes the general form

$$G(1';1) = \left(G^{\mu}(\omega_1)\sigma^{\mu}_{\alpha_{1'}\alpha_1}\right)\delta_{i_{1'}i_1}\delta_{\omega_{1'}\omega_1} \quad . \tag{2.69}$$

Here, the index μ takes values $0\ldots3$ and σ^0 is the identity matrix, while σ^1, σ^2, and σ^3 represent the three Pauli matrices. We can proceed similarly with the two-particle correlation function. Employing the local U(1) symmetry it can be brought into its bi-local form, while frequency conservation ensures that the correlation function effectively depends only on three frequency arguments,

$$\begin{aligned} &G(1',2';1,2) \\ &\quad = \left(G_{i_1 i_2}(\omega_{1'}\alpha_{1'},\omega_{2'}\alpha_{2'};\omega_1\alpha_1,\omega_2\alpha_2)\delta_{i_{1'}i_1}\delta_{i_{2'}i_2} - (1'\leftrightarrow 2')\right)\delta_{\omega_{1'}+\omega_{2'}-\omega_1-\omega_2} \quad . \end{aligned} \tag{2.70}$$

We state this intermediate result explicitly because it marks the important step of removing the redundancy of site-exchanging and site-preserving terms in the bi-local four-point vertex. In Sec. 2.3 we make use of this result and introduce a diagrammatic language based on the bi-local expression $G_{i_1 i_2}(1',2';1,2)$. To proceed, we expand the spin indices in the basis of Pauli matrices, which yields the general form of the two-particle

$$
\begin{aligned}
G^{\mu}(\omega) &= \xi(\mu) G^{\mu}(\omega) && \text{(H} \circ \text{TR)} \\
G^{\mu}(\omega) &= -\xi(\mu) G^{\mu}(-\omega) && \text{(PH)} \\
G^{\mu}(\omega) &= -G^{\mu}(\omega)^{*} && \text{(TR} \circ \text{PH)} \\
G^{\mu\nu}_{i_1 i_2}(s,t,u) &= G^{\nu\mu}_{i_2 i_1}(-s,t,u) && \text{(X} \circ \text{H} \circ \text{TR} \circ \text{PH1} \circ \text{PH2)} \\
G^{\mu\nu}_{i_1 i_2}(s,t,u) &= \xi(\mu)\xi(\nu) G^{\mu\nu}_{i_1 i_2}(s,-t,u) && \text{(H} \circ \text{TR)} \\
G^{\mu\nu}_{i_1 i_2}(s,t,u) &= \xi(\mu)\xi(\nu) G^{\nu\mu}_{i_2 i_1}(s,t,-u) && \text{(X} \circ \text{H} \circ \text{TR)} \\
G^{\mu\nu}_{i_1 i_2}(s,t,u) &= -\xi(\nu) G^{\mu\nu}_{i_1 i_2}(u,t,s) && \text{(PH2)} \\
G^{\mu\nu}_{i_1 i_2}(s,t,u) &= \xi(\mu)\xi(\nu) G^{\mu\nu}_{i_1 i_2}(s,t,u)^{*} && \text{(TR} \circ \text{H} \circ \text{TR} \circ \text{PH1} \circ \text{PH2)}
\end{aligned}
$$

Table 2.3. **Symmetry constraints for the basis functions** of the single-particle (first three identities) and two-particle (remaining five identities) correlation functions. The equations are labeled by the symmetries which have been used in their derivation. The label 'H' denotes the hermitian symmetry, 'TR' is time reversal, 'X' is particle exchange, and 'PH' denotes the local particle-hole symmetry. For the two-particle correlation function we discriminate the two scenarios of applying the particle-hole transformation either to the first pair of lattice site indices ('PH1') or the to the second pair ('PH2'). See text for additional details.

correlation function

$$
G(1',2';1,2) = \left[\left(G^{\mu\nu}_{i_1 i_2}(s,t,u) \sigma^{\mu}_{\alpha_{1'}\alpha_1} \sigma^{\nu}_{\alpha_{2'}\alpha_2} \right) \delta_{i_{1'} i_1} \delta_{i_{2'} i_2} - (1' \leftrightarrow 2') \right] \delta_{\omega_{1'}+\omega_{2'}-\omega_1-\omega_2} \quad , \tag{2.71}
$$

where we have introduced the bosonic transfer frequencies

$$
\begin{aligned}
s &= \omega_{1'} + \omega_{2'} \\
t &= \omega_{1'} - \omega_1 \\
u &= \omega_{1'} - \omega_2 \quad .
\end{aligned} \tag{2.72}
$$

In this notation additional constraints on the basis functions $G^{\mu}(\omega)$ and $G^{\mu\nu}_{i_1 i_2}(s,t,u)$ can be derived by applying and combining the symmetry relations in Table 2.1 and Table 2.2, respectively. A list of composite symmetries and their implications on the basis functions is given in Table 2.3, where we have introduced the sign function $\xi(\mu)$ which is defined as

$$
\xi(\mu) = \begin{cases} +1 & \text{if } \mu = 0 \\ -1 & \text{otherwise} \end{cases} \quad . \tag{2.73}
$$

Its appearance is a consequence of making use of the identity

$$
\alpha\alpha' \sigma^{\mu}_{\bar{\alpha}\bar{\alpha}'} = \alpha\alpha' \left(\sigma^{\mu *} \right)_{\bar{\alpha}'\bar{\alpha}} = \xi(\mu) \sigma^{\mu}_{\alpha'\alpha} \tag{2.74}
$$

to undo the appearance of spin-dependent prefactors in the course of applying symmetry transformations. Most importantly, the symmetries imply that the single-particle

correlation function is diagonal in all its arguments and that it depends only on the frequency argument.

In the final step, in order to make the symmetry classification accessible in the language of the functional renormalization group we need to provide reason that the symmetries of the (disconnected) correlation functions carry over to the one-particle irreducible (1PI) vertex functions which we have introduced in Sec. 2.1. The necessary argument is fairly simple for the single-particle vertex function; the disconnected correlation function is related to the 1PI single-particle vertex via the Dyson equation as seen in Eq. 2.26,

$$G = [[G_0]^{-1} + \gamma_1]^{-1} \quad . \tag{2.75}$$

For the pseudo-fermion Hamiltonian (2.35), which does not comprise any quadratic terms, the bare propagator $G_0(1';1) = \frac{1}{i\omega}$ becomes maximally simple and the Dyson equation assumes the form

$$G(1';1) = \frac{1}{i\omega + \gamma_1(1';1)} \quad . \tag{2.76}$$

In this simplified form we can directly read off that – given that $G(1';1)$ is diagonal in all arguments (which is the case, according to the identities given in Table 2.3[1]) – the 1PI single-particle vertex necessarily also is diagonal in all arguments and has the same symmetries as $G(1';1)$. The reasoning about the 1PI two-particle vertex function follows the same line of thought. We have mentioned in Sec. 2.1 that the 1PI vertex function can be related to the connected correlation function via the so-called tree expansion, which for the two-particle vertices is given by [59]

$$G_c(1',2';1,2) = -\sum_{3,4,5,6} \gamma_2(3,4;5,6) G(1';3) G(2';4) G(5;1) G(6;2) \quad . \tag{2.77}$$

Given that the propagators are diagonal (which we have just shown) the structure is simple enough for all symmetries to directly carry over from the connected Green's function to the 1PI vertex function; we point out that also the connected Green's function and the disconnected correlation function have the same symmetries since diagrammatically one is a subset of the other. The symmetry relation between the connected Green's function and the disconnected correlation function can also be shown explicitly on the level of generating functionals [59].

In summary, we have demonstrated that the pseudo-fermionic one-particle irreducible vertex functions can be efficiently parametrized according to Eqs. (2.69, 2.71) under the additional symmetry constraints listed in Table 2.3, given that the underlying spin Hamiltonian is hermitian and time-reversal invariant. We leverage this insight in the next section to transition from the general fermionic formulation of the functional renormalization group to the pseudo-fermion functional renormalization group.

[1] Its diagonality in the lattice site and frequency indices has already been discussed. Diagonality in the spin arguments results from the first identity in Table 2.3 which implies that all non-diagonal components must vanish.

2.3. Pseudo-fermion functional renormalization group

This section is a central piece of the thesis and is dedicated to the derivation of the general formulation of the pseudo-fermion functional renormalization group (pf-FRG) for time-reversal invariant systems whose spin interactions are of the form

$$H = \sum_{i,j} J_{ij}^{\mu\nu} S_i^\mu S_j^\nu \quad . \tag{2.78}$$

The general formulation as presented here is an extension of the original formulation of the pf-FRG which had originally been derived for the Heisenberg model [6, 60]. Extensions to spin models with slightly reduced spin symmetries, for example the Kitaev model [33] or a restricted version of Dzyaloshinskii-Moriya (DM) interactions [39], have been formulated before, but it has long been thought that the incorporation of general off-diagonal spin interactions is accompanied by a dramatic increase of computational complexity in the flow equations [39]. In this section we argue that in the presence of time-reversal symmetry the increase in complexity is only moderate as compared to the highly symmetric Heisenberg model. The section is based on our results as published in Ref. [P6].

Incited by Kitaev's proposal of a quantum spin liquid on the honeycomb lattice in 2006 [4] the study of strongly spin-orbit coupled Mott insulators [68] has received great attention as a potential platform to realize significant bond-directional spin interactions, and researchers have since been working vividly towards the fabrication of such materials. These efforts have lead to the discovery of a variety of Kitaev materials, with prominent examples being Na_2IrO_3, (α, β, γ)-Li_2IrO_3, and $RuCl_3$ [62]. Although the original Kitaev model includes only diagonal bond-dependent couplings, actual materials also feature off-diagonal interactions which are often referred to as Γ-terms. The minimal model can be written in the form

$$H = \sum_{\langle i,j\rangle_\gamma} J\mathbf{S}_i\mathbf{S}_j + KS_i^\gamma S_j^\gamma + \Gamma \sum_{\alpha,\beta\neq\gamma} \left(S_i^\alpha S_j^\beta + S_i^\beta S_j^\alpha \right) \quad , \tag{2.79}$$

where the conventional Heisenberg and Kitaev terms are augmented by the Γ-term which couples the off-diagonal spin components $\alpha, \beta \neq \gamma$. Depending on the material other combinations of off-diagonal couplings, e.g. Γ'-terms or DM interactions, may also be relevant [51]. Yet all of the above interaction types have in common that they can be captured within the general Hamiltonian (2.78) and can thus be efficiently simulated in pf-FRG calculations [P6, P7].

The relevance of non-diagonal spin interaction terms is not limited to Kitaev materials. They frequently appear at the interface between the idealized theoretical study of spin liquid models and the experimental reality of non-ideal materials. They are being discussed for example in renowned spin liquid candidate materials like the quasi two-dimensional compound $ZnCu_3(OH)_6Cl_2$ (herbertsmithite) [50, 63] which we discuss in

Sec. 3.3, or in the family of three-dimensional rare-earth pyrochlore materials [64, 65]. Their pervasiveness in spin liquid candidate materials underlines the importance to further our understanding of their influence on underlying microscopic theories and on the stability of spin liquid phases. However, as we have briefly reviewed in Sec. 1.2 the numerical simulation of frustrated quantum many-body systems is inherently difficult and poses a serious problem to many established numerical techniques.

In this section we present the pf-FRG flow equations in a symmetry-constrained form which sufficiently reduces the computational complexity to make general spin models of the form (2.78) amenable to a numerical analysis within the framework of pf-FRG. Focusing in this section mostly on the technical derivation, we reserve the subsequent Sections 2.4–2.5 for a more detailed discussion of the approximations which are involved in the construction of pf-FRG. Most importantly we later also address the question of why – despite the pseudo-fermion model being in the strong coupling limit – the pf-FRG is capable to successfully model the delicate interplay between magnetic ordering tendencies and disordering mechanisms.

2.3.1 Flow equations. The pf-FRG flow equations are derived from the general fermionic flow equations which we have previously stated in Eqs. (2.28, 2.29). Throughout the course of the symmetry classification of the pseudo-fermion Hamiltonian in Section 2.2 we have seen that the pseudo-fermion model due to locality constraints on the fermions is most naturally described in a real space picture, i.e. the three relevant quantum numbers of the fermionic degrees of freedom are: lattice site index i, Matsubara frequency ω, and spin index α.

The renormalization group flow is generated by a sharp multiplicative cutoff function in the frequency dependence, $\theta(|\omega| - \Lambda)$, set by a frequency cutoff Λ. The cutoff dependent bare propagator by this definition is given by

$$G_0^\Lambda(\omega) = \frac{\theta(|\omega| - \Lambda)}{i\omega} \tag{2.80}$$

and hence fulfills the boundary conditions $G_0^{\Lambda\to\infty} = 0$ and $G_0^{\Lambda=0} = G_0$, as required in Eqs. (2.15, 2.16). Including the self-energy corrections, the full cutoff-dependent propagator can be written as

$$G^\Lambda(\omega) = \frac{\theta(|\omega| - \Lambda)}{i\omega - \Sigma^\Lambda(\omega)} \quad , \tag{2.81}$$

and the single scale propagator therefore results to

$$S^\Lambda(\omega) = \frac{\delta(|\omega| - \Lambda)}{i\omega - \Sigma^\Lambda(\omega)} \quad . \tag{2.82}$$

In this parametrization we have implied already that the propagator is diagonal in all its arguments and depends only on the frequency argument. Note that the calculation of the single-scale propagator must be performed carefully with regard to the appearance

of products of the step function $\theta(\omega)$ with the delta distribution $\delta(\omega)$. Their product can be resolved by considering an infinitesimal broadening of the functions [60, 66].

We have argued in the derivation of the general fermionic functional renormalization group that one obtains an infinite hierarchy of coupled differential equations for the 1PI n-particle vertices up to arbitrary order. The level of approximation which is implemented in the pf-FRG in order to obtain a finite set of equations is to neglect the three-particle vertex and higher orders [6]. The truncation is further improved by employing the Katanin scheme which amounts to a substitution of the single-scale propagator in the flow equation for the two-particle vertex with the dressed expression [67]

$$S^{\Lambda}_{\mathrm{kat}}(\omega) = S^{\Lambda}(\omega) - \left(G^{\Lambda}(\omega)\right)^2 \frac{\mathrm{d}}{\mathrm{d}\Lambda}\Sigma^{\Lambda}(\omega) \quad . \tag{2.83}$$

It has been demonstrated phenomenologically that the Katanin scheme is necessary in order for the pf-FRG to correctly resolve paramagnetic phases. When using the conventional truncation scheme (without the Katanin extension) only magnetic phases would be indicated in pf-FRG calculations [6]. Beyond phenomenological arguments one can show formally that the flow equations on the Katanin truncation level become exact for SU(N) quantum spins in the limit of large N – which is a limit that naturally suppresses magnetic order, c.f. the discussion in Sec. 1.1.4. We address the Katanin truncation and the large-N limit of the flow equations in more detail in Sections 2.5.2 and 2.5.4, respectively.

With these ingredients at hand, the flow equation for the self-energy[2] assumes the form

$$\frac{d}{d\Lambda}\Sigma^{\Lambda}(1';1) = -\frac{1}{2\pi}\sum_{2}\Gamma^{\Lambda}(1',2;1,2)S^{\Lambda}(\omega_2) \quad . \tag{2.84}$$

The flow equation for the 1PI two-particle vertex[3] $\Gamma(1',2';1,2)$ is given by

$$\begin{aligned}\frac{d}{d\Lambda}\Gamma^{\Lambda}(1',2';1,2) = \frac{1}{2\pi}\sum_{3,4}\Big[&\Gamma^{\Lambda}(1',2';3,4)\Gamma^{\Lambda}(3,4;1,2)\\ &- \Gamma^{\Lambda}(1',4;1,3)\Gamma^{\Lambda}(3,2';4,2) - (3 \leftrightarrow 4)\\ &+ \Gamma^{\Lambda}(2',4;1,3)\Gamma^{\Lambda}(3,1';4,2) + (3 \leftrightarrow 4)\Big]\\ &\times G^{\Lambda}(\omega_3)S^{\Lambda}_{\mathrm{kat}}(\omega_4) \quad .\end{aligned} \tag{2.85}$$

Both flow equations have been assigned a prefactor of $1/(2\pi)$ which results from the internal integration over all Matsubara frequencies; the pf-FRG flow equations are conventionally formulated at zero temperature where Matsubara frequencies become continues

[2] The self-energy is equivalent to the 1PI single-particle vertex function $\gamma_1(1';1) = -\Sigma(1';1)$ up to a minus sign, see Sec. 2.1.

[3] In the general fermionic flow equations we labeled the 1PI n-particle vertex with γ_n since the formalism comprises vertex functions up to arbitrary order. In the literature on pf-FRG, where the hierarchy of flow equations is truncated after the first two orders, it has become customary to label the single-particle vertex γ and the two-particle vertex Γ, which is the notation that we adopt here.

and summations are replaced by the integrals, $\sum_\omega \to \frac{1}{2\pi}\int_\omega$. Hence, the symbol $\sum_{3,4}$ now stands for a summation over lattice site and spin indices and an integration over frequencies, $\sum_{i_3,i_4}\sum_{\alpha_3,\alpha_4}\int_{\omega_3,\omega_4}$. As a consequence of frequency conservation both flow equations effectively have one internal frequency integration, which is why both of them have the same prefactor of $1/(2\pi)$. Even though the calculation is formally performed at zero temperature it is possible to extract thermodynamic properties from the simulation via a linear rescaling of the frequency cutoff Λ to temperature $T = \frac{\pi}{2}\Lambda$ [36]. We discuss the rescaling trick in more detail in Sec. 2.5.6.

Before inserting the final symmetry-constrained parametrization of the vertex functions it is instructive to make the intermediate step of implementing only the local U(1) gauge redundancy, which enforces locality of the single-particle vertex and bi-locality of the two-particle vertex. In this spirit we formulate the ansatz (c.f. Sec. 2.2.1)

$$\Gamma^\Lambda(1',2';1,2) = \Gamma^\Lambda_{i_1 i_2}(1',2';1,2)\delta_{i_{1'}i_1}\delta_{i_{2'}i_2} - \Gamma^\Lambda_{i_1 i_2}(2',1';1,2)\delta_{i_{2'}i_1}\delta_{i_{1'}i_2} \quad , \tag{2.86}$$

where the multi-indices $n = (\omega_n, \alpha_n)$ represent the Matsubara frequency and spin dependence, and we insert the ansatz into the general flow equations (2.84, 2.85). By collecting the coefficients of all site-conserving terms $\sim \delta_{i_{1'}i_1}\delta_{i_{2'}i_2}$ we obtain a set of flow equations for the n-local vertex functions (the naming n-local refers to the locality of the single-particle vertex, the bi-locality of the two-particle vertex, and in principle also to tri-locality of the three-point vertex which is neglected in pf-FRG).

The n-local flow equations are a good starting point for understanding the structure of the pf-FRG. First of all, they always have the same structure for arbitrary spin models since the local U(1) gauge redundancy exists in all pseudo-fermionic models regardless of the presence or absence of any additional physical symmetries. As such, the n-local flow equations are a convenient starting point for the derivation of more specialized pf-FRG approaches where one can derive special parametrizations of the remaining frequency and spin dependence. Paying tribute to their importance, we write the n-local flow equations down explicitly for the single-particle vertex

$$\frac{\mathrm{d}}{\mathrm{d}\Lambda}\Sigma^\Lambda(1';1) = \frac{1}{2\pi}\sum_2 \Big[\Gamma^\Lambda_{i_1 i_1}(2,1';1,2) - \sum_j \Gamma^\Lambda_{i_1 j}(1',2;1,2)\Big] S^\Lambda(\omega_2) \tag{2.87}$$

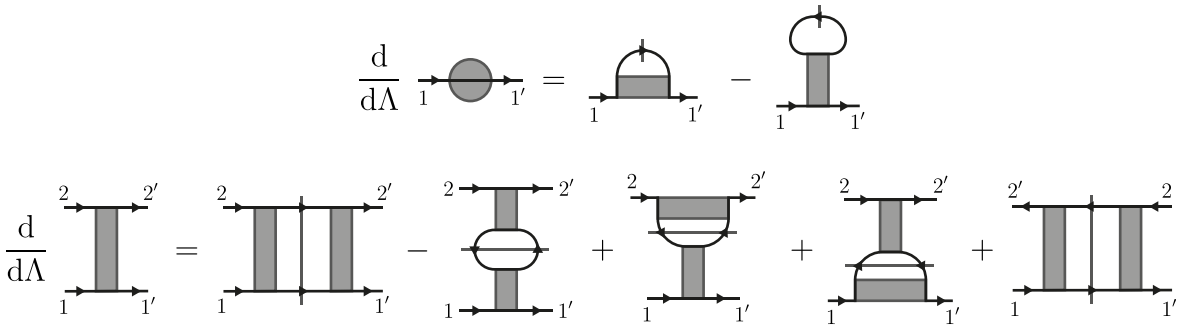

Figure 2.3. **n-local pf-FRG flow equations** for the 1PI single-particle vertex (top row) and the 1PI two-particle vertex (bottom row). The lattice site index is preserved along the solid black lines. In the single-particle flow equation the slashed propagator line denotes the single-scale propagator. In the two-particle flow equation the pair of slashed propagator lines denotes the sum $G(\omega_1)S_{\mathrm{kat}}(\omega_2)+S_{\mathrm{kat}}(\omega_1)G(\omega_2)$. The order of diagrams is as they appear in Eqs. (2.87) and (2.88), respectively. We occasionally refer to important diagrams by their names. The first and second diagram on the right hand side of the single-particle flow equation are the Hartree and Fock diagram, respectively. The first and last diagram of the two-particle flow equation are the particle-particle ladder diagram and the particle-hole ladder diagram, respectively; the second diagram is the RPA diagram; the third and fourth diagram are additional vertex correction diagrams.

and for the two-particle vertex

$$\begin{aligned}\frac{\mathrm{d}}{\mathrm{d}\Lambda}\Gamma^{\Lambda}_{i_1 i_2}(1',2';1,2) = \frac{1}{2\pi}\sum_{3,4}\Big[&\Gamma^{\Lambda}_{i_1 i_2}(3,4;1,2)\Gamma^{\Lambda}_{i_1 i_2}(1',2';3,4) + (3\leftrightarrow 4)\\ &- \sum_j \Gamma^{\Lambda}_{i_1 j}(1',4;1,3)\Gamma^{\Lambda}_{j i_2}(3,2';4,2) - (3\leftrightarrow 4)\\ &+ \Gamma^{\Lambda}_{i_1 i_2}(1',4;1,3)\Gamma^{\Lambda}_{i_2 i_2}(3,2';2,4) + (3\leftrightarrow 4)\\ &+ \Gamma^{\Lambda}_{i_1 i_1}(3,1';1,4)\Gamma^{\Lambda}_{i_1 i_2}(4,2';3,2) + (3\leftrightarrow 4)\\ &+ \Gamma^{\Lambda}_{i_1 i_2}(3,2';1,4)\Gamma^{\Lambda}_{i_1 i_2}(1',4;3,2) + (3\leftrightarrow 4)\Big]\\ &\times G^{\Lambda}(\omega_3)S^{\Lambda}_{\mathrm{kat}}(\omega_4) \quad . \end{aligned} \tag{2.88}$$

The n-local flow equations can conveniently be represented diagrammatically as displayed in Fig. 2.3. In this notation it becomes evident that in both, the single-particle flow equation and the two-particle flow equation, there is one term each which contains an internal summation over all lattice sites; in the single-particle flow equation this is the Hartree diagram (last diagram in the top line of Fig. 2.3) and in the two-particle flow equation it is the RPA diagram (second diagram on the right-hand side, bottom line of Fig. 2.3). One may expect that these diagrams play an important role in the formation of magnetic long-ranger order. Indeed, one can show explicitly that these diagrams are the leading order contributions in the classical limit where magnetic long-range order is likely to develop. We discuss the generalization of the pf-FRG formalism to arbitrary

spin lengths (and ultimately to the classical limit) in more detail in Sec. 2.5.5.

We now proceed with the presentation of the general pf-FRG flow equations, where we make use of the fully symmetry-constrained parametrization of the 1PI vertices which we have derived in Section 2.2. The self-energy is thereby constrained to be diagonal in all its arguments,

$$\Sigma(1';1) = \Sigma(\omega)\delta_{i'i}\delta_{\omega'\omega}\delta_{\alpha'\alpha} \quad , \tag{2.89}$$

it is anti-symmetric in the frequency dependence, and it takes on only imaginary values,

$$\begin{aligned} &\Sigma(\omega) \in i\mathbb{R} \\ &\Sigma(\omega) = -\Sigma(-\omega) \quad . \end{aligned} \tag{2.90}$$

Similarly, the results of our symmetry analysis of the pseudo-fermion Hamiltonian (Table 2.3) imply that the two-point vertex should be written in the form

$$\Gamma(1',2';1,2) = \left[\left(\Gamma^{\mu\nu}_{i_1 i_2}(s,t,u)\sigma^{\mu}_{\alpha_{1'}\alpha_1}\sigma^{\nu}_{\alpha_{2'}\alpha_2}\right)\delta_{i_{1'}i_1}\delta_{i_{2'}i_2} - (1' \leftrightarrow 2')\right]\delta_{\omega_{1'}+\omega_{2'}-\omega_1-\omega_2} \quad , \tag{2.91}$$

where basis functions $\Gamma^{\mu\nu}_{i_1 i_2}(s,t,u)$ with $\mu = 0,\ldots,3$ are either purely real or purely imaginary, and they fulfill certain symmetry relations in their Matsubara frequency dependence:

$$\begin{aligned} &\Gamma^{\mu\nu}_{i_1 i_2}(s,t,u) \in \begin{cases} \mathbb{R} & \text{if } \xi(\mu)\xi(\nu) = 1 \\ i\mathbb{R} & \text{if } \xi(\mu)\xi(\nu) = -1 \end{cases} \\ &\Gamma^{\mu\nu}_{i_1 i_2}(s,t,u) = \Gamma^{\nu\mu}_{i_2 i_1}(-s,t,u) \\ &\Gamma^{\mu\nu}_{i_1 i_2}(s,t,u) = \xi(\mu)\xi(\nu)\Gamma^{\mu\nu}_{i_1 i_2}(s,-t,u) \\ &\Gamma^{\mu\nu}_{i_1 i_2}(s,t,u) = \xi(\mu)\xi(\nu)\Gamma^{\nu\mu}_{i_2 i_1}(s,t,-u) \\ &\Gamma^{\mu\nu}_{i_1 i_2}(s,t,u) = -\xi(\nu)\Gamma^{\mu\nu}_{i_1 i_2}(u,t,s) \quad . \end{aligned} \tag{2.92}$$

For a concise notation we are referring to the identity matrix as σ^0 while σ^1, σ^2, and σ^3 represent the three Pauli matrices. Furthermore, we have made use of the sign function

$$\xi(\mu) = \begin{cases} +1 & \text{if } \mu = 0 \\ -1 & \text{otherwise} \end{cases} \tag{2.93}$$

and we have introduced the three bosonic transfer frequencies s, t, and u which are defined as the sum or the differences of the original fermionic frequencies,

$$\begin{aligned} s &= \omega_{1'} + \omega_{2'} \\ t &= \omega_{1'} - \omega_1 \\ u &= \omega_{1'} - \omega_2 \quad . \end{aligned} \tag{2.94}$$

The individual flow equations for the self-energy and for the 16 basis functions of the two-particle vertex are obtained by inserting the parametrizations (2.89, 2.91) into the general form of the flow equations (2.84, 2.85). After inserting the ansätze into the

flow equations all internal summations over spin indices can be computed explicitly, as they are now reduced to different contractions of Pauli matrices. The remaining spin-dependent terms are of the form[4] $\sim \sigma^{\mu}_{\alpha_1'\alpha_1}\sigma^{\nu}_{\alpha_2'\alpha_2}$, and collecting their coefficients obtains the set of flow equations.

For each of the five diagram classes in the FRG flow equation of the two-particle vertex, after substituting vertex functions by their parametrization in terms of 16 basis functions and respecting also the possible particle exchange, one obtains a maximum of 512 contributing terms. In practice, however, some of the Pauli matrix contractions in the derivation of the flow equations vanish or become redundant, in particular for the computationally expensive RPA diagrams which contain a summation over all lattice sites. We separately address the question of computational complexity in more detail in Sec. 2.4.4.

Due to the large number of terms in the flow equations for the basis functions we do not state them explicitly. However, a diagrammatic representation is included in Appendix A.

The initial conditions for the flow equations, according to the prescription (2.31) which we formulated in the derivation of the general fermionic flow equations, are defined by the couplings constants $J^{\mu\nu}_{i_1 i_2}$ of the underlying spin Hamiltonian,

$$\Sigma^{\Lambda\to\infty}(\omega) = 0 \quad \text{and} \quad \Gamma^{\mu\nu,\Lambda\to\infty}_{i_1 i_2}(s,t,u) = \frac{J^{\mu\nu}_{i_1 i_2}}{4} \quad . \tag{2.95}$$

We shall take note that the model specific interaction parameters only enter in the initial conditions of the flow. Hence, in the course of exploring the model's parameter space it is not necessary to make modifications to the structure of the flow equations – once they have been derived and implemented for a specific symmetry class (in this chapter we focused on general time-reversal symmetric, hermitian models) they can be readily applied to arbitrary points of the phase space by merely adjusting their initial conditions.

2.3.2 Observables. Once the flow equations have been solved numerically, a process which we discuss in more details in Sec. 2.4, all vertex functions are known (that is, of course, within the scope of the approximations which are incorporated in the pf-FRG scheme), and the problem of simulating a strongly interacting quantum magnet has been solved – at least formally. The natural question to ask next is how to extract physical observables from the vertex functions.

In quantum magnetism, a central observable of great interest is the spin-spin correlation function (the magnetic susceptibility)

$$\chi^{\mu\nu}_{ij}(\omega) = \int_0^\beta \mathrm{d}\tau e^{i\omega\tau} \left\langle T_\tau \left[S^{\mu}_i(\tau) S^{\nu}_j(0) \right] \right\rangle \tag{2.96}$$

[4]The three Pauli matrices in combination with the identity matrix form a complete basis of the spin space. Therefore all spin-dependent expressions can be brought into this form.

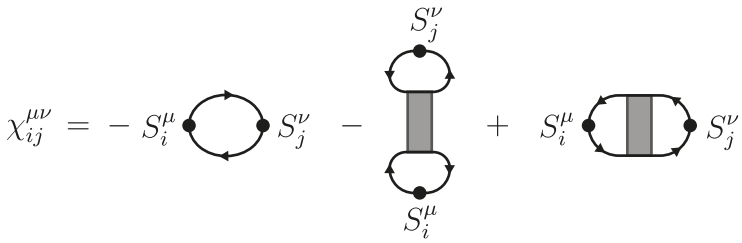

Figure 2.4. **Spin-spin correlations** expressed in terms of n-local vertex functions (c.f. discussion in Sec. 2.3.1). The black dots signal external spin operators and should be read to contribute a factor $S_i^\mu \sim \frac{1}{2}\sigma^\mu_{\alpha_1'\alpha_1}$ while being diagonal in the frequency arguments and fixing the site index.

which is expected to diverge at a phase transition into a magnetically ordered phase. Re-expressing the spin operators in terms of pseudo-fermions by the usual construction (2.33) and following the tree expansion (2.77) one obtains the relation [60]

$$\begin{aligned}\chi_{ij}^{\mu\nu,\Lambda}(\omega) = &-\frac{1}{4\pi}\int \mathrm{d}\omega_1 G^\Lambda(\omega_1)G^\Lambda(\omega_1+\omega)\delta_{ij} \\ &-\frac{1}{16\pi^2}\int \mathrm{d}\omega_1\mathrm{d}\omega_2 G^\Lambda(\omega_1)G^\Lambda(\omega_1+\omega)G^\Lambda(\omega_2)G^\Lambda(\omega_2+\omega) \\ &\times \sum_{\alpha_1'\alpha_2'\alpha_1\alpha_2} \Gamma^\Lambda(i\ \omega_1+\omega\ \alpha_{1'}, j\ \omega_2\ \alpha_{2'}; i\ \omega_1\ \alpha_1, j\ \omega_2+\omega\ \alpha_2)\sigma^\mu_{\alpha_1\alpha_1'}\sigma^\nu_{\alpha_2\alpha_2'} \quad .\end{aligned} \tag{2.97}$$

Although the spin correlations $\chi_{ij}^{\mu\nu,\Lambda}(\omega)$ can, in principle, be calculated at arbitrary Matsubara frequencies ω, the analytic continuation to real frequencies is generally known to pose a serious challenge to any (approximate) numerical technique [68]. Consequently, in the existing literature on pf-FRG the focus has been on the calculation of the static spin-spin correlations at $\omega = 0$. By imposing the n-locality constraint on the vertex functions the static susceptibility can be diagrammatically represented as shown in Fig. 2.4.

Knowledge of the full spatial structure of the spin correlations also allows to compute the elastic component ($\omega = 0$) of the structure factor via a straightforward Fourier transformation

$$\chi^{\mu\nu,\Lambda}(\mathbf{k}) = \frac{1}{N}\sum_{i,j} e^{i\mathbf{k}(\mathbf{r}_i-\mathbf{r}_j)}\chi_{ij}^{\mu\nu,\Lambda}(0) \quad . \tag{2.98}$$

The assessment of the structure factor is a convenient way to determine and characterize the onset of magnetic long-range order. We discuss this in more detail in Sec. 2.5.1.

2.3.3 Précis. In this section we have presented an efficient, symmetry constrained parametrization of the pf-FRG flow equations for time-reversal invariant, hermitian models of quantum magnetism with two-spin interactions. Furthermore we have presented a way to extract physical observables from the solution of the flow equations. In an effort

to present a concise, well-structured derivation of the flow equations we have been brief on providing justifications for the implementation of the Katanin truncation scheme, which is the most central approximation within the pf-FRG approach. We have also held out on giving details about the interpretation of results which can be obtained in pf-FRG calculations. We pick up these discussions in the next two sections where we spotlight different aspects of the practical application of pf-FRG. Sec. 2.4 focuses on aspects which are related to the numerical solution of the flow equations. In Sec. 2.5, we focus more on the underlying methodological aspects.

2.4. Numerical solution of the flow equations

In the derivation of the pf-FRG flow equations, we have performed a truncation of the infinite hierarchy of coupled differential equations. However, this truncation alone is not sufficient to obtain a finite set of differential equations because on every level of the hierarchy (single-particle vertex functions, two-particle vertex functions, ...) the vertex functions still depend on an infinitely large parameter space spanned by a Matsubara frequency dependence, the frequency cutoff, and in the case of the two-particle vertex also by the lattice site index.

In this section we address further approximations which are necessary in order to obtain a finite set of differential equations and we give practical guidance on their implementation. Details on the differential equation solver are provided in Subsection 2.4.1. In Subsection 2.4.2 we describe the discretization scheme which is used to treat the Matsubara frequency dependence. Subsection 2.4.3 addresses the implementation of infinite lattice structures in pf-FRG. Ultimately, in Subsection 2.4.4, we give estimates on the computational costs for solving pf-FRG flow equations for different lattice spin models.

We shall point out that none of these approximations is as severe as the truncation of the flow equation hierarchy because they can be controlled much better. The discretization of the Matsubara frequency space or the cutoff parameter resolution of the differential equation solver may always be refined to a level where the results are well converged, without the problem becoming computationally too expensive; shifting the truncation of the flow equations from the two-particle level to three particles, on the other hand, is not feasible numerically – although attempts have been made to include feedback from the three-particle vertex beyond the Katanin truncation scheme, see the discussion in Section 2.5.2.

2.4.1 Differential equation solver. The solution of the pf-FRG flow equations is the equivalent of solving a set of coupled integro-differential equations where the initial conditions are defined by the coupling constants of the spin model. The physical solution at zero cutoff is obtained by re-integrating the flow equations

$$\begin{cases} \Sigma^{\Lambda=0}(\omega) &= \Sigma^{\Lambda\to\infty}(\omega) + \int\limits_{\infty}^{0} \mathrm{d}\Lambda \left[\frac{\mathrm{d}}{\mathrm{d}\Lambda}\Sigma^{\Lambda}(\omega)\right] \\ \Gamma^{\mu\nu,\Lambda=0}_{i_1 i_2}(s,t,u) &= \Gamma^{\mu\nu,\Lambda\to\infty}_{i_1 i_2}(s,t,u) + \int\limits_{\infty}^{0} \mathrm{d}\Lambda \left[\frac{\mathrm{d}}{\mathrm{d}\Lambda}\Gamma^{\mu\nu,\Lambda}_{i_1 i_2}(s,t,u)\right] \quad . \end{cases} \tag{2.99}$$

Pictorially, the re-integration of the flow equations is equivalent to a re-summation of diagrams where the individual terms in the flow equations provide the prescription of how to 'glue together' two diagrams (or chains of diagrams) – by taking this perspective it becomes clear that the pf-FRG is not just a resummation scheme for separate diagram classes (e.g. a ladder diagram resummation) but that it combines interactions across different diagram classes.

In Sections 2.5.4 and 2.5.5 we discuss implementation of Heisenberg spin models in the

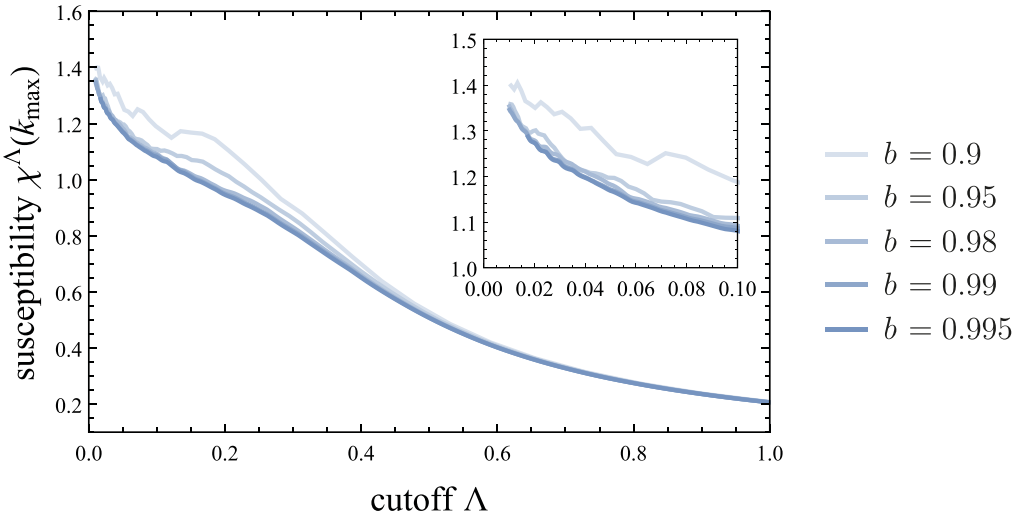

Figure 2.5. **Discretization of the cutoff parameter.** The numerical re-integration of the flow equations can only be performed with finite accuracy. This plot compares the solutions at different at different step widths b of the differential equation solver. In all cases, the integration has been started at $\Lambda_{\max} = 500$. Sufficient convergence is reached at $b = 0.98$. The data has been obtained for the Heisenberg antiferromagnet on the hyperkagome lattice.

classical limit as well as implementations of their generalization to SU(N) spins. We shall see that in these limits the flow equations assume a particularly simple form which allows to solve the flow equations analytically exact; it is the reduction of the flow equations to only a single non-vanishing diagram which that constitutes the simplicity of the solution. In the more complicated setting of spin-1/2 SU(2) moments an exact solution of the flow equations is no longer possible, yet they can still be solved numerically.

For obtain a numerical solution of the flow equations by applying the Euler scheme, i.e. by iteratively calculating the linear extrapolation of the differential equation starting from its initial values, according to the iteration scheme

$$\left\{ \begin{array}{rcl} \Sigma^{\Lambda_{n+1}}(\omega) & = & \Sigma^{\Lambda_n}(\omega) + (\Lambda_{n+1} - \Lambda_n) \left[\frac{\mathrm{d}}{\mathrm{d}\Lambda} \Sigma^{\Lambda}_n(\omega) \right] \\ \Gamma^{\mu\nu,\Lambda_{n+1}}_{i_1 i_2}(s,t,u) & = & \Gamma^{\mu\nu,\Lambda_n}_{i_1 i_2}(s,t,u) + (\Lambda_{n+1} - \Lambda_n) \left[\frac{\mathrm{d}}{\mathrm{d}\Lambda} \Gamma^{\mu\nu,\Lambda_n}_{i_1 i_2}(s,t,u) \right] \end{array} \right. \quad , \tag{2.100}$$

where Λ_n defines a set of N_Λ discrete cutoff values at which the flow equations are evaluated. Since we anticipate that non-trivial phenomena occur mainly in the low cutoff regime, we solve the flow equations on an exponential cutoff mesh which extends from large cutoff values (thereby approximating the limit of infinite cutoff where the initial conditions of the flow equations are known) down to very small cutoff values (as an approximation for the zero cutoff limit where the physically meaningful result is obtained). The series of cutoff points on the mesh can be defined as

$$\Lambda_n = b^n \Lambda_{\max} \quad , \tag{2.101}$$

where the parameter $b < 1$ is a measure for the step width and therefore a measure for the precision of the numerical solution.

Typically we choose an initial cutoff value $\Lambda_{\max} \approx 500$ to approximate the limit of infinite cutoff. It turns out that the pf-FRG flow equations are sufficiently well behaved and that the simple Euler algorithm is sufficient in order to obtain a stable solution of the differential equations. As depicted in Fig. 2.5 a well converged result is obtained at $b = 0.98$, which is the typical value which we use in our simulations. Notably, even in the presence of a phase transition enhancing the resolution of the differential equation solver often does not strengthen signatures of a flow breakdown (see Sec. 2.5.1); there seem to be other limitations to the pf-FRG algorithm which conceal true divergences in the renormalization group flow.

2.4.2 Matsubara frequency discretization. The pf-FRG flow equations have formally been derived at zero temperature where Matsubara frequencies become continuous and internal frequency sums are converted into integrals. It is certainly also possible to derive and solve the flow equations at finite temperatures where Matsubara frequencies are naturally discrete and their numerical implementation is straightforward – yet this is not necessarily desirable since it has been demonstrated that finite-temperature properties can, to some extent, be extracted also from the $T = 0$ solution without the need to perform individual simulations for each temperature point [36] (see Sec. 2.5.6).

When attempting to numerically solve the flow equations at $T = 0$, however, it is necessary to map the flow equations from the continuous frequency space to a discrete model thereof. Therefore we discretize the frequency axis and approximate it by a mesh of N_ω discrete points. The frequency mesh is chosen to be an approximately logarithmic distribution such that it can potentially resolve subtle features of the low-energy theory and at the same time also capture information at much higher energy scales. An illustration of the typical shape of the self-energy in frequency space is shown in Fig. 2.6. We shall note, however, that the structure of the two-particle vertex functions $\Gamma^{\mu\nu}_{i_1 i_2}(s,t,u)$ which are embedded in a three-dimensional frequency space can be much more complicated. In order to approximate the frequency dependence of the vertex functions sufficiently well we perform a linear interpolation in between the mesh points and a constant extrapolation for frequencies which lie beyond the mesh boundaries. Attempts have been made in the context of strongly correlated fermion systems to improve the frequency discretization by splitting the vertex function into different contributions with potentially different asymptotic behavior for large frequencies such that each individual channel is easier to model [69]. Yet, at least within the conventional pf-FRG scheme such a refinement is not necessary.

In the pf-FRG scheme as present here it is sufficient to approximate Matsubara frequencies in the range $-250 \leq \omega \leq 250$ with a mesh of between $N\omega = 66$ and $N\omega = 144$ discrete points given that the internal energy scale of the system, set by the interaction constants, is on the order of one. A coarse frequency grid typically leads to numerical artifacts in the flow of observables which take the form of unphysical oscillations as illustrated in Fig. 2.7 – at an increased frequency resolution the artifacts vanish.

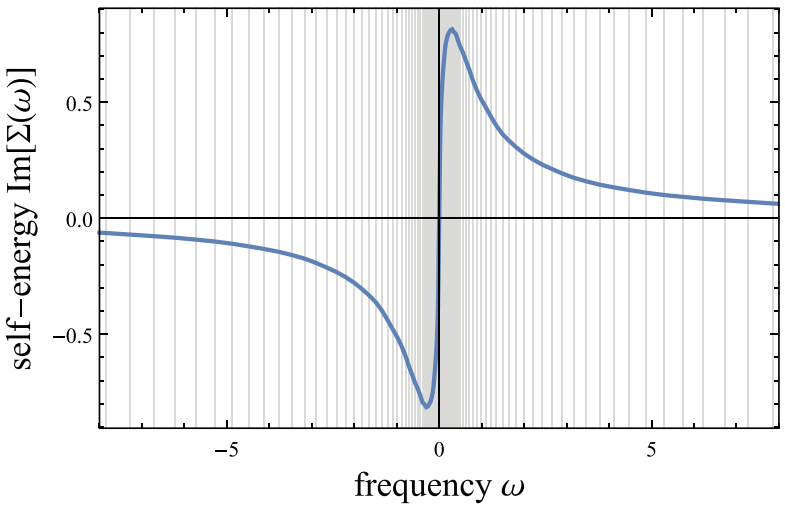

Figure 2.6. **Frequency structure** of the self-energy. The figure shows the self-energy of the kagome antiferromagnet, obtained from pf-FRG calculations on a frequency mesh with $N_\omega = 144$ discrete points and plotted at zero cutoff. The grey lines indicate the set of discrete mesh points which have been used to model the Matsubara frequency space. The increased density of points at low frequencies helps to properly resolve relevant features of the self-energy, while at higher frequencies the information content is lower and can be resolved by fewer mesh points.

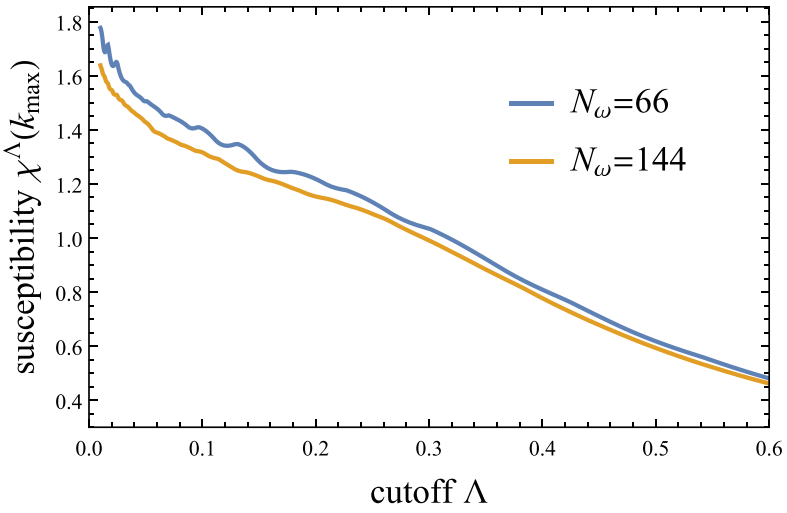

Figure 2.7. **Discretization of frequencies.** Numerical artifacts arise from the finite resolution of the frequency mesh which is being used to model the continuous Matsubara frequencies at $T = 0$. At a lower mesh resolution ($N_\omega = 66$ discrete points) the flow of the susceptibility is affected by additional unphysical oscillations which vanish at a better resolution ($N_\omega = 144$). The flow of the observable does not change qualitatively between the two examples and the numerical error is small, but due to the oscillations it becomes more difficult at lower frequency resolutions to locate a potential flow breakdown (c.f. Sec. 2.5.1). The data has been obtained for the Heisenberg antiferromagnet on the kagome lattice.

Internal frequency integrations are approximated by a trapezoidal integration scheme. The integrand is evaluated on the same frequency grid which is being used to model the frequency dependence of vertex functions – with the exception that the grid is augmented by a few additional points which improve the resolution of discontinuities in the integrand function. Such discontinuities appear as a consequence of the sharp cutoff function $\theta(|\omega| - \Lambda)$ which had been introduced in the Gaussian propagator in order to generate the renormalization group flow (see Sec. 2.3.1), and their position in frequency space depends on the cutoff parameter Λ. The sharp cutoff function effectively defines integration boundaries for internal frequency integrals and we resolve them by adding extra points to the frequency mesh at their respective positions. Treating the integration boundaries less carefully (e.g. by numerically evaluating the step function on a grid that is not compatible with the location of the discontinuity) significantly increases the numerical artifacts.

2.4.3 Lattice size. The efficient implementation of lattice graphs is a central issue in any simulation of condensed matter systems. Unless one is expressly interested in the study of surface phenomena lattice graphs should ideally extend infinitely in space, which is at odds with the limited resources of computing machines. In this subsection we discuss the implementation of lattices models in pf-FRG calculations and show that it is possible to retain infinite lattice geometries without artificial surfaces.

In the construction of the pf-FRG we have explicitly made use of lattice symmetries, which we have discussed in the context of the symmetry classification of the pseudo-fermion Hamiltonian in Section 2.2.3. With the help of lattice symmetries we had argued that the single-particle vertex function becomes lattice site independent and only the basis functions of the two-particle vertex $\Gamma^{\mu\nu}_{i_1 i_2}(s,t,u)$ depend on a pair of lattice sites i_1 and i_2 (for simplicity, we suppress the frequency and spin dependence of the vertex functions throughout the remainder of this section). Furthermore we had established that the dependence on two lattice sites can be reduced to an effective dependence on only a single lattice site by employing a lattice transformation T which maps one of the two sites, say i_1, to a fixed reference site which we refer to as i_0 (see Fig. 2.8a). Additional transformations from the point group of the lattice which leave i_0 invariant may be used to identify additional equivalence classes among the vertex functions, see Fig. 2.8b. However, even the symmetry-reduced two-particle vertex $\Gamma_{i_0 i_n}$ depends on one lattice site index i_n which runs over all (infinitely many) lattice sites.

There are two possible ways to approximate the spatial structure of the vertex functions by only a finite number of N_L components. One option which is often applied e.g. in Monte Carlo simulations is to approximate an infinite lattice by a finite sub-region that is equipped with periodic boundary conditions. Since periodic boundary conditions restore lattice symmetries even for finite lattice graphs the scheme is, in principle, also applicable in the context of pf-FRG. The other option, which we argue is the natural way to approximate the spatial structure of the vertex in pf-FRG calculations, implies a truncation of the vertex $\Gamma_{i_0 i_n}$ if the distance between i_0 and i_n exceeds a certain threshold. To this end we introduce a length scale L and approximate the vertex function

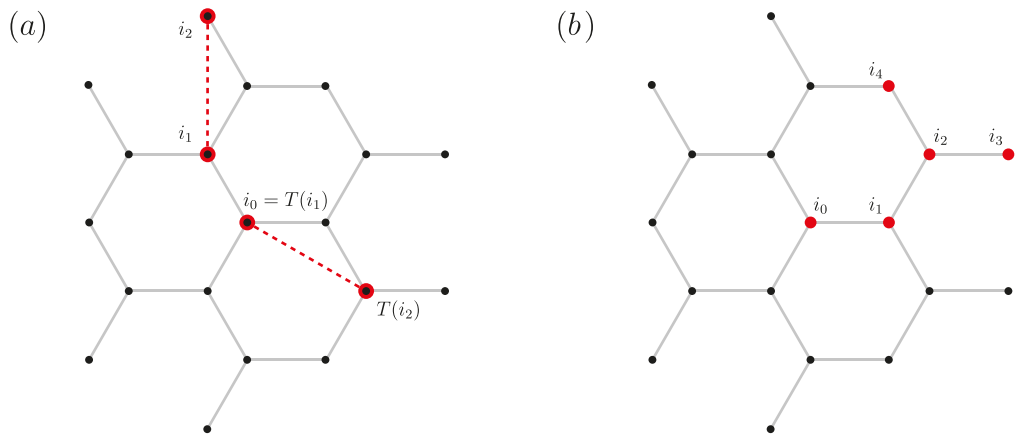

Figure 2.8. **Lattice symmetries.** The transformation behavior of the two-particle vertex under lattice symmetries is depicted here for the honeycomb lattice. (a) One lattice site index of the two-particle vertex function $\Gamma_{i_1 i_2}$, indicated by the dashed red line connecting sites i_1 and i_2, can be mapped onto the reference site i_0 by applying a lattice automorphism T which fulfills $T(i_1) = i_0$. The remaining lattice site is mapped onto $T(i_2)$ under this transformation, thereby establishing the symmetry equivalence $\Gamma_{i_1 i_2} = \Gamma_{i_0 T(i_2)}$. (b) Additional lattice symmetries can be exploited to map any two-particle vertex function $\Gamma_{i_n i_m}$ onto either one of the five vertex functions $\Gamma_{i_0 i_0}, \ldots, \Gamma_{i_0 i_4}$, such that these vertex functions form a symmetry reduced complete basis for the real-space structure of the general vertex function.

by

$$\Gamma^{\mu\nu}_{i_0 i_n}(s,t,u) = \begin{cases} \Gamma^{\mu\nu}_{i_0 i_n}(s,t,u) & \text{if } ||i_0 - i_n||_b \leq L \\ 0 & \text{otherwise} \end{cases} , \tag{2.102}$$

where the norm $||.||_b$ (bond distance) measures the distance between two lattice sites as the minimal number of lattice bonds which are required to connect the sites. Consequently there is only a finite number N_L of non-zero components of the vertex function $\Gamma_{i_0 i_n}$ which need to be computed. Constraining the number of non-zero vertex functions whose flow equations need to be solved automatically also places a constraint on the number of terms which contribute to each flow equation. This is particularly relevant for classes of diagrams in the flow equations which contain an internal summation over the entire lattice. RPA diagrams (c.f. Fig. 2.3), for example, have a spatial structure $\sim \sum_j \Gamma_{i_0 j}\Gamma_{j i_n}$. Once the vertex functions have been truncated in their spatial extent the RPA diagrams only contribute a finite number of terms where the virtual lattice site j simultaneously is within the truncation range around site i_0 and site i_n, respectively, as illustrated in Fig. 2.9. Numerically this is desirable, because the number of non-zero contributions remains small as compared to the implementation of a finite lattice with periodic boundary conditions.

Physically, the spatial truncation scheme is motivated by the typical real-space structure of vertex functions which decay with increasing distance between the lattice sites, as schematically depicted in Fig. 2.10. Furthermore the vertex range truncation has the advantage that it does not introduce an artificial boundary to the system – which is

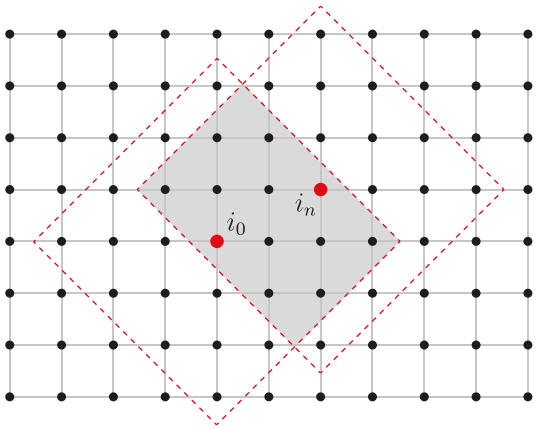

Figure 2.9. **Finite vertex range.** The vertex $\Gamma_{i_0 j}$ is non-zero only for lattice sites i_1 and j which are a maximum of L lattice bonds apart. This is illustrated for $L = 3$ on the square lattice where the vertex is only finite if j lies within the dashed square around i_0. A product of the form $\sum_j \Gamma_{i_0 j}\Gamma_{j i_n}$, as it appears in the RPA term of the pf-FRG flow equation for the vertex $\Gamma_{i_0 i_n}$, is only non-zero if j lies within the gray shaded region.

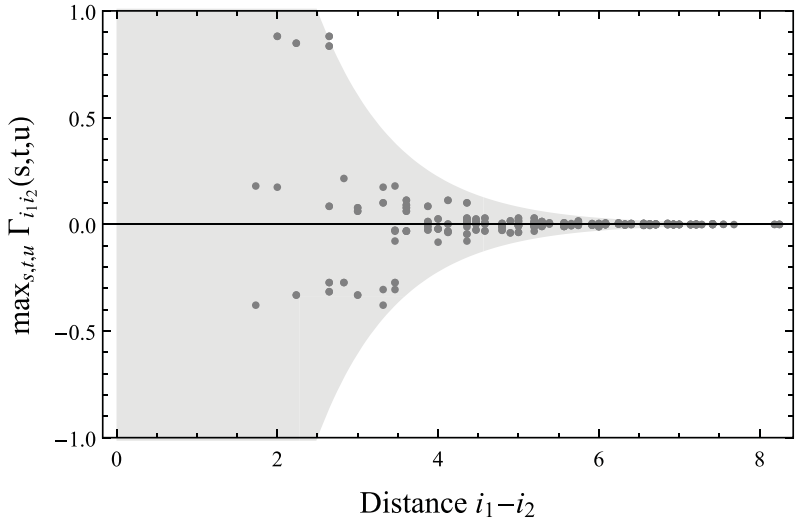

Figure 2.10. **Spatial decay of the two-particle vertex.** The vertex function $\Gamma_{i_1 i_2}$ quickly decays as a function of the distance between the two lattice sites i_1 and i_2 measured in unites of the nearest neighbor distance in the lattice. For each lattice site the plot shows the maximum component of the vertex function within its three-dimensional frequency dependence. This example is based on simulations of the Heisenberg antiferromagnet on the hyperkagome lattice at $L = 10$.

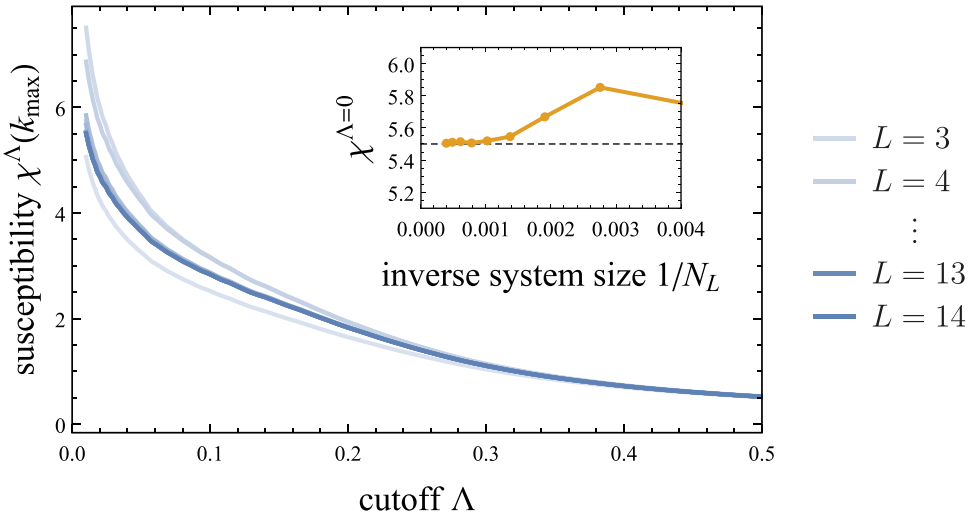

Figure 2.11. **Finite size convergence.** The plot illustrates the convergence behavior of the magnetic susceptibility as a function the system size. The susceptibility is evaluated at its maximum value in momentum space and has been obtained for the diamond lattice with competing nearest neighbor and next-nearest neighbor interactions $J_2/|J_1| = 0.225$, c.f. Sec. 3.1. Sufficient convergence is reached around $L = 10$ ($1/N_L \approx 0.001$).

particularly favorable in the simulation of systems which exhibit incommensurate magnetic long-range order (we discuss such an example in Sec. 3.1). The resulting notion of 'finite size' in pf-FRG calculations can be interpreted in analogy to a series expansion in the system size: at $L \to \infty$ one naturally recovers the correct result for infinite systems, but starting from finite values of L the corrections which are obtained from successively increasing the system size quickly diminish due to the fast decay of the vertex function; this is illustrated in Fig. 2.11.

2.4.4 Computational complexity. In the previous subsections we have seen three instances of approximations whose quality is measured by one parameter each: the number of discrete points in the frequency mesh N_ω determines the extent of oscillatory artifacts in the flow of observables; the number of lattice sites within the truncation range of a vertex N_L determines the convergence in the system size; finally, the number of discrete points on the cutoff scale N_Λ determines the numerical error which accumulates in the re-integration of the flow equations. These parameters need to be tuned to values which are sufficiently large in order to produce sensible, converged results. However, increasing the parameters can also significantly boost the computational complexity of the flow equations. Here we briefly discuss the algorithmic scaling of the computational complexity for solving pf-FRG flow equations.

The computational complexity of the overall pf-FRG flow equations is determined by the complexity of the flow equations for the two-particle vertex since the complexity of the single-particle vertex is negligible; within the Katanin truncation scheme (Sec. 2.5.2) the flow equations for the two-particle vertex, unlike the single-particle vertex, contain

Model	Relative Complexity N_σ
Heisenberg model	1
Kitaev model	2
General time-reversal symmetric model	32
General time-reversal breaking model	2048

Table 2.4. **Relative computational complexity** for spin models with different symmetries. These numbers do not regard lattice symmetries. Additional complexity may therefore arise if the spin interactions break lattice symmetries, as it is the case e.g. for Dzyaloshinskii-Moriya interactions.

an internal frequency integral which makes them significantly more complicated. More specifically, to leading order the complexity is governed only by the calculation of RPA diagrams, because they – in addition to an internal frequency integral – also have an internal summation over all lattice sites.

The number of diagrams which need to be computed scales with N_L since the lattice site structure of the bi-local two-particle vertex $\Gamma^{\mu\nu}_{i_1 i_2}(s,t,u)$ can be reduced to an effective dependence on just a single lattice site, as discussed in Sec. 2.4.3. Every RPA diagram contains an internal summation over the entire lattice, such that N_L enters quadratically in the overall computational complexity. Similarly, the number of diagrams scales with N_ω^3 with an additional power entering from the internal frequency integration, such that the overall computational complexity scales with N_ω^4. The number of frequency points on the cutoff scale N_Λ enters linearly in the computational complexity – for each cutoff value the flow equations need to be evaluated once in order to perform their numerical re-integration.

Ultimately, besides depending on the resolution of numerical approximation schemes, the computational complexity also strongly depends on the symmetries of the underlying Hamiltonian. The general flow equations for time-reversal invariant systems, as we presented them in Sec. 2.3, is versatile in its application but it is also inefficient to apply to spin systems with higher symmetry. For more symmetric models, e.g. models with only diagonal spin exchange terms like Heisenberg or Kitaev couplings, the flow equations simplify significantly – we discuss this in Sec. 2.5.3. The spin symmetries provide relations between the basis functions $\Gamma^{\mu\nu}_{i_1 i_2}(s,t,u)$ for different μ, ν and hence directly affect the number of RPA diagrams which need to be computed. In contrast, if the symmetry of the Hamiltonian is even lower, i.e. if the model breaks time-reversal symmetry, the computational complexity skyrockets since many symmetries in the frequency arguments are then lost (see the discussion in Sec. 2.2). A comparison of the relative complexity N_σ for prominent spin models is shown in Table 2.4. The overall computational complexity scales as

$$\mathcal{O}\left(N_\sigma \cdot N_\Lambda \cdot N_L^2 \cdot N_\omega^4\right) \quad . \tag{2.103}$$

2.5. Methodological case studies

Up to this point we have reviewed the derivation of the general pf-FRG flow equations as well as their numerical solution. It is the goal of this chapter to complement the theoretical derivation with practical guidance for conducting and interpreting pf-FRG simulations of quantum magnetism. To this end we highlight individual aspects of the pf-FRG which elaborate on concepts that we have mentioned in the previous sections but not discussed in detail. These aspects include the detection of phase transitions within pf-FRG and the role of the Katanin truncation scheme. Furthermore, we discuss specialized formulations of the flow equations for microscopic models with highly symmetric spin exchange, with a particular focus on the flow equations for Heisenberg models of arbitrary spin length S and on the generalization of the Heisenberg model to SU(N) spins. Lastly, we address the calculation of thermodynamic properties within pf-FRG.

2.5.1 Phase transitions. Arguably one of the most fundamental points about a microscopic model for quantum magnetism is the characterization of its ground state phase diagram, rendering the detection of phase transitions a central task in quantum many-body simulations. A large class of phase transitions, especially transitions into magnetically ordered phases, can be described within the Landau theory of phase transitions [70], such that a phase transition can often be determined by uncovering spontaneous symmetry breaking. In pf-FRG calculations the detection of spontaneous symmetry breaking is straightforward. When we constructed an ansatz for the effective action (c.f. Eqs. 2.89 and 2.91) we have explicitly made use of symmetries in the underlying Hamiltonian. As a consequence the flow equations are not suited to describe a system where the symmetry has been spontaneously broken. Below a critical cutoff scale Λ_c which marks the phase transition the solution of the flow equations must therefore be unphysical. At the critical cutoff itself the physical solution of the flow equations is formally expected to break down and diverge – at least if the symmetry-breaking is captured by an order parameter which is a fermionic bilinear, see below. However, in realistic pf-FRG calculations which involve necessarily approximations the flow breakdown often manifests in a kink or cusp-like feature instead.

As discussed in Ref. [P2] we can develop an intuition for the flow breakdown by considering a general system with Gaussian action S_0 and a quartic exchange term

$$S_{\text{int}} = J \sum_{1',2',1,2} \bar{\psi}_{1'} \bar{\psi}_{2'} \psi_1 \psi_2 \quad , \tag{2.104}$$

where for simplicity we assume that the coupling $J = J(1', 2'; 1, 2)$ is independent of the fermion structure. Let us further assume that spontaneous symmetry breaking is detected by the onset of a bosonic order parameter $\phi_{1'1} = \bar{\psi}_{1'} \psi_1$. By means of a

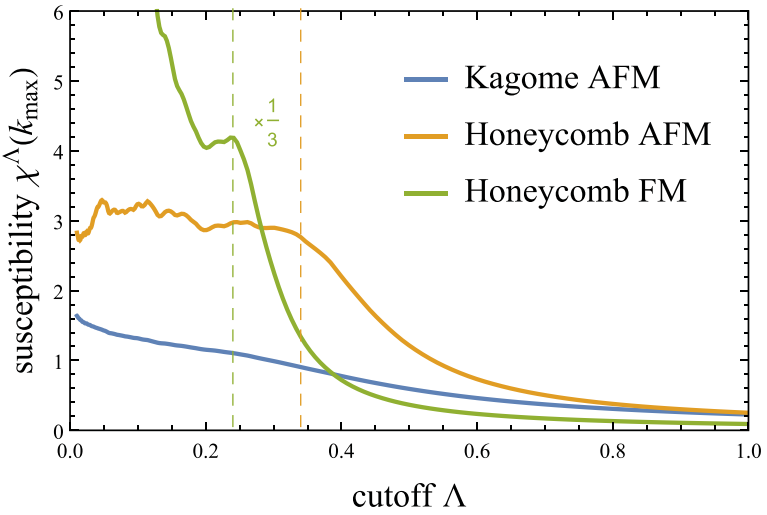

Figure 2.12. **Breakdown of the renormalization group flow.** Symmetry-breaking phase transitions manifest themselves in a breakdown of the smooth renormalization group flow. Ideally, the breakdown is a true divergence but in practice it can be more subtle. The breakdown scales Λ_c for the antiferromagnet and the ferromagnet on the honeycomb lattice are indicated by the dashed lines. The susceptibility for the honeycomb ferromagnet has been rescaled by a factor of 1/3. There is no indication of a breakdown in the flow of the kagome antiferromagnet, signaling a paramagnetic ground state which does not break symmetries.

Hubbard-Stratonovich transformation the functional integral can then be written as

$$Z = \int \mathcal{D}(\bar{\psi}, \psi, \bar{\phi}, \phi) e^{-S_0 - \sum_{1',2',1,2} \left(J^{-1} \phi^*_{1'1} \phi_{2'2} + \phi^*_{1'1} \bar{\psi}_{2'} \psi_2 + \bar{\psi}_{1'} \psi_1 \phi_{2'2} \right)} \tag{2.105}$$

in order to expose the order parameter. Once we use this model as a starting point for a renormalization group analysis effective higher order terms of the order parameter field $\phi_{1'1}$ are generated as the renormalization group flow evolves, giving rise to an order-parameter potential $U(\phi)$ in the Landau sense. A potential phase transition is then indicated by a sign change in the second order term $J^{-1}\phi^*\phi$, implying a zero-crossing of the inverse coupling J^{-1}. Since the Hubbard-Stratonovich decoupling can in principle be applied at any point throughout the renormalization group flow, the relation between the scale-dependent quartic coupling in the purely fermionic model $\sim J^\Lambda \bar{\psi}\bar{\psi}\psi\psi$ and the scale-dependent mass of the order parameter field $J^{-1,\Lambda}\phi^*\phi$ holds at any scale Λ. Consequently, a phase transition (i.e. a zero-crossing of the inverse coupling) is tied to a divergence of quartic interaction in the purely fermionic model – up to artifacts which result from the truncation of the hierarchy of flow equations.

In practice the flow breakdown can be observed in the flow of the vertex functions themselves, but often it is more convenient to find signatures of the breakdown in the magnetic susceptibility $\chi^\Lambda(k)$, where it is often sufficient to evaluate only the dominant component, i.e. the component at the momentum point $k_{\max}$ where the susceptibility

$\chi^\Lambda(k_{\max})$ is largest. A true divergence of the flow equations, however, is often only observed in classical spin systems [38] or in the large-N limit of generalized SU(N) models [P2] where the pf-FRG scheme is known to faithfully reproduce mean-field results, see also Sections 2.5.4 and 2.5.4. The actual shape of the flow breakdown depends also on the nature of the ground state; typically, a flow breakdown is most pronounced in ferromagnetic phases. In Néel ordered phases (or phases of more intricate magnetic order) where quantum fluctuations become more relevant the breakdown tends to be more subtle, as shown in Fig. 2.12. Once a magnetic ordering transition has been located there is a clear-cut route to further classify the type of order: since spin correlations already build up before the actual transition point is reached, one can directly evaluate the real-space structure of the spin-spin correlations, which can be explicitly computed as discussed in Sec. 2.3.2.

Phase transitions into paramagnetic phases can also be detected via a flow breakdown, given that the phases spontaneously break symmetries. This has been observed in the SU(N) generalized Heisenberg antiferromagnet on the square lattice where pseudo-fermions assume the role of non-local fermionic partons which break the SU(2) gauge redundancy that is inherent to the pseudo-fermion construction [P2, P3]. In such a case the magnetic susceptibility remains featureless within the Brillouin zone. More subtle paramagnetic phases which evade a description in the Landau picture, including e.g. topological order, can only be observed indirectly by the absence of a flow breakdown.

2.5.2 Katanin truncation. The truncation of the hierarchy of flow equations is a serious approximation in the derivation of the pf-FRG formalism. When we reviewed the derivation of the general flow equations in Sec. 2.3 we only briefly stated the importance of the Katanin truncation scheme [67] and its improvements over the conventional truncation of neglecting the three-particle vertex entirely. In this subsection we provide an intuitive picture of the Katanin truncation and discuss phenomenological evidence for its necessity. In the subsequent Sections 2.5.3–2.5.5 we also show that the truncation exactly reproduces the mean-field results of Heisenberg models in the large-S limit and in the large-N limit, which are typically associated with the formation of magnetic order and paramagnetic behavior, respectively.

The Katanin truncation amounts to a substitution of the single-scale propagator $S^\Lambda(\omega)$ with the cutoff-derivative of the full propagator $S^\Lambda_{\text{kat}}(\omega) = -\frac{\mathrm{d}}{\mathrm{d}\Lambda} G^\Lambda(\omega)$ in the flow equations for the two-particle vertex, yielding an effective Katanin propagator

$$S^\Lambda_{\text{kat}}(\omega) = S^\Lambda(\omega) - \left(G^\Lambda(\omega)\right)^2 \frac{\mathrm{d}}{\mathrm{d}\Lambda} \Sigma^\Lambda(\omega) \tag{2.106}$$

which contains two terms: the original single-scale propagator and a correction term that involves the flow of the self-energy. The appearance of the latter does not overly complicate the numerical calculations since the term already needs to be computed for the solution of the single-particle flow equation regardless of the choice of truncation scheme. Still, the Katanin truncation significantly increases the computational complexity in comparison the the conventional truncation. While in the conventional truncation

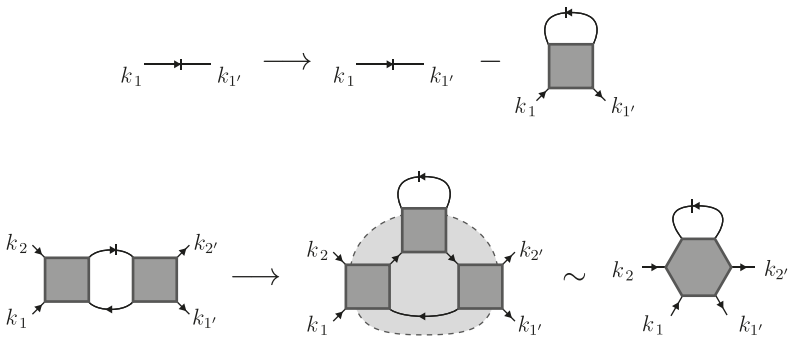

Figure 2.13. **Katanin truncation.** Diagrammatically the Katanin truncation amounts to the replacement of the single-scale propagator by a two-particle vertex where one virtual particle is contracted via a single-scale propagator (top row). Making this replacement in diagrams which appear in the flow equations for the two-particle vertex generates diagrams with topologies that are otherwise not generated in the renormalization group flow. The newly generated diagram classes can be traced back to contributions from the three-particle vertex (bottom row).

scheme the calculation of internal frequency loops is decisively simplified by the appearance of a δ-function in the single-scale propagator (c.f. Sec. 2.3) this is not the case for the newly generated correction terms in the Katanin scheme. As a consequence, the scaling of computational complexity increases from $\mathcal{O}(N_\omega^3)$ to $\mathcal{O}(N_\omega^4)$, where N_ω is the number of discrete frequencies which are being used to model the continuous Matsubara frequency axis (see also the discussion in Sec. 2.4.4).

The Katanin truncation is designed to partially recover contributions in the flow equation for the two-particle vertex which originate from the three-particle and are otherwise neglected. Diagrammatically the Katanin scheme can be understood as an insertion of the single-particle flow equation into the two-particle vertex flow (Fig. 2.13). The insertion gives rise to effective non-nested two-loop diagrams of third order in the two-particle vertex that would naturally be generated in the flow equation for the three-particle vertex [67]. The truncation scheme can furthermore be generalized to include multi-loop diagrams beyond third order in the two-particle vertex by an iterative self insertion of the two-particle vertex flow [71, 72]. Due to its iterative nature the computational complexity grows only linearly with the number of self-insertions.

It had been realized early on in the development of the pf-FRG that the Katanin truncation is a crucial ingredient in order to obtain sensible results in the simulation of frustrated quantum magnetism [6]. Particularly in highly frustrated spin models the conventional truncation does not suffice to reliably determine the ground state, since it does not properly capture paramagnetic phases. This is exemplified by a comparison of the predictions made by employing the conventional truncation scheme and the Katanin truncation scheme for the kagome antiferromagnet in Fig. 2.14. While the renormalization group flow which has been obtained by means of the conventional truncation scheme diverges – thus falsely suggesting a transition into a magnetically ordered ground state –, the extended calculations based on the Katanin truncation correctly predict a spin-liquid

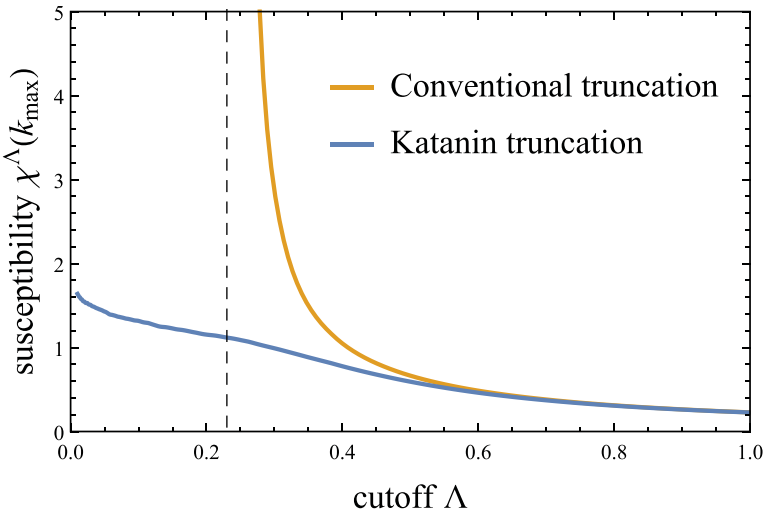

Figure 2.14. **Comparison of truncation schemes.** This figure contrasts different schemes to truncate the infinite hierarchy of flow equations. The Katanin truncation is usually implemented in pf-FRG calculations. If the three-particle vertex is completely neglected (conventional truncation) the flow diverges even in parameter regions where one expects a paramagnetic ground state, illustrated here for the kagome antiferromagnet. The dashed line indicates the critical cutoff scale Λ_c.

ground state.

Recently, efforts have been made to make use of the generalized multi-loop truncation scheme in the context of pseudo-fermionic models, where it has been reported that the inclusion of fourth order contributions in the tow-particle vertex is in principle possible, and while not changing the results qualitatively it does push potential flow breakdowns in two-dimensional spin models towards lower scales, suggesting an improved fulfillment of the Mermin Wagner theorem [73]. However, it has also been observed that the iterative self-insertion leads to a considerable growth of numerical artifacts which derive from the discretization of Matsubara frequencies.

2.5.3 Flow equations with extra symmetries. In the derivation of the pseudo-fermionic flow equations we have made only few assumptions on the symmetries of the model Hamiltonian and only required it to be time-reversal invariant. This allowed us to derive a very general formulation of the flow equations which can be applied to a broad variety of different spin models. For actual calculations, however, it can be helpful not to use the general parametrization but to consider a specific implementation of the pf-FRG which incorporates any additional symmetries of the Hamiltonian that go beyond the invariance under time reversal. As we have mentioned in the discussion of the computational complexity of the pf-FRG flow equations (Sec. 2.4.4) one can significantly simplify the calculation by exploiting additional symmetries of the spin model. In fact, most of the studies involving pf-FRG which have been published so far have employed such parametrizations of the flow equations with extra symmetries.

In this subsection we exemplify the simplification of flow equations for two well-known spin models: the Heisenberg model, which has an SU(2) spin rotational symmetry, and the Kitaev honeycomb model with bond directional interactions, which has a $\mathbb{Z}_2 \times \mathbb{Z}_2 \times \mathbb{Z}_2$ symmetry.

Heisenberg model.— We first address the Heisenberg model, which has only diagonal spin exchange terms of equal strength for all components. Its Hamiltonian reads

$$H = \sum_{ij} J_{ij} \mathbf{S}_i \mathbf{S}_j \quad , \tag{2.107}$$

where the spin operators $\mathbf{S}_i$ represent quantum mechanical spin-1/2 moments. Being invariant under continuous (global) SU(2) spin rotations the Heisenberg model has a particularly high symmetry and we anticipate the pf-FRG flow equations to become maximally simple. In comparison to the general Hamiltonian of two-spin interactions (2.78) the exchange constants are constrained to $J_{ij}^{\mu\nu} = J_{ij}\delta_{\mu\nu}$, thus reducing the structure of the initial conditions for the two-particle vertices $\Gamma_{i_1 i_2}^{\mu\nu}(s,t,u)$ in the general flow equations for time-reversal symmetric models. The structure of the flow equations is such that the symmetries are preserved throughout the entire renormalization group flow. In fact, one can define simply two vertex functions

$$\begin{aligned} \Gamma_{i_1 i_2}^{\mathrm{d}}(s,t,u) &= \Gamma_{i_1 i_2}^{00}(s,t,u) \\ \Gamma_{i_1 i_2}^{\mathrm{s}}(s,t,u) &= \Gamma_{i_1 i_2}^{11}(s,t,u) + \Gamma_{i_1 i_2}^{22}(s,t,u) + \Gamma_{i_1 i_2}^{33}(s,t,u) \end{aligned} \tag{2.108}$$

that capture all symmetry-allowed degrees of freedom and, upon substitution in the general flow equations, obtain a closed set of flow equations for the SU(2) spin model. All remaining off-diagonal components of the two-particle vertex have vanishing initial conditions, remain zero throughout the flow, and can therefore be neglected.

The nomenclature of the two-particle vertices Γ^{d} and Γ^{s} refers to the density-like and spin-like character of the vertices; in the original derivation of the pf-FRG flow equations a bottom-up approach has been employed (as opposed to the top-down approach outlined above, in which we derive the SU(2) flow equations as a special case of the general flow equations for time-reversal invariant systems) where the full two-particle vertex needs to be parametrized as

$$\begin{aligned} \Gamma(1',2';1,2) = \Big[\Big(\Gamma_{i_1 i_2}^{\mathrm{d}}(s,t,u) \delta_{\alpha_{1'}\alpha_1} \delta_{\alpha_{2'}\alpha_2} + \Gamma_{i_1 i_2}^{\mathrm{s}}(s,t,u) \sigma_{\alpha_{1'}\alpha_1}^{\mu} \sigma_{\alpha_{2'}\alpha_2}^{\mu} \Big) \delta_{i_{1'} i_1} \delta_{i_{2'} i_2} \\ - (1' \leftrightarrow 2') \Big] \delta_{\omega_{1'} + \omega_{2'} - \omega_1 - \omega_2} \quad , \end{aligned} \tag{2.109}$$

i.e. it has two components whose spin dependence is governed by delta functions (density-like terms) and Pauli matrices (spin-like terms), respectively [6].

Kitaev model.— Next, we review the flow equations for the Kitaev model, or generally any model with diagonal spin exchange terms. In the Kitaev honeycomb model spin

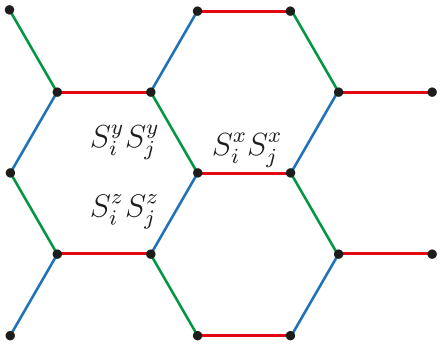

Figure 2.15. **Kitaev honeycomb model**. All bonds in the honeycomb lattice are sub-divided into three types: x, y, and z, represented in red, green, and blue, respectively. Along each bond type only the spin components of the corresponding label interact.

interactions are not isotropic on the lattice. The honeycomb lattice is subdivided into three types of lattice bonds, labeled x, y, and z-bonds, and along every lattice bond the spins interact via their component which matches the bond type, see the illustration in Fig. 2.15. The model is captured by the Hamiltonian

$$H = \sum_{\langle i,j\rangle_\gamma} J_{ij}^\gamma S_i^\gamma S_j^\gamma \quad , \tag{2.110}$$

where $\langle i,j\rangle$ denotes a sum over nearest neighbor sites i and j, and $\gamma = x, y, z$ labels the bond type. Clearly the Kitaev model breaks the SU(2) spin rotation symmetry. Yet it separately preserves mirror symmetries in all three spin axes, $S^x \to -S^x$, $S^y \to -S^y$, and $S^z \to -S^z$.

Similar to what we have discussed for the Heisenberg model only some of the basis functions of the two-particle vertex can be non-zero throughout the renormalization group flow. Since only the spin-diagonal components

$$\begin{aligned}
\Gamma^{\mathrm{d}}_{i_1 i_2}(s,t,u) &= \Gamma^{00}_{i_1 i_2}(s,t,u) \\
\Gamma^{\mathrm{x}}_{i_1 i_2}(s,t,u) &= \Gamma^{11}_{i_1 i_2}(s,t,u) \\
\Gamma^{\mathrm{y}}_{i_1 i_2}(s,t,u) &= \Gamma^{22}_{i_1 i_2}(s,t,u) \\
\Gamma^{\mathrm{z}}_{i_1 i_2}(s,t,u) &= \Gamma^{33}_{i_1 i_2}(s,t,u)
\end{aligned} \tag{2.111}$$

can have finite initial conditions and the structure of the flow equations is such that no additional finite terms can be generated it is sufficient to consider only those four vertex functions and neglect all remaining ones.

However, unlike in the Heisenberg model the different vertex functions can now have a more complicated spatial structure as a consequence of the bond directional interactions; The spatial structure of the initial couplings explicitly breaks lattice rotation symmetries, yet the underlying lattice itself remains unchanged and it is possible to recover lattice symmetries by combining them with transformations in spin space. For

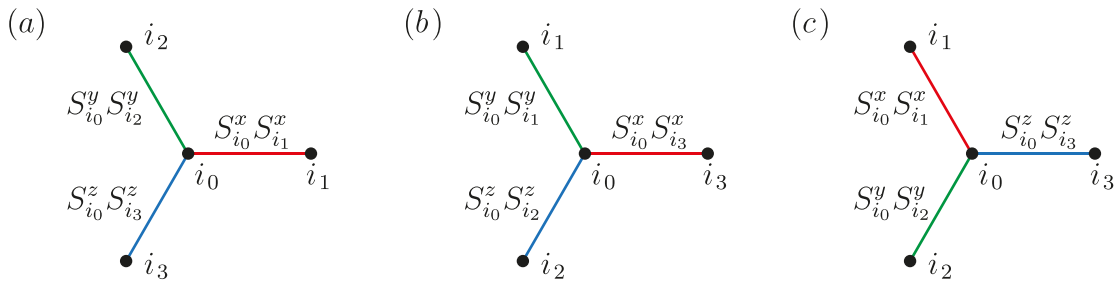

Figure 2.16. **Composite symmetries in lattice and spin space**. (a) The initial Kitaev honeycomb Hamiltonian couples a spin at lattice site i_0 to its nearest neighbors at i_1, i_2, and i_3 via interactions in the x, y, and z component, respectively. (b) A rotation by $2\pi/3$ permutes the lattice site indices but does not alter the spin components, such that the Hamiltonian is not preserved. (c) This is remedied by a composite symmetry transformation which also permutes the spin components $\{S^x, S^y, S^z\} \to \{S^z, S^x, S^y\}$. The original Hamiltonian is then recovered.

the Kitaev honeycomb model, the composite transformations of spin and lattice degrees of freedom are relatively simple; they amount to permutations of the x, y, and z spin components in combination with lattice rotations or mirror planes. This is best illustrated on the example of an anti-clockwise lattice rotation by $2\pi/3$ around a fixed lattice site i_0. Obviously the lattice rotation alone does not leave the Hamiltonian (2.110) invariant (Figs. 2.16a–b) but augmenting the transformation with permutations of the spin components can restore the symmetry (Fig. 2.16c).

2.5.4 Quantum limit at large N. In the previous subsection we have discussed the pf-FRG flow equations for spin models with only diagonal interaction terms; in particular, we addressed also the Heisenberg model. Here we extend our analysis to the generalized Heisenberg model of SU(N) spins. When the symmetry group becomes particularly large – i.e. in the large-N limit – spin models can become amenable to a mean-field solution; additional corrections at finite values of N can afterwards be included perturbatively. Furthermore, the fermionic representation of SU(N) moments (see below) in the large-N limit does not display magnetically ordered phases and favors paramagnetic ground states instead [14]. As such, the large-N generalization provides a good benchmark for the pf-FRG implementation to assess its capability to capture quantum spin liquid phases. In the following, based on our results as published in Ref. [P2], we outline the extension of the pf-FRG scheme to SU(N) symmetric models and demonstrate that in the large-N limit the pf-FRG solution coincides with the mean-field result.

The general SU(N) spin Hamiltonian reads as

$$H = \sum_{ij} J_{ij} \mathbf{S}_i \mathbf{S}_j \quad , \tag{2.112}$$

where the spin operators $\mathbf{S}_i$ and $\mathbf{S}_j$ now represent spin-1/2 SU(N) symmetric moments. There are different ways to represent SU(N) generalizations on the (bosonic or fermionic)

Hilbert space of auxiliary particles [74]. In the context of pf-FRG calculations it is most convenient to represent the SU(N) moments in analogy to the pseudo-fermion construction (2.33) via

$$S_i^\mu = f_{i\alpha}^\dagger T_{\alpha\beta}^\mu f_{i\beta} \quad , \tag{2.113}$$

where the T^μ represent the N^2-1 generators of the SU(N) group and the spin index α takes values $1,\ldots,N$. By convention the SU(N) generators are normalized such that $\mathrm{Tr}(T^\mu T^\nu) = \frac{1}{2}\delta_{\mu\nu}$. The pseudo-fermion construction is a faithful representation of the SU(N) spin algebra upon imposing the local half-filling constraint

$$\sum_\alpha f_{i\alpha}^\dagger f_{i\alpha} = \frac{N}{2} \quad . \tag{2.114}$$

Just like in the general formulation of the pf-FRG one can argue that due to a particle-hole symmetry of the model the half-filling constraint is automatically fulfilled on average by setting the chemical potential to zero. Since violations of the half-filling constraint effectively amount to defects in the spin model local fluctuations around the average are assumed to be suppressed by an energy barrier [6]. Furthermore, if the local half-filling constraint is explicitly implemented in the large-N mean-field solution the associated Lagrange multipliers vanish [P3] – suggesting that the local constraint is indeed redundant at zero chemical potential.

The pf-FRG formalism for the SU(2) symmetric Heisenberg model, which is based on a parametrization of the two-particle vertex in terms of spin and density-like contributions (c.f. Sec. 2.5.3), can be extended to the SU(N) case in a straightforward manner by replacing Pauli matrices with generalized SU(N) generators [P2], yielding the two-particle vertex parametrization

$$\begin{aligned}\Gamma(1',2';1,2) = \Big[&\Big(\Gamma^{\mathrm{d}}_{i_1 i_2}(s,t,u)\delta_{\alpha_{1'}\alpha_1}\delta_{\alpha_{2'}\alpha_2} + \Gamma^{\mathrm{s}}_{i_1 i_2}(s,t,u) T^\mu_{\alpha_{1'}\alpha_1} T^\mu_{\alpha_{2'}\alpha_2}\Big)\delta_{i_{1'} i_1}\delta_{i_{2'} i_2} \\ &- (1' \leftrightarrow 2')\Big]\delta_{\omega_{1'}+\omega_{2'}-\omega_1-\omega_2} \quad .\end{aligned} \tag{2.115}$$

Inserting the ansatz into the general fermionic flow equations and calculating all internal summations over the spin indices yields the flow equations for the basis functions $\Gamma^{\mathrm{d}}_{i_1 i_2}(s,t,u)$ and $\Gamma^{\mathrm{s}}_{i_1 i_2}(s,t,u)$. The full flow equations for the self-energy and the basis functions are presented in Appendix A.1. Since the parametrization of the two-particle vertex has the same structure as the ansatz for SU(2) spin models, the resulting flow equations are the same up to modified prefactors, thereby providing a straightforward systematic relation between the conventional SU(2) formulation of the pf-FRG and its large-N limit.

In order to see that the pf-FRG solution in the large-N limit coincides with the mean-field result, however, it is instructive to make a more general ansatz which does not impose any symmetry constraints on the vertex parametrization – since the fermionic SU(N) representation favors dimerized ground state configurations [15] its description naturally requires non-local vertex functions. We shall therefore consider a general form

of the self-energy $\Sigma^\Lambda(1';1)$ and parametrize the two-particle vertex as

$$\Gamma^\Lambda(1',2';1,2) = \Gamma^\Lambda(1',2';1,2)\left(\delta_{\alpha_{1'}\alpha_1}\delta_{\alpha_{2'}\alpha_2} - \delta_{\alpha_{1'}\alpha_2}\delta_{\alpha_{2'}\alpha_1}\right) \quad , \tag{2.116}$$

where on the left hand side of the equation the composite indices n represent a lattice site index i_n, a Matsubara frequency ω_n, and the spin index α_n, whereas on the right hand side they only denote a Matsubara frequency and a lattice site while the spin dependence is stated explicitly. Note that this parametrization of the spin structure forms a complete basis of SU(N) – since it relates to the usual expansion in terms of the SU(N) generators (see above) via

$$T^\mu_{\alpha_{1'}\alpha_1} T^\mu_{\alpha_{2'}\alpha_2} = \frac{1}{2}\left(\delta_{\alpha_{1'}\alpha_2}\delta_{\alpha_{2'}\alpha_1} - \frac{1}{N}\delta_{\alpha_{1'}\alpha_1}\delta_{\alpha_{2'}\alpha_2}\right) \quad , \tag{2.117}$$

i.e. to leading order in the large-N expansion the spin-like interaction is equivalent (up to a factor of 2) to the exchange of spin indices.

Inserting the parametrization into the general fermionic flow equations obtains the flow of the self-energy, which to leading order in N read as

$$\frac{\mathrm{d}}{\mathrm{d}\Lambda}\Sigma^\Lambda(1';1) = \frac{1}{2\pi}\sum_{2',2}\Gamma^\Lambda(1',2';1,2)S^\Lambda(2;2') \quad , \tag{2.118}$$

and the two-particle vertex flow

$$\frac{\mathrm{d}}{\mathrm{d}\Lambda}\Gamma^\Lambda(1',2';1,2) = -\frac{1}{2\pi}\sum_{3',4',3,4}\Gamma^\Lambda(1',4';1,3)\Gamma^\Lambda(3',2';4,2) \times \left[S^\Lambda_{\mathrm{kat}}(3;3')G^\Lambda(4;4') + G^\Lambda(3;3')S^\Lambda_{\mathrm{kat}}(4;4')\right] \quad . \tag{2.119}$$

In the latter we have implied the Katanin truncation as detailed in Sec. 2.5.2. Since by construction $S^\Lambda_{\mathrm{kat}} = -\frac{\mathrm{d}}{\mathrm{d}\Lambda}G^\Lambda$ the flow equation for the two-particle vertex can be conveniently rewritten as

$$\frac{\mathrm{d}}{\mathrm{d}\Lambda}\Gamma^\Lambda(1',2';1,2) = \frac{1}{2\pi}\sum_{3',4',3,4}\Gamma^\Lambda(1',4';1,3)\Gamma^\Lambda(3',2';4,2) \times \frac{\mathrm{d}}{\mathrm{d}\Lambda}\left[G^\Lambda(3;3')G^\Lambda(4;4')\right] \quad . \tag{2.120}$$

We emphasize that this rewriting is only possible when the Katanin truncation scheme is used instead of the conventional truncation. The simplified structure of the flow equations in the large-N limit (the flow of the two-particle vertex depends only on a

single diagram class) allows to formulate an implicit solution [44]

$$\Gamma^{\Lambda}(1',2';1,2) = \Gamma^{\Lambda\to\infty}(1',2';1,2) + \frac{1}{2\pi}\sum_{3',4',3,4}\Gamma^{\Lambda\to\infty}(1',4';1,3)\Gamma^{\Lambda}(3',2';4,2) \times G^{\Lambda}(3;3')G^{\Lambda}(4;4') \tag{2.121}$$

which effectively describes a resummation of spin loops, thus ensuring relevance to leading order in N. The solution can be inserted into the flow equation for the self-energy (2.118) to obtain

$$\frac{\mathrm{d}}{\mathrm{d}\Lambda}\Sigma^{\Lambda}(1';1) = \frac{1}{2\pi}\sum_{2',2}\Gamma^{\Lambda\to\infty}(1',2';1,2)\frac{\mathrm{d}}{\mathrm{d}\Lambda}G^{\Lambda}(2;2') \quad , \tag{2.122}$$

which due to the vanishing initial value of the propagator is straightforward to re-integrate. Finally, by exercising the re-integration, we obtain the self-energy

$$\Sigma^{\Lambda}(1';1) = \frac{1}{2\pi}\sum_{2',2}\Gamma^{\Lambda\to\infty}(1',2';1,2)G^{\Lambda}(2;2') \quad , \tag{2.123}$$

which by identifying the initial value of the two-particle vertex with the bare coupling constant of the spin model (2.112) matches the self-consistent gap equation that is obtained in the analogous mean-field calculation [P2, P3].

We note that in principle the above calculations would also have been possible to conduct using the usual bi-local parametrization of the two-particle vertex. In that parametrization, however, it is impossible to generate non-local fermions which are predicted by the general mean-field solution. Consequently, once the local SU(2) symmetry that protects the locality of pseudo-fermions is broken spontaneously, the vertex function is expected to diverge – see Sec. 2.5.1 for the discussion of spontaneous symmetry breaking and Sec. 2.5.6 for an explicit solution of the diverging flow equations in the large-N limit.

In this case study we have demonstrated that in the large-N limit the pf-FRG approach becomes exact in a mean-field sense, given that the Katanin truncation is being implemented. Since the fermionic SU(N) generalization of spin models is considered a suitable starting point to explore quantum spin liquid phases [14] these results provide justification that the pf-FRG formalism can faithfully capture quantum spin liquids phases. Certainly these results do not imply that the pf-FRG approach is exact also at finite values of N. Intuitively, one may expect that at smaller values of N other interaction channels become important which enhance magnetic ordering tendencies – yet we shall see in the next subsection that such contributions are also resolved within the pf-FRG approach.

2.5.5 Classical limit at large S. Quantum fluctuations are most relevant in models with small spin length S=1/2, making such systems prime candidates in the search for quantum spin liquids. Yet the search is by no means limited to spin-1/2 models,

and systems with larger spin length S can be of interest for a multitude of reasons. The reasons can be very practical: we discuss a model in Sec. 3.1 for which candidate materials for the realization so far only exist with spin S=1 and larger. But the reasons can also be more academic: by varying the spin length, one can systematically tune the relevance of quantum fluctuations between the strong quantum limit ($S = 1/2$) and the classical limit ($S \to \infty$). Spin wave calculations frequently make use of this relation in an attempt to include quantum fluctuations perturbatively around the classical solution [75, 76].

In this section we review an implementation of the pf-FRG for spin models with unrestricted spin length S, which has first been presented in Ref. [38]. We shall see that in the classical limit the pf-FRG approach becomes exact in a mean-field sense and that it can thus be considered suitable to capture magnetically ordered phases.

Let us consider the general Heisenberg Hamiltonian

$$H = \sum_{ij} J_{ij} \mathbf{S}_i \mathbf{S}_j \quad , \tag{2.124}$$

where the operators $\mathbf{S}_i$ and $\mathbf{S}_j$ represent SU(2) moments of spin length S. In practical calculations the spin length S is determined by the dimensionality of the SU(2) representation; a conventional spin-1/2 moment is associated with a two-dimensional configuration space comprising the spin configurations 'up' and 'down'. On this two-dimensional space the spin operators are represented by the 2×2 Pauli matrices. Larger spins require higher dimensional representations. Analogously, on the space of pseudo-fermions spin-1/2 moments are represented by two different flavors of fermions which are subject to a local single-occupancy (half-filling) constraint, see the discussion in Sec. 2.2. A straightforward generalization of the representation exists also for spin-S moments, where $2S+1$ different fermion flavors are introduced (in analogy to the $2S+1$ quantized eigenvalues of the S^z operator) [77]. Just like the spin-1/2 representation the generalized spin-S representation also requires a local single-occupancy constraint. However, for spins $S > 1/2$ single occupancy is not equivalent to half filling and can thus not be implemented simply by imposing a vanishing chemical potential [38].

It is more convenient in the context of pf-FRG calculations to introduce an even larger Hilbert space of $4S$ fermion flavors which is – besides additional constraints – subject to half-filling. This construction goes back to introducing $2S$ replicas of spin-1/2 moments, such that every spin operator is expressed as the sum

$$\mathbf{S}_i = \sum_{\kappa=1}^{2S} \mathbf{S}_{i,\kappa} \quad , \tag{2.125}$$

where κ is an extra flavor index which denotes the different replicas [78]. It is clear from the addition rules of angular momenta that this construction must include the physical spin-S subspace, but it also includes unphysical subspaces with a smaller effective spin. For example, combining two replicas of spin-1/2 moments yields the direct sum of the physical spin-1 space and the unphysical spin-0 space. On the space of pseudo-fermions

the spin operator can thus be constructed as

$$S_i^\mu = \frac{1}{2}\sum_{\kappa=1}^{2S} f_{i\alpha\kappa}^\dagger \sigma_{\alpha\beta}^\mu f_{i\beta\kappa} \quad , \tag{2.126}$$

where the fermion occupation number is constrained to half-filling and the overall effective spin length must be maximized. Both constraints can be implemented exactly by implementing an imaginary chemical potential [79] (c.f. also the discussion in Sec. 2.5.6). Alternatively the half-filling constraint can be realized by a vanishing chemical potential (see Sec. 2.2) and the maximization of the effective spin length can be enforced energetically by adding a level repulsion term to the Hamiltonian (2.124)

$$H = \sum_{ij} J_{ij} \left(\sum_{\kappa=1}^{2S} \mathbf{S}_{i,\kappa}\right)\left(\sum_{\kappa=1}^{2S} \mathbf{S}_{j,\kappa}\right) - A\sum_i \left(\sum_{\kappa=1}^{2S} \mathbf{S}_{i,\kappa}\right)^2 \quad , \tag{2.127}$$

where A is chosen positive. It has been demonstrated, however, that the spin system tends to naturally remain in the physical part of the Hilbert space where the angular momentum eigenvalues are maximized – even in the absence of a level repulsion term [38]. By means of this construction the two-particle vertex can be parametrized as

$$\begin{aligned}\Gamma(1',2';1,2) = \Big[\Big(&\Gamma^{\mathrm{d}}_{i_1 i_2,\kappa_1\kappa_2}(s,t,u)\delta_{\alpha_{1'}\alpha_1}\delta_{\alpha_{2'}\alpha_2} + \Gamma^{\mathrm{s}}_{i_1 i_2,\kappa_1\kappa_2}(s,t,u)\sigma^\mu_{\alpha_{1'}\alpha_1}\sigma^\mu_{\alpha_{2'}\alpha_2}\Big) \\ &\times \delta_{i_{1'}i_1}\delta_{i_{2'}i_2}\delta_{\kappa_{1'}\kappa_1}\delta_{\kappa_{2'}\kappa_2} - (1'\leftrightarrow 2')\Big]\delta_{\omega_{1'}+\omega_{2'}-\omega_1-\omega_2} \quad .\end{aligned} \tag{2.128}$$

We note that the flavor index κ is intimately tied to the lattice site index, since both of them draw from a locality property (local in real space and local in the flavor index) that is protected by a local $SU(2)\otimes U(1)$ gauge redundancy, c.f. also Sec. 2.2.1. Yet the initial condition of the flow equations only has a spatial structure – which is defined by the spatial structure of the coupling constants J_{ij} – while it is constant in the flavor index. The combination of featureless initial conditions in the flavor index and the (bi-)locality constraint leads to a preservation of the flavor-index independence throughout the entire renormalization group flow, and one can identify the vertex functions $\Gamma^{\mathrm{d}}_{i_1 i_2,\kappa_1\kappa_2}(s,t,u)$ and $\Gamma^{\mathrm{s}}_{i_1 i_2,\kappa_1\kappa_2}(s,t,u)$ with their flavor-independent analogs in the spin-1/2 theory [38]. Despite the vertex functions remaining independent of the flavor index, however, every internal summation over all replicas κ contributes an additional factor of $2S$; due to their similar structure an internal summation over the flavor index occurs in all diagrams that also contain a summation over all lattice sites.

The extension of pf-FRG flow equations to systems with unrestricted spin length S thus amounts to a mere modification of prefactors in the diagrammatic calculation of the original pf-FRG flow equations for spin-1/2 systems. The resulting flow equations are given in Appendix A.2. In the classical limit (which corresponds to the large-S limit) only those diagram classes contribute to leading order in S which contain an internal lattice site summation. This coincides with our naive expectation that magnetic order

– which is the expected ground state in classical models – is driven by diagrams which contain long-range interactions, i.e. diagrams that imply summations over the entire lattice.

In fact, the pf-FRG flow equations in the large-S limit become simple enough to be amenable to an analytic solution, which is an RPA-like resummation of the leading order loop diagrams and which is equivalent to the classical Luttinger-Tisza solution [38, 80]. The possibility to construct a spin-S extension of the pf-FRG flow equations without altering the diagrammatic structure of the flow equations provides a deep connection between the classical limit and the original formulation at spin-1/2. In particular it implies that the pf-FRG formalism includes all interaction channels which are necessary to exactly describe magnetically ordered systems in the sense of a Luttinger-Tisza solution. Although this does not imply that the solution remains exact at finite spin length we have demonstrated in the previous section, based on a fermionic SU(N) generalization, that the pf-FRG formalism also includes all interaction channels which are necessary to model spin-liquid phases as seen in the large-N limit. It therefore seems likely that the pf-FRG approach is suited to model the competition of the two limiting cases – magnetic order and spin liquids – in systems of SU(2)-symmetric spin-1/2 moments.

2.5.6 Finite temperature. Regardless of the nature of the low-temperature phase – whether it is magnetically ordered or a quantum spin liquid – the question of the ground state's thermal stability is highly relevant particularly when relating the theory to experimental observations. In field-theoretical calculations the notion of temperature is usually associated with the spacing of discrete Matsubara frequencies, an intimate relation which holds by construction of the functional integral [47]. As such it is possible to perform pf-FRG calculations at finite temperatures by choosing an appropriate mesh of underlying Matsubara frequencies [60]. However, at finite temperature extra care has to be taken in order to ensure the that the half-filling constraint in the pseudo-fermion construction is fulfilled (see Sec. 2.2). Previously we argued that the unphysical states, which correspond to doubly occupied or vacant sites which effectively have zero spin and thus can be interpreted as lattice defects, are energetically unfavorable and their appearance is suppressed at zero temperature [6]. At finite temperatures, however, their thermal weight is expected to increase; it is necessary in this case to implement the half-filling constraint exactly [54]. One way to accomplish this is by simply introducing an imaginary chemical potential

$$\mu = -\frac{i\pi T}{2} \quad . \tag{2.129}$$

This can be understood as follows: the pseudo-fermionic Hilbert space is a direct sum of the half-filled (single occupancy) physical subspace and the unphysical sectors of double occupations and vacancies. The pseudo-fermion Hamiltonian only generates dynamics within the physical subspace and becomes zero when applied to the unphysical sectors (hence the earlier remark that those states can be interpreted as effective $S = 0$ states). Yet the unphysical subspace still contributes to the total partition function. It is, how-

ever, possible to extend the pseudo-fermion Hamiltonian by terms which are non-zero only on the unphysical part of the Hilbert space and which are constructed such that the sum of all unphysical contributions in the partition sum effectively cancels [53]. The requirements of this construction are fulfilled e.g. by the imaginary chemical potential as given in Eq. (2.129).

Unfortunately, the introduction of an imaginary chemical potential breaks time-reversal symmetry and the hermitian symmetry of the pseudo-fermion Hamiltonian, which significantly complicates the solution of the pf-FRG flow equations, see Sec. 2.4.4. Yet it turns out, fortunately, that pf-FRG calculations at finite temperatures can be avoided altogether; one can simply extract thermodynamic properties from the $T = 0$ solution of the flow equations by relating the frequency cutoff parameter to a temperature according to $T = \frac{\pi}{2}\Lambda$ [36]. Finite temperatures and the cutoff scale Λ both act as an effective low-energy cutoff, so already intuitively they can be expected to be at least loosely related.

In order to make the relation more rigorous and to obtain the rescaling factor we consider – following our arguments as presented in Ref. [P2] – the flow equations for the SU(N) generalized Heisenberg model in the large-N limit, which are parametrized by a spin-like vertex $\Gamma^{s,\Lambda}_{i_1 i_2}(s,t,u)$ and a density-like vertex $\Gamma^{\mathrm{d},\Lambda}_{i_1 i_2}(s,t,u)$ as discussed in Sections 2.5.3 and 2.5.4. In this limit only the particle-hole ladder diagram contributes to the flow of the spin-like vertex; the density-like vertex as well as the self-energy are decoupled and remain identically zero throughout the flow. It is implied by the vanishing self-energy that the Katanin truncation scheme in this case is equivalent to the conventional truncation, since any correction terms depend on a finite flow of the self-energy. The resulting flow equation for the spin-like vertex reads as

$$\begin{aligned}\frac{\mathrm{d}}{\mathrm{d}\Lambda}\Gamma^{s,\Lambda}_{i_1 i_2}(s,t,u) = -\frac{1}{4\pi}\int \mathrm{d}\omega \frac{\delta(|\omega|-\Lambda)}{\omega}\frac{\theta(|u+z\omega|-\Lambda)}{u+\omega} \\ \times\Big[\Gamma^{s,\Lambda}_{i_1 i_2}(\omega_{2'}-\omega,-\omega_1-\omega,u)\Gamma^{s,\Lambda}_{i_1 i_2}(\omega_2-\omega,\omega_{1'}+\omega,u) \\ -\Gamma^{s,\Lambda}_{i_1 i_2}(\omega_1+\omega,-\omega_{2'}+\omega,u)\Gamma^{s,\Lambda}_{i_1 i_2}(\omega_{1'}+\omega,\omega_2-\omega_{1'},u)\Big] \quad , \end{aligned} \tag{2.130}$$

where the bosonic transfer frequencies s, t, and u are defined as usual,

$$\begin{aligned} s &= \omega_{1'} + \omega_{2'} \\ t &= \omega_{1'} - \omega_1 \\ u &= \omega_{1'} - \omega_2 \quad , \end{aligned} \tag{2.131}$$

and we assume the model to have only nearest neighbor interactions such that the initial condition is finite only for nearest neighbor lattice sites i_1 and i_2,

$$\Gamma^{s,\Lambda\to\infty}_{i_1 i_2}(s,t,u) = \begin{cases} J & \text{for } i_1,\, i_2 \text{ nearest neighbors} \\ 0 & \text{otherwise} \end{cases} \quad . \tag{2.132}$$

Since the initial condition of the vertex function does not have a frequency dependence

and the propagators only explicitly depend on a single frequency, u, the vertex function remains constant in its s and t dependence throughout the flow. Furthermore, since there is no mixing of spatial components of the vertex function only those components which have a finite initial value can assume non-zero values. Thus it is sufficient to consider only components with finite initial value and, for simplicity, suppress all arguments except for the non-trivial dependence on the third transfer frequency u, introducing the notation $\Gamma^{\Lambda}(u) = \Gamma^{s,\Lambda}_{i_1 i_2}(s,t,u)$. The internal frequency integration can be computed analytically to obtain the minimal flow equation

$$\frac{\mathrm{d}}{\mathrm{d}\Lambda}\Gamma^{\Lambda}(u) = -\frac{1}{2\pi}\frac{\left[\Gamma^{\Lambda}(u)\right]^2}{\Lambda(\Lambda+u)} \tag{2.133}$$

with the initial condition $\Gamma^{\Lambda\to\infty}(u) = J$. The structure of the differential equation is simple enough that it allows for an analytic solution, which is given by

$$\Gamma^{\Lambda}(u) = \frac{J}{1 - \frac{J}{2\pi u}\ln\left(1+\frac{u}{\Lambda}\right)} \quad . \tag{2.134}$$

Clearly, the vertex function diverges when the expression in the denominator vanishes. The first component to diverge is the $u = 0$ component, which breaks down at the critical cutoff scale $\Lambda_c = \frac{J}{2\pi}$. The structure of the uniform magnetic susceptibility $\chi(k=0)$, too, becomes remarkably simple in the large-N limit since to leading order in N all contributions from the two-particle vertex vanish. Consequently, the uniform magnetic susceptibility depends only on local contributions from the single-particle propagator,

$$\chi^{\Lambda}(k=0) = -\frac{1}{4\pi}\int \mathrm{d}\omega\,[G(\omega)]^2 \quad . \tag{2.135}$$

Since the self-energy contribution in the propagators vanishes in the large-N limit the integration can be performed analytically, yielding

$$\chi^{\Lambda}(k=0) = \frac{1}{2\pi\Lambda} \quad . \tag{2.136}$$

The simple structure of the magnetic susceptibility should not be a surprise since the SU(N) generalization, by construction, is expected to enhance quantum fluctuations and suppress magnetic order at large values of N.

When comparing the results for the vertex function (2.134) and for the magnetic susceptibility (2.136) it stands out that only one of them diverges at a finite breakdown scale Λ_c. It is important to recall in this context that the renormalization group flow – and any observables derived thereof – is only valid until a critical breakdown scale is reached; any solution is invalid below the breakdown scale. The physical interpretation of the flow breakdown can be traced back to a phase transition into a paramagnetic ground state where the pseudo-fermions become true non-local partons [15, P3]. This also manifests in the structure factor at the phase transition which, unlike near a phase

transition into a magnetically ordered state, is featureless [P2]. The fact that the flow breakdown cannot be observed in the magnetic susceptibility is because that in the large-N limit the diverging vertex functions do not couple back into the calculation of the susceptibility. At any finite values for N this is no longer the case and sub-leading terms drive a breakdown also in the magnetic susceptibility [P2].

We have argued in Sec. 2.5.4 that the pf-FRG approach is expected to exactly reproduce the mean-field result in the large-N limit. This is confirmed by comparing the pf-FRG result on the SU(N) Heisenberg model in the large-N limit, which is formally computed at zero temperature, to a mean-field calculation which is explicitly performed at finite temperatures [P3]; both approaches correctly predict the phase transition. Moreover, the cutoff-dependence of the pf-FRG result for the magnetic susceptibility coincides with the temperature-dependence of the mean-field calculation up to a rescaling of

$$T = \frac{\pi}{2}\Lambda \quad , \tag{2.137}$$

which suggests that thermodynamic properties can be extracted from pf-FRG calculations at $T = 0$ simply by rescaling the results. The same relation between temperature and cutoff scale can also be obtained from calculations of classical systems in the large-S limit [36], which corroborates the assumption that the relation also holds for systems with a more delicate interplay between magnetic ordering tendencies and quantum fluctuations, as it is the case in frustrated spin-1/2 SU(2) quantum magnets.

2.5.7 Précis and future prospects. In the previous sections and subsections we have reviewed the derivation of the pseudo-fermion functional renormalization group for general time-reversal invariant hermitian spin systems with two-spin interactions as well as for special spin models with larger symmetries. And we have discussed the different approximations which are incorporated in the pf-FRG scheme. Most importantly, at no point in the construction of the flow equations was it necessary to fix the spatial dimensionality, such that the pf-FRG scheme can naturally be applied to three-dimensional quantum magnets.

We argued that some of the approximations (the discretization of the cutoff parameter for the solution of the differential equations, the discretization of otherwise continuous Matsubara frequencies, and the spatial truncation of vertex functions) are well controlled and that their convergence to a stable value can be verified. We have also addressed the most severe approximation, which is the truncation of the flow equation hierarchy (according to the Katanin scheme) to neglect the three-particle vertex and higher orders of the vertex functions. We have elucidated the truncation to see that it successfully recovers the exact mean-field results separately in the classical limit and in the quantum limit – which is why there is reason to believe that the flow equations at this level of truncation are a good approximation for the competition between magnetic order and spin liquid physics in frustrated quantum magnets. But without doubt the truncation also has its drawbacks. It is clearly not possible to simulate microscopic models which include interactions of three or more spin operators since even their bare exchange constants cannot be incorporated in the pf-FRG scheme at this level of truncation (they would enter in the

three-particle vertex). Besides, a three-spin interaction explicitly breaks time-reversal symmetry, which severely complicates the solution of the flow equations. For the same reason models which include magnetic fields have not yet been systematically studied in the pf-FRG formalism, which leaves room for future projects.

Furthermore it is not yet fully clear how the Katanin truncation – despite yielding controlled results in the separate limits of large-S and large-N – affects the qualitative behavior of flow breakdowns and phase transitions for spin-1/2 SU(2) spins. Often one observes that a flow breakdown is most pronounced in the ferromagnetic phase, while it is less distinct e.g. in antiferromagnetic phases where quantum fluctuations play a more important role. There is no indication so far that the detection of a flow breakdown can be improved by further increasing the resolution of the frequency discretization, which suggests that artifacts from the truncation of the flow equation hierarchy itself in combination with other necessary numerical approximations might conceal a divergence of the flow. Since the occurrence of a flow breakdown can consequently not be tracked with arbitrary precision, the current implementation of pf-FRG is not ideally suited for the exact determination of phase boundaries.

Away from these uncertainties near phase boundaries, however, the pf-FRG can readily be employed to discriminate phases of magnetic order and paramagnetic regions in the phase diagram. With the pf-FRG approach providing direct access to the real-space structure of spin-spin correlations at a magnetic phase transition it is straight-forward to classify the type of magnetic order which is about to form. The ability to classify spin liquid ground states, however, is limited in current pf-FRG calculations. Yet recent efforts have been made to probe the structure of spin-liquid ground states by augmenting the pf-FRG scheme with mean-field calculations [81] or by explicitly including and probing emergent parton degrees of freedom in the FRG scheme itself [54, P3]. Potentially, despite the necessity to perform an analytic continuation, it might also be possible to extract the full frequency dependence of the dynamic structure factor from pf-FRG calculations since the full Matsubara frequency structure of the vertex functions is computed in any case. Access to the full dynamic correlation functions would then give important insight into the structure of a spin liquid.

With these prospects we conclude the methodological discussion of the pseudo-fermion functional renormalization group. In the next chapter we discuss three different models of frustrated quantum magnetism and perform numerical simulations on them, based on pf-FRG techniques. In these simulations many of the concepts which we have discussed so far come to life.

3. Frustrated magnets and quantum spin liquids

Frustrated quantum magnets are the prime models to potentially stabilize spin liquid ground states. In Chapter 1, we have outlined several mechanisms that can inhibit magnetic long-range order and favor the formation of unconventional ground states: Strong quantum fluctuations, frustrating spin interactions, and potentially a low coordination number. All these aspects collude in frustrated quantum magnets to defy the proliferation of magnetic order. While the quantum spin-1/2 or spin-1 moments are certainly required in order to maximize quantum fluctuations, and the choice of lattice geometries in two and three spatial dimensions is limited, there are countless ways to devise spin interaction terms which generate additional exchange frustration.

In this chapter, we present three incarnations of frustrated magnets where quantum fluctuations and frustration act in concert to suppress magnetic order. We discuss models for the underlying microscopic theory and present their relevance to materials that have been synthesized in the past. In Section 3.1, we discuss a frustrated spin model on the diamond lattice and apply the description to the spin-1 material $NiRh_2O_4$, for which no indications of a magnetically ordered ground state have been reported so far. In Section 3.2, we address the compound Ba_2CeIrO_6, which despite exhibiting magnetic order at low temperatures has been measured to have an unusually high frustration parameter. In an attempt to understand the phenomenology, we study competing Heisenberg and Kitaev interactions on the fcc lattice. Section 3.3 is dedicated to the kagome material herbertsmithite, for which we discuss the role of non-diagonal, inversion symmetry breaking Dzyaloshinskii-Moriya interactions.

3.1. Quantum spiral spin liquids

Consider materials of the chemical composition AB_2X_4, where either the atoms on the A-site or on the B-site carry a magnetic moment. The family of materials which is obtained by varying the specific constituents goes by the name 'spinel materials', and one can discriminate between two profoundly different cases: if the ion of type A is chosen to be magnetic and ion B is non-magnetic, the resulting effective lattice structure of magnetic moments is a diamond lattice (Fig. 3.1a). Alternatively, if B is the magnetic ion, the effective lattice structure is a pyrochlore lattice (Fig. 3.1b). The latter has long been known as a suitable candidate to cultivate spin liquid ground states – with its structure of corner sharing tetrahedra, the triangular motif in every tetrahedron may naturally give rise to geometric frustration. Consequently, an industrious branch of physics has evolved

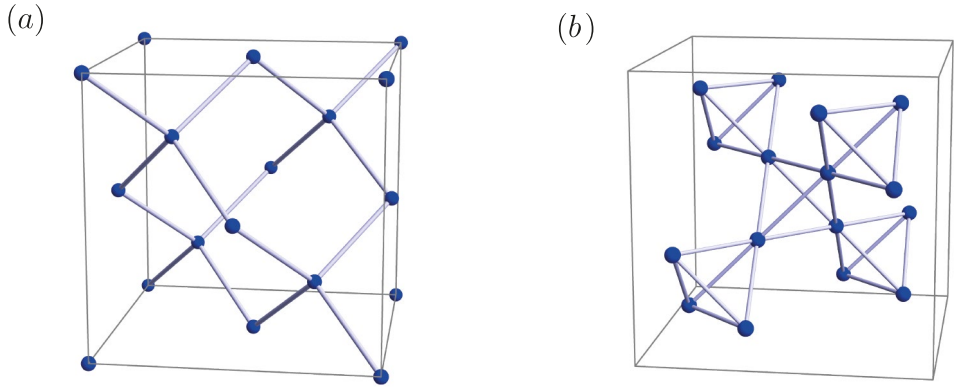

Figure 3.1. **Lattice structure of spinel materials.** (a) Magnetic moments in A-site spinels are arranged on a diamond lattice. (b) B-site spinels form a pyrochlore lattice, which is composed of corner-sharing tetrahedra.

around the study of the pyrochlore lattice as a host for classical spin liquids [82, 83] as well as quantum spin liquids [84, 85]. In the search for experimental realizations of the pyrochlore antiferromagnet, the B-site spinel materials play an important role. Many examples among them can be stabilized which have dominant antiferromagnetic exchange interactions and exhibit strong frustration, e.g. ACr_2O_4 or AV_2O_4 (A = Mg, Zn, Cd) [86].

In this chapter, which is based on our results as published in Ref. [P4], we concentrate on A-site spinels, which form a diamond lattice of magnetic moments. Although the diamond lattice is bipartite and hence cannot mediate geometric frustration on the level of nearest neighbor interactions, it is possible to generate frustration by introducing antiferromagnetic exchange couplings among next-nearest neighbors. In the limit of exclusive next-nearest neighbor couplings the diamond lattice effectively decomposes into two interpenetrating fcc lattices, which have the triangular motif required for geometric frustration to emerge. It has been demonstrated some ten years ago for classical spin models on the diamond lattice that competing interactions between nearest neighbors and next-nearest neighbors can give rise to a highly degenerate ground state that ultimately leads to non-trivial magnetic order as a consequence of a subtle order-by-disorder mechanism whose details depend on the relative strength of the two couplings [87]. Most importantly, these theoretical predictions have recently been confirmed in an experiment on the spin-5/2 A-site spinel $MnSc_2S_4$ [88]. Besides $MnSc_2S_4$ [89], a selection of other A-site spinal materials can also be stabilized, including $FeSc_2S_4$ [89], and $CoAl_2O_4$ [90, 91]; the three materials have different spin lengths of 5/2, 2, and 3/2, respectively[1]. Recently, the list of A-site spinels has been extended by the spin-1 compound $NiRh_2O_4$ for which no signs of a magnetic ordering transfition have been reported down to a temperature of 0.1K [92], which hints at a potential spin liquid ground state.

The remainder of this chapter is structured as follows. We first briefly review the

[1] In the spin-2 spinel material $FeSc_2S_4$, the spin degree of freedom is dressed with additional orbital degrees of freedom, see Ref. [89]

phenomenology of the aforementioned model and the minimal model itself in the classical limit. In this context, we introduce the notion of spiral surfaces and spiral spin liquids. We complement the review of the classical limit with the discussion of a previous analysis that addressed the approximate role of quantum fluctuations on the basis of an Sp(N) generalization of the magnetic moments. Thereafter, we discuss our analysis of the full quantum model at finite temperature, as presented in Ref. [P4]. This discussion is centered around the role of quantum fluctuations and their dependence on the spin length S, as well as their interplay with thermal fluctuations. We conclude the discussion by pointing out the applicability of the theory to the spin-1 A-site spinel material $NiRh_2O_4$.

3.1.1 Minimal model and classical spins. As a minimal model for the description of $MnSc_2S_4$, we consider a Heisenberg model with nearest neighbor interactions J_1 and sizable next-nearest neighbor interactions J_2,

$$H = J_1 \sum_{\langle i,j \rangle} \mathbf{S}_i \mathbf{S}_j + J_2 \sum_{\langle\langle i,j \rangle\rangle} \mathbf{S}_i \mathbf{S}_j \quad , \tag{3.1}$$

where $\langle i,j \rangle$ denotes a sum over all nearest neighbor sites i and j and $\langle\langle i,j \rangle\rangle$ denotes a sum over next-nearest neighbors. The spin operators $\mathbf{S}_i$ denote conventional SU(2) spin-S moments, whose length S can in principle be varied. Yet, throughout this sub-section we consider the spins to be in the classical limit, i.e. $S \to \infty$. It has been conceptualized [87, 88] that this microscopic description, in the classical limit, is suited to capture the main phenomenology observed in the spin-5/2 spinel material $MnSc_2S_4$.

The energy of the classical Hamiltonian (3.1) can be readily minimized by means of a Luttinger Tisza analysis [80]. Remarkably, one finds that above a threshold of $J_2/J_1 = 1/8$ the ferromagnetic order (or Néel order, depending on the choice of the sign for nearest neighbor couplings, while J_2 is always kept antiferromagnetic) gives way to a highly degenerate coplanar spin-spiral configuration on the diamond lattice [87]. These coplanar spin spirals are magnetization patterns which are roughly of the form[2]

$$\mathbf{S}_i = \mathbf{s}_1 \cos(\mathbf{k}\mathbf{r}_i) + \mathbf{s}_2 \sin(\mathbf{k}\mathbf{r}_i) \quad , \tag{3.2}$$

where the spin is located at $\mathbf{r}_i$, and the orthonormal vectors $\mathbf{s}_1$ and $\mathbf{s}_2$ span a plane in which the spins on the lattice wind. The winding speed and direction is uniquely determined by the momentum $\mathbf{k}$. However, minimizing the energy of the classical spin Hamiltonian (3.1) does not just yield one such defining momentum vector, but one finds that over a large range of coupling constants J_2/J_1 there exists a sub-extensive number of momenta which are associated with spin spirals of equal ground state energy. These degenerate points form two-dimensional manifolds in momentum space, the so-called 'spiral surfaces', whose exact shape and topology depend on the choice of coupling constants J_2/J_1, see Fig. 3.2. The appearance of spiral surfaces is not unique to this model on the diamond lattice [93, 94]; they can also been observed in a similar setting on

[2] The precise expression includes a $\mathbf{q}$-dependent phase shift between the spins on the two fcc sublattices, as discussed in detail in Ref. [87].

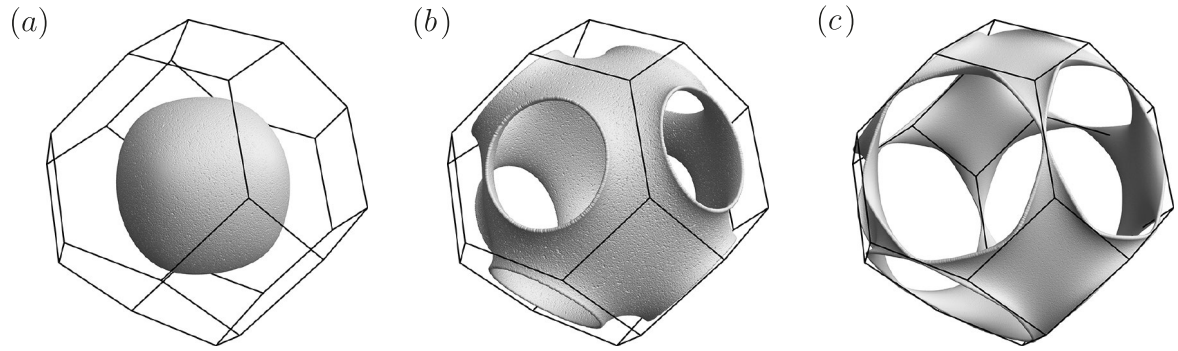

Figure 3.2. **Spiral surface.** The spiral surface indicates all points in momentum space for which the associated coplanar spin spiral minimizes the system's ground state energy. Here, the surface is plotted within the first Brillouin zone. The shape of the spiral surface depends on the choice of coupling constants. Initially, the spiral surface is almost spherical, but as the next-nearest neighbor coupling is increased, the surface inflates and eventually breaks open once it touches the Brillouin zone boundary. The plots are shown at different interaction parameters (a) $J_2/J_1 = 0.2$, (b) $J_2/J_1 = 0.4$, and (c) $J_2/J_1 = 0.85$.

the fcc lattice with competing nearest and next-nearest Heisenberg interactions [P5] (see Sec. 3.2), or in the two dimensions on the honeycomb lattice [38]. However, they often only appear at singular points in the phase diagram that require fine tuning of coupling constants, and they reduce to lower-dimensional manifolds upon adding perturbations away from the singular point. In the diamond lattice (and also on the honeycomb lattice in two dimensions), the spiral surfaces remain robust over a large range of coupling constants J_2/J_1.

The degeneracy of configurations on the spiral surfaces can be broken in the presence of thermal fluctuations, in the spirit of the 'order by disorder' mechanism (c.f. Sec. 1.1.2) – at finite temperatures the true ground state is not selected by its internal energy E but rather by minimizing its free energy F. Since the free energy

$$F = E - TS \tag{3.3}$$

contains a negative contribution from the entropy S, the system, by minimizing its free energy, strives to maximize its entropy. This is achieved by the system assuming those configurations that give access via thermal fluctuations to the largest part of the system's configuration space. For each point on the spiral surface, the effect of thermal fluctuations away from the spiral surface can be computed perturbatively, and the entropy gain is found to vary within the spiral surface [87]. The free energy is minimized by a discrete set of high-symmetry points on the spiral surfaces, as shown in Fig. 3.3 for selected values of the coupling constants. Similar to the evolution of the spiral surface upon tuning the ratio of coupling constants J_2/J_1, the locations of the minima vary depending on the choice of interaction parameters. Thereby one may discriminate four different spiral regimes: the 111 phase which has a single free-energy minimum in the (111) direction (Fig. 3.3a), the 111^* phase which has six minima around the (111)

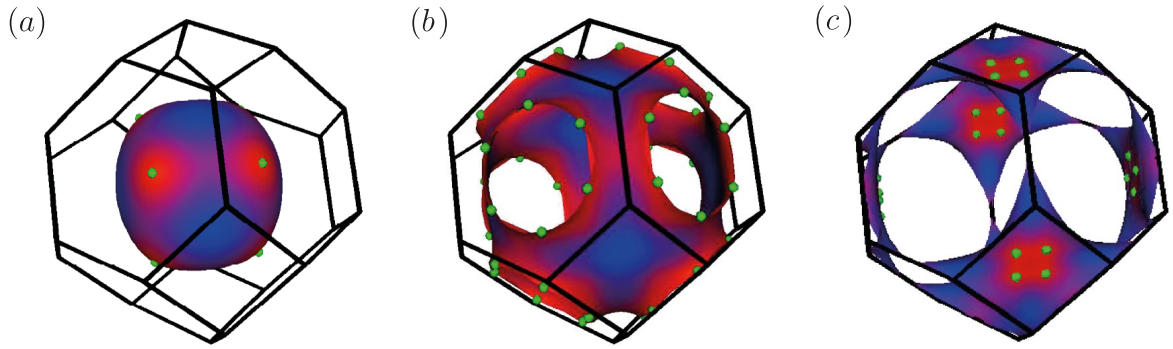

Figure 3.3. **Order by disorder** acting as an entropic selection mechanism to break the degeneracy of the spiral surfaces. The colored surfaces displayed here are the spiral surfaces as depicted in Fig. 3.2. The color code indicates the free energy associated with the corresponding coplanar spin spiral for each momentum point on the spiral surface. Red indicates low free energy, blue higher free energy. The green points indicate the global minima of the free energy. (a) Coupling ration $J_2/J_1 = 0.2$ with a free-energy minimum in the (111) direction. (b) $J_2/J_1 = 0.4$ with six minima around the (111) direction, labeled 111*. (c) $J_2/J_1 = 0.85$ with four maxima around the (100) direction, labeled 100*. The plots are taken from Ref. [87].

direction (Fig. 3.3b), the 110 phase which a minimum in the the (110) direction, and the 100* phase which has four minima around the (100) direction (Fig. 3.3c). At low temperatures, the variation of the free energy within the spiral surfaces is ultimately expected to drive a thermal phase transition into a state of magnetic long-range order. The ordered phase then corresponds to the proliferation of a single spin spiral which is characterized by the single momentum point of minimal free energy.

By employing classical Monte Carlo simulations of the system it has been demonstrated that the system indeed undergoes a magnetic ordering transition at finite temperatures [87]. The finite-temperature phase diagram is depicted in Fig. 3.4, where it can be seen that the critical temperature is strongly suppressed in regions of the phase diagram where spin spirals dominate. The suppression of the critical temperature suggests that the ordering mechanism within the manifold of degenerate states – order by disorder – is much more subtle than e.g. regular Néel order in the absence of degeneracies which is seen to have a much higher transition temperature. Furthermore, the Monte Carlo simulations have confirmed that not only the magnetically ordered phases can be identified by their distinct peaks in the structure factor, but also the the spiral surfaces can be observed in the structure factor at temperatures shortly above the transition point. As displayed in Fig. 3.4b, when computing the structure factor just above the transition temperature and plotting only those those regions which show largest intensities one recovers the spiral surface almost perfectly. Moreover, within the spiral surface the intensity distribution of the structure factor as computed with Monte Carlo reflects the modulation of the ground state free energy predicted in the perturbative expansion (c.f. Fig. 3.3).

The existence of a spiral surface in the spin-5/2 spinel material $MnSc_2S_4$ has recently

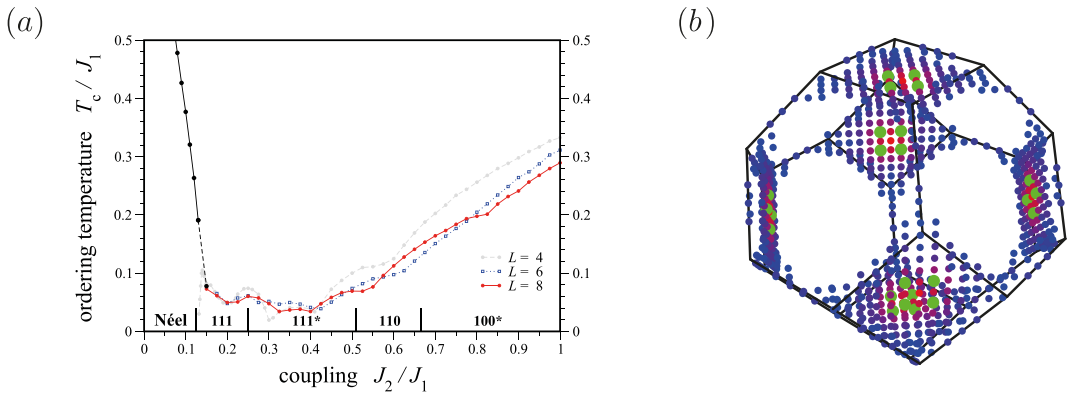

Figure 3.4. **Finite-temperature simulations** performed with classical Monte Carlo. (a) Finite-temperature phase diagram as a function of the ratio of interaction parameters J_2/J_1. The transition temperature is strongly suppressed in the spin spiral regime. The labeled regions 111, 111*, 110, and 110* describe the types of coplanar spiral order which are selected as the ground state (see text for details). (b) High intensity regions in the (equal time) structure factor at $J_2/J_1 = 0.85$, just above the critical temperature. The color code indicates variations of the structure factor; blue signals lower intensity, while red denotes high intensity. The maxima are indicated in green. The plots are taken from Ref. [87].

been confirmed by neutron diffraction measurements [88]. A comparison of the precise shape of the spiral surface with the theoretical predictions revealed the ratio of coupling constants in $MnSc_2S_4$ to be approximately $J_2/J_1 = 0.85$. At lower temperatures the material undergoes a multi-step ordering process towards a helical ground state, which is not captured by the minimal model presented in Eq. (3.1). However, it can be argued that the more complicated ordering process is due to additional perturbations, e.g. small third-nearest neighbor interactions that are not covered in the minimal model [87, 95].

3.1.2 Quantum order by disorder. In a subsequent study the influence of quantum fluctuations on the ground state energy of the minimal model (3.1) has been investigated within the approximation of an Sp(N) generalization of the physical SU(2) spins [96]. It has been reported that, to leading order in the large-N correction terms, the quantum fluctuations can provide a selection mechanism to lift the degeneracy within the classical spiral surface, similar to what has been observed in the classical model for thermal fluctuations. It seems, however, that the selection via quantum order by disorder is not as strong as the thermal order by disorder mechanism.

While thermal fluctuations always lift the degeneracy up to a discrete set of momentum space points, for quantum fluctuations there exist regimes where the degenerate manifold is reduced from a two-dimensional submanifold to a one-dimensional submanifold, but the degeneracy is not lifted completely. These regimes include for example the 111° phase where the degeneracy is reduced to a circle around the (111) direction, or the $100^{\times}$ phase where two cross-shaped lines remain degenerate around the (100) direction. These phases do not have a direct analogue in the classical phase diagram, yet they often

Figure 3.5. **Phase diagrams** of the classical model, where selection occurs by thermal order by disorder, and of the Sp(N) generalized model, where ground state energy corrections result from quantum fluctuations. The labels refer to the fluctuation-induced selection of momentum space points. 111: one point in (111) direction. 111*: six points around (111) direction. 110: one point in (110) direction. 100*: four points around (100) direction. dgn: no selection within the spiral surface occurs. 111°: circle around (111) direction. 111**: six points around (111) direction, rotated in comparison to the 111* configuration. 100×: cross around (100) direction. 100: one maximum in (100) direction. The classical phase diagram is taken from Ref. [87], the Sp(N) quantum phase diagram from Ref. [96].

turn out to be supersets of the points which would be selected by thermal fluctuations, as can be seen in the comparison of phase diagrams shown in Fig. 3.5. In those regions of the phase diagram where quantum fluctuations prefer the circle around the (111) direction and the cross around (100), thermal fluctuations in the corresponding parts of the classical phase diagram would select six points around (111) and four points around the (100) direction, respectively – both of these configurations form subsets of the momentum space points selected by quantum fluctuations. Similarly, between $J_2/J_1 = 1/2$ and $J_2/J_1 \approx 2/3$ quantum fluctuations favor six points around the (111) direction, three of which are oriented towards to the (110) direction (in Fig. 3.5 this phase is labeled 111**; note that this phase is not equivalent to 111*, whose six points do not include the points in (110) direction). Such a phase does not exist in the classical phase diagram, yet thermal fluctuations in the classical model would give preference to the three points in (110) direction, which, again, are a subset of the points favored by quantum fluctuations.

In a nutshell, the comparison between the classical phase diagram and the quantum phase diagram shows that the two types of fluctuations – thermal fluctuations in the classical model and leading order quantum fluctuations of Sp(N) spins in the quantum theory – do not necessarily lift the ground state degeneracy in the same way. However, both scenarios provide a similar explanation as to how the sub-extensive manifold of degenerate configurations can be lifted.

In the following subsection we address the question of how the two mechanisms act jointly in the full SU(2) quantum model at finite temperatures. We will demonstrate that the general picture of spiral surfaces holds also in that setting. Yet, the presence of quantum and thermal fluctuations, besides favoring individual coplanar spin spiral states within the spiral surface, may also deform the underlying spiral surface altogether, suggesting that an analysis of the structure factor away from the classically degenerate spiral surfaces can be interesting.

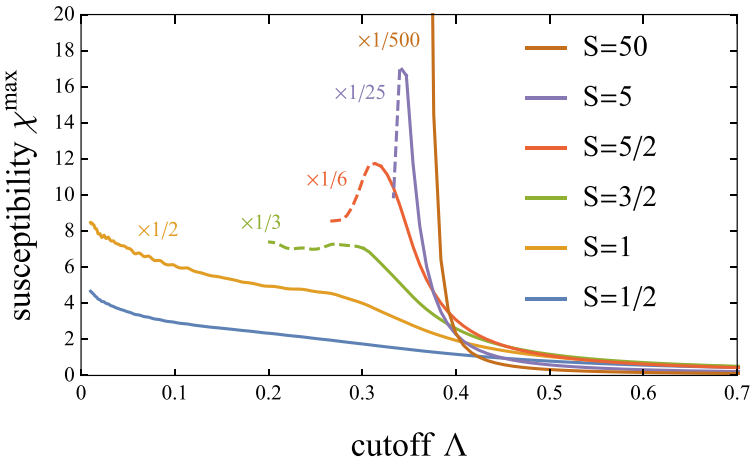

Figure 3.6. **Renormalization group flow breakdown.** The maximum $\chi^{\max} = \max_{\mathbf{k}} \chi^{\Lambda}(\mathbf{k})$ of the structure factor is plotted as a function of the RG cutoff parameter for different spin lengths. For systems of large spin length $S \geq 3/2$ the smooth flow eventually breaks down, indicated by a cusp or a divergence at some critical cutoff scale Λ_c which signals the onset of magnetic long-range order. At small spins $S = 1/2$ and $S = 1$ no sign of magnetic order is observed. The values are computed for interaction constants $J_2/|J_1| = 0.73$.

3.1.3 Thermodynamics of quantum spiral spin liquids. We now discuss the full quantum model of SU(2) spins which is governed by the general Hamiltonian of nearest neighbor interactions on the diamond lattice that are augmented with frustrating antiferromagnetic next-nearest neighbor interactions, as given in Eq. (3.1). For our analysis, we employ the pf-FRG formalism in its generalized form to spin-S moments, which we have reviewed in Section 2.5.5. We closely follow the presentation of results as published in Ref. [P4].

Within our pf-FRG calculations, it is straightforward to determine the elastic ($\omega = 0$) component $\chi(\mathbf{k})$ of the dynamical structure factor (in the following, for simplicity, we refer to this as the 'structure factor' or the magnetic susceptibility),

$$\chi(\mathbf{k}) = S(\mathbf{k}, \omega = 0) = \frac{1}{N} \int \mathrm{d}t \sum_{i,j} e^{i\omega t + i\mathbf{k}(\mathbf{r}_i - \mathbf{r}_j)} \langle \mathbf{S}_i(t) \mathbf{S}_j(0) \rangle \quad . \tag{3.4}$$

Note that this definition differs from the equal-time structure factor which is displayed in Fig. 3.4b; the equal-time structure factor is equivalent to the frequency-integrated dynamical structure factor. Unfortunately, in pf-FRG, the inelastic components of the dynamical structure factor cannot be accessed directly, as they would require to perform an analytic continuation from Matsubara frequencies (in which the pf-FRG approach is naturally formulated) to real frequencies. Only at $\omega = 0$ where the bosonic Matsubara frequency coincides with the real frequency axis, the analytic continuation is not needed. We perform pf-FRG simulations on a frequency mesh of up to $N_\omega = 144$ discrete points and we truncate the two-particle vertex for interactions between lattice sites which are

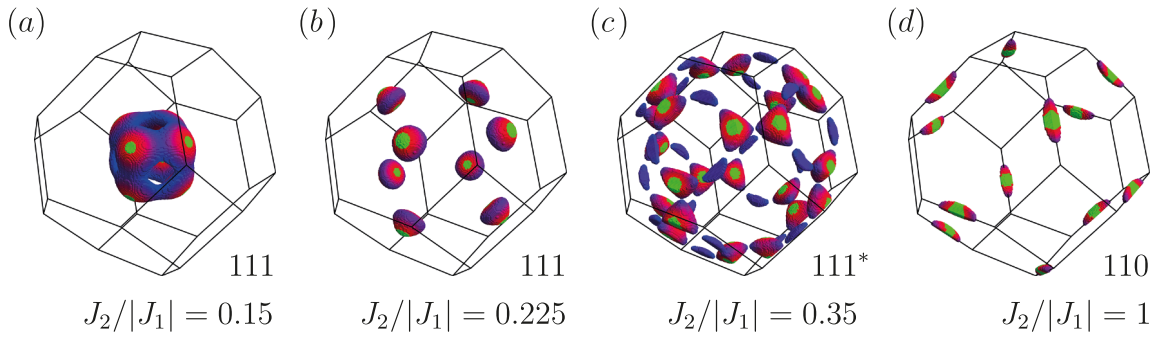

Figure 3.7. **Structure factors in the classical limit.** The figures display regions of high intensity in the structure factor computed at large spins $S = 50$, which resembles the classical limit. The colored regions within the first Brillouin zone correspond to the top 20% of intensity in the structure factor. The color code signals the relative intensity distribution within the top 20% – blue corresponds to low intensity, red signals high intensity. The overall top 0.4% are colored in green. Since the maxima are typically hidden inside the center of the colored manifolds, we radially project the color associated with the highest intensity onto the manifold's surface. The structure factors are computed just above the flow breakdown (see text for details). They are plotted for different ratios of the interaction constants $J_2/|J_1|$; the ratios in panels (a) – (d) are given by $J_2/|J_1| = 0.15$, 0.225, 0.35, and 1, respectively.

more than $L = 10$ lattice bonds apart. These parameters lead to a system of approximately $2.4 \cdot 10^7$ coupled differential equations per set of coupling constants that need to be solved numerically, see the discussion about the numerical solution of pf-FRG flow equations in Sec. 2.4.

To begin with, we revisit the classical limit which we approximate by assuming large spins S=50. In the previous subsections, we have argued that in this case we can expect magnetic order to proliferate. In pf-FRG calculations, the onset of magnetic order is indicated by a breakdown of the smooth renormalization group flow at some critical cutoff value Λ_c, see the discussion of spontaneous symmetry breaking in Sec. 2.5.1. Plotting the evolution of the structure factor as a function of the cutoff parameter Λ confirms the existence of a magnetic ordering transition for systems in the classical limit, see Fig. 3.6. The specific type of magnetic ground-state order can be inferred from the full momentum dependence of the structure factor, more specifically from the position of peaks within the Brillouin zone. The structure factors are plotted in Fig. 3.7 for a selection of different coupling constant ratios $g = J_2/|J_1|$ (note that throughout this chapter we are using ferromagnetic nearest-neighbor couplings in the pf-FRG calculations, which ensures that the high-intensity regions of the structure factor lie within the first Brillouin zone). The structure factors bear a striking resemblance to the types of magnetic order that have been discussed in the classical phase diagram, which was based on the consideration of infinitesimal fluctuations away from the classically degenerate spiral surface (for simplicity we will refer to this solution as LT+fluctuations, since the degenerate spiral surface can be obtained by means of a Luttinger Tisza approach). We find that at small coupling ratios $g = 0.15$ and $g = 0.225$ the highest intensity of the structure

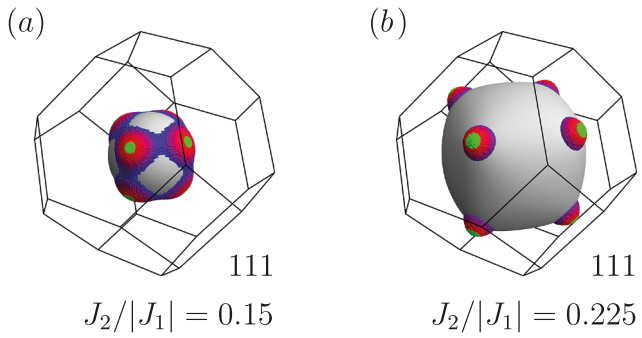

Figure 3.8. **Structure factors in the classical limit.** The figures display regions of high intensity in the structure factor computed at large spins $S = 50$ and plotted just above the breakdown scale Λ_c. The color code is identical to Fig. 3.7. Indicated in gray are the classically degenerate spiral surfaces at exchange constants (a) $J_2/|J_1| = 0.15$ and (b) $J_2/|J_1| = 0.225$.

factor is in (111) direction, which is in line with the LT+fluctuations result. At larger coupling ratio $g = 0.35$ we find that six points around the (111) direction have high intensity in the structure factor. However, only three of the points are degenerate and have maximal intensity while the other three points are slightly less pronounced, which marks a deviation from the phase diagram as obtained by LT+fluctuations. The deviation persists to even higher coupling ratio $g = 1$ where pf-FRG finds strong peaks in the (110) direction, yet LT+fluctuations predict four maxima around the (100) direction.

Let us reconcile these differences. We have discussed in Sec. 2.5.5 that in the classical limit pf-FRG reproduces the Luttinger Tisza solution which obtains the classical spiral surfaces. However, the equivalence only holds when the RG flow is traced down to zero cutoff where the physical solution is retrieved and the details of the regulator function become irrelevant. In practice, however, it is difficult to completely integrate out the cutoff function since this would require going past potential phase transitions of spontaneous symmetry breaking. Although attempts to enter the symmetry-broken regime have been made in other formulations of FRG [44, 54, P3], in the pseudo-fermion FRG the presence of symmetries is necessary in order to keep the computational effort manageable. Therefore, it can be expected that the pf-FRG solution does not yield the exact degenerate spiral surfaces. Rather, since finite cutoff values in the pf-FRG scheme can be interpreted as finite temperatures [36, 97], the pf-FRG solution at the flow breakdown point Λ_c may be interpreted as the physical system at its transition temperature into the ordered state. As for the thermal selection of coplanar spiral configurations within the spiral surface, one should note that pf-FRG can only resolve a single phase transition at highest temperature. Any successive transition at lower temperatures, as observed e.g. in the multi-stage ordering process for the spin-5/2 spinel material $MnSc_2S_4$, is not captured within the pf-FRG approach. Nevertheless, we can confirm that the maxima of the structure factor in momentum space lie within the classical spiral surface, as shown in Fig. 3.8.

We now move away from the classical limit and consider spin systems of spin S=5/2, as realized in the spinel material $MnSc_2S_4$. Reducing the spin length implies weakening

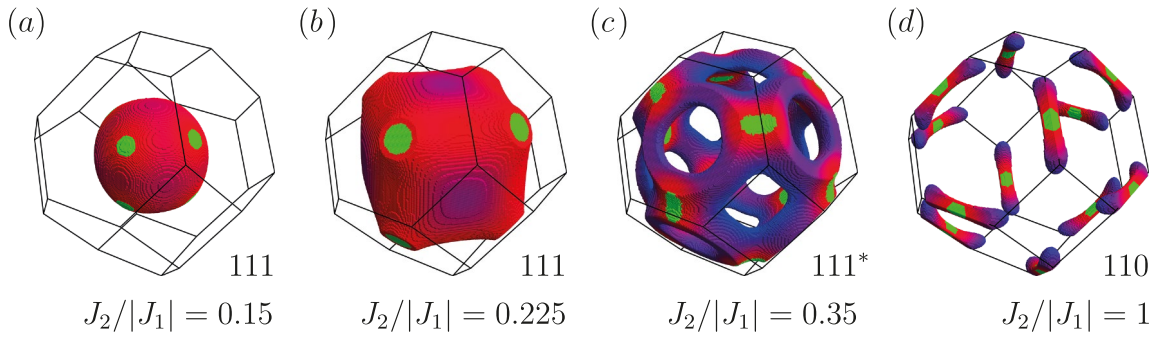

Figure 3.9. **Structure factors at S=5/2.** The figures display regions of high intensity in the structure factor, determined just above the breakdown scale Λ_c. The color code is identical to Fig. 3.7. The structure factors are computed for different ratios of the interaction constants $J_2/|J_1|$; the ratios in panels (a) – (d) are given by $J_2/|J_1| = 0.15$, 0.225, 0.35, and 1, respectively.

the preference towards magnetic order, which manifests in less pronounced maxima in the structure factor. Consequently, the regions of high intensity are now more expansive, as shown in Fig. 3.9. The position of the peaks, on the other hand, remains largely unaffected by the reduction of spin length. For spin S=5/2, since the system orders magnetically for all ratios of coupling constants, it is also instructive to study the transition temperature, which linearly relates to the breakdown scale Λ_c. The critical cutoff as a function of the ratio of coupling constants is shown in Fig. 3.10. Similar to the classical model (c.f. Fig. 3.4a) the transition temperature into the magnetically ordered state is significantly reduced upon entering the spin spiral regime above $g = 1/8$. The transition temperature recovers and goes back up again as the next-nearest neighbor coupling further increases. Since a straightforward increase of the next-nearest neighbor exchange coupling leads to a growth of the exchange energy per lattice site, thus implying an increase of the total energy scale (in particular of the breakdown scale), the energy scale has been normalized by a phenomenological factor of $\sqrt{J_1^2 + J_2^2}$ [38] for compensation.

[p] The sequence of different magnetic ordering patterns which is obtained upon continuously increasing next-nearest neighbor interactions comprises (i) a single maximum in (111) direction between $1/8 \leq g \lesssim 0.225$, labeled the 111 phase, (ii) three maxima around the (111) direction in the range $0.225 \lesssim g \lesssim 0.35$, labeled the 111* phase, (iii) a single maximum in the (110) direction between $0.35 \lesssim g \lesssim 1.2$, labeled the 110 phase, and (iv) two maxima around the (110) direction for $g \gtrsim 1.2$, labeled the 110* phase. As g is increased further, the maxima continuously shift towards $(1\frac{1}{2}0)$. The latter can be understood by thinking of the diamond lattice in the limit of large next-nearest neighbor coupling $J_2 \gg |J_1|$ as two (almost) decoupled fcc lattices; within each fcc sublattice the nearest-neighbor interaction is then given by the antiferromagnetic J_2. It has been established for the fcc antiferromagnet that its ground state is magnetically ordered with the ordering wave vector (100) [98, 99]. Yet, it is known that the fcc antiferromagnet, upon adding just small next-nearest neighbor interactions, is instable towards either magnetic order with the ordering vector $(1\frac{1}{2}0)$ or magnetic order with the ordering vector (100),

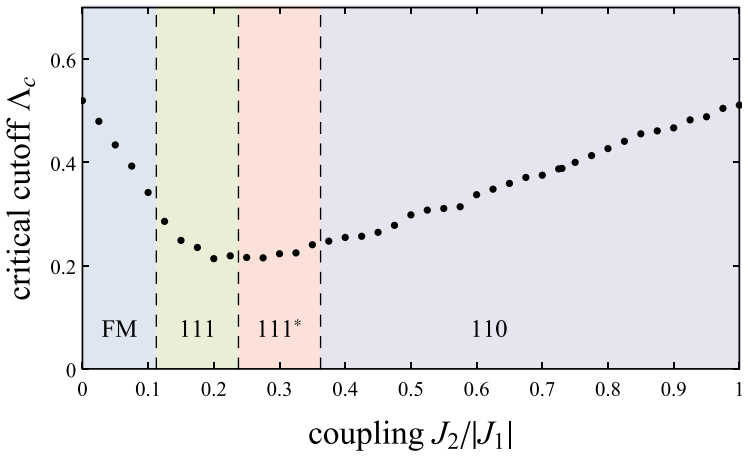

Figure 3.10. **Suppression of ordering transition at spin S=5/2.** The critical cutoff scale Λ_c, which can be linearly related to the transition temperature of the magnetically ordered ground state [36], is displayed as a function of the ratio of interaction constants (the nearest neighbor coupling is fixed at $J_1 = -1$). The critical cutoff is significantly suppressed upon entering the spin spiral regime at $J_2/|J_1| > 1/8$.

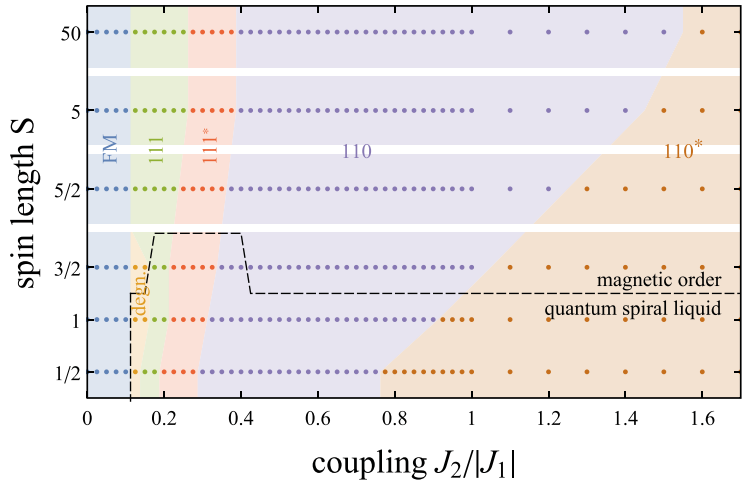

Figure 3.11. **Phase diagram.** The full phase diagram is spanned by the variation of the spin length S and the ratio of coupling constants $J_2/|J_1|$. It can be separated into two qualitatively different parameter regimes, one favoring a magnetically ordered ground state (above the dashed line), and one with a quantum spiral spin liquid ground state (below the dashed line). In both regimes a spiral surface proliferates and fluctuations enhance spin correlations along certain high-symmetry directions, as indicated by the labels (see text for details). Only for a slim parameter window at small spins a selection of momentum points does not occur and the spiral surface remains degenerate.

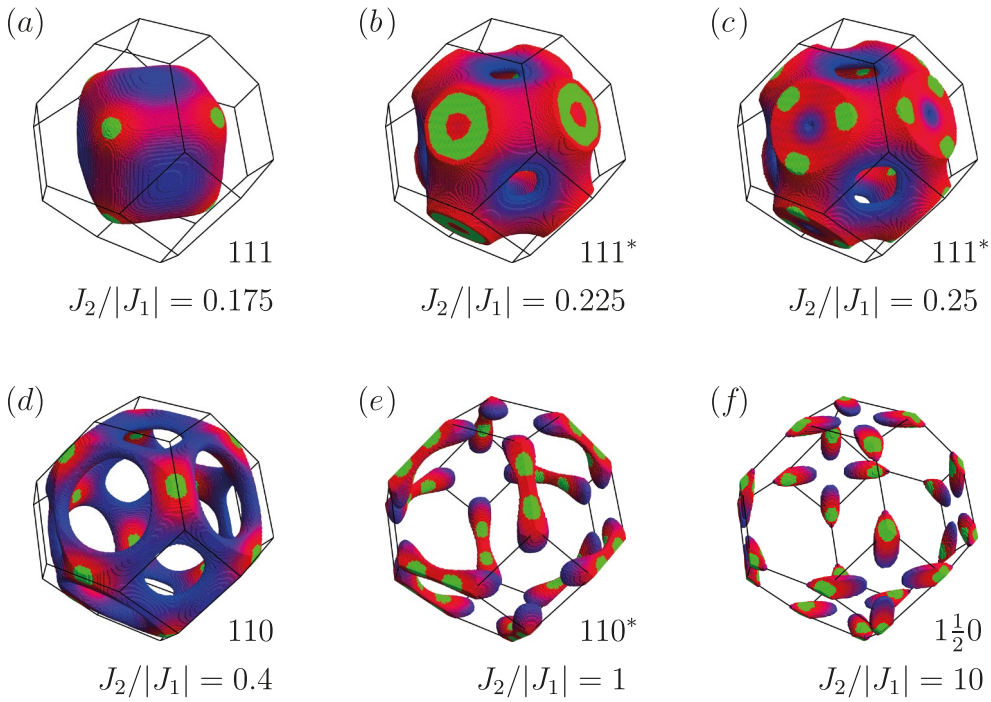

Figure 3.12. **Structure factor at S=1.** The figures display regions of high intensity in the structure factor. The structure factor is computed at the lowest cutoff scale $\Lambda = 0$. The color code is identical to Fig. 3.7. The structure factor is computed for different ratios of the interaction constants $J_2/|J_1|$; the ratios in panels (a) – (f) are given by 0.175, 0.225, 0.25, 0.4, 1, and 10, respectively.

depending on the sign of the perturbation. For ferromagnetic next-nearest neighbor interactions the (100) order is favored, while for antiferromagnetic interactions $(1\frac{1}{2}0)$ is the preferred order [100]. For the diamond lattice at strong next-nearest neighbor interactions J_2 one can therefore anticipate that the effective interactions which are perturbatively mediated within and in between the two fcc sublattices by nearest neighbor interactions J_1 play a delicate role. In our pf-FRG simulations, the interactions appear to stabilize magnetic order of type $(1\frac{1}{2}0)$.

The 110 configuration has also been measured to be the ground state of the spin-5/2 spinel material $MnSc_2S_4$ [101]. In this material, at temperatures slightly above the ordering transition, the shape of the degenerate spiral surface can be fitted to predictions of the model Hamiltonian (3.1) to yield the approximate ratio of exchange constants $g = 0.85$ [88]. The observed ground state magnetization is well described by the phase diagram obtained with pf-FRG, where a system at $g = 0.85$ lies deep within the 110 ordered phase, see Fig. 3.10.

Next, we address the case of small spins $S = 1$ and $S = 1/2$ where quantum fluctuations become significant. Unlike implementations at larger spins, the spin-1 model is not observed to exhibit magnetic order. Yet, within the paramagnetic phase, the system still develops a modulation in the momentum dependence of the structure factor that is rem-

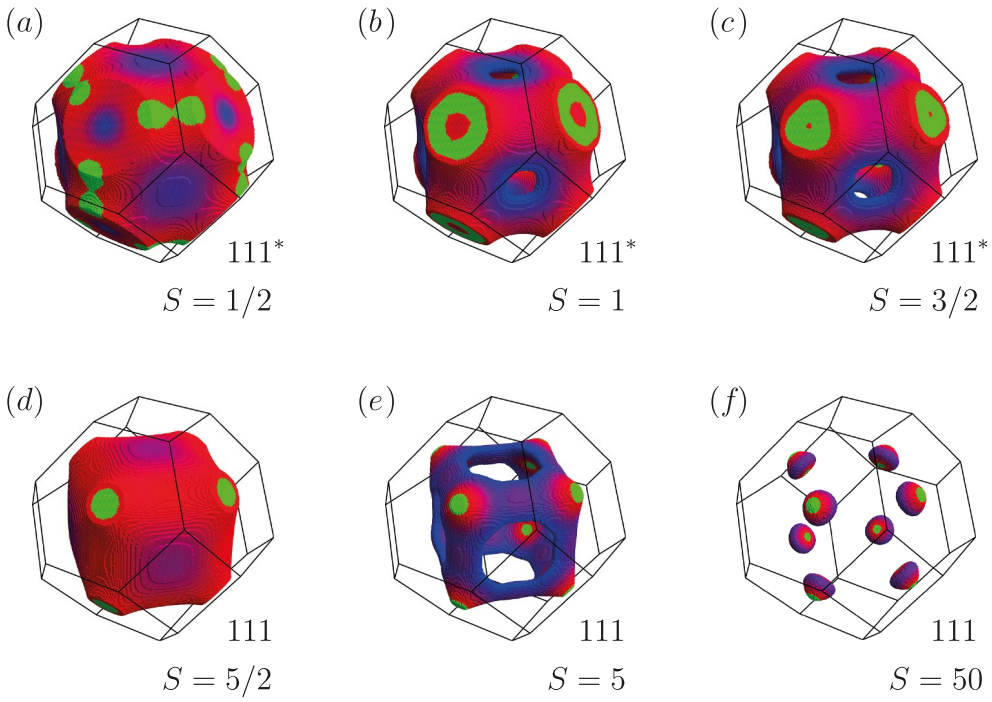

Figure 3.13. **Structure factor at $J_2/|J_1| = 0.225$.** The figures display regions of high intensity in the structure factor. The color code is identical to Fig. 3.7. The structure factor is computed for different spin lengths S; the spin lengths in panels (a) – (f) are given by $S = 1/2$, 1, 3/2, 5/2, 5, and 50, respectively. Panels (a) – (c) are plotted close to zero cutoff, while panels (d) – (f) are plotted at the critical cutoff scale Λ_c since they are in a parameter region where the ground state is magnetically ordered.

iniscent of spiral surfaces. Therefore, we refer to the paramagnetic phase as a quantum spiral spin liquid. Despite the absence of an ordering transition, even within the spiral surface certain momentum points are preferred over others. The sequence of preferred momentum points on the spiral surface which is obtained by tuning the ratio of coupling constants remains qualitatively unchanged as compared to the classical phase diagram. Only a slim parameter window next to the ferromagnetically ordered phase at small spins implies no intensity modulation within the spiral surface, see the phase diagram in Fig. 3.11. A similar phenomenon occurs for small spins at the transition between the 111 region and 111*, where a ring around the (111) direction remains degenerate, see Fig. 3.12b. However, this scenario only seems to occur in singular points of the phase diagram and is not resolved sufficiently well in our study. Therefore, we incorporate these special cases into the 111* region, which collectively refers to configurations with features around the (111) direction. Such special cases where the degeneracy of the spiral surface is not lifted entirely have also been reported in the model of generalized Sp(N) spins [96], c.f. the phase diagram in Fig. 3.5.

In general, while the sequence of preferred momentum points upon tuning the ratio of coupling constants is largely invariant under variation of the spin length, there is a trend

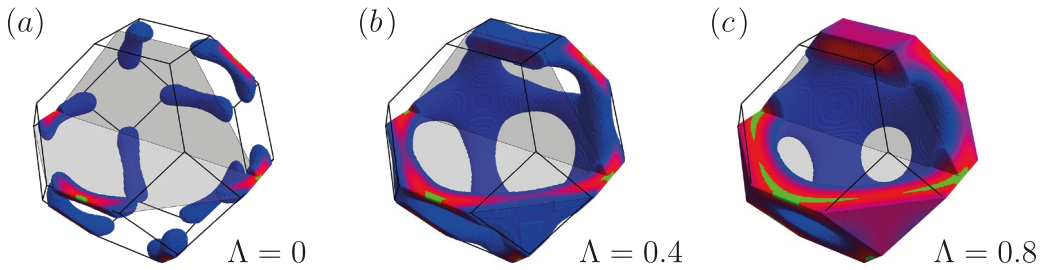

Figure 3.14. **Thermodynamics of the spiral surface at S=1.** The three panels show regions of highest intensity in the structure factor, computed at $J_2/|J_1| = 0.73$. Colored regions indicate the upper 20% of the structure factor. The color code indicates the relative distribution of intensity within those regions, where blue indicates lower intensity and red indicates high intensity. The overall top 0.4% is colored in green. The three panels (a) – (c) are plotted at different values of the cutoff parameter Λ. At lowest cutoff, the selection of momentum points within the spiral surface is strongest, while at higher cutoff the full spiral surface becomes visible.

for the different spiral regions in the phase diagram to become narrower for systems with smaller spins, see Fig. 3.11. This effect can be traced back to the observation that the boundaries between the different spiral regions mainly depend on the size of the spiral surface. In the classical model the size of the spiral surface is determined only by the ratio of couplings constants; in the quantum model, however, the reduction of the spin length further augments the expansion of the spiral surface, as depicted in Fig. 3.13. As a consequence, the sequence of different spiral regions is traversed more quickly in regions of the phase diagram with small spins, while the same sequence of phases extends over a broader interval of coupling constant ratios at larger spins.

Finally, we discuss the role of temperature in the formation of spiral surfaces. In the original model [87] of classical spins the spiral surface has been defined as the manifold of momentum points which characterize degenerate coplanar spin spiral configurations. In the pf-FRG calculations on quantum spins, on the other hand, the spiral surface appears naturally as a region of high intensity in the structure factor; we have seen many illustrations thereof throughout the course of this chapter. All structure factor plots which we have seen so far have been plotted either at zero cutoff $\Lambda = 0$ in cases where no magnetic order sets in, or at the critical cutoff Λ_c in cases where a magnetic ordering transition exists. An example for a structure factor in the quantum spiral spin liquid regime which is evaluated at non-zero cutoff values is displayed in Fig. 3.14 for the spin-1 model at $g = 0.73$. At zero cutoff the enhancement of individual points on the spiral surface is strongest (yet not strong enough to drive the system into a thermal phase transition). At larger values of the cutoff, $\Lambda = 0.4$ (Fig. 3.14b), the regions of high intensity in the structure factor form a connected manifold which is reminiscent of the classical spiral surface. When the cutoff is increased further to $\Lambda = 0.8$ (Fig. 3.14c) the spiral surface becomes thicker and the intensity distribution within the spiral surface is much more uniform, i.e. the fluctuation induced intensity modulation becomes weaker. For the interpretation of these findings we recall that the cutoff scale can be

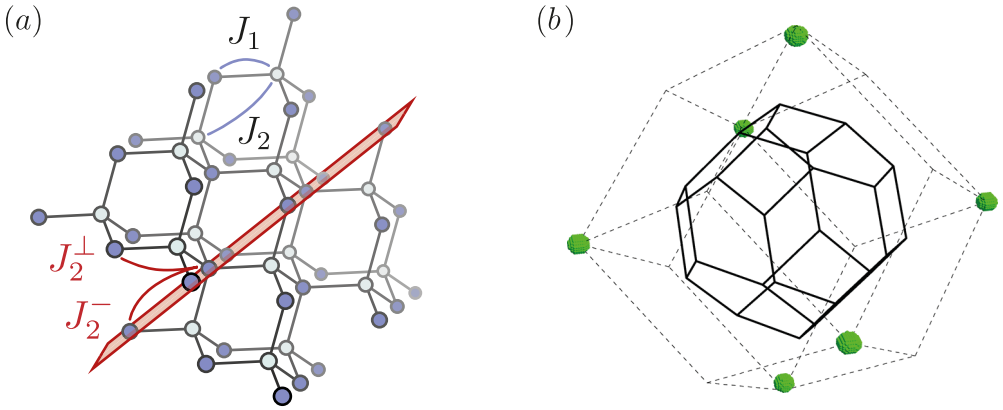

Figure 3.15. **Effect of tetragonal deformation.** (a) A tetragonal deformation in the diamond lattice is defined by the deformation plane indicated in red. Lattice axes that lie within the plane are left invariant under the deformation, while the direction orthogonal to the plane is shortened or elongated. As a consequence, the global next-nearest neighbor coupling J_2 splits into couplings J_2^- that lie within the plane and out-of-plane couplings $J_2^\perp$. The nearest neighbor coupling remains universal since all nearest neighbor lattice bonds have equal components parallel to the deformation axis. (b) Structure factor of the magnetically ordered ground state which is obtained from the set of coupling constants determined via ab-initio calculations (see text for details). Pronounced peaks at the corners of the extended Brillouin zone, that is indicated by dashed lines, signal Néel order.

re-interpreted as a temperature via a linear rescaling [36, 97]. With this perspective we confirm earlier findings in the classical model [87] and in the spin-5/2 spinel material $MnSc_2S_4$ [88], reporting that the selection of individual momentum points at low temperatures is dominant (possibly strong enough to induce magnetic long range order), but at higher temperatures the full spiral surface re-appears.

3.1.4 Application to $NiRh_2O_4$. Finally, we discuss the implications for the spin-1 spinel material $NiRh_2O_4$ whose recent synthesis is a key motivation to generalize the underlying theory to arbitrary spin lengths, covering also spin-1. Due to the short spin length there is reason to hope that strong quantum fluctuations may stabilize a quantum spin liquid ground state. Indeed, no signs of magnetic order have been reported down to temperatures as low as 0.1K [92], which is in line with the predictions of our minimal model for a broad range of coupling constants. It is arguable, however, that the minimal Hamiltonian (3.1), which includes only Heisenberg-like nearest neighbor and next-nearest neighbor interactions, may not be sufficient to fully capture all mechanisms at play in $NiRh_2O_4$ since the material has been reported to undergo a structural phase transition from cubic to tetragonal symmetry at temperatures around 400K, which implies that at relevant temperature scales far below the transition point the exchange constants do not necessarily need to be isotropic. The crystal symmetry allows for a splitting between couplings that lie within the tetragonal deformation plane and couplings that are out of plane, as illustrated in Fig. 3.15.

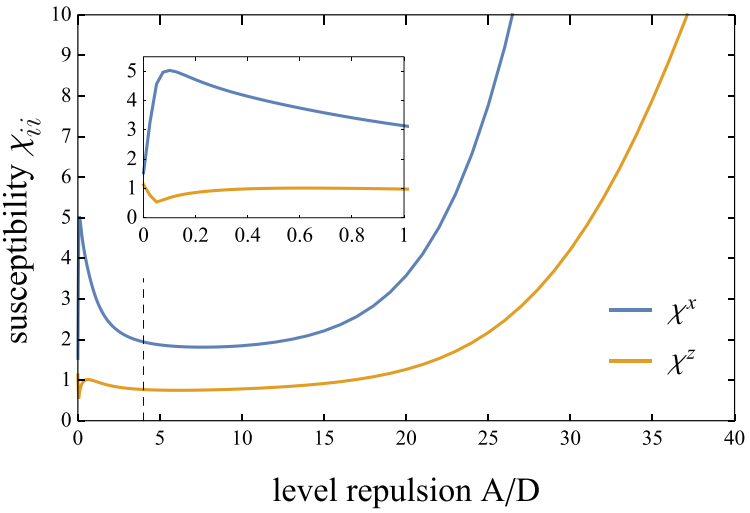

Figure 3.16. **Single ion anisotropy.** The figure shows the susceptibility measurement for a single spin-1 moment with S^z anisotropy complemented by a level repulsion term. The plateau around $4 \lesssim A/D \lesssim 10$ suggests that in this range the result is largely independent of the level repulsion term. At lower values for A/D the unphysical singlet state contributes significantly, while at larger values for A/D numerical errors spoil the result.

On the basis of ab-initio calculations, it has been suggested that the splitting between in-plane and out-of-plane interactions is remarkably strong, effectively resulting in next-nearest neighbor couplings of opposite sign, $J_1 = 2.2$ meV, $J_2^- = 1.6$ meV, and $J_2^\perp = -2.0$ meV [102]. These numbers, however, are based on density functional theory calculations close to their limiting resolution and must therefore be interpreted with caution. Using these numbers in our pf-FRG simulations, we find strong peaks in the structure factor at the corners of the extended Brillouin zone, indicating a Néel ordered ground state (see Fig. 3.15b).

This apparent mismatch between model calculations and the experimentally observed paramagnetic state indicates that our theory cannot be complete. One possible aspect which has not been included so far is the potential appearance of a local spin anisotropy term, which is allowed by symmetry in the tetragonally deformed model [103]. We therefore extend the minimal model to obtain the Hamiltonian

$$H = J_1 \sum_{\langle i,j\rangle} \mathbf{S}_i\mathbf{S}_j + J_2^- \sum_{\langle\langle i,j\rangle\rangle^-} \mathbf{S}_i\mathbf{S}_j + J_2^\perp \sum_{\langle\langle i,j\rangle\rangle^\perp} \mathbf{S}_i\mathbf{S}_j + D\sum_i S_i^z S_i^z - A\sum_i \mathbf{S}_i\mathbf{S}_i \quad , \quad (3.5)$$

where $\langle\langle i,j\rangle\rangle^-$ and $\langle\langle i,j\rangle\rangle^\perp$ denote summations over all next-nearest neighbors within the deformation plane and out of plane, respectively. We have added the local spin anisotropy of strength D which is complemented by a level repulsion term A that is required for technical reasons [38]: since the spin-1 generalization of pf-FRG constructs the spin-1 Hilbert space from two copies of spin-1/2 Hilbert spaces, one needs an additional constraint to ensure that all copies of spin-1/2 moments align ferromagnetically, effec-

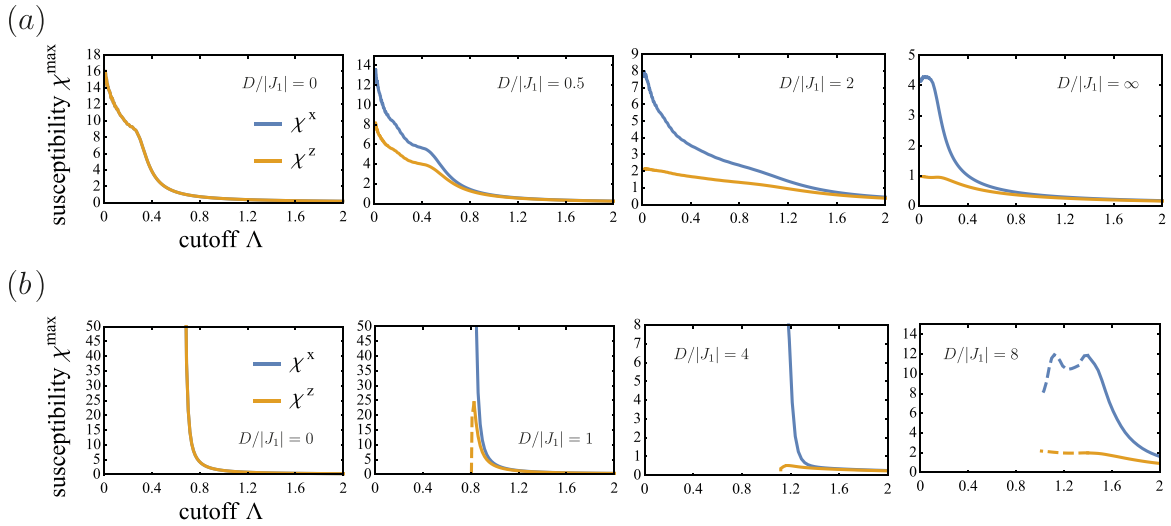

Figure 3.17. **Renormalization group flow with local spin anisotropy.** This figure shows the renormalization group flow for selected values of the local spin anisotropy D at fixed ratio $A/D = 4$. (a) The calculations are performed for the diamond lattice without a tetragonal deformation at $J_2/|J_1| = 0.73$. The transition into a featureless paramagnet (i.e. the $D \to \infty$ limit) is observed at $D/|J_1| \approx 2$. (b) In the presence of tetragonal deformation at exchange constants predicted by ab-initio calculations (see text for details) the Néel ordered state persists even to large values of the local spin anisotropy, indicated by the flow breakdown.

tively forcing the system into triplet states – while the unphysical singlet state in this construction is suppressed energetically by the level repulsion term (see also the discussion of the spin-S generalization of the pf-FRG framework in Sec. 2.5.5). The strength of the level repulsion term that is necessary to constrain the system to the physical sector of the Hilbert space can be determined by considering a single, anisotropic spin. The resulting local spin correlation of the single spin should in principle be independent of the level repulsion term, given that the spin remains in its physical configuration space. In practice, however, if the level repulsion term is chosen too large it can cause numerical artifacts that result from the introduction of a new, larger energy scale, which is not optimally resolved in the logarithmic discretization scheme of the underlying Matsubara frequency mesh. We find that there exists a range $4 \lesssim A/D \lesssim 10$, where the result is independent of the level repulsion term, see Fig. 3.16.

Keeping the ratio $A/D = 4$ fixed, we investigate the impact of the additional spin anisotropy term on the ground state of the tetragonally deformed diamond lattice model (3.5). Benchmarking the stability of the quantum spiral liquid in the diamond lattice in the absence of deformation we find that at $J_2/|J_1| = 0.73$ (which is the ratio of J_2^- and J_1 as suggested by ab-initio calculations) the system transitions from the quantum spiral spin liquid into a featureless paramagnet at a local anisotropy of $D/|J_1| \approx 2$, see Fig. 3.17a. This transition is in accordance with estimates based on mean-field theory calculations [103]. In the tetragonally deformed diamond model, with the set of coupling constants obtained from ab-initio calculations, however, the magnetically

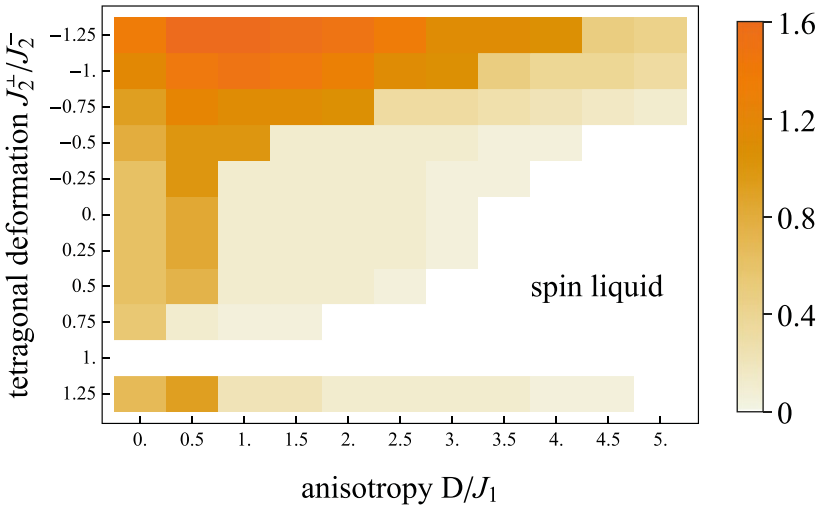

Figure 3.18. **Effect of tetragonal deformation.** The phase diagram of the tetragonally deformed diamond model with local spin anisotropy (3.5) obtained by varying the strength of the local spin anisotropy D and the strength of the next-nearest neighbor couplings $J_2^\perp/J_2^-$ (as a measure for the deformation) distinguishes regions of magnetic order and paramagnetic ground states. The color code indicates the RG breakdown scale Λ_c; a finite value indicates the onset of magnetic order, while a vanishing breakdown scale signals the absence of magnetic long-range order in the ground state.

ordered ground state is much more robust, with magnetic order persisting up to values of the spin anisotropy of $D/|J_1| \approx 8$.

Since the local spin anisotropy has not been included in the ab-initio theory for $NiRh_2O_4$, it is possible that upon inclusion of potential anisotropies the overall resulting parameter set is subject to change. In order to obtain an estimate for the interplay of tetragonal deformation and local spin anisotropy it is instructive to compute the ground state phase diagram as a function of the splitting of next-nearest neighbor interactions and the spin anisotropy. To this end, we fix the nearest neighbor and the in-plane next-nearest neighbor interaction at $J_2^-/|J_1| = 0.73$. Variation of $J_2^\perp$ and D obtains the phase diagram displayed in Fig. 3.18, where a finite critical RG cutoff scale Λ_c indicates the onset of magnetic order. The phase diagram reveals that in the absence of a local spin anisotropy a magnetic ordering transition is observed for arbitrary tetragonal deformation $J_2^\perp/J_2^- \neq 0$ – which corresponds to the classical result where the spiral surface is also found to be unstable under tetragonal deformations. Yet, at moderate values of the local anisotropy, the quantum spiral spin liquid regime becomes robust against finite tetragonal deformations.

Recent ab-initio calculations, in contrast to the first set of coupling constants which we have discussed in this chapter, report a vanishing effect of the tetragonal deformation on the coupling constants, $J_1 \approx 1.2$ meV and $J_2^- \approx J_2^\perp \approx 0.5$ meV [104]. With a ratio of $J_2/J_1 \approx 0.4$ these parameters are well located in the quantum spiral spin liquid regime, which is compatible with experimental observations of the absence of magnetic

long-range order.

3.1.5 Summary. In this section, we have discussed a minimal model of quantum spins on the diamond lattice where frustration is generated by antiferromagnetic next-nearest neighbor interactions. The classical analogue of the model had been shown to provide a good description of the spin-5/2 spinel material $MnSc_2S_4$, whose physics is governed by the presence of a sub-extensively degenerate spin spiral surface. The degeneracy of the spiral surface is lifted in the presence of thermal fluctuations, giving way to a magnetically ordered ground state. We have studied the full quantum model with a particular focus on spin-1 systems where we have shown that quantum fluctuations prevent the formation of magnetic long-range order. We dubbed the resulting ground state a quantum spiral spin liquid because it exhibits spin correlations that are reminiscent of the spin spiral surface in the classical model above the ordering transition. In view of the recent synthesis of the spin-1 spinel compound $NiRh_2O_4$ which has been reported not to order magnetically down to a temperature of 0.1K, we discussed the impact of tetragonal lattice deformations on the quantum spiral spin liquid. We have seen that the quantum spiral spin liquid is unstable towards such deformations, but we argued that a finite local spin anisotropy can stabilize the spin liquid. To further assess the suitability of our model calculations for $NiRh_2O_4$, one might perform neutron diffraction experiments on the material to reveal whether the paramagnetism is indeed driven by a quantum spin spiral surface, or if the paramagnetic state is trivial.

3.2. Magnetic order from Kitaev interactions

Whenever we formulate a spin model of localized magnetic moments, the description is only an approximation of the underlying electronic degrees of freedom. The electrons, which carry the spin degree of freedom, are in principle mobile and it requires additional correlation driven effects to localize them and turn them into (Mott) insulators. Even richer physics arises when large electronic correlations concur with strong spin-orbit coupling [68]. Among such spin-orbit entangled Mott insulators the family of materials with partially filled 4d or 5d orbitals has aroused particular interest – similar energy scales of crystal field splitting, spin-orbit coupling, and electronic correlations can give rise to effective local $j = 1/2$ moments [62]. Iridates, where the elementary building block IrO_6 is an iridium ion enclosed by an octahedral cage of oxygen atoms, fall into this category and can give rise to qualitatively different interactions depending on the arrangement of the octahedra; in corner-sharing arrangements the isotropic Heisenberg interaction is dominant, while edge-sharing octahedra are likely to have strongly anisotropic, bond-directional interactions [105].

In this section, which is based on our results as presented in Ref. [P5], we address the physics of Ba_2CeIrO_6 where the effective $j = 1/2$ moments on the iridium sites form a face-centered cubic (fcc) lattice. Ab-inito calculations on the compound suggest that the material has dominant Heisenberg nearest neighbor interactions J_1 which are accompanied by subdominant next-nearest neighbor couplings $J_2 \approx 0.2J_1$ and nearest neighbor Kitaev interactions $K \approx 0.2J_1$. Additional non-diagonal couplings $\Gamma \lesssim 0.05J_1$ are found to be negligible [P5]. This set of interaction constants implies two different mechanisms of frustration: firstly, the fcc lattice is geometrically frustrated in the presence of antiferromagnetic nearest neighbor interactions due to a triangular motif in the the lattice structure, while, secondly, competing Kitaev couplings generate additional exchange frustration. Indeed, Ba_2CeIrO_6 is found to have a large frustration parameter (see below for details) of $f > 13$, which is usually considered as 'highly frustrated' [106]. Yet, despite the large frustration, the material has been reported to have a magnetically ordered ground state [107].

In the remainder of this section we formulate a minimal model to discuss the interplay of relevant couplings in Ba_2CeIrO_6 and determine its ground state phase diagram. We analyze the frustration parameter and its dependence on the different interaction terms to elucidate the interplay of geometric frustration and exchange frustration. Finally, we review the role of tetragonal deformations in Ba_2CeIrO_6 and their impact on the type of ground state order.

3.2.1 Minimal model. Guided by ab-initio calculations, we formulate a minimal model that includes isotropic nearest and next-nearest neighbor Heisenberg interactions J_1 and J_2, respectively, which are augmented by bond-directional Kitaev interactions K. The Hamiltonian therefore reads as

$$H = J_1 \sum_{\langle i,j \rangle} \mathbf{S}_i \mathbf{S}_j + J_2 \sum_{\langle\langle i,j \rangle\rangle} \mathbf{S}_i \mathbf{S}_j + K \sum_{\langle i,j \rangle_\gamma} S_i^\gamma S_j^\gamma \quad , \tag{3.6}$$

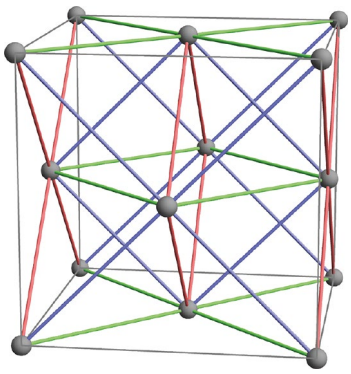

Figure 3.19. **Fcc lattice** with bond-directional couplings. The fcc lattice has a large coordination number of 12 nearest neighbors that we consider to interact via Heisenberg and Kitaev exchange couplings. The x, y, and z component of the Kitaev coupling is defined within the plane that is perpendicular to the x, y, and z direction, respectively. The three different Kitaev couplings are indicated by bond color, where red, green, and blue correspond to x, y, and z-type interaction.

where the expression $\langle i,j\rangle$ denotes a sum over nearest neighbors, $\langle\langle i,j\rangle\rangle$ is a summation over next-nearest neighbors and the index $\gamma = x, y, z$ indicates the bond type as defined in Fig. 3.19. The x, y, and z components of the bond-directional Kitaev couplings are defined in the planes that are orthogonal to the respective directions.

This model has an intimate connection to the one we discussed in the previous Section 3.1, where frustrated Heisenberg interactions on the diamond lattice gave rise to quantum spiral spin liquids. Both models coincide if one considers the limit of dominant next-nearest neighbor interactions in the diamond lattice and dominant nearest neighbor interactions in the fcc lattice – this is by construction, since the fcc lattice is a sublattice of the diamond lattice (note also that due to this construction both lattices have the same Brillouin zone). On the level of classical spins the spiral surface of the diamond model – which in the limit of dominant next-nearest neighbor couplings reduces to a cross-like shape on the quadratic surface plaquettes of the Brillouin zone – must therefore also appear in the fcc lattice, see Fig. 3.20b. The decisive difference between the diamond model and the fcc model becomes apparent once we include further neighbor interactions; while in the diamond lattice the spiral surface continuously evolved upon tuning the coupling ration J_2/J_1, in the fcc lattice the sub-extensively degenerate spiral surface is immediately destabilized and reduces to a discrete set of points upon including interactions beyond nearest-neighbors. Nevertheless, one can find a fine-tuned point in the fcc model at $J_2/J_1 = 1/2$ where the classical ground state reaches a particularly high level of degeneracy signaled by the formation of a two-dimensional spiral surface shown in Fig. 3.20c.

We study the model Hamiltonian (3.6) for quantum spin-1/2 moments by performing pf-FRG calculations that are analogous to the calculations outlined in the previous section. While classical spins favor a magnetically ordered ground state for any combination

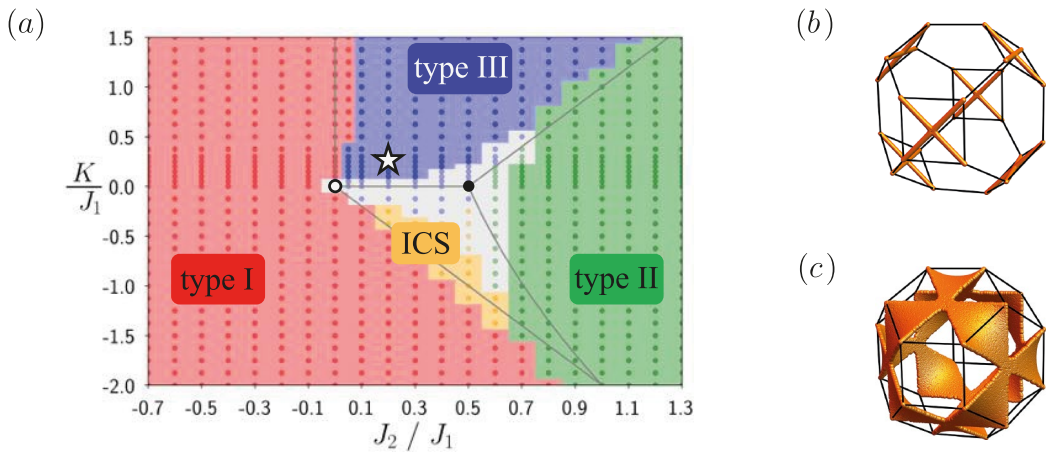

Figure 3.20. **Phase diagram** of the Heisenberg-Kitaev model on the fcc lattice. (a) The phase diagram is dominated by three types of commensurate magnetic order with ordering vectors (100), $(\frac{1}{2}\frac{1}{2}\frac{1}{2})$, and $(1\frac{1}{2}0)$, labeled type I, type II, and type III order. They are accompanied by a fourth phase of incommensurate spiral order, indicated by the yellow region. The paramagnetic region is indicated by the gray shaded area, where the color of the individual data points denotes the dominant type of correlations. The gray lines denote phase boundaries of the analogous classical model. The white and black circles denote points of high classical ground state degeneracy with their spiral surfaces visualized in subplots (b) and (c), respectively. The star denotes an estimate for the interaction parameters in Ba_2CeIrO_6, which is obtained from ab-initio calculations.

of coupling constants, when promoting the classical spins to quantum moments (and neglecting the Kitaev interaction $K = 0$ for a moment) a small paramagnetic region nucleates around the high degeneracy point $J_2/J_1 = 1/2$, see the phase diagram in Fig. 3.20a. Therefore, this model constitutes a second example (besides the diamond model) where a particularly large classical ground state degeneracy leads to the emergence of a paramagnetic phase in the corresponding quantum model. The same mechanism has also been demonstrated to function in the hcp lattice or even in two-dimensional honeycomb lattice [38, 94]. The paramagnetic ground state persists for moderate antiferromagnetic contributions in the range $0 \leq J_2/J_1 \lesssim 0.6$. If the next-nearest neighbor interactions are ferromagnetic the system transitions into a magnetically ordered ground state of type I, which is characterized by the ordering wave vector (100). If, on the other hand, next-nearest neighbor interactions are antiferromagnetic and become more sizable the system seeks magnetic order of type II, characterized by the wave vector $(\frac{1}{2}\frac{1}{2}\frac{1}{2})$. Note that both of these ordered phases are well known from the classical limit [100], and their phase boundaries are similar in the quantum model and in the classical model. The real space structure of type I order is such that spins within each of the four simple cubic (sc) sublattices of the fcc structure align ferromagnetically under the constraint that the combined spin of all sublattices vanishes (c.f. Fig. 3.21). Interpreting the fcc lattice as a network of edge sharing tetrahedra, the constraint is equivalent to vanishing

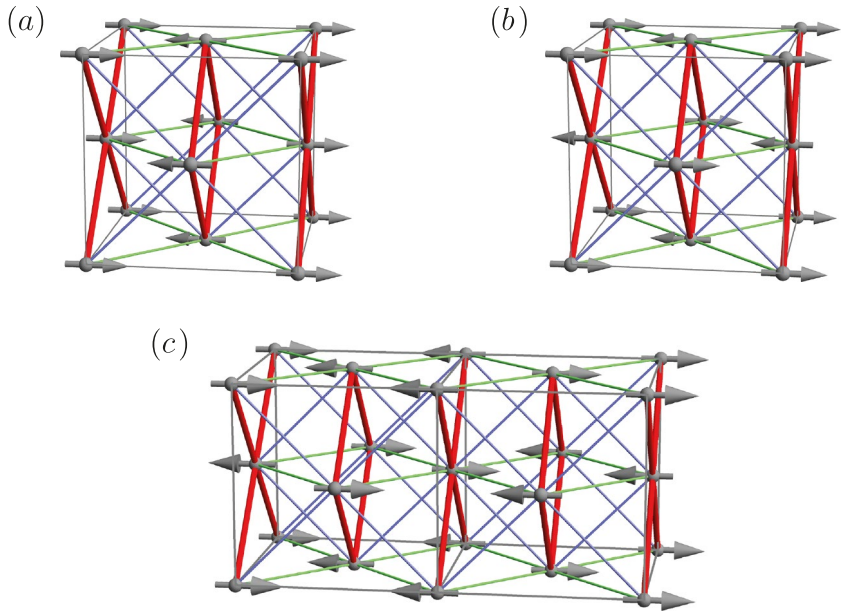

Figure 3.21. **Kitaev interactions and magnetic order.** Bond-directional Kitaev interactions in the fcc lattice are defined such that a single Kitaev channel effectively couples spins within stacked square lattices, while inter-plane couplings are given by the other two Kitaev channels. Since in magnetic order of type I the four ferromagnetically ordered sc sublattices can be rotated independently – under the constraint that the total spin on every tetrahedron vanishes –, the configuration is compatible (i.e. its energy is lowered even further) with both, (a) ferromagnetic and (b) antiferromagnetic Kitaev interactions by forming a collinear spin configuration. Exchange energy from the Kitaev interactions is then gained on the bonds indicated in red, while couplings along the remaining bonds do not contribute. (c) Magnetic order of type III, by a similar construction, is compatible with antiferromagnetic Kitaev interactions.

total spin on every tetrahedron in the lattice. It is therefore natural that ferromagnetic next-nearest neighbor interactions, which act within the sc sublattices, further stabilize type I magnetic order. Type II magnetic order implies that each sc sublattice orders antiferromagnetically. Naturally, this type of magnetic order is further stabilized in the presence of dominant antiferromagnetic next-nearest neighbor interactions.

Upon inclusion of finite Kitaev interactions it is possible to stabilize two additional magnetically ordered phases: antiferromagnetic Kitaev interactions favor magnetic order of type III with the ordering vector $(1\frac{1}{2}0)$ over a broad parameter regime. In the case of ferromagnetic Kitaev interactions there exists a small parameter window where incommensurate spiral order manifests as the ground state of the system. Over large parts of the phase diagram, however, Kitaev interactions seem to favor magnetic order of type I (Fig. 3.20). The role of Kitaev interactions in the fcc lattice – acting as stabilizer for magnetically ordered phases – may be counter-intuitive since often Kitaev interactions are associated with the (generalized) Kitaev honeycomb model on tricoordinate lattices where they generate strong exchange frustration that leads to a Kitaev spin liquid ground state. Yet, we shall point out that Kitaev couplings on the fcc lattice have

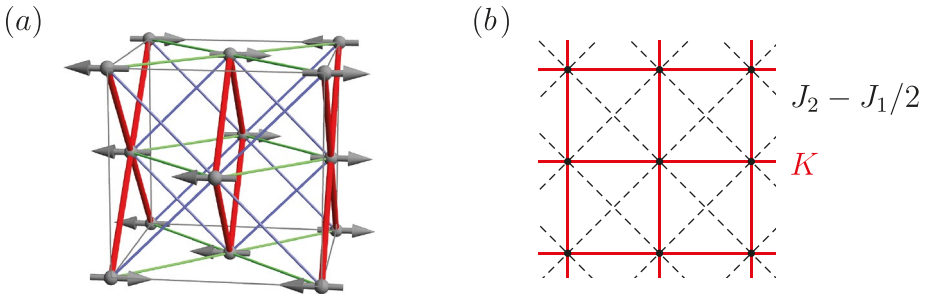

Figure 3.22. **Kitaev interactions and type II magnetic order.** (a) Type II magnetic order implies Néel order on the four simple cubic sublattices of the fcc lattice. It is incompatible with Kitaev interactions in the sense that their presence cannot further lower the energy of the configuration. (b) The quasi two-dimensional planes defined by the Kitaev interactions form square lattices with effective nearest neighbor interactions set by K and next-nearest neighbor interactions of strength $J_2 - J_1/2$ (see text for details). Note that this is a simplified picture for collinear spin configurations where all couplings are effectively Ising-like.

a decisively different structure than on tricoordinate lattices: in the limit of anisotropic Kitaev exchange, where the coupling is non-zero and Ising-like e.g. only along x-bonds, tricoordinate lattices decompose into quasi one-dimensional spin pairs, while the fcc lattice decouples into quasi two-dimensional square lattices with Ising-like in-plane coupling, c.f. Fig. 3.21. And indeed, in the classical Kitaev model on the honeycomb lattice it is known that the ground state is a dimer configuration where individual pairs of neighboring spins maximize their exchange energy by aligning with the local Ising axis [108] – similarly, in the quantum Kitaev model spin-spin correlations are non-zero only for nearest neighbors [109]. Postulating an analogous mechanism in the fcc lattice, i.e. spins aligning either in x, y, or z direction to maximize one of the Kitaev interaction channels, results in quasi two-dimensional magnetic long-range order. Furthermore, this long-range order is fully compatible with magnetic order of type I (for ferromagnetic or antiferromagnetic Kitaev interactions, see Fig. 3.21a–b) and with type III magnetic order (for antiferromagnetic Kitaev interactions, see Fig. 3.21c). It is, however, incompatible with type II magnetic order. Comparison of the classical phase phase diagram and the quantum phase diagram (Fig. 3.20) shows that this intuition about classical spin configurations does carry over to the quantum model, where at dominant Kitaev interaction the phases of type I and type III magnetic order are the preferred ground state, while magnetic order of type II is suppressed.

3.2.2 Frustration parameter. Similar to our thoughts on the interplay between Kitaev interactions and magnetic order of type I and III, respectively, we can gain an intuition about type II magnetic order by envisioning the corresponding classical spin configuration and considering additional Kitaev interactions on a perturbative basis. The incompatibility of Kitaev interactions with type II magnetic order (in the sense of the previous discussion) goes back to the Néel order in the simple cubic sublattices which is the defining property of type II magnetic order on the fcc lattice (Fig. 3.22a).

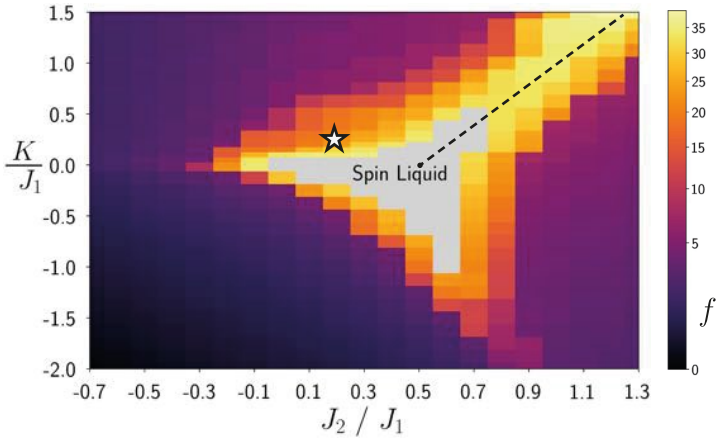

Figure 3.23. **Frustration parameter** of the Heisenberg-Kitaev model on the fcc lattice. The value of the frustration parameter $f = |\theta_{\mathrm{CW}}|/T_c$ is displayed by the color code. The frustration parameter diverges in the spin liquid phase (gray region), where $T_c = 0$. The star denotes an estimate for the interaction parameters in Ba_2CeIrO_6, obtained from ab-initio calculations. The dashed line denotes points which fulfill the relation $K/J_1 = 2J_2/J_1 - 1$ (see text for details).

Envisioning a collinear configuration which maximizes one component of the Kitaev coupling obtains a quasi two-dimensional square lattice model where antiferromagnetic next-nearest neighbor interactions are stabilized by type II magnetic order and nearest neighbor interactions are mediated by the Kitaev terms (Fig. 3.22b).

In the discussion of the ground state phase diagram we have stated that in the classical limit type II magnetic order in the fcc lattice is stabilized by nearest and next-nearest neighbor interactions at a ratio of $J_2/J_1 > 1/2$. One can assume that the 'excess' energy $J_2 - J_1/2$ beyond the transition point is a good measure for the stability of the magnetic order, with energy gains by next-nearest neighbor interactions in the quasi two-dimensional planes, while the scale for nearest neighbor interactions is set by the Kitaev interaction K (as depicted in Fig. 3.22b). It is known for the square lattice that strong frustration is achieved when the ratio of antiferromagnetic next-nearest neighbor interactions and nearest neighbor interactions is 1/2 [14]. Hence, based on the picture of quasi two-dimensional planes in the Kitaev-Heisenberg fcc model, we may expect large frustration along the line defined by $K/J_1 = 2J_2/J_1 - 1$, which happens to coincide with the classical phase boundary of magnetic type II order.

Indeed, we shall see that this expectation also holds in the quantum model. In order to estimate the level of frustration we compute the frustration parameter

$$f = \frac{|\theta_{\mathrm{CW}}|}{T_c} \quad , \tag{3.7}$$

where T_c is the transition temperature in the magnetically ordered ground state and θ_{CW} is the Curie-Weiss temperature. In pf-FRG calculations, due to the linear relation

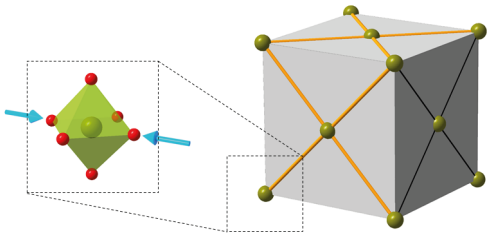

Figure 3.24. **Tetragonal deformation** in Ba_2CeIrO_6. Every magnetic moment in the effective spin model on the fcc lattice (right panel) arises from the interplay of electronic correlations, spin-orbit coupling, and the crystal field of the octahedral oxygen cage surrounding the iridium atoms (left panel). Altering the crystal field by a tetragonal deformation of the oxygen cage, as indicated by the arrows, results in a splitting of interaction constants in the effective model into in-plane couplings (black lattice bonds) and out-of-plane couplings (yellow bonds) with respect to the defining plane of the tetragonal deformation.

between temperatures and frequency cutoff values, the frustration parameter can be estimated from the ratio $|\Lambda_{\mathrm{CW}}|/\Lambda_c$, where Λ_c is the breakdown scale of the RG flow and Λ_{CW} is obtained from fitting the Curie-Weiss behavior of the susceptibility $\chi = C/(\Lambda - \Lambda_{\mathrm{CW}})$ [33, 36].

The values of the frustration parameter as a function of nearest neighbor Kitaev coupling K/J_1 and next-nearest neighbor Heisenberg coupling J_2/J_1 are shown in Fig. 3.23. The frustration parameter is naturally large near the boundary of the spin liquid region since per definition it diverges inside the spin liquid phase. However, the parameter window in which the frustration parameter remains large near the phase boundary is only small – with the exception of points near the line $K/J_1 = 2J_2/J_1 - 1$, where we anticipated a strong competition between Heisenberg interactions and Kitaev terms. Therefore, along that line the frustration parameter generally remains large.

3.2.3 Application to Ba_2CeIrO_6. Let us now return to our initial motivation to study the Heisenberg-Kitaev model on the fcc lattice and discuss the implications on Ba_2CeIrO_6. Based on the exchange constants as determined in ab-initio calculations, $J_2 \approx 0.2J_1$ and $K \approx 0.2J_1$ [P5], we find that the minimal model (3.6) supports large frustration values $f > 13$ as determined in experiment. However, in neutron scattering experiments Ba_2CeIrO_6 has been found to exhibit type I magnetic order in the ground state while the minimal model predictes type III order. In order to reconcile the experimental observation with our theory, we note that Ba_2CeIrO_6 due to lattice defects potentially suffers from local tetragonal lattice distortions which are statistically distributed [P5]. In the presence of such local lattice distortions the crystal field of the oxygen cage around the iridium ions is altered, yielding modified exchange constants in the spin model. The coupling constants under the influence of tetragonal lattice deformations may split into components that lie within the deformation plane and out of plane, see Fig. 3.24.

Although we cannot study local distortions within our pf-FRG analysis, we can nev-

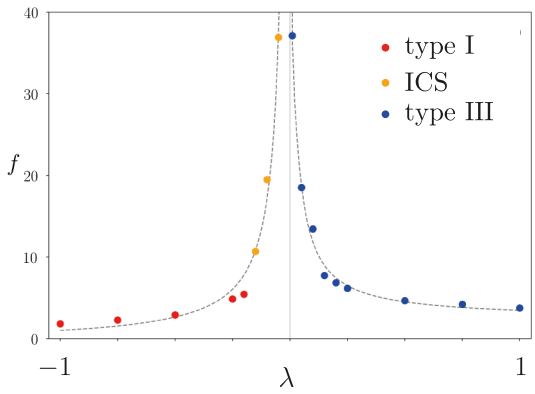

Figure 3.25. **Frustration parameter** in the presence of tetragonal deformation. Finite tetragonal distortion quickly suppresses the frustration parameter while simultaneously altering the magnetic ground state order. Depending on the strength of the deformation the ground state exhibits magnetic order of type I or type III, or it is an incommensurate spiral configuration, as indicated by the color of the data points.

ertheless extend the minimal model to capture a global tetragonal distortion. To this end, we extend the minimal model to discriminate between in-plane and out-of-plane interactions

$$H = \sum_{\langle i,j\rangle^\alpha} J_1^\alpha(\lambda)\mathbf{S}_i\mathbf{S}_j + \sum_{\langle\langle i,j\rangle\rangle^\alpha} J_2^\alpha(\lambda)\mathbf{S}_i\mathbf{S}_j + \sum_{\langle i,j\rangle_\gamma^\alpha} K^\alpha(\lambda)S_i^\gamma S_j^\gamma \quad , \tag{3.8}$$

where α discriminates in-plane couplings ($\alpha = -$) and out-of-plane couplings ($\alpha = \perp$) and the exchange constants now depend on the strength of the tetragonal deformation λ. We model the coupling constants such that at zero deformation $\lambda = 0$ we obtain the original model with the coupling constants predicted by ab-initio calculations, $J_1 = 1$, $J_2 = 0.2$, and $K = 0.2$. At deformation $\lambda = 1$, the in-plane couplings are $J_1^- = 2$, $J_2^- = 1.2$, and $K^- = 1.2$, while the out-of-plane couplings equal $J_1^\perp = 0.6$, $J_2^\perp = 0.7$, and $K^\perp = 0.8$. At intermediate splittings, the exchange constants are interpolated linearly. We assume the deformation to be symmetric, such that at negative sign of the deformation the in-plane couplings are weakened, while out-of-plane couplings are enhanced. The relative strength of coupling constants and the strength of the deformation is estimated based on measurements of the crystal field induced level splitting in Ba_2CeIrO_6, obtained in resonant inelastic X-ray scattering (RIXS) [P5]. The deformation parameter $\lambda = \pm 1$ corresponds to the values obtained experimentally (for local deformations).

Analyzing the extended Hamiltonian (3.8) as a function of the global tetragonal deformation, we find that the frustration parameter is strongly suppressed once the cubic lattice symmetry is broken. Already at $\lambda \approx 0.25$ the frustration parameter is approaching the regime $f \lesssim 5$ where magnets are generally no longer considered as frustrated, see Fig. 3.25. For $\lambda < 0$, the suppression of the frustration parameter is accompanied by a change of the magnetic ground state order to an incommensurate spiral state for

$-0.25 \lesssim \lambda < 0$ and to type I magnetic order for larger deformation $\lambda \lesssim -0.25$. These results suggest that the statistical distribution of local deformations may play an important role in recovering the large frustration parameter $f > 13$ determined in experiment – while the frustration parameter is strongly suppressed by a global deformation, the suppression may be less severe for local deformations. Moreover, we have seen qualitatively that a tetragonal deformation can favor magnetic ground state order of type I, which has been measured in Ba_2CeIrO_6.

3.2.4 Summary. In this section, we have discussed a minimal model of competing antiferromagnetic nearest and next-nearest neighbor Heisenberg interactions of the fcc lattice. We have seen that a particularly large classical ground state degeneracy can be achieved at the fine-tuned point $J_2/J_1 = 1/2$, around which a paramagnetic ground state nucleates in the quantum model. We have augmented the model with additional nearest-neighbor Kitaev interactions as an additional source of frustration. We have reviewed the interplay between the different types of exchange frustration generated from Heisenberg interactions and Kitaev interactions, respectively, and found that in large parts of the phase diagram both mechanisms are generally compatible and do not lead to an unusual increase in the frustration parameter. We did, however, point out a special set of parameters where the frustration mechanisms play against each other and further enhance the overall frustration. Guided by experiments and ab-initio calculations we have discussed the applicability of the model to the $j = 1/2$ iridate compound Ba_2CeIrO_6. We concluded, based on simulations of a global tetragonal lattice, that statistically distributed local lattice distortions may play an important role in the phenomenology that has been observed in experiments.

3.3. Dzyaloshinskii-Moriya interactions in herbertsmithite

Material realizations of the spin-1/2 kagome antiferromagnet are thought to be among the most promising models in frustrated magnetism to give rise to a quantum spin liquid ground state [1]. The kagome antiferromagnet has a low coordination number and its classical ground state is highly degenerate; thus, one can expect that quantum fluctuations become sizable. Already early on, it was suggested that the model evades magnetic order in the ground state [110], yet to this day it remains an open question of what the true nature of the ground state is. Over the course of time, many different methods have been employed in the analysis of the kagome antiferromagnet, predicting different candidate ground states. Among these candidates, series expansion techniques predicted a valence bond crystal [111], while fermionic variational wave function calculations suggest a gapless Dirac quantum spin liquid ground state [112]. Early DMRG studies, on the other hand, suggested the formation of a gapped Z_2 quantum spin liquid [113, 114]. Furthermore, it was shown that, unlike fermionic variational wave function calculations, a bosonic variational approach can generate competitive ground state energies also for a Z_2 quantum spin liquid. All these different perspectives (and more) lead to a standoff between the gapped Z_2 spin liquid candidate and the gapless Dirac spin liquid. Recently, however, it was pointed out that the emergence of a Z_2 spin liquid in DMRG calculations may only be an artifact of finite system sizes, and by treating the boundaries carefully one can indeed observe Dirac cones also in DMRG simulations [23].

Vivid research on the pure kagome Heisenberg antiferromagnet (KHAFM) also sparked interest in variations of the original model that include additional interaction terms beyond nearest-neighbor exchange. These generalizations were not only formulated for academic reasons – although insightful, since it is assumed that the spin liquid ground state of the KHAFM is further stabilized by small contributions of antiferromagnetic next-nearest neighbor interactions [114], and a different, unambiguous chiral spin liquid regime can be explored in the KHAFM model that is augmented by second-nearest and third-nearest Heisenberg interactions [29, 30] – but also to match the experimental reality and make predictions for real materials that naturally include deviations from the perfect KHAFM. Unfortunately, only few kagome materials exist that have spin-1/2. Many of the recurrent materials in the field are not ideally suited for cultivating the kagome spin liquid; volborthite and vesignieite, for example, are spatially anisotropic. Kapellasite, despite featuring longer-range exchange terms, has ferromagnetic nearest-neighbor interactions [115]. The hitherto cleanest realization of the KHAFM is found in herbertsmithite [116–118], $ZnCu_3(OH)_6Cl_2$, which retains a perfect three-fold symmetry and is believed to be dominated by antiferromagnetic nearest neighbor Heisenberg interactions. However, sub-dominant perturbations are also present in herbertsmithite and it is thus worthwhile to study the stability of the kagome spin liquid with respect to those additional perturbations. Extended models of the KHAFM with Heisenberg interactions beyond nearest neighbors have previously been analyzed within pf-FRG calculations (among many other techniques) [32, 119, P1].

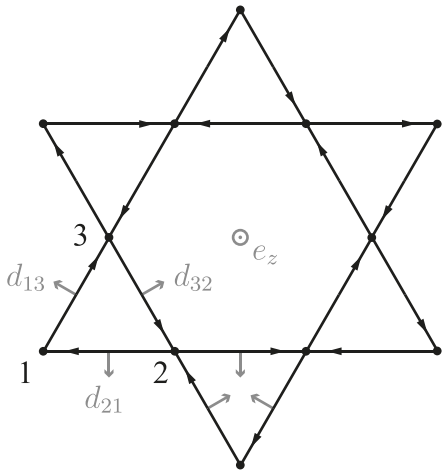

Figure 3.26. **Kagome lattice with Dzyaloshinskii-Moriya interactions.** The sign of the inversion symmetry breaking DM exchange terms $(D\mathbf{e}_z + D'\mathbf{d}_{ij}) \cdot (\mathbf{S}_i \times \mathbf{S}_j)$ is determined on each lattice bond by the black arrows pointing from site i to site j, while the orientation of the DM vectors is indicated by the gray arrows. The DM vectors $\mathbf{d}_{ij}$ are defined differently on up-pointing triangles and down-pointing triangles, reducing the six-fold rotation symmetry to three-fold. The DM vectors have unit length.

In the scope of this chapter, which closely follows our presentation of results as published in Ref. [P6], we focus on a less symmetric type of perturbations, a nearest neighbor Dzyaloshinskii-Moriya (DM) interaction. It is argued that these interactions appear subdominantly in herbertsmithite, accompanying the dominant Heisenberg nearest neighbor exchange [50, 63]. We therefore formulate the model Hamiltonian

$$\sum_{\langle i,j \rangle} J\mathbf{S}_i\mathbf{S}_j + (D\mathbf{e}_z + D'\mathbf{d}_{ij}) \cdot (\mathbf{S}_i \times \mathbf{S}_j) \quad , \tag{3.9}$$

where J is the antiferromagnetic Heisenberg contribution, D is the out-of-plane component of DM interactions, and D' is the in-plane DM component. The orientation of the DM vectors is illustrated in Fig. 3.26.

3.3.1 Out-of-plane DM interactions. Previous studies have analyzed the model at vanishing in-plane DM interactions $D' = 0$, in which case the model is simplified by retaining a spin rotational symmetry around the z-axis. An early implementation of the pf-FRG which was constructed specifically to incorporate the spin rotational symmetry has established that in this simplified model the quantum spin liquid ground state of the unperturbed Heisenberg antiferromagnet remains stable against out-of-plane DM perturbations D up to a ratio of approximately $D/J \approx 0.1$ [39]. In our generalized formulation of pf-FRG (see Sec. 2.3), we perform calculations that use between $N_\omega = 66$ and $N_\omega = 144$ discrete frequency points to approximate the continuous Matsubara frequency space and we incorporate correlations for spins which are up to seven lattice

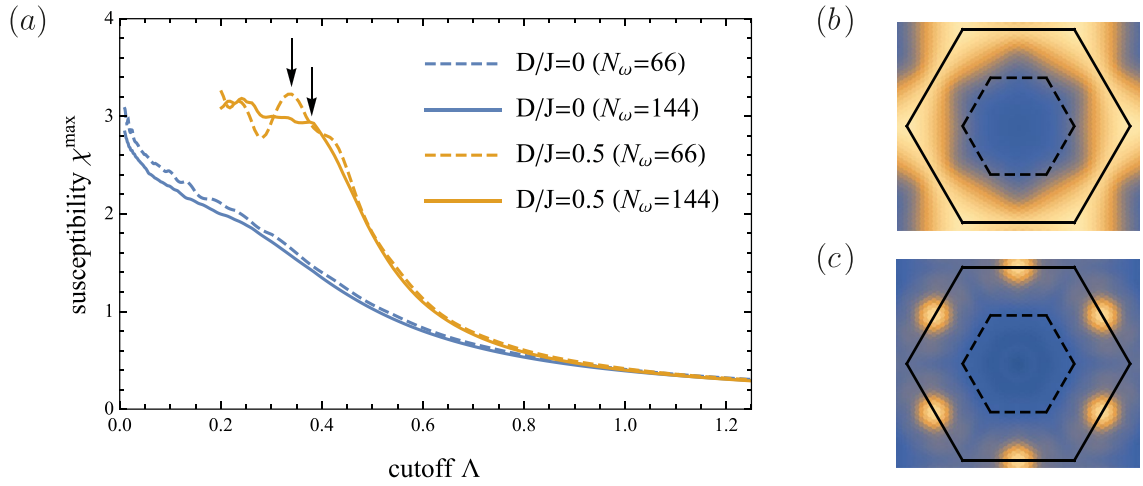

Figure 3.27. **Breakdown scale** of the smooth RG flow. (a) At vanishing DM interactions the kagome antiferromagnet does not show any sign of magnetic long range order, indicated by the absence of a flow breakdown. At sizable out-of-plane DM interaction one finds a flow breakdown at some critical cutoff scale Λ_c, indicated by the black arrows. The breakdown point is resolved sufficiently well at a frequency mesh of $N_\omega = 144$ points, while a lower frequency resolution introduces numerical artifacts in the form of additional oscillations in the flow, making the precise location of the breakdown scale more difficult, c.f. Sec 2.4.2. (b) Structure factor of the unperturbed Heisenberg antiferromagnet. The structure factor is featureless and shows no indication of magnetic order. (c) The structure factor at sizable DM interaction, plotted here at $D/J = 1$, reveals clear peaks at points in momentum space that are associated with $q = 0$ order.

bonds apart. The calculations therefore involve the numerical solution of up to 3.7×10^8 coupled integro-differential equations per set of interaction parameters, see also the discussion of the numerical solution of pf-FRG flow equations in Sec. 2.4.

The pf-FRG simulations allow us to explore the parameter space of D/J and confirm the previous result of a $q = 0$ magnetically ordered ground state at $D/J \gtrsim 0.1$ via the detection of a flow breakdown in the magnetic susceptibility as displayed in Fig. 3.27.

We may also compare our findings to the classical analogue of the model. While the unperturbed classical kagome antiferromagnet features a highly degenerate ground state, whose analysis is a challenge on its own [120–122], any finite DM interaction induces magnetic order of $q = 0$ type [123]. For classical spins the magnetic ground state order at sufficiently large values of D/J is expected to be slightly more robust than in the quantum model, due to the disordering tendency of quantum fluctuations – which manifests in a somewhat lower transition temperature in the quantum model (Fig. 3.28). Note that the finite-temperature phase diagram in pf-FRG calculations is obtained via a linear rescaling of the critical cutoff Λ_c to temperature, $T_c = \frac{\pi}{2}\Lambda_c$ [36], as discussed in Section 2.5.6.

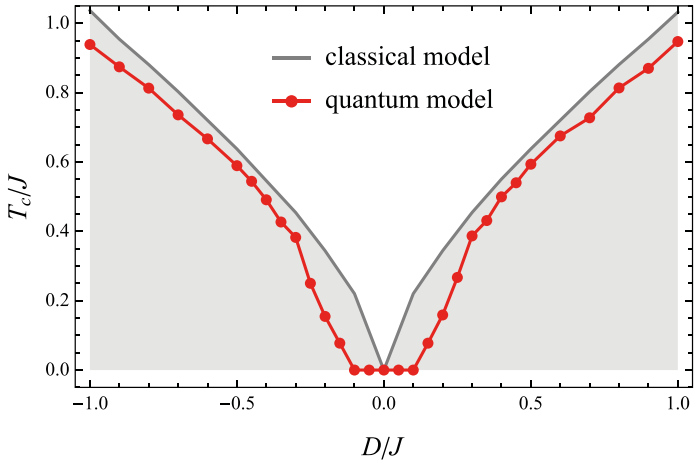

Figure 3.28. **Transition temperature** of the kagome antiferromagnet with additional out-of-plane DM interactions D. The classical model transitions into a magnetically ordered phase for any finite DM interactions while the quantum model remains in a quantum spin liquid ground state for values up to $D/J \approx 0.1$. The classical data is taken from Ref. [123].

3.3.2 In-plane DM interactions. Ultimately, we turn on the in-plane DM interaction D', and we again ask about the stability of the quantum spin liquid phase. We find that the spin liquid phase is very robust against in-plane DM perturbations and remains stable even when the DM interaction is comparable in strength to the Heisenberg exchange, see Fig. 3.29. We have seen before, that if the DM interaction is purely out of plane, the phase diagram is symmetric around $D/J = 0$. This changes mildly in the presence of in-plane DM interactions which introduce a slight bending of the phase boundaries. As a consequence, the spin liquid phase in the presence of finite in-plane DM interaction is most stable around some finite, ferromagnetic out-of-plane contribution D. This trend can also be observed in the classical analogue of the model, with the difference that in the classical model there is a direct transition between the two $q = 0$ magnetically ordered phases – the intermediate quantum spin liquid phase does not have a classical analogue. Classically, the two magnetically ordered phases can be distinguished by the sign of their scalar spin chirality $\chi_{ijk} = \mathbf{S_i} \cdot (\mathbf{S_j} \times \mathbf{S_k})$ – unfortunately, we cannot access this quantity in pf-FRG calculations. Since the chirality is a three-spin operator which explicitly breaks time-reversal symmetry it significantly increases the computational complexity of the flow equations to a level that is beyond current pf-FRG implementations, see the discussion of computational complexity in pf-FRG simulations in Sec. 2.4.4.

3.3.3 Application to herbertsmithite. An estimate for the strength of DM interactions in herbertsmithite has been obtained in electron spin resonance measurements, which suggest a leading out-of-plane component $D/J \approx 0.08$ complemented by weak in-plane interactions $D'/J \approx 0.01$ [63]. Other model calculations around thermodynamic properties of herbertsmithite report similar out-of-plane DM interactions but significantly stronger in-plane interactions up to $D'/J \approx 0.3$ [50]. We have established by

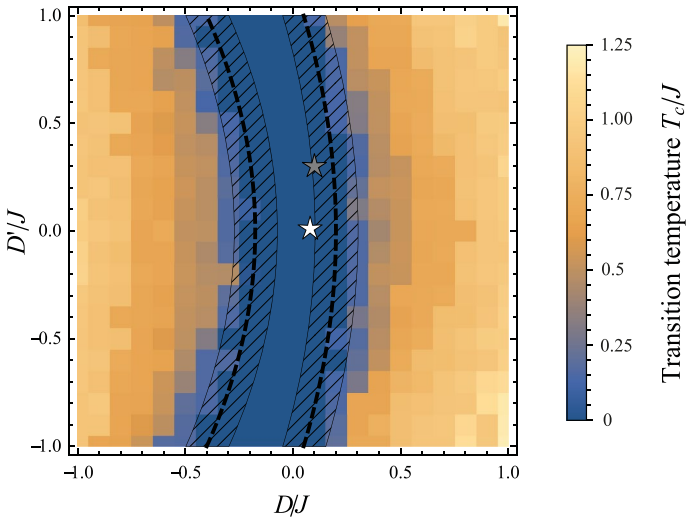

Figure 3.29. **Phase diagram** of the kagome Heisenberg antiferromagnet with additional out-of-plane DM interactions D and in-plane DM interactions D'. A finite transition temperature T_c indicates a magnetically ordered ground state, while vanishing T_c indicates a paramagnetic ground state. The phase diagram is calculated with a frequency mesh of $N_\omega = 66$ points, which leads to an uncertainty of the phase boundaries of approximately $D/J \pm 0.1$ due to reduced precision in locating potential flow breakdowns, c.f. Fig. 3.27. A lower frequency resolution is typically associated with a stronger tendency towards magnetic order. The white and gray stars indicate estimates of the coupling constants in herbertsmithite as obtained in Refs. [63] and [50], respectively.

calculating the full phase diagram of DM interactions with arbitrary orientations of the DM vector (Fig. 3.29) that the in-plane component D' only has a small impact on the ground state as long as it remains moderate in strength. Yet, our results imply that any finite in-plane DM couplings, regardless of their precise strength, will drive the system closer to a $q = 0$ magnetically ordered ground state. We have also established that both suggested sets of coupling parameters seem to lie close to the phase boundary between the quantum spin liquid ground state and the $q = 0$ magnetically ordered phase (Fig. 3.29), which can explain the weak maxima the structure factor at points associated with $q = 0$ order that have been measured in neutron diffraction experiments [124]. Beyond the scope of our research, it remains an interesting question to see how the role of DM interactions changes in the presence of additional perturbations in herbertsmithite, e.g. interactions beyond nearest neighbors or in the presence of inter-layer couplings.

3.4. Précis

In this section we have put the spotlight on three different examples of frustrated magnetism in three different materials: the spin-1 spinel compound $NiRh_2O_4$, forming a diamond lattice with frustrating next-nearest neighbor interactions (Sec. 3.1), the frustrated fcc magnet Ba_2CeIrO_6 with additional Kitaev interactions that stabilize magnetic order (Sec. 3.2), and the well known kagome antiferromagnet material herbertsmithite (Sec. 3.3).

Throughout the discussion of these materials we have focused on the phenomenology and the effective description thereof in terms of a minimal model. For the spinel compound, we have seen that a quantum spiral spin liquid emerges around regions where the classical analogue of the model is governed by the degeneracy of sub-extensively many coplanar spin spirals. We have studied the stability of the quantum spiral spin liquid under tetragonal lattice deformations, which are present in $NiRh_2O_4$, and we discussed local spin anisotropies as a potential way to stabilize the quantum spiral spin liquid even in the presence of those lattice deformations. For the frustrated fcc magnet, we have studied a minimal model that includes nearest-neighbor and next-nearest neighbor Heisenberg interactions which are complemented by Kitaev interactions. Just like in the diamond model we have observed the nucleation of a quantum spin liquid ground state around a point of large classical degeneracy. Curiously, we have seen that the Kitaev interactions seem to favor the proliferation of magnetic long-range order, which is in stark contrast to their role e.g. in the honeycomb Kitaev model. We have argued that the different roles of Kitaev interactions can be traced back to decisively different structures of the Kitaev interactions in the anisotropic limit – the fcc lattice effectively reduces to quasi two-dimensional stacked square lattices, while tricoordinate lattices would reduce to quasi one-dimensional structures. In that context, we have formulated a condition on the interplay between Heisenberg and Kitaev interactions that leads to particularly large frustration. Addressing the kagome material herbertsmithite, we have discussed the stability of the kagome spin liquid in the presence of Dzyaloshinskii-Moriya interactions, which are believed to appear in herbertsmithite with both finite in-plane and out-of-plane components. We have seen that any finite in-plane components of the DM interaction drive the system closer to magnetic order, although for realistic coupling strengths the effect is only weak.

Besides the interesting phenomenology of emerging quantum spin liquids, each project also highlights compelling methodological aspects of our pf-FRG calculations. Our calculations on the diamond lattice, most importantly, underline that the pf-FRG scheme can straightforwardly be applied to three-dimensional frustrated quantum magnets. Furthermore, we have performed extensive calculations for systems at various spin lengths, employing the spin-S generalized formulation of the pf-FRG as discussed in Sec. 2.5.5. Another strong suit of pf-FRG, which we did not overly emphasize, is its operation on infinite systems, which is highly relevant in the presence of coplanar spin spirals – it is inherently difficult to resolve spin spirals in any finite system since they are generally incompatible with periodic boundary conditions. The notion of finite system size in

pf-FRG calculations, however, does not introduce artificial boundaries to the system, which is discussed extensively in Sec. 2.4.3. Calculations on the fcc lattice are similar to those on the diamond lattice, since one is a sublattice of the other. Yet, on the fcc lattice we have computed a model that includes Kitaev interactions, whose efficient parametrization in pf-FRG is discussed more thoroughly in Sec. 2.5.3. Our calculations of Dzyaloshinskii-Moriya interactions on the kagome lattice are special because they fully rely on the general parametrization of pf-FRG flow equations for time-reversal invariant systems, as discussed in Sec. 2.3. All previous pf-FRG studies have only addressed models with additional spin symmetries. Furthermore, we made use of a trick to extract finite-temperature properties from pf-FRG calculations that are formally performed at zero temperature. The trick relies on a linear relation between the renormalization group cutoff scale and temperature which is discussed in Sec. 2.5.6. Finally, we also briefly touched the subject of numerical uncertainties which arise from the discretization of continuous Matsubara frequencies. Details on the discretization and interpolation schemes are discussed in Sec. 2.4.2.

4. Concluding remarks

The research which has been conducted in the context of this theses has made valuable contributions to the methodological toolset of techniques to study the fermionic quantum many-body problem; the toolset's capabilities are particularly being challenged in the strong coupling limit where perturbative approaches can no longer be employed. Yet, many open questions of current research are associated with this regime, including frustrated quantum magnetism and quantum spin liquids. While a battery of techniques already exists for the simulation of two-dimensional quantum magnets, the pf-FRG formalism stands out by its straightforward applicability also to three-dimensional frustrated quantum magnets – a challenging field where many established methods fail.

Like many other methods at the spearhead of modern computational physics, adopting the pf-FRG approach comes with a significant overhead of time which needs to be invested into the development of an efficient software implementation for the numerical solution of the large number of integro-differential equations; moreover, the derivation of the pf-FRG formalism itself requires a thorough understanding of the underlying field-theoretical methods. Fortunately, we have seen that the principal structure of the necessary numerical calculations, which is defined by the structure of the pf-FRG flow equations, is largely independent of the microscopic details of the target model of quantum magnetism – concrete values of the microscopic exchange constants merely enter in the initial conditions of the differential equations, while the principal structure only depends on the symmetry class of the Hamiltonian. Once implemented, the pf-FRG approach therefore is very flexible and can be applied to a great number of different quantum spin models.

Research on the pf-FRG formalism has reached a stage where it would be desirable to supply a reusable software basis which provides implementations of the core concepts of the generalized pf-FRG approach as discussed in this thesis. Such core concepts include: (i) concrete implementations of the flow equations in their most general form for time-reversal invariant systems as well more specific implementations for the SU(N) Heisenberg model and the generalization to arbitrary spin length; (ii) the approximation of vertex functions in continuous zero-temperature Matsubara frequency space on a mesh of discrete frequency points which is refined by an interpolation scheme; (iii) the approximation of vertex functions on a lattice graph with a finite truncation range of the interaction length, potentially automating the identification of lattice symmetries and the construction of the lattice graph from a single unit cell; (iv) a differential equation solver which is capable of simultaneously solving millions of coupled flow equations by means of the Euler scheme, possibly providing a parallelization scheme across multiple nodes in a computer cluster and performing automatic load balancing.

The deployment of such a software package in a user-friendly way would allow a much

broader community to exploit the potential held by pf-FRG calculations. This thesis contributes to the reduction of the entry barrier into the field of pf-FRG by reviewing the theoretical groundwork, conveying the necessary understanding for the design and interpretation of pf-FRG studies, and by providing examples for applications in the study of frustrated quantum magnets. In particular, within this thesis we have demonstrated the applicability of the pf-FRG approach to systems with arbitrary two-spin interactions including also off-diagonal interaction terms, thus opening up methodological access to a plethora of models of current interest. This broad applicability goes back to very recent methodological developments [P6]; consequently, many models are yet to be explored.

Nevertheless, the pf-FRG approach is still relatively young and there remain many aspects about the method which have not yet been fully studied and should be addressed in future research. One of the biggest limitations of the pf-FRG formalism to this day is that – while the method can successfully discriminate between magnetically ordered phases and nonmagnetic ground states – it is difficult to obtain knowledge about the nature of spin-liquid ground states. Although first steps have been taken towards explicitly probing emergent parton dynamics in spin-liquid phases, they rely on custom implementations of the pf-FRG, which limits their use case scenarios [54, 81, P3]. A more general solution for the characterization of different paramagnetic ground states could be the study of dynamic observables. Currently, excitations at finite frequencies are inaccessible because the pf-FRG is intrinsically formulated in imaginary Matsubara frequencies, not in real frequencies. It is not clear yet whether pf-FRG calculations can be pushed to a frequency resolution which is sufficient to allow for the execution of a reliable analytic continuation to real frequencies. Alternatively, one could aim for a complete reformulation of the pf-FRG approach in the domain of real frequencies based on the Keldysh formalism [125]. It is then to be explored whether the flow equations in real frequency space remain sufficiently well-behaved to enable a numerical solution at justifiable computational costs.

An orthogonal approach which would also allow for deeper insight into spin-liquid phases would be the implementation of finite magnetic fields. The associated explicit breaking of time-reversal symmetry would complicate the calculations by approximately two orders of magnitude compared to current implementations of pf-FRG (see Sec. 2.4.4); yet in efficient software implementations this slowdown is tolerable, at least for moderate system sizes. The benefits would be great: the simulation of finite magnetic fields would allow one to further probe the stability of spin-liquid phases while also opening up access to an entirely new class of models which inherently rely on magnetic fields. Furthermore, dismissing the enforcement of time-reversal symmetry would extend our perspective on spontaneous time-reversal symmetry breaking and could potentially increase the precision at which phase boundaries between spin-liquid phases and symmetry-breaking magnetically ordered phases can be determined.

Lastly, the ultimate goal would be the inclusion of the three-particle vertex in the pf-FRG flow equations. While this is numerically unfeasible (the simulation of a third interacting particle adds a large number of extra degrees of freedom which severely affect the scaling of the computational complexity as a function of the frequency resolution

and the system size), it seems within reach to routinely improve the Katanin truncation scheme to higher loop orders [71, 73] and control numerical errors resulting from the finite frequency resolution by employing more sophisticated discretization schemes [69].

We have illustrated in this thesis that the pf-FRG approach offers a fresh perspective on fermionic many-body simulations and that it can provide us with answers to long-standing questions in the field of three-dimensional frustrated quantum magnetism. The long list of models which have been made accessible by recent refinements and extensions of the pf-FRG approach leaves us with exciting prospects for future research.

A. Pf-FRG flow equations

A.1. SU(N) Heisenberg model

In this section we present the pf-FRG flow equations for SU(N) generalized spin-1/2 Heisenberg models, which has first been presented in Ref. [P2]. The associated Hamiltonian assumes the form

$$H = \sum_{i,j} J_{ij} \mathbf{S}_i \mathbf{S}_j \quad , \tag{A.1}$$

where the spin operators obey the SU(N) algebra, represented on the pseudo-fermion space by

$$S_i^\mu = f_{i,\alpha}^\dagger T_{\alpha\beta}^\mu f_{i,\beta} \quad . \tag{A.2}$$

The SU(N) spin operators have $\mu = 1, \ldots, N^2 - 1$ generators and their spin index runs in the range $\alpha = 1, \ldots, N$; the generators are normalized to $\mathrm{Tr}(T^\mu T^\nu) = \frac{1}{2}\delta_{\mu\nu}$. It is convenient to parametrize the single-particle vertex according to

$$\Sigma(1';1) = \Sigma(\omega)\delta_{i'i}\delta_{\omega'\omega}\delta_{\alpha'\alpha} \quad , \tag{A.3}$$

and the two-particle vertex as

$$\begin{aligned}\Gamma(1',2';1,2) = \Big[\Big(&\Gamma^{\mathrm{d}}_{i_1 i_2}(s,t,u)\delta_{\alpha_{1'}\alpha_1}\delta_{\alpha_{2'}\alpha_2} + \Gamma^{\mathrm{s}}_{i_1 i_2}(s,t,u) T^\mu_{\alpha_{1'}\alpha_1} T^\mu_{\alpha_{2'}\alpha_2}\Big)\delta_{i_{1'} i_1}\delta_{i_{2'} i_2} \\ &- (1' \leftrightarrow 2')\Big]\delta_{\omega_{1'}+\omega_{2'}-\omega_1-\omega_2} \quad ,\end{aligned} \tag{A.4}$$

see also the discussion in Sec. 2.5.3. Comparison of the Hamiltonian (A.1) with the vertex parametrization yields the initial conditions for the basis functions of the parametrization,

$$\Sigma^{\Lambda\to\infty}(\omega) = 0 \qquad \Gamma^{\mathrm{d},\Lambda\to\infty}_{i_1 i_2}(s,t,u) = 0 \qquad \Gamma^{\mathrm{s},\Lambda\to\infty}_{i_1 i_2}(s,t,u) = J_{ij} \quad . \tag{A.5}$$

The flow equations for the basis functions are obtained by inserting the vertex parametrization into the general fermionic FRG flow equations and computing internal summations over spin indices, as detailed in Sections 2.1 and 2.3. The flow equations result to

$$\begin{aligned}\frac{\mathrm{d}}{\mathrm{d}\Lambda}\Sigma^\Lambda(\omega) = \frac{1}{2\pi}\int \mathrm{d}\omega' \Big[&\Gamma^{\mathrm{d},\Lambda}_{i_1 i_1}(\omega'+\omega, \omega'-\omega, 0) + \frac{N^2-1}{2N}\Gamma^{\mathrm{s},\Lambda}_{i_1 i_1}(\omega'+\omega,\omega'-\omega,0) \\ &- N\sum_j \Gamma^{\mathrm{d},\Lambda}_{i_1 j}(\omega+\omega', 0, \omega-\omega')\Big] \times S^\Lambda(\omega')\end{aligned} \tag{A.6}$$

$$
\begin{aligned}
\frac{\mathrm{d}}{\mathrm{d}\Lambda}\Gamma^{\mathrm{d}}_{i_1 i_2}(s,t,u) = \frac{1}{2\pi}\int \mathrm{d}\omega \Big[& \\
& \Big(\Gamma^{\mathrm{d}}_{i_1 i_2}(s,\omega-\omega_1,\omega-\omega_2)\Gamma^{\mathrm{d}}_{i_1 i_2}(s,\omega_{1'}-\omega,\omega-\omega_{2'}) \\
& + \frac{N^2-1}{4N^2}\Gamma^{\mathrm{s}}_{i_1 i_2}(s,\omega-\omega_1,\omega-\omega_2)\Gamma^{\mathrm{s}}_{i_1 i_2}(s,\omega_{1'}-\omega,\omega-\omega_{2'})\Big) \\
& \times \big(S^{\Lambda}_{\mathrm{kat}}(\omega)G^{\Lambda}(s-\omega) + G^{\Lambda}(\omega)S^{\Lambda}_{\mathrm{kat}}(s-\omega)\big) \\
& + \Big(-N\sum_j \Gamma^{\mathrm{d}}_{i_1 j}(\omega_1+\omega,t,\omega_{1'}-\omega_3)\Gamma^{\mathrm{d}}_{j i_2}(\omega_{2'}+\omega,t,\omega-\omega_2) \\
& + \Gamma^{\mathrm{d}}_{i_1 i_2}(\omega_1+\omega,t,\omega_{1'}-\omega)\Gamma^{\mathrm{d}}_{i_2 i_2}(\omega_{2'}+\omega,\omega-\omega_2,t) \\
& + \frac{N^2-1}{2N}\Gamma^{\mathrm{d}}_{i_1 i_2}(\omega_1+\omega,t,\omega_{1'}-\omega)\Gamma^{\mathrm{s}}_{i_2 i_2}(\omega_{2'}+\omega,\omega-\omega_2,t) \\
& + \Gamma^{\mathrm{d}}_{i_1 i_1}(\omega_1+\omega,\omega-\omega_{1'},-t)\Gamma^{\mathrm{d}}_{i_1 i_2}(\omega+\omega_{2'},t,\omega-\omega_2) \\
& + \frac{N^2-1}{2N}\Gamma^{\mathrm{s}}_{i_1 i_1}(\omega_1+\omega,\omega-\omega_{1'},-t)\Gamma^{\mathrm{d}}_{i_1 i_2}(\omega+\omega_{2'},t,\omega-\omega_2)\Big) \\
& \times \big(S^{\Lambda}_{\mathrm{kat}}(\omega)G^{\Lambda}(\omega-t) + G^{\Lambda}(\omega)S^{\Lambda}_{\mathrm{kat}}(\omega-t)\big) \\
& + \Big(\Gamma^{\mathrm{d}}_{i_1 i_2}(\omega_1+\omega,\omega-\omega_{2'},u)\Gamma^{\mathrm{d}}_{i_1 i_2}(\omega_{1'}+\omega,\omega_2-\omega,u) \\
& + \frac{N^2-1}{4N^2}\Gamma^{\mathrm{s}}_{i_1 i_2}(\omega_1+\omega,\omega-\omega_{2'},u)\Gamma^{\mathrm{s}}_{i_1 i_2}(\omega_{1'}+\omega,\omega_2-\omega,u)\Big) \\
& \times \big(S^{\Lambda}_{\mathrm{kat}}(\omega)G^{\Lambda}(\omega+u) + G^{\Lambda}(\omega)S^{\Lambda}_{\mathrm{kat}}(\omega+u)\big)\Big]
\end{aligned}
\tag{A.7}
$$

$$
\begin{aligned}
\frac{\mathrm{d}}{\mathrm{d}\Lambda}\Gamma^{\mathrm{s}}_{i_1 i_2}(s,t,u) = \frac{1}{2\pi}\int \mathrm{d}\omega \Big[& \\
& \Big(\Gamma^{\mathrm{d}}_{i_1 i_2}(s,\omega-\omega_1,\omega-\omega_2)\Gamma^{\mathrm{s}}_{i_1 i_2}(s,\omega_{1'}-\omega,\omega-\omega_{2'}) \\
& + \Gamma^{\mathrm{s}}_{i_1 i_2}(s,\omega-\omega_1,\omega-\omega_2)\Gamma^{\mathrm{d}}_{i_1 i_2}(s,\omega_{1'}-\omega,\omega-\omega_{2'}) \\
& - \frac{1}{N}\Gamma^{\mathrm{s}}_{i_1 i_2}(s,\omega-\omega_1,\omega-\omega_2)\Gamma^{\mathrm{s}}_{i_1 i_2}(s,\omega_{1'}-\omega,\omega-\omega_{2'})\Big) \\
& \times \big(S^{\Lambda}_{\mathrm{kat}}(\omega)G^{\Lambda}(s-\omega) + G^{\Lambda}(\omega)S^{\Lambda}_{\mathrm{kat}}(s-\omega)\big) \\
& + \Big(-\frac{1}{2}\sum_j \Gamma^{\mathrm{s}}_{i_1 j}(\omega_1+\omega,t,\omega_{1'}-\omega_3)\Gamma^{\mathrm{s}}_{j i_2}(\omega_{2'}+\omega,t,\omega-\omega_2) \\
& + \Gamma^{\mathrm{s}}_{i_1 i_2}(\omega_1+\omega,t,\omega_{1'}-\omega)\Gamma^{\mathrm{d}}_{i_2 i_2}(\omega_{2'}+\omega,\omega-\omega_2,t) \\
& - \frac{1}{2N}\Gamma^{\mathrm{s}}_{i_1 i_2}(\omega_1+\omega,t,\omega_{1'}-\omega)\Gamma^{\mathrm{s}}_{i_2 i_2}(\omega_{2'}+\omega,\omega-\omega_2,t) \\
& + \Gamma^{\mathrm{d}}_{i_1 i_1}(\omega_1+\omega,\omega-\omega_{1'},-t)\Gamma^{\mathrm{s}}_{i_1 i_2}(\omega+\omega_{2'},t,\omega-\omega_2) \\
& - \frac{1}{2N}\Gamma^{\mathrm{s}}_{i_1 i_1}(\omega_1+\omega,\omega-\omega_{1'},-t)\Gamma^{\mathrm{s}}_{i_1 i_2}(\omega+\omega_{2'},t,\omega-\omega_2)\Big) \\
& \times \big(S^{\Lambda}_{\mathrm{kat}}(\omega)G^{\Lambda}(\omega-t) + G^{\Lambda}(\omega)S^{\Lambda}_{\mathrm{kat}}(\omega-t)\big)
\end{aligned}
$$

$$
\begin{aligned}
&+\Big(\Gamma^{\mathrm{d}}_{i_1 i_2}(\omega_1+\omega,\omega-\omega_{2'},u)\Gamma^{\mathrm{s}}_{i_1 i_2}(\omega_{1'}+\omega,\omega_2-\omega,u)\\
&\quad+\Gamma^{\mathrm{s}}_{i_1 i_2}(\omega_1+\omega,\omega-\omega_{2'},u)\Gamma^{\mathrm{d}}_{i_1 i_2}(\omega_{1'}+\omega,\omega_2-\omega,u)\\
&+\frac{N^2-2}{2N}\Gamma^{\mathrm{s}}_{i_1 i_2}(\omega_1+\omega,\omega-\omega_{2'},u)\Gamma^{\mathrm{s}}_{i_1 i_2}(\omega_{1'}+\omega,\omega_2-\omega,u)\Big)\\
&\qquad\times\left(S^{\Lambda}_{\mathrm{kat}}(\omega)G^{\Lambda}(\omega+u)+G^{\Lambda}(\omega)S^{\Lambda}_{\mathrm{kat}}(\omega+u)\right)\Big] \quad . \qquad \text{(A.8)}
\end{aligned}
$$

Since the flow equations are bulky expressions it is convenient to formulate them diagrammatically. Therefore we introduce two types of diagrams for $\Gamma^{\mathrm{d}}_{i_1 i_2}(\omega_{1'},\omega_{2'};\omega_1,\omega_2)$ and $\Gamma^{\mathrm{s}}_{i_1 i_2}(\omega_{1'},\omega_{2'};\omega_1,\omega_2)$, respectively. Note that in this diagrammatic language we are not using the transfer frequencies s, t, and u. Instead we are stating all four frequencies explicitly and implicitly assume energy conservation. The diagrams should be read as

$\Gamma^{\mathrm{d}}_{i_1 i_2}(\omega_{1'},\omega_{2'};\omega_1,\omega_2) \sim$ 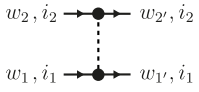

$\Gamma^{\mathrm{s}}_{i_1 i_2}(\omega_{1'},\omega_{2'};\omega_1,\omega_2) \sim$ 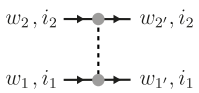

. (A.9)

The single-scale propagator $S(\omega)$ is denoted by a slashed line. A pair of slashed propagator lines should be read as $S_{\mathrm{kat}}(\omega_1)G(\omega_2)+G(\omega_1)S_{\mathrm{kat}}(\omega_2)$. In this diagrammatic form the flow equation for the self-energy becomes

$\frac{\mathrm{d}}{\mathrm{d}\Lambda}\Sigma^{\Lambda}(\omega) =$ 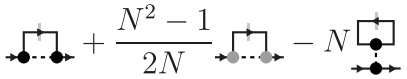 (A.10)

and the flow equations for the basis functions of the two-particle vertex read as

$\frac{\mathrm{d}}{\mathrm{d}\Lambda}$ 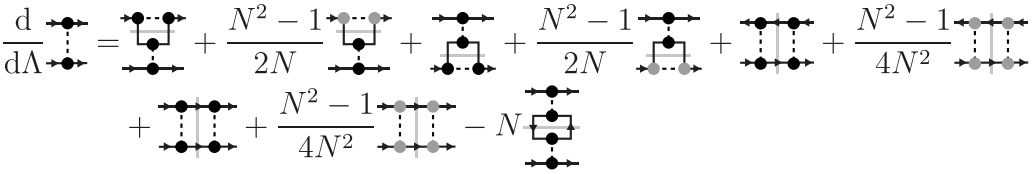 (A.11)

$\frac{\mathrm{d}}{\mathrm{d}\Lambda}$ 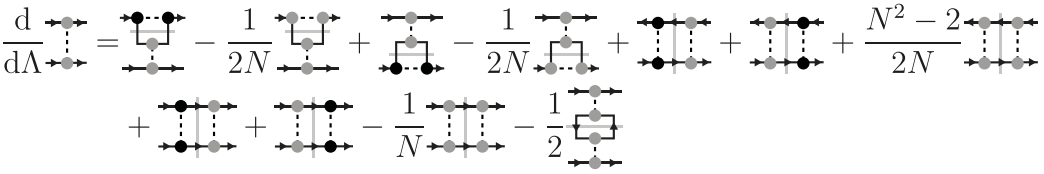 . (A.12)

A.2. Spin-S Heisenberg model

In this section we present the pf-FRG flow equations for spin-S generalized Heisenberg models, which has first been presented in Ref. [38]. The associated Hamiltonian assumes the form

$$H = \sum_{i,j} J_{ij} \mathbf{S}_i \mathbf{S}_j \quad , \tag{A.13}$$

where the spin-S operators obey the SU(2) algebra, represented on the pseudo-fermion space by

$$S_i^\mu = \sum_{\kappa=1}^{2S} f_{i,\kappa,\alpha}^\dagger T_{\alpha\beta}^\mu f_{i,\kappa,\beta} \quad , \tag{A.14}$$

see the discussion in Sec. 2.5.5 for details on the auxiliary flavor index κ. The SU(2) spin operators have $\mu = 1, \ldots, 3$ generators and their spin index assumes values $\alpha = 1, 2$ denoting the spin configurations $\uparrow, \downarrow$. The generators are normalized to $\mathrm{Tr}(T^\mu T^\nu) = \frac{1}{2}\delta_{\mu\nu}$, such that they are related to the conventional Pauli matrices σ^μ via $T^\mu = \frac{1}{2}\sigma^\mu$. It has been demonstrated in Ref. [38] that almost the same pf-FRG formalism which has been developed for spin-1/2 models can be employed also for the simulation of spin-S models. The only necessary extension is to weigh every diagram that contains an internal lattice summation by an additional factor of 2S, which is a consequence of the introduction of 2S different fermion flavors; note that this factor must also be added in the calculation of observables.

Implementing the extra factors in the SU(2)-symmetric flow equations for spin-1/2 moments (as presented in Sec. A.1) the flow equations are given by

$$\frac{\mathrm{d}}{\mathrm{d}\Lambda}\Sigma^\Lambda(\omega) = + \frac{3}{4} - 4S \tag{A.15}$$

$$\frac{\mathrm{d}}{\mathrm{d}\Lambda} = + \frac{3}{4} + + \frac{3}{4} + + \frac{3}{16} + + \frac{3}{16} - 4S \tag{A.16}$$

$$\frac{\mathrm{d}}{\mathrm{d}\Lambda} = - \frac{1}{4} + - \frac{1}{4} + + + \frac{1}{2} + + - \frac{1}{2} - S \tag{A.17}$$

and their initial conditions remain unchanged as compared to the case of spin-1/2 moments,

$$\Sigma^{\Lambda\to\infty}(\omega) = 0 \qquad \Gamma_{i_1 i_2}^{\mathrm{d},\Lambda\to\infty}(s,t,u) = 0 \qquad \Gamma_{i_1 i_2}^{\mathrm{s},\Lambda\to\infty}(s,t,u) = J_{ij} \quad . \tag{A.18}$$

A.3. Off-diagonal spin interactions

In this section we present the general pf-FRG flow equations for spin models with off-diagonal exchange couplings which has first been presented in Ref. [P6]. The associated Hamiltonian assumes the form

$$H = \sum_{i,j} J_{ij}^{\mu\nu} S_i^\mu S_j^\nu \quad , \tag{A.19}$$

where the spin operators obey the SU(2) algebra, represented on the pseudo-fermion space by

$$S_i^\mu = \frac{1}{2} f_{i,\alpha}^\dagger \sigma_{\alpha\beta}^\mu f_{i,\beta} \quad , \tag{A.20}$$

where σ^μ, $\nu = 1, 2, 3$, are the Pauli matrices. As discussed in Sec. 2.3, it is convenient to parametrize the single-particle vertex according to

$$\Sigma(1'; 1) = \Sigma(\omega)\delta_{i'i}\delta_{\omega'\omega}\delta_{\alpha'\alpha} \quad , \tag{A.21}$$

and the two-particle vertex as

$$\Gamma(1', 2'; 1, 2) = \left[\left(\Gamma_{i_1 i_2}^{\mu\nu}(s, t, u) \sigma_{\alpha_{1'}\alpha_1}^\mu \sigma_{\alpha_{2'}\alpha_2}^\nu \right) \delta_{i_{1'}i_1} \delta_{i_{2'}i_2} - (1' \leftrightarrow 2') \right] \delta_{\omega_{1'}+\omega_{2'}-\omega_1-\omega_2} \quad , \tag{A.22}$$

where μ, ν now takes values from 0 to 3 and σ^0 is the identity matrix. Comparison of the Hamiltonian (A.19) with the vertex parametrization yields the initial conditions for the basis functions of the parametrization,

$$\Sigma^{\Lambda\to\infty}(\omega) = 0 \qquad \Gamma_{i_1 i_2}^{\mu\nu,\Lambda\to\infty}(s, t, u) = \frac{1}{4} J_{ij}^{\mu\nu} \quad . \tag{A.23}$$

The flow equations for the basis functions of the vertex parametrization can be represented in a diagrammatic language that is similar to the one introduced in Sec. A.1. Instead of two basis functions for the two-particle vertex in the SU(N) model there are now 16 functions; they are visualized by the diagrams

$$\Gamma_{i_1 i_2}^{\mu\nu}(\omega_{1'}, \omega_{2'}; \omega_1, \omega_2) \sim$$

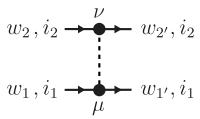

, (A.24)

where the values of μ (ν) are represented by the color of the circles: black is $\mu = 0$, red is $\mu = 1$, green is $\mu = 2$, and blue is $\mu = 3$. In this notation the flow equation for the self-energy reads as

$$\frac{\mathrm{d}}{\mathrm{d}\Lambda}\Sigma^\Lambda(\omega) =$$

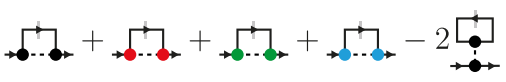

(A.25)

and the flow of the two-particle vertex is given by

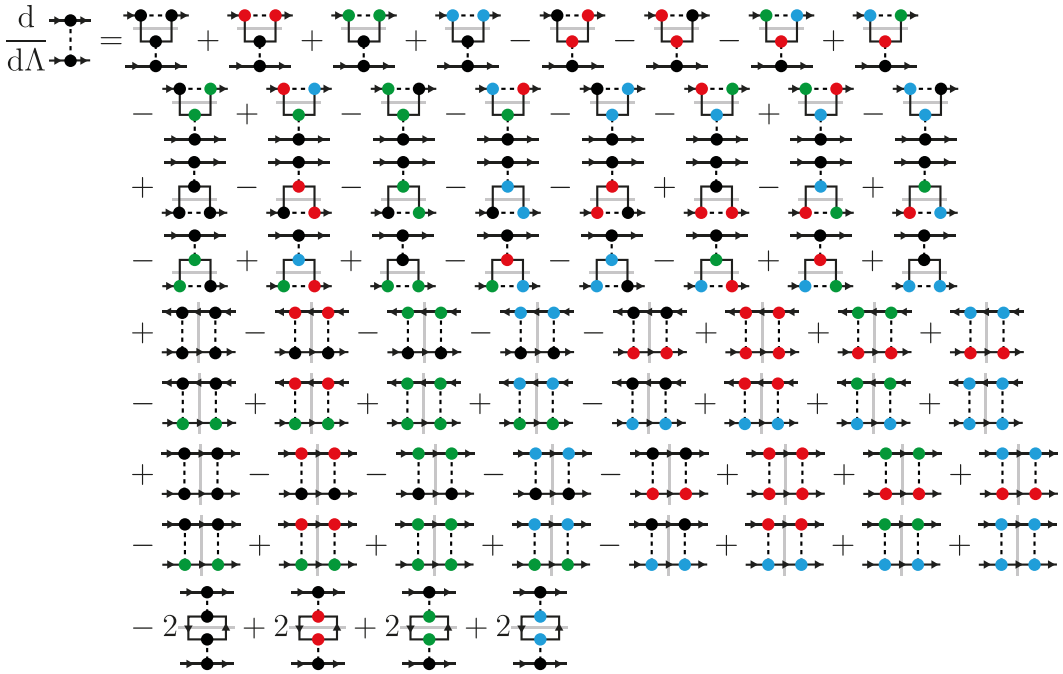

(A.26)

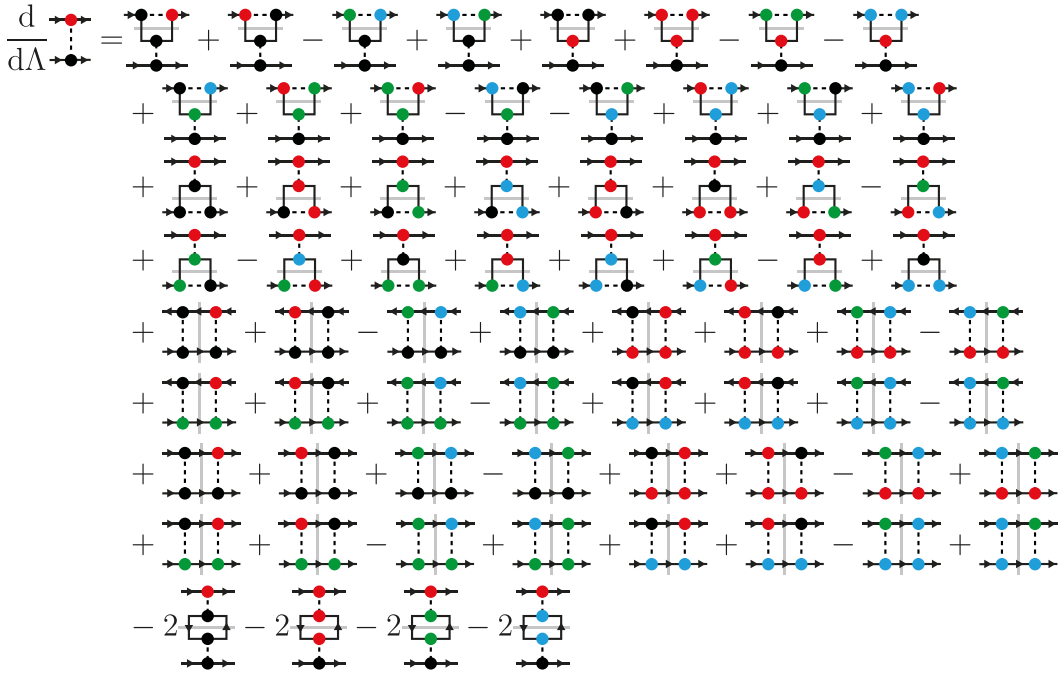

(A.27)

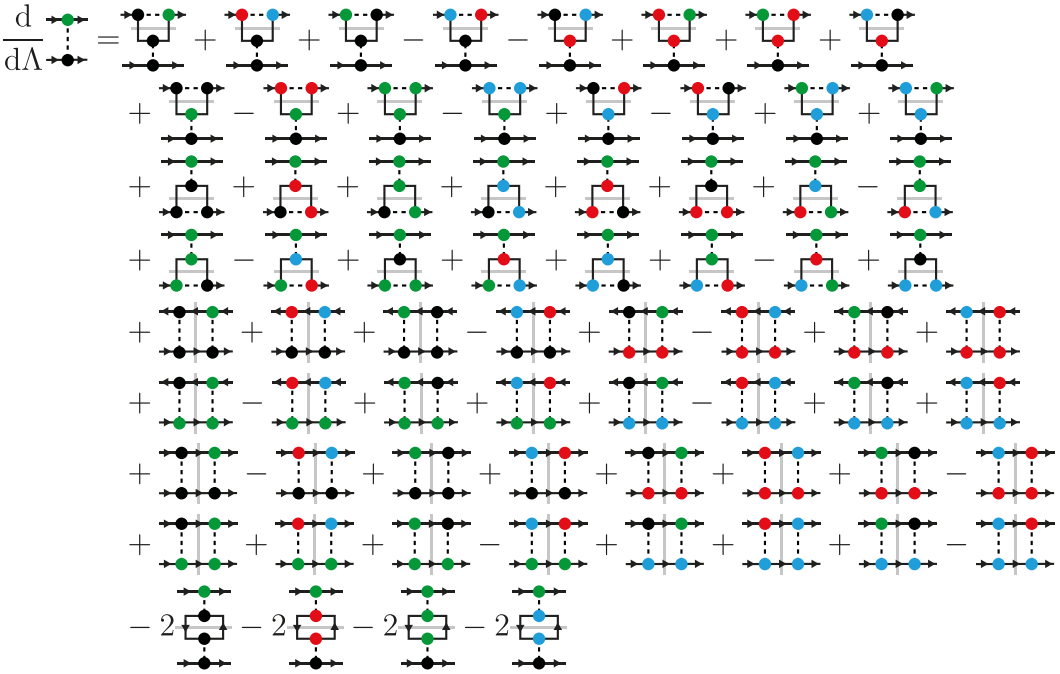

(A.28)

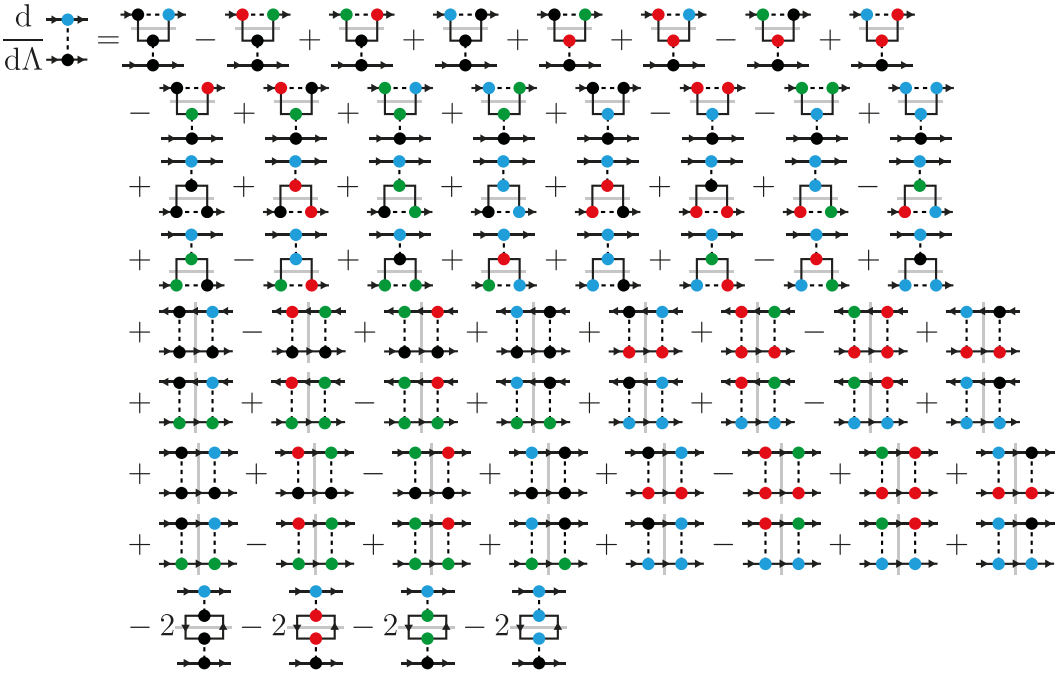

(A.29)

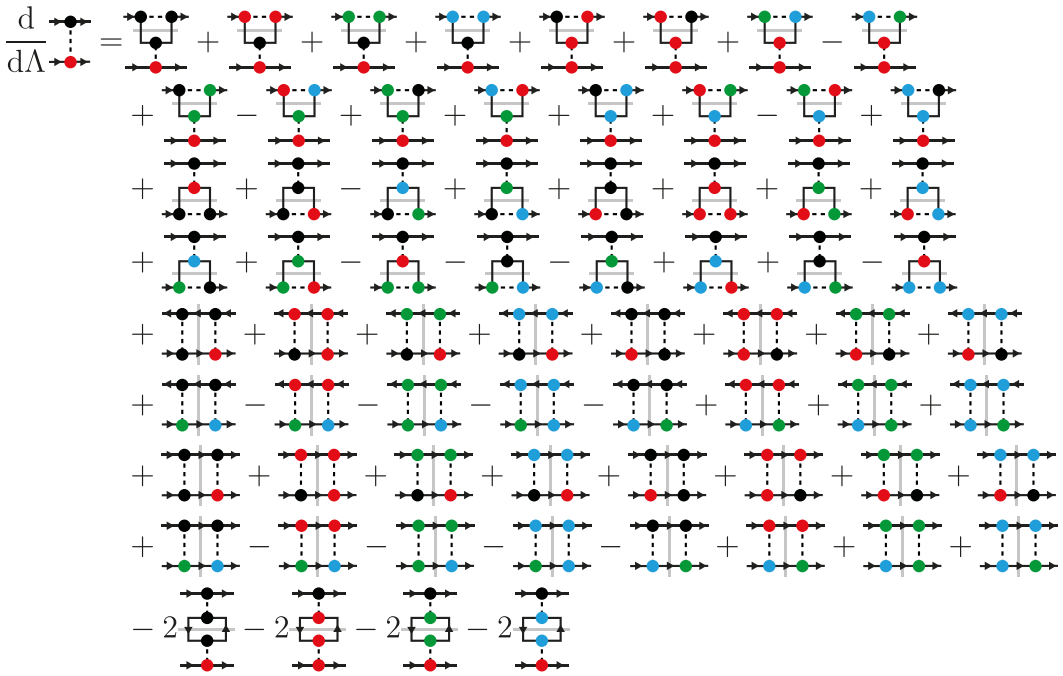

(A.30)

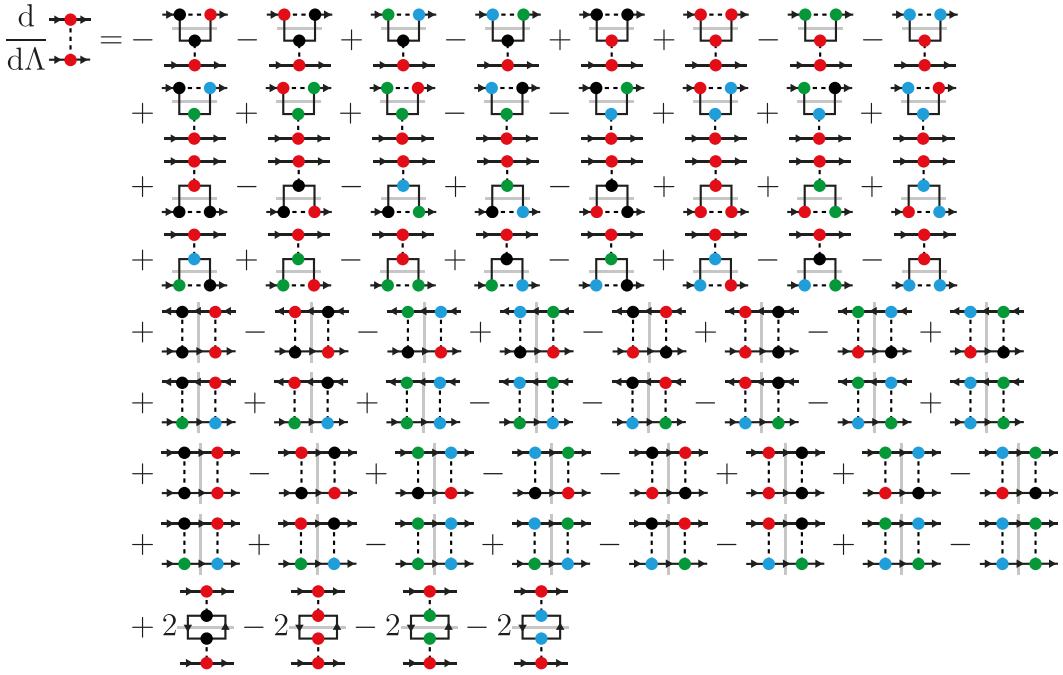

(A.31)

$\frac{\mathrm{d}}{\mathrm{d}\Lambda}$ =

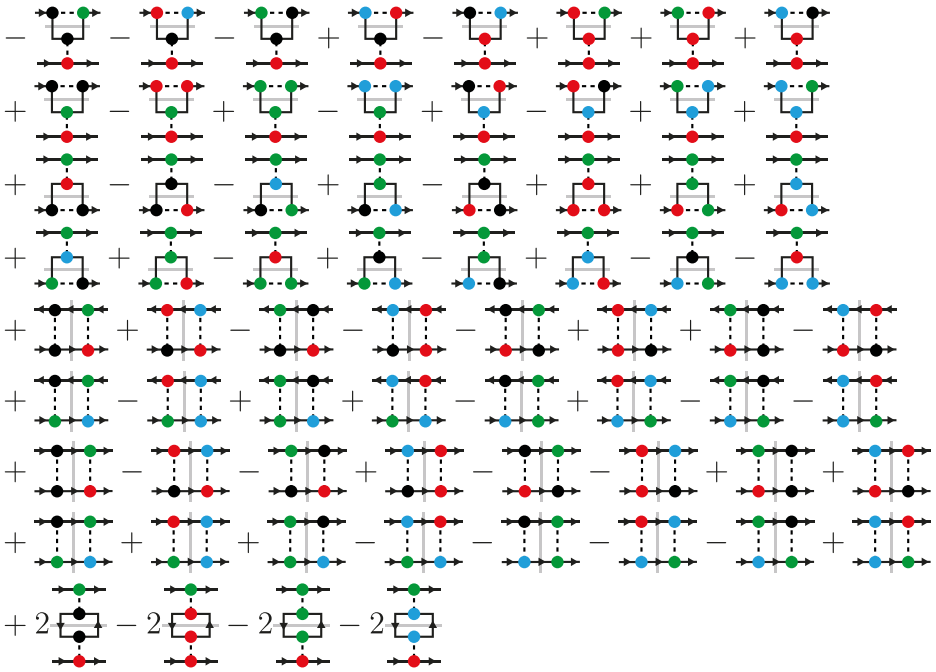

(A.32)

$\frac{\mathrm{d}}{\mathrm{d}\Lambda}$ =

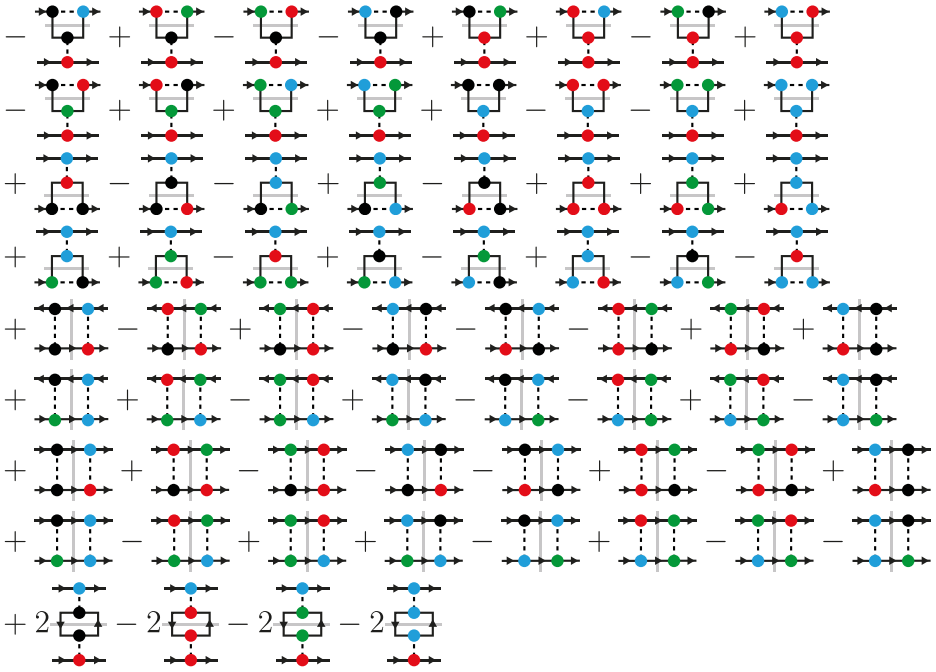

(A.33)

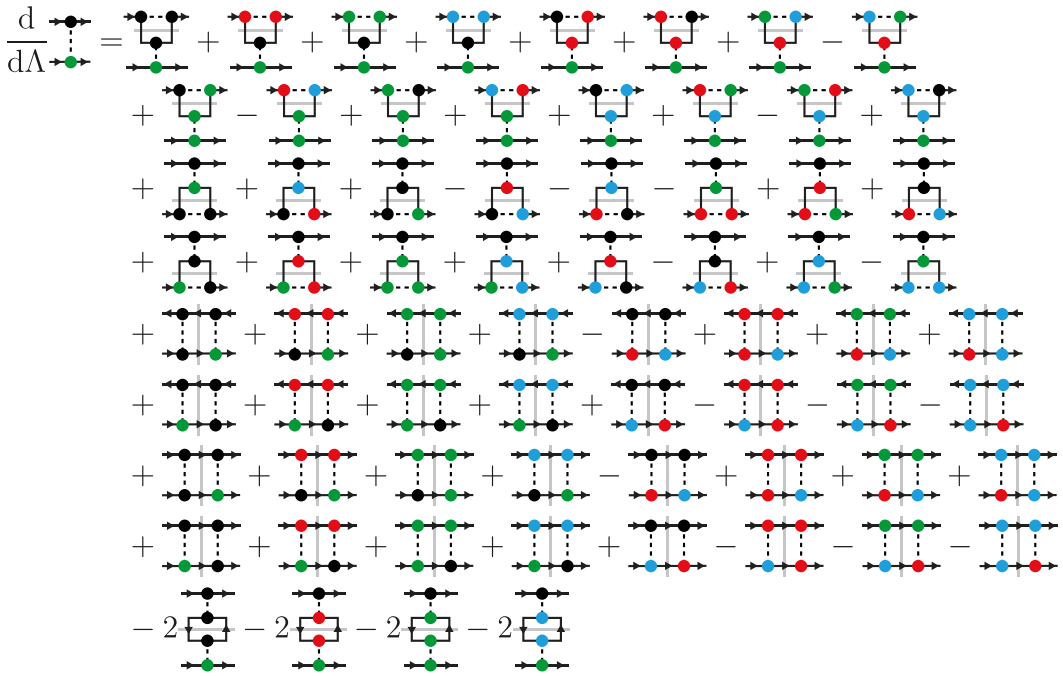

(A.34)

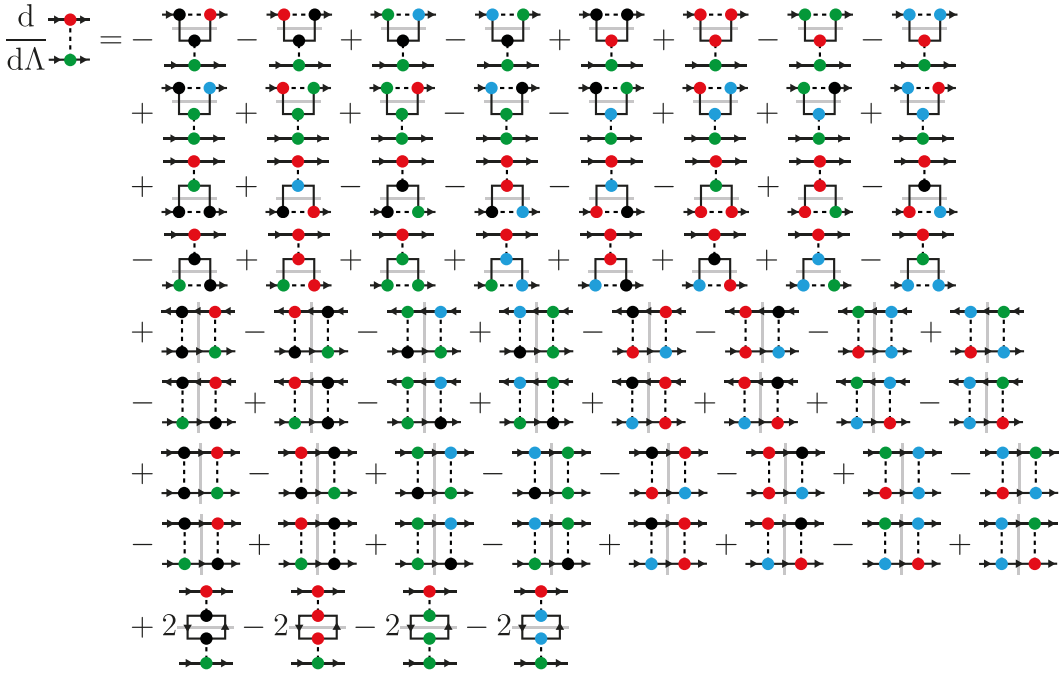

(A.35)

$\frac{\mathrm{d}}{\mathrm{d}\Lambda}$ =

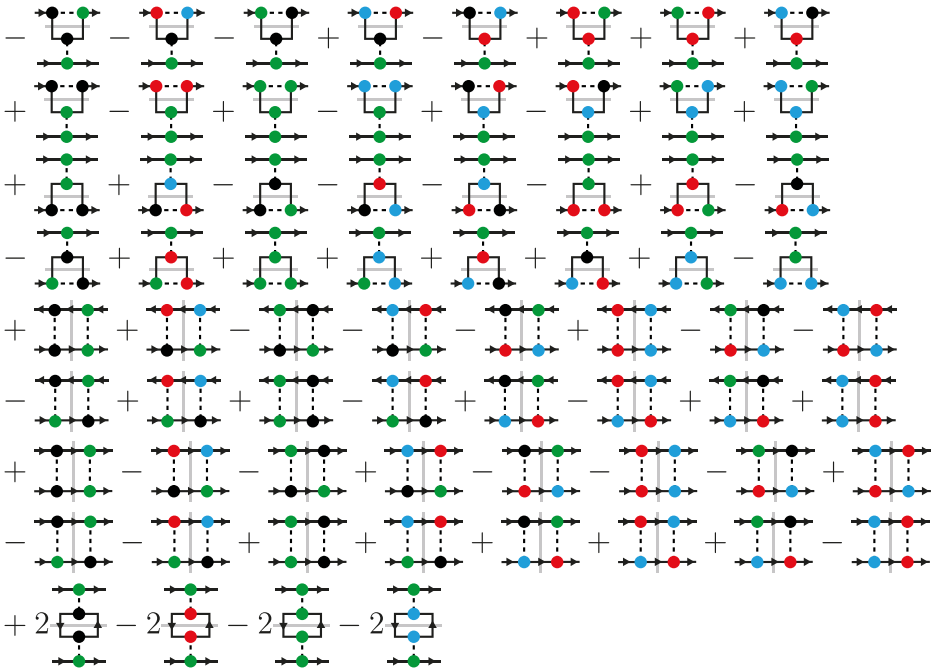

(A.36)

$\frac{\mathrm{d}}{\mathrm{d}\Lambda}$ =

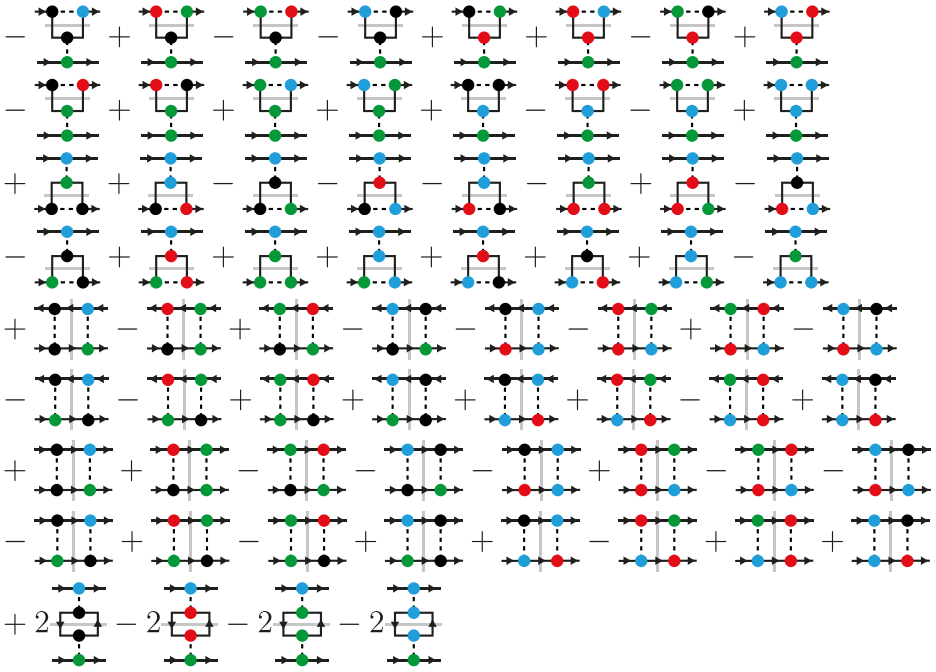

(A.37)

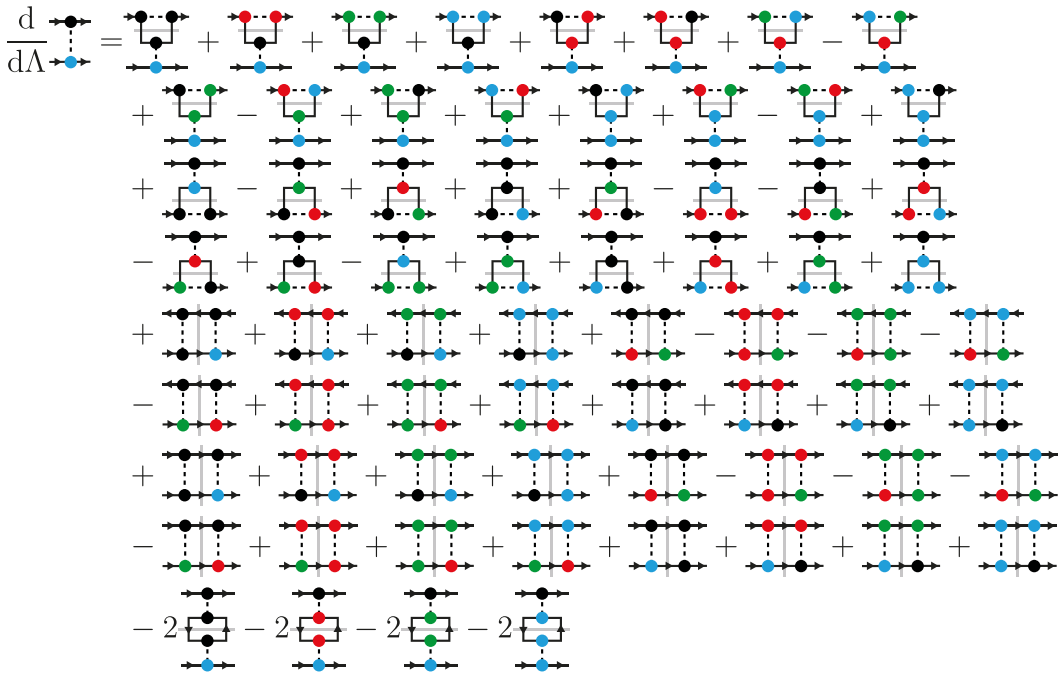

(A.38)

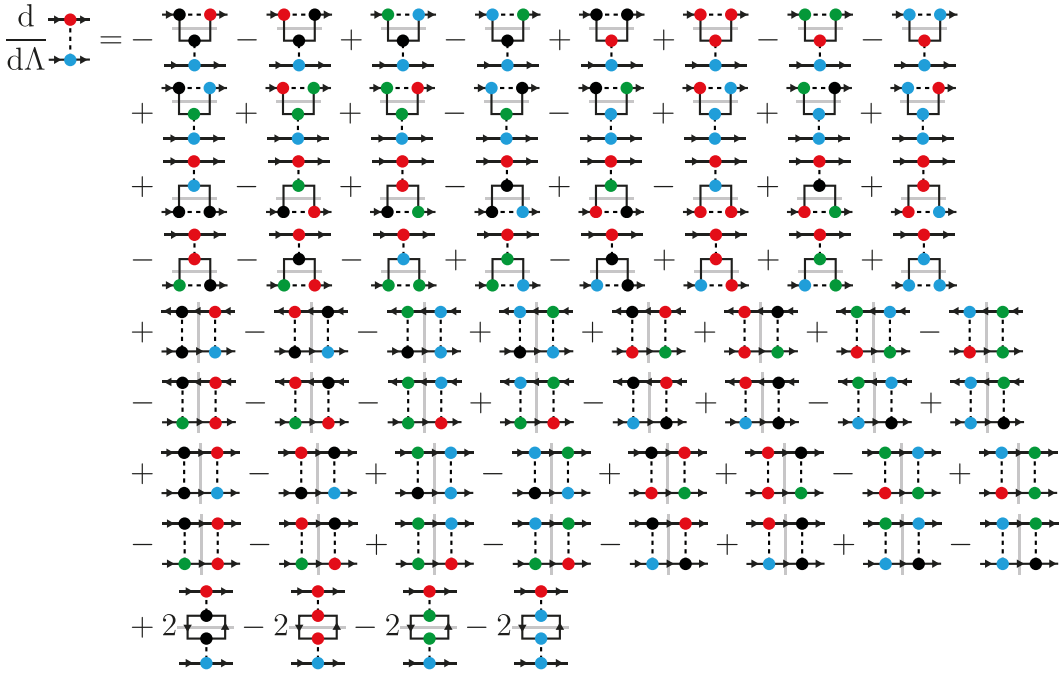

(A.39)

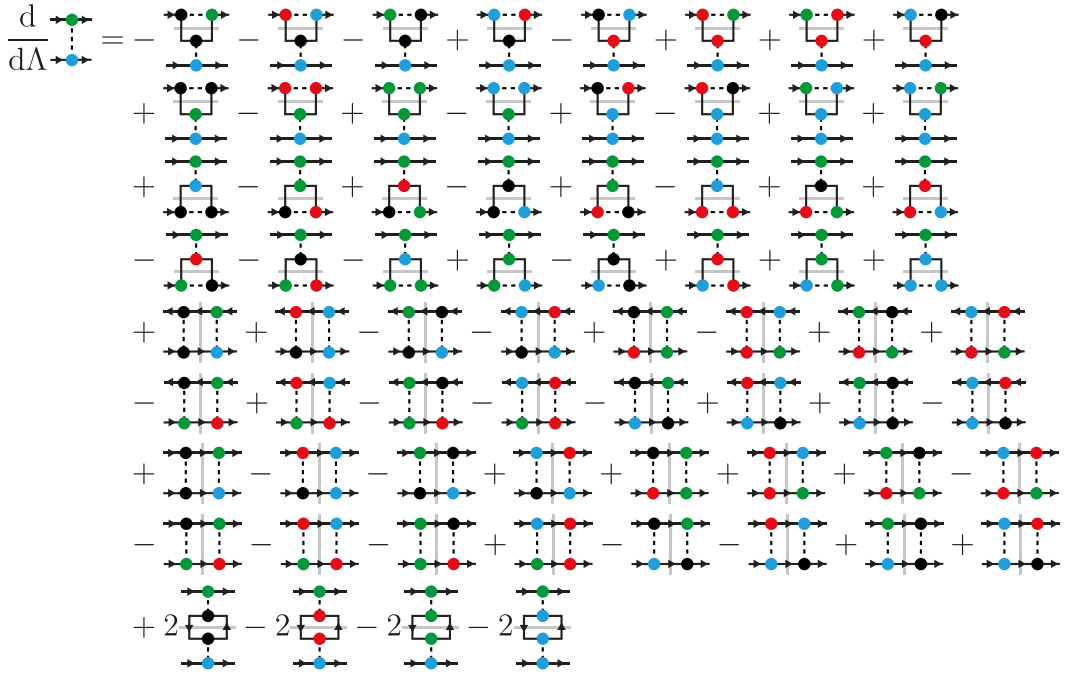

(A.40)

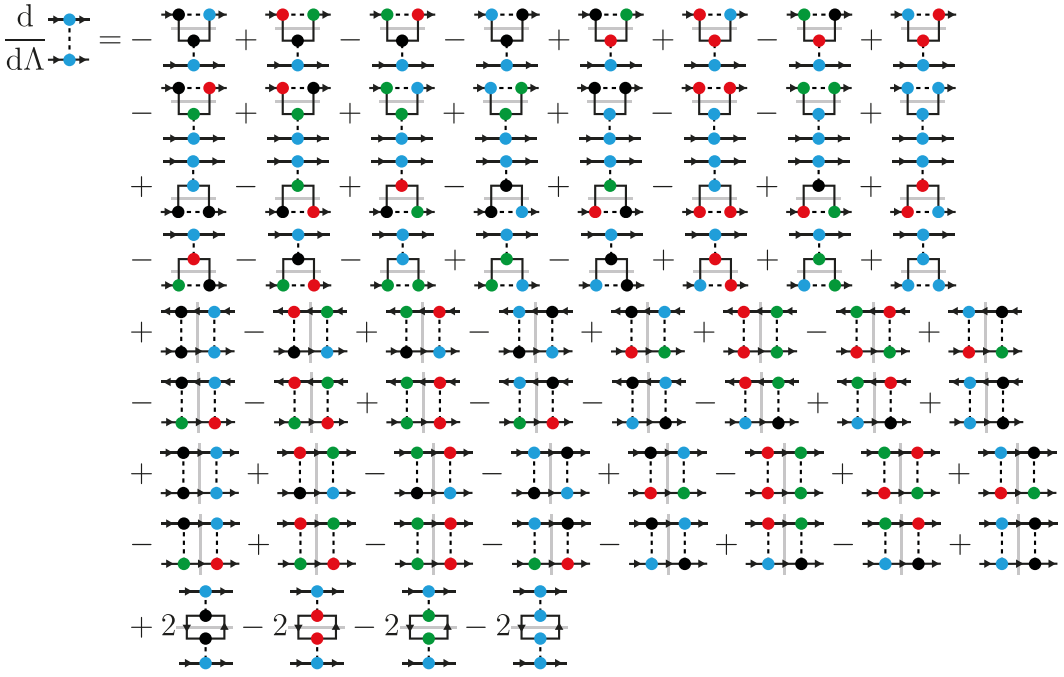

(A.41)

Bibliography

[P1] F. L. Buessen and S. Trebst, Competing magnetic orders and spin liquids in two- and three-dimensional kagome systems: Pseudofermion functional renormalization group perspective, Physical Review B **94**, 235138 (2016).

[P2] F. L. Buessen, D. Roscher, S. Diehl, and S. Trebst, Functional renormalization group approach to SU(N) Heisenberg models: Real-space RG at arbitrary N, Physical Review B **97**, 064415 (2018).

[P3] D. Roscher, F. L. Buessen, M. M. Scherer, S. Trebst, and S. Diehl, Functional renormalization group approach to SU(N) Heisenberg models: Momentum-space RG for the large-N limit, Physical Review B **97**, 064416 (2018).

[P4] F. L. Buessen, M. Hering, J. Reuther, and S. Trebst, Quantum Spin Liquids in Frustrated Spin-1 Diamond Antiferromagnets, Physical Review Letters **120**, 057201 (2018).

[P5] A. Revelli, C. C. Loo, D. Kiese, P. Becker, T. Fröhlich, T. Lorenz, M. M. Sala, G. Monaco, F. L. Buessen, J. Attig, M. Hermanns, S. V. Streltsov, D. I. Khomskii, J. van den Brink, M. Braden, P. H. M. van Loosdrecht, S. Trebst, A. Paramekanti, and M. Grüninger, Spin-orbit entangled j=1/2 moments in Ba2CeIrO6 - a frustrated fcc quantum magnet, arXiv:1901.06215 .

[P6] F. L. Buessen, V. Noculak, S. Trebst, and J. Reuther, Functional renormalization group for frustrated magnets with non-diagonal spin interactions, arXiv:1905.04190 .

[P7] A. Revelli, M. M. Sala, G. Monaco, C. Hickey, P. Becker, F. Freund, A. Jesche, P. Gegenwart, T. Eschmann, F. L. Buessen, S. Trebst, P. H. M. van Loosdrecht, J. van den Brink, and M. Grüninger, Fingerprints of Kitaev physics in the magnetic excitations of honeycomb iridates, arXiv:1905.13590 .

[1] L. Savary and L. Balents, Quantum Spin Liquids, Rep. Prog. Phys. **80**, 016502 (2017).

[2] C. Broholm, R. J. Cava, S. A. Kivelson, D. G. Nocera, M. R. Norman, and T. Senthil, Quantum Spin Liquids, arXiv:1905.07040 .

[3] A. Kitaev and J. Preskill, Topological Entanglement Entropy, Physical Review Letters **96**, 110404 (2006).

[4] A. Kitaev, Anyons in an exactly solved model and beyond, Annals of Physics **321**, 2 (2006).

[5] S. Trebst, Kitaev Materials, arXiv:1701.07056 .

[6] J. Reuther and P. Wölfle, J1-J2 frustrated two-dimensional Heisenberg model: Random phase approximation and functional renormalization group, Physical Review B **81**, 144410 (2010).

[7] A. Auerbach, *Interacting Electrons and Quantum Magnetism* (Springer New York, 1998).

[8] B. C. den Hertog and M. J. P. Gingras, Dipolar Interactions and Origin of Spin Ice in Ising Pyrochlore Magnets, Physical Review Letters **84**, 3430 (2000).

[9] M. Koshino, N. F. Q. Yuan, T. Koretsune, M. Ochi, K. Kuroki, and L. Fu, Maximally Localized Wannier Orbitals and the Extended Hubbard Model for Twisted Bilayer Graphene, Physical Review X **8**, 031087 (2018).

[10] K. Everschor-Sitte, J. Masell, R. M. Reeve, and M. Kläui, Perspective: Magnetic skyrmions—Overview of recent progress in an active research field, Journal of Applied Physics **124**, 240901 (2018).

[11] J. Villain, R. Bidaux, J.-P. Carton, and R. Conte, Order as an effect of disorder, Journal de Physique **41**, 1263 (1980).

[12] T. Holstein and H. Primakoff, Field Dependence of the Intrinsic Domain Magnetization of a Ferromagnet, Physical Review **58**, 1098 (1940).

[13] X. G. Wen, Quantum orders and symmetric spin liquids, Physical Review B **65**, 165113 (2002).

[14] G. Misguich and C. Lhuillier, Two-dimensional quantum antiferromagnets, in *Frustrated Spin Systems* (World Scientific, Singapore, 2004) p. 229.

[15] I. Affleck and J. B. Marston, Large-n limit of the Heisenberg-Hubbard model: Implications for high-T_c superconductors, Physical Review B **37**, 3774 (1988).

[16] M. A. Cazalilla and A. M. Rey, Ultracold Fermi gases with emergent SU(N) symmetry, Reports on Progress in Physics **77**, 124401 (2014).

[17] C. Xu and L. Balents, Topological Superconductivity in Twisted Multilayer Graphene, Physical Review Letters **121**, 087001 (2018).

[18] N. F. Q. Yuan and L. Fu, Model for the metal-insulator transition in graphene superlattices and beyond, Physical Review B **98**, 045103 (2018).

[19] E. Manousakis, The spin-1/2 Heisenberg antiferromagnet on a square lattice and its application to the cuprous oxides, Reviews of Modern Physics **63**, 1 (1991).

[20] P. Anderson, Resonating valence bonds: A new kind of insulator? Materials Research Bulletin **8**, 153 (1973).

[21] L. Balents, Spin liquids in frustrated magnets, Nature **464**, 199 (2010).

[22] B. Bernu, P. Lecheminant, C. Lhuillier, and L. Pierre, Exact spectra, spin susceptibilities, and order parameter of the quantum Heisenberg antiferromagnet on the triangular lattice, Physical Review B **50**, 10048 (1994).

[23] Y.-C. He, M. P. Zaletel, M. Oshikawa, and F. Pollmann, Signatures of Dirac Cones in a DMRG Study of the Kagome Heisenberg Model, Physical Review X **7**, 031020 (2017).

[24] C. Lanczos, An Iteration Method for the Solution of the Eigenvalue Problem of Linear Differential and Integral Operators, Journal of research of the National Bureau of Standards **45**, 255 (1950).

[25] Z. Y. Meng, T. C. Lang, S. Wessel, F. F. Assaad, and A. Muramatsu, Quantum spin liquid emerging in two-dimensional correlated Dirac fermions, Nature **464**, 847 (2010).

[26] J. Nasu, M. Udagawa, and Y. Motome, Vaporization of kitaev spin liquids, Physical Review Letters **113**, 197205 (2014).

[27] S. R. White, Density Matrix Formulation for Quantum Renormalization Groups, Physical Review Letters **69**, 2863 (1992).

[28] U. Schollwöck, The density-matrix renormalization group, Reviews of Modern Physics **77**, 259 (2005).

[29] S.-S. Gong, W. Zhu, and D. N. Sheng, Emergent Chiral Spin Liquid: Fractional Quantum Hall Effect in a Kagome Heisenberg Model, Scientific Reports **4**, 6317 (2014).

[30] S.-S. Gong, W. Zhu, L. Balents, and D. N. Sheng, Global phase diagram of competing ordered and quantum spin-liquid phases on the kagome lattice, Physical Review B **91**, 075112 (2015).

[31] J. Reuther and R. Thomale, Functional renormalization group for the anisotropic triangular antiferromagnet, Physical Review B **83**, 024402 (2011).

[32] R. Suttner, C. Platt, J. Reuther, and R. Thomale, Renormalization group analysis of competing quantum phases in the J1-J2 Heisenberg model on the kagome lattice, Physical Review B **89**, 020408 (2014).

[33] J. Reuther, R. Thomale, and S. Trebst, Finite-temperature phase diagram of the Heisenberg-Kitaev model, Physical Review B **84**, 100406(R) (2011).

[34] J. Reuther, P. Wölfle, R. Darradi, W. Brenig, M. Arlego, and J. Richter, Quantum phases of the planar antiferromagnetic J1-J2-J3 Heisenberg model, Physical Review B **83**, 064416 (2011).

[35] J. Reuther, D. A. Abanin, and R. Thomale, Magnetic order and paramagnetic phases in the quantum J1-J2-J3 honeycomb model, Physical Review B **84**, 014417 (2011).

[36] Y. Iqbal, R. Thomale, F. Parisen Toldin, S. Rachel, and J. Reuther, Functional renormalization group for three-dimensional quantum magnetism, Phys. Rev. B **94**, 140408(R) (2016).

[37] Y. Iqbal, T. Müller, K. Riedl, J. Reuther, S. Rachel, R. Valentí, M. J. P. Gingras, R. Thomale, and H. O. Jeschke, Signatures of a gearwheel quantum spin liquid in a spin-1/2 pyrochlore molybdate Heisenberg antiferromagnet, Physical Review Materials **1**, 071201 (2017).

[38] M. L. Baez and J. Reuther, Numerical treatment of spin systems with unrestricted spin length S: A functional renormalization group study, Physical Review B **96**, 045144 (2017).

[39] M. Hering and J. Reuther, Functional renormalization group analysis of Dzyaloshinsky-Moriya and Heisenberg spin interactions on the kagome lattice, Physical Review B **95**, 054418 (2017).

[40] J. Krieg and P. Kopietz, Exact renormalization group for quantum spin systems, Physical Review B **99**, 060403(R) (2019).

[41] M. Reuter and F. Saueressig, *Quantum Gravity and the Functional Renormalization Group* (Cambridge University Press, 2018).

[42] F. Kopietz, Peter and Bartosch, Lorenz and Schütz, *Introduction to the Functional Renormalization Group* (Springer, Berlin, Heidelberg, 2010).

[43] R. Hedden, V. Meden, T. Pruschke, and K. Schönhammer, A functional renormalization group approach to zero-dimensional interacting systems, Journal of Physics: Condensed Matter **16**, 5279 (2004).

[44] M. Salmhofer, C. Honerkamp, W. Metzner, and O. Lauscher, Renormalization Group Flows into Phases with Broken Symmetry, Progress of Theoretical Physics **112**, 943 (2004).

[45] W. Metzner, M. Salmhofer, C. Honerkamp, V. Meden, and K. Schönhammer, Functional renormalization group approach to correlated fermion systems, Reviews of Modern Physics **84**, 299 (2012).

[46] C. Wetterich, Exact evolution equation for the effective potential, Physics Letters B **301**, 90 (1993).

[47] A. Altland and B. Simons, *Condensed Matter Field Theory* (Cambridge University Press, Cambridge, 2010).

[48] J. W. Negele and H. Orland, *Quantum many particle systems* (Addison-Wesley, New York, 1988).

[49] P. Kopietz, L. Bartosch, and F. Schütz, Exact FRG flow equations, in *Lecture Notes in Physics*, Vol. 798 (Springer, Berlin, Heidelberg, 2010) p. 181.

[50] M. Rigol and R. R. P. Singh, Kagome lattice antiferromagnets and Dzyaloshinsky-Moriya interactions, Physical Review B **76**, 184403 (2007).

[51] S. M. Winter, Y. Li, H. O. Jeschke, and R. Valentí, Challenges in design of Kitaev materials: Magnetic interactions from competing energy scales, Physical Review B **93**, 214431 (2016).

[52] A. A. Abrikosov, Electron scattering on magnetic impurities in metals and anomalous resistivity effects, Physics Physique Fizika **2**, 5 (1965).

[53] V. N. Popov and S. A. Fedotov, The functional-integration method and diagram technique for spin systems, Journal of Experimental and Theoretical Physics **67**, 535 (1988).

[54] D. Roscher, N. Gneist, M. M. Scherer, S. Trebst, and S. Diehl, Cluster functional renormalization group and absence of a bilinear spin liquid in the J1-J2-Heisenberg model, arXiv:1905.01060 .

[55] I. Affleck, Z. Zou, T. Hsu, and P. W. Anderson, SU(2) gauge symmetry of the large-U limit of the Hubbard model, Physical Review B **38**, 745 (1988).

[56] B. Bauer, L. Cincio, B. Keller, M. Dolfi, G. Vidal, S. Trebst, and A. Ludwig, Chiral spin liquid and emergent anyons in a Kagome lattice Mott insulator, Nature Communications **5**, 5137 (2014).

[57] B. Bauer, B. P. Keller, S. Trebst, and A. W. W. Ludwig, Symmetry-protected non-Fermi liquids, kagome spin liquids, and the chiral Kondo lattice model, Physical Review B **99**, 035155 (2019).

[58] H. Yao and S. A. Kivelson, Exact Chiral Spin Liquid with Non-Abelian Anyons, Physical Review Letters **99**, 247203 (2007).

[59] P. Kopietz, L. Bartosch, and F. Schütz, Functional Methods, in *Lecture Notes in Physics*, Vol. 798 (Springer, Berlin, Heidelberg, 2010) p. 147.

[60] J. Reuther, *Frustrated quantum Heisenberg antiferromagnets: functional renormalization-group approach in auxiliary-fermion representation*, Ph.D. thesis (2011).

[68] W. Witczak-Krempa, G. Chen, Y. B. Kim, and L. Balents, Correlated Quantum Phenomena in the Strong Spin-Orbit Regime, Annual Review of Condensed Matter Physics **5**, 57 (2014).

[62] J. G. Rau, E. K.-H. Lee, and H.-Y. Kee, Spin-Orbit Physics Giving Rise to Novel Phases in Correlated Systems: Iridates and Related Materials, Annual Review of Condensed Matter Physics **7**, 195 (2016).

[63] A. Zorko, S. Nellutla, J. van Tol, L. C. Brunel, F. Bert, F. Duc, J.-C. Trombe, M. A. de Vries, A. Harrison, and P. Mendels, Dzyaloshinsky-Moriya Anisotropy in the Spin-1/2 Kagome Compound ZnCu3(OH)6Cl2, Physical Review Letters **101**, 026405 (2008).

[64] J. D. Thompson, P. A. McClarty, D. Prabhakaran, I. Cabrera, T. Guidi, and R. Coldea, Quasiparticle Breakdown and Spin Hamiltonian of the Frustrated Quantum Pyrochlore Yb2Ti2O7 in a Magnetic Field, Physical Review Letters **119**, 057203 (2017).

[65] H. Yan, O. Benton, L. Jaubert, and N. Shannon, Theory of multiple-phase competition in pyrochlore magnets with anisotropic exchange with application to Yb2Ti2O7, Er2Ti2O7, and Er2Sn2O7, Physical Review B **95**, 094422 (2017).

[66] T. R. Morris, The exact renormalization group and approximate solutions, International Journal of Modern Physics A **09**, 2411 (1994).

[67] A. A. Katanin, Fulfillment of Ward identities in the functional renormalization group approach, Physical Review B **70**, 115109 (2004).

[68] D. Bergeron and A.-M. S. Tremblay, Algorithms for optimized maximum entropy and diagnostic tools for analytic continuation, Physical Review E **94**, 023303 (2016).

[69] N. Wentzell, G. Li, A. Tagliavini, C. Taranto, G. Rohringer, K. Held, A. Toschi, and S. Andergassen, High-frequency asymptotics of the vertex function: diagrammatic parametrization and algorithmic implementation, arXiv:1610.06520 .

[70] L. D. Landau, On the theory of phase transitions, Zh. Eksp. Teor. Fiz. **7**, 19 (1937).

[71] F. B. Kugler and J. von Delft, Multiloop functional renormalization group for general models, Physical Review B **97**, 035162 (2018).

[72] A. Tagliavini, C. Hille, F. Kugler, S. Andergassen, A. Toschi, and C. Honerkamp, Multiloop functional renormalization group for the two-dimensional Hubbard model: Loop convergence of the response functions, SciPost Physics **6**, 009 (2019).

[73] M. Rueck and J. Reuther, Effects of two-loop contributions in the pseudofermion functional renormalization group method for quantum spin systems, Physical Review B **97**, 144404 (2018).

[74] D. P. Arovas and A. Auerbach, Functional integral theories of low-dimensional quantum Heisenberg models, Physical Review B **38**, 316 (1988).

[75] F. Bloch, Zur Theorie des Ferromagnetismus, Zeitschrift für Physik **61**, 206 (1930).

[76] F. J. Dyson, General Theory of Spin-Wave Interactions, Physical Review **102**, 1217 (1956).

[77] Z.-X. Liu, Y. Zhou, and T.-K. Ng, Fermionic theory for quantum antiferromagnets with spin $S > 1/2$, Physical Review B **82**, 144422 (2010).

[78] I. Affleck and F. D. M. Haldane, Critical theory of quantum spin chains, Physical Review B **36**, 5291 (1987).

[79] N. Prokof'ev and B. Svistunov, From Popov-Fedotov trick to universal fermionization, Physical Review B **84**, 073102 (2011).

[80] J. M. Luttinger and L. Tisza, Theory of Dipole Interaction in Crystals, Physical Review **70**, 954 (1946).

[81] M. Hering, J. Sonnenschein, Y. Iqbal, and J. Reuther, Characterization of quantum spin liquids and their spinon band structures via functional renormalization, Physical Review B **99**, 100405(R) (2019).

[82] R. Moessner and J. T. Chalker, Low-temperature properties of classical geometrically frustrated antiferromagnets, Physical Review B **58**, 12049 (1998).

[83] R. Moessner and J. T. Chalker, Properties of a Classical Spin Liquid: The Heisenberg Pyrochlore Antiferromagnet, Physical Review Letters **80**, 2929 (1998).

[84] B. Canals and C. Lacroix, Pyrochlore Antiferromagnet: A Three-Dimensional Quantum Spin Liquid, Physical Review Letters **80**, 2933 (1998).

[85] B. Canals and C. Lacroix, Quantum spin liquid: The Heisenberg antiferromagnet on the three-dimensional pyrochlore lattice, Physical Review B **61**, 1149 (2000).

[86] H. Takagi and S. Niitaka, Highly Frustrated Magnetism in Spinels, in *Introduction to Frustrated Magnetism: Materials, Experiments, Theory* (Springer Berlin Heidelberg, Berlin, Heidelberg, 2011) p. 155.

[87] D. Bergman, J. Alicea, E. Gull, S. Trebst, and L. Balents, Order-by-disorder and spiral spin-liquid in frustrated diamond-lattice antiferromagnets, Nature Physics **3**, 487 (2007).

[88] S. Gao, O. Zaharko, V. Tsurkan, Y. Su, J. S. White, G. S. Tucker, B. Roessli, F. Bourdarot, R. Sibille, D. Chernyshov, T. Fennell, A. Loidl, and C. Rüegg, Spiral spin-liquid and the emergence of a vortex-like state in MnSc2S4, Nature Physics **13**, 157.

[89] V. Fritsch, J. Hemberger, N. Büttgen, E.-W. Scheidt, H.-A. Krug von Nidda, A. Loidl, and V. Tsurkan, Spin and Orbital Frustration in MnSc2S4 and FeSc2S4, Physical Review Letters **92**, 116401 (2004).

[90] N. Tristan, J. Hemberger, A. Krimmel, H.-A. Krug von Nidda, V. Tsurkan, and A. Loidl, Geometric frustration in the cubic spinels MAl2O4 (M=Co, Fe, and Mn), Physical Review B **72**, 174404 (2005).

[91] T. Suzuki, H. Nagai, M. Nohara, and H. Takagi, Melting of antiferromagnetic ordering in spinel oxide CoAl2O4, Journal of Physics: Condensed Matter **19**, 145265 (2007).

[92] J. R. Chamorro and T. M. McQueen, Frustrated Spin One On A Diamond Lattice, Physical Review Materials , 034404 (2018).

[93] J. Attig and S. Trebst, Classical spin spirals in frustrated magnets from free-fermion band topology, Physical Review B **96**, 085145 (2017).

[94] N. Niggemann, M. Hering, and J. Reuther, Classical spiral spin liquids as a possible route to quantum spin liquids, arXiv:1905.11318 .

[95] S. Lee and L. Balents, Theory of the ordered phase in A-site antiferromagnetic spinels, Physical Review B **78**, 144417 (2008).

[96] J. S. Bernier, M. J. Lawler, and Y. B. Kim, Quantum order by disorder in frustrated diamond lattice antiferromagnets, Physical Review Letters **101**, 047201 (2008).

[97] Y. Iqbal, T. Müller, P. Ghosh, M. J. Gingras, H. O. Jeschke, S. Rachel, J. Reuther, and R. Thomale, Quantum and Classical Phases of the Pyrochlore Heisenberg Model with Competing Interactions, Physical Review X **9**, 011005 (2019).

[98] H. T. Diep and H. Kawamura, First-order phase transition in the fcc Heisenberg antiferromagnet, Physical Review B **40**, 7019 (1989).

[99] M. V. Gvozdikova and M. E. Zhitomirsky, A Monte Carlo study of the first-order transition in a Heisenberg FCC antiferromagnet, Journal of Experimental and Theoretical Physics Letters **81**, 236 (2005).

[100] C. L. Henley, Ordering by disorder: Ground-state selection in fcc vector antiferromagnets, Journal of Applied Physics **61**, 3962 (1987).

[101] A. Krimmel, M. Mücksch, V. Tsurkan, M. M. Koza, H. Mutka, C. Ritter, D. V. Sheptyakov, S. Horn, and A. Loidl, Magnetic ordering and spin excitations in the frustrated magnet MnSc2S4, Physical Review B **73**, 014413 (2006).

[102] J. R. Chamorro, L. Ge, J. Flynn, M. Subramanian, M. Mourigal, and T. M. McQueen, Frustrated S=1 On A Diamond Lattice, arXiv:1701.06674v1 .

[103] G. Chen, Quantum Paramagnet and Frustrated Quantum Criticality in a Spin-One Diamond Lattice Antiferromagnet, Physical Review B **96**, 020412(R) (2017).

[104] S. Das, D. Nafday, T. Saha-Dasgupta, and A. Paramekanti, The Curious Case of NiRh2O4: A Spin-Orbit Entangled Diamond Lattice Paramagnet, arXiv:1905.11403 .

[105] S. V. Streltsov and D. I. Khomskii, Orbital physics in transition metal compounds: new trends, Physics-Uspekhi **60**, 1121 (2017).

[106] A. P. Ramirez, Strongly Geometrically Frustrated Magnets, Annual Review of Materials Science **24**, 453 (1994).

[107] A. A. Aczel, J. P. Clancy, Q. Chen, H. D. Zhou, D. Reig-i Plessis, G. J. MacDougall, J. P. C. Ruff, M. H. Upton, Z. Islam, T. J. Williams, S. Calder, and J.-Q. Yan, Revisiting the Kitaev material candidacy of Ir4+ double perovskite iridates, Physical Review B **99**, 134417 (2019).

[108] G. Baskaran, D. Sen, and R. Shankar, Spin-S Kitaev model: Classical ground states, order from disorder, and exact correlation functions, Physical Review B **78**, 115116 (2008).

[109] M. Hermanns, I. Kimchi, and J. Knolle, Physics of the Kitaev Model: Fractionalization, Dynamic Correlations, and Material Connections, Annual Review of Condensed Matter Physics **9**, 17 (2018).

[110] V. Elser, Nuclear antiferromagnetism in a registered He3 solid, Physical Review Letters **62**, 2405 (1989).

[111] R. R. P. Singh and D. A. Huse, Ground state of the spin-1/2 kagome-lattice Heisenberg antiferromagnet, Physical Review B **76**, 180407 (2007).

[112] Y. Ran, M. Hermele, P. A. Lee, and X.-G. Wen, Projected-Wave-Function Study of the Spin-1/2 Heisenberg Model on the Kagomé Lattice, Physical Review Letters **98**, 117205 (2007).

[113] S. Yan, D. A. Huse, and S. R. White, Spin-liquid ground state of the S=1/2 kagome Heisenberg antiferromagnet. Science **332**, 1173 (2011).

[114] H.-C. Jiang, Z. Wang, and L. Balents, Identifying topological order by entanglement entropy, Nature Physics **8**, 902 (2012).

[115] B. Fåk, E. Kermarrec, L. Messio, B. Bernu, C. Lhuillier, F. Bert, P. Mendels, B. Koteswararao, F. Bouquet, J. Ollivier, A. D. Hillier, A. Amato, R. H. Colman, and A. S. Wills, Kapellasite: A Kagome Quantum Spin Liquid with Competing Interactions, Physical Review Letters **109**, 037208 (2012).

[116] M. P. Shores, E. A. Nytko, B. M. Bartlett, and D. G. Nocera, A Structurally Perfect S=1/2 Kagomé Antiferromagnet, Journal of the American Chemical Society **127**, 13462 (2005).

[117] P. Mendels and F. Bert, Quantum Kagome Antiferromagnet ZnCu3(OH)6Cl2, Journal of the Physical Society of Japan **79**, 011001 (2010).

[118] M. Norman, Colloquium: Herbertsmithite and the search for the quantum spin liquid, Reviews of Modern Physics **88**, 041002 (2016).

[119] Y. Iqbal, H. O. Jeschke, J. Reuther, R. Valentí, I. I. Mazin, M. Greiter, and R. Thomale, Paramagnetism in the kagome compounds (Zn,Mg,Cd)Cu3(OH)6Cl2, Physical Review B **92**, 220404(R) (2015).

[120] J. N. Reimers and A. J. Berlinsky, Order by disorder in the classical Heisenberg kagomé antiferromagnet, Physical Review B **48**, 9539 (1993).

[121] M. E. Zhitomirsky, Octupolar ordering of classical kagome antiferromagnets in two and three dimensions, Physical Review B **78**, 094423 (2008).

[122] G.-W. Chern and R. Moessner, Dipolar Order by Disorder in the Classical Heisenberg Antiferromagnet on the Kagome Lattice, Physical Review Letters **110**, 077201 (2013).

[123] M. Elhajal, B. Canals, and C. Lacroix, Symmetry breaking due to Dzyaloshinsky-Moriya interactions in the kagomé lattice, Physical Review B **66**, 014422 (2002).

[124] T.-H. Han, M. R. Norman, J.-J. Wen, J. A. Rodriguez-Rivera, J. S. Helton, C. Broholm, and Y. S. Lee, Correlated impurities and intrinsic spin-liquid physics in the kagome material herbertsmithite, Physical Review B **94**, 060409 (2016).

[125] R. Gezzi, T. Pruschke, and V. Meden, Functional renormalization group for nonequilibrium quantum many-body problems, Physical Review B **75**, 045324 (2007).

Acknowledgements

First and foremost, I want to express my deepest gratitude to Simon Trebst for collaborating with me on all these projects and for providing invaluable guidance in the first steps of my scientific career. I feel that I have received the best possible education under his mentorship.

I genuinely thank everyone who has collaborated with me over the years. I have particularly enjoyed working with other FRG practitioners in Cologne: Michael Scherer, Dietrich Roscher, Sebastian Diehl, and Dominik Kiese who has been the leading force behind running the pf-FRG calculations on the fcc lattice model. Likewise, I have very much enjoyed collaborating with the experimentalists from Cologne around Alessandro Revelli and Markus Grüninger. My thanks also go out to Johannes Reuther who has generously shared his expertise on pf-FRG calculations with me ever since I started working in the field.

Andreas Sindermann and Petra Neubauer-Guenther deserve special credit for the great deal of work they put into administrative tasks around the Institute of Theoretical Physics at the University of Cologne and the Bonn-Cologne Graduate School of Physics and Astronomy, respectively, and for ensuring a smooth-running work environment. I thank the Bonn-Cologne Graduate School of Physics and Astronomy for support and for their well thought-out study program.

Numerical simulations have been performed on the JUWELS cluster and the JURECA Booster at the Forschungszentrum Juelich, as well as on the CHEOPS cluster at RRZK Cologne.

I thank Jan Attig, Dominik Kiese, and Henry Legg who have been a big help in proofreading the thesis.

During my time in Cologne I have had the pleasure of meeting countless new friends and colleagues, and I expressly want to thank every single one of them for making my time here very enjoyable. I am deeply grateful to all of my close friends, my siblings, and to my parents whose continuous support and encouragement has been instrumental in writing this thesis.

Eigenständigkeitserklärung

Ich versichere, dass ich die von mir vorgelegte Dissertation selbständig angefertigt, die benutzten Quellen und Hilfsmittel vollständig angegeben und die Stellen der Arbeit – einschließlich Tabellen, Karten und Abbildungen –, die anderen Werken im Wortlaut oder dem Sinn nach entnommen sind, in jedem Einzelfall als Entlehnung kenntlich gemacht habe; dass diese Dissertation noch keiner anderen Fakultät oder Universität zur Prüfung vorgelegen hat; dass sie – abgesehen von unten angegebenen Teilpublikationen – noch nicht ver öffentlicht worden ist, sowie, dass ich eine solche Veröffentlichung vor Abschluss des Promotionsverfahrens nicht vornehmen werde. Die Bestimmungen der Promotionsordnung sind mir bekannt. Die von mir vorgelegte Dissertation ist von Prof. Dr. Simon Trebst betreut worden.

Finn Lasse Büßen

Bereits veröffentlichte Teilpublikationen sind auf der Folgeseite aufgeführt.

Publikationen

[P1] F. L. Buessen and S. Trebst, Competing magnetic orders and spin liquids in two- and three-dimensional kagome systems: Pseudofermion functional renormalization group perspective, Physical Review B **94,** 235138 (2016)

[P2] F. L. Buessen, D. Roscher, S. Diehl, and S. Trebst, Functional renormalization group approach to SU(N) Heisenberg models: Real-space RG at arbitrary N, Physical Review B **97,** 064415 (2018)

[P3] D. Roscher, F. L. Buessen, M. M. Scherer, S. Trebst, and S. Diehl, Functional renormalization group approach to SU(N) Heisenberg models: Momentum-space RG for the large-N limit, Physical Review B **97,** 064416 (2018)

[P4] F. L. Buessen, M. Hering, J. Reuther, and S. Trebst, Quantum Spin Liquids in Frustrated Spin-1 Diamond Antiferromagnets, Physical Review Letters **120,** 057201 (2018)

[P5] A. Revelli, C. C. Loo, D. Kiese, P. Becker, T. Fröhlich, T. Lorenz, M. M. Sala, G. Monaco, F. L. Buessen, J. Attig, M. Hermanns, S. V. Streltsov, D. I. Khomskii, J. van den Brink, M. Braden, P. H. M. van Loosdrecht, S. Trebst, A. Paramekanti, and M. Grüninger, Spin-orbit entangled j=1/2 moments in Ba2CeIrO6 – a frustrated fcc quantum magnet, arXiv:1901.06215

[P6] F. L. Buessen, V. Noculak, S. Trebst, and J. Reuther, Functional renormalization group for frustrated magnets with non-diagonal spin interactions, arXiv:1905.04190

[P7] A. Revelli, M. Moretti Sala, G. Monaco, C. Hickey, P. Becker, F. Freund, A. Jesche, P. Gegenwart, T. Eschmann, F. L. Buessen, S. Trebst, P. H. M. van Loosdrecht, J. van den Brink, and M. Grüninger, Fingerprints of Kitaev physics in the magnetic excitations of honeycomb iridates, arXiv:1905.13590

When sizable quantum fluctuations and strong frustration mechanisms act in concert to repel the formation of conventional long-range order in quantum magnets, they can make way for massively entangled spin liquid phases which may imbue the material with extraordinary properties. However, the simulation of such quantum many-body systems poses a serious challenge even to modern numerical techniques, particularly in the case of frustrated quantum magnetism in three spatial dimensions. Such models evade tractability by many established approaches, leaving a methodological void.

In this thesis, we present a generalized implementation of the pseudofermion functional renormalization group (pf-FRG) which is suited to numerically simulate arbitrary microscopic models with diagonal or off-diagonal two-spin interactions even in three-dimensional frustrated quantum magnets. We provide insight into the inner workings of the method which has emerged over the course of the last couple of years, arguing that the pf-FRG formalism simultaneously combines aspects of a large-S expansion as well as a large-N expansion on equal footing, thus being able to resolve the subtle interplay between magnetic ordering tendencies and disruptive quantum fluctuations. Moreover, on a case by case basis we explore the stability of quantum spin liquids in paradigmatic models of frustrated quantum magnetism and elucidate the joint action of geometric frustration, exchange frustration, and quantum fluctuations to inhibit the formation of magnetic long-range order.

University of Cologne

thp Institute for Theoretical Physics University of Cologne